Quantum control of interacting nuclear and electron spins in diamond

Bartling, H.P.

DOI
10.4233/uuid:5c27f652-137c-46ec-b31b-ba01367323b4

Publication date
2023

Document Version
Final published version

Citation (APA)
Bartling, H. P. (2023). *Quantum control of interacting nuclear and electron spins in diamond*. [Dissertation (TU Delft), Delft University of Technology]. https://doi.org/10.4233/uuid:5c27f652-137c-46ec-b31b-ba01367323b4

Important note
To cite this publication, please use the final published version (if applicable).
Please check the document version above.

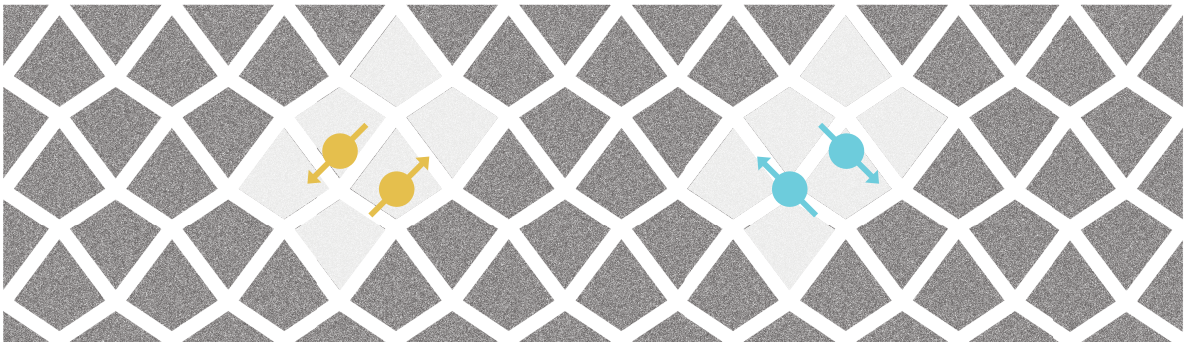

QUANTUM CONTROL OF INTERACTING NUCLEAR AND ELECTRON SPINS IN DIAMOND

Hans Bartling

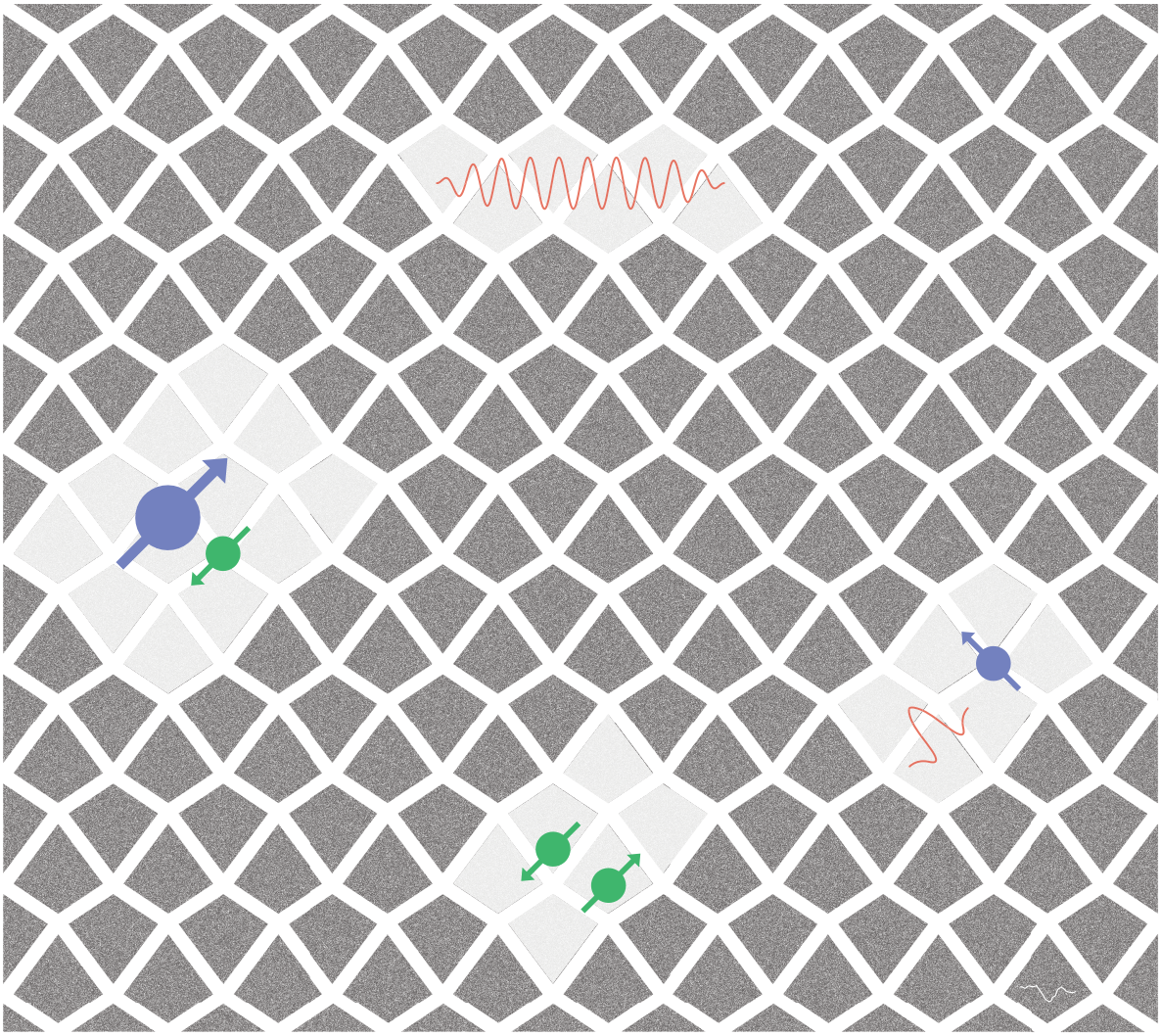

QUANTUM CONTROL OF INTERACTING NUCLEAR AND ELECTRON SPINS IN DIAMOND

Dissertation

for the purpose of obtaining the degree of doctor
at Delft University of Technology,
by the authority of the Rector Magnificus, Prof. dr. ir. T.H.J.J. van der Hagen,
Chair of the Board for Doctorates,
to be defended publicly on
Friday 13 October 2023 at 10:00 o'clock

by

Hans Peter BARTLING

Master of Science in Applied Physics,
Delft University of Technology, The Netherlands,
born in Apeldoorn, The Netherlands.

This dissertation has been approved by the promotor:
Prof. dr. ir. R. Hanson

Composition of the doctoral committee:

Rector Magnificus	Chairperson
Prof. dr. ir. R. Hanson	Delft University of Technology, Promotor
Dr. ir. T. H. Taminiau	Delft University of Technology, Copromotor
Independent members:	
Dr. P. Bertet	CEA Paris-Saclay, France
Prof. dr. ir. F.A. Zwanenburg	University of Twente
Prof. dr. A.F. Otte	Delft University of Technology
Prof. dr. L. DiCarlo	Delft University of Technology
Prof. dr. B.M. Terhal	Delft University of Technology

Printed by: Gildeprint - Enschede

Cover design: Victoria Imasaki Affonso, Hans Bartling

Casimir PhD Series, Delft-Leiden 2023-26

ISBN 978-90-8593-574-2

An electronic version of this dissertation is available at
`http://repository.tudelft.nl/`.

CONTENTS

SUMMARY

Quantum technologies promise to have a profound impact on society. A quantum computer will be able to solve particular computational problems, the quantum internet brings forth a new, fundamentally secure communication paradigm and quantum sensors enable unprecedented sensitivity. While the exact areas of application and societal value are still largely unknown, the underlying technologies are being improved steadily.

There is a wide variety of hardware that quantum technologies can be built with. In this thesis, we perform experiments with the nitrogen-vacancy (NV) center in diamond, which is a defect in the diamond lattice that traps an optically active electron spin. Several hallmark experiments have been performed with the NV center in recent years, including (but not limited to) the demonstration of a three-node quantum network, the control over a 10-qubit register and the fault-tolerant encoding of a logical qubit. To go beyond current experiments, two key areas of improvement can be identified. First, the generation of entanglement between NV centers should be improved. And second, the control of spins surrounding the NV center in the diamond lattice should be extended and improved. This thesis focuses on the latter challenge.

^{13}C nuclear spins surrounding the NV center serve as a source of additional qubits. In this thesis, we first show that pairs of close-by ^{13}C spins form a new type of qubit with a coherence time of $T_2^* = 1.9(6)$ min, which is four orders-of-magnitude larger than single ^{13}C nuclear spins. These ^{13}C spin pairs are promising as memories for quantum information.

Next, we demonstrate initialisation, control and entanglement of individual electron spins in the neighbourhood of the NV center. These electron spins are associated to another type of defect, the P1 center. Analogously to ^{13}C spins, two P1 electron spins can also be in close proximity. In what follows, we develop initialisation, control and readout of a pair of P1 electron spins. We then image the P1 centers with sub-nm resolution, indicating that such methods might create opportunities towards imaging individual molecules.

The NV center consists of an optically active electron spin, but also hosts a ^{14}N nuclear spin that can be used as an additional qubit. In this thesis' final work, we develop full two-qubit control over the electron and nitrogen spin of the NV center. We use a tool called gate set tomography to characterise and improve our quantum gates. We demonstrate single-qubit fidelities of 99.999(1)% and two-qubit fidelities exceeding 99.9%, amongst the highest fidelities reported to this day for all qubit platforms.

Together, the work presented in this thesis contributes to the quantum control of the nuclear- and electron-spin environment of the NV center in diamond. While the experiments have been performed on the NV center, the methods introduced can be extended to other defects in other materials.

SAMENVATTING

Quantumtechnologieën beloven een vergaande impact op onze maatschappij te hebben. Een quantumcomputer kan specifieke rekenproblemen oplossen, het quantuminternet biedt een nieuwe, fundamenteel veilige manier van communicatie en quantumsensoren maken ongeëvenaarde gevoeligheid mogelijk. Hoewel de precieze toepassingen en maatschappelijke waarde nog grotendeels onbekend zijn, worden de onderliggende technologieën gestaag verbeterd.

Er is een grote variëteit aan hardware waar quantumtechnologieën mee gebouwd kunnen worden. In deze scriptie doen we experimenten met het stikstof-gat (nitrogen-vacancy, NV) defect in diamant. Dit is een defect in de diamantstructuur waar een optisch actief elektron gevangen zit. Er zijn de laatste jaren verschillende, belangrijke experimenten met het stikstof-gat defect gedaan, waaronder de demonstratie van een quantumnetwerk bestaande uit drie knooppunten, de controle over een register bestaande uit 10 qubits en de fout-tolerante encodering van een logische qubit. Om verder te gaan dan de huidige experimenten, kunnen er twee globale gebieden van verbetering worden onderscheiden. Ten eerste moet het creëren van verstrengeling tussen stikstof-gat defecten worden verbeterd. En ten tweede moet de controle over qubits rondom het stikstof-gat defect in diamant worden uitgebreid en verbeterd. Het is de laatstgenoemde uitdaging waar deze scriptie zich mee bezig houdt.

^{13}C kernspins rondom het stikstof-gat defect dienen als een bron van aanvullende qubits. In deze scriptie laten we eerst zien dat paren van ^{13}C kernspins een nieuw soort qubit vormen met een coherentie tijd van $T_2^* = 1.9(6)$ min, vier orders van grootte langer dan enkele ^{13}C kernspins. Deze ^{13}C spin paren zijn dan ook veelbelovend als geheugen voor quantuminformatie.

Daarna demonstreren we initialisatie, controle en verstrengeling van individuele elektronen in de omgeving van het stikstof-gat defect. Deze elektronen behoren tot een ander soort defect, het P1 center. Overeenkomstig met ^{13}C spins, kunnen twee P1 elektronen ook in elkaars nabijheid voorkomen. In wat volgt, ontwikkelen we initialisatie, controle en uitlezing van een paar van P1 elektronen. We vinden de posities van de P1 centers met sub-nanometer resolutie, wat de belofte van de gebruikte methoden laat zien om individuele moleculen te bekijken.

Het stikstof-gat defect bestaat uit een optisch actief elektron, maar ook uit een ^{14}N kernspin die gebruikt kan worden als extra qubit. In het laatste experiment van deze scriptie ontwikkelen we volledige, twee-qubit controle over het elektron-stikstof systeem van het stikstof-gat defect. We gebruiken een methode genaamd 'gate set tomography' om onze quantumoperaties te karakteriseren en te verbeteren. We laten één-qubit fidelities zien van 99.999(1)% en twee-qubit fidelities boven 99.9%, wat onder de hoogste gerapporteerde waardes valt voor alle qubitplatforms.

Als geheel draagt het werk in deze scriptie bij aan de quantumcontrole over de kernspin- en elektronomgeving van het stikstof-gat defect in diamant. Hoewel de experi-

menten op het stikstof-gat defect zijn uitgevoerd, kunnen de geïntroduceerde methodes worden uitgebreid naar andere defecten in andere materialen.

1

INTRODUCTION

Radically new technologies do not start out solving a well-defined problem. The computer or the Internet was not initially envisaged to take its role in society that it does today. The development of quantum technologies promises a similar trajectory. Not in that we will reread our favourite Cicero biography on a quantum e-reader in 2050, but in that its future role in society is very much unknown right now.

The promises of quantum technologies are there. Broadly speaking, we can discern four different categories where quantum technologies can contribute: computation, simulation, communication and metrology. We will briefly discuss each of these now.

The basic building block of a quantum computer is a quantum bit (or qubit) as opposed to the classical bit. Together with the property of entanglement between two qubits, we enter a new computing paradigm. Quantum computers promise to solve important challenges in fields as diverse as physics, medicine and material science[1,2]. Algorithms designed for a quantum computer show exponential speed-up compared to their classical counterparts[1]. While proof-of-principle experiments of the advantage of quantum computers in dedicated tasks have been performed[3,4], practical applications are not yet within reach of current hardware.

Quantum simulation takes a different approach. When the quantum hardware has characteristics that map well to a specific problem in physics, it can be used directly to simulate that physical system. In particular, quantum simulators can be used to investigate phases of matter and strongly correlated systems[5–8]. While the classes of problems that map to a specific quantum hardware are likely limited, a number of interesting physical problems can be simulated[5–8].

Quantum communication promises fundamentally secure information transfer between remote locations[9,10]. With the advent of the quantum computer, current cryptographic methods are under threat of becoming decipherable through Shor's algorithm[11]. To maintain information security, a switch to quantum-robust cryptographic methods is therefore required. A classical approach is to base cryptographic methods on mathematical problems that are difficult to solve even for large-scale quantum computers[12]. Alternatively, quantum techniques such as quantum key distribution[13] can be used to generate secure keys between remote locations.

Quantum sensing and metrology use quantum systems to measure a physical quantity of interest. Quantum systems can be sensitive to their environment, ranging from

magnetic and electric fields to temperature and gravitational fields[14]. The high degree of sensitivity of these quantum systems can allow for better-than-classical sensing of environmental perturbations[14]. An interesting example is the prospect of imaging individual molecules with quantum sensors[15–19]. Alternatively, a quantum system's insensitivity to environmental perturbations makes extremely accurate measurements of its frequency possible. Such atomic clocks can serve as improved frequency standards[20].

Each application of quantum technologies mentioned above may have different optimal hardware, ranging from superconducting qubits to neutral atom arrays to spin qubits. A promising general architecture is a distributed architecture, where small-scale quantum information processors are connected together in a network fashion (Fig. 1.1)[21,22].

Depending on the application, the distances between the quantum information processing nodes can vary. For distributed quantum computation, the distances are likely small. The connections between separate nodes can then be made by for example microwave photons for superconducting qubits[23], on-chip or short-range optical connections for optically active spin qubits[24–26] or electron shuttling for semiconductor spin qubits[27–29].

For quantum communication, this distributed architecture is a necessary requirement to set up connections between remote locations. Therefore, larger distances need to be covered compared to distributed quantum computation. Optical photons are promising as a medium of information transfer due to their speed and long coherence. Likely candidates are therefore quantum systems that naturally possess an optical interface, such as trapped ions, neutral atoms, quantum dots or optically active defects[30–33]. At telecom wavelengths the photon loss in optical fibers is particularly low, motivating the conversion of photons to telecom and the search for quantum systems naturally operating at those wavelengths[34–36]. Quantum hardware systems that do not naturally operate at optical frequencies, such as superconducting qubits, can also be part of a quantum network. A translation between the qubit's native frequency and the optical frequencies is then necessary. Recent progress in quantum transduction between microwave and optical frequencies can help bridge this gap[37,38].

In the quantum sensing domain, distances between nodes can be either small or large depending on the quantity of interest. Networks of entangled quantum sensors can enhance sensitivity, for example for magnetic field sensing, phase sensing or precision clocks[39–42].

Colour centers in diamond or other materials are a promising candidate for a node in such a distributed architecture[43–46]. They offer several advantages. First, they naturally have an optical interface combined with a local spin register[47]. Second, solid-state spins have long coherence times[47–52]. Third, the operating temperature for a number of colour centers can be relatively high at 1-10 K, or even higher. Finally, colour centers are compatible with on-chip photonic integration[26,53].

The nitrogen-vacancy (NV) center in diamond is a prime example. The NV electron spin and surrounding nuclear spins have shown excellent coherence[47,49–52]. Optical initialisation and readout can be performed with high fidelity either resonantly at low temperature[54] or off-resonantly at room temperature[55–57]. Entanglement between remote nodes has been demonstrated with up to three nodes[58–62]. Each node provides a register

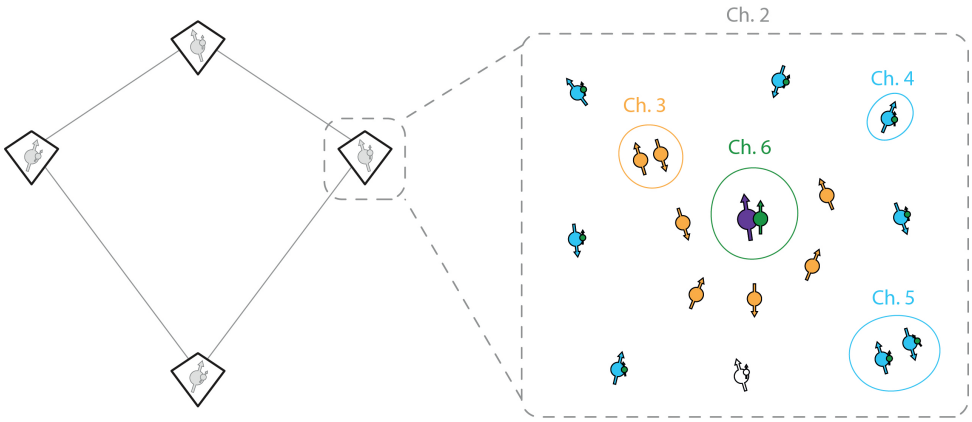

Figure 1.1: **A diamond-based quantum network.** Illustration of a diamond-based quantum network (left), with a zoom-in of a single network node (right). Individual nodes are connected by optical links that are used to generate inter-node entanglement. The network node consists of a central NV center with an electron (purple) and nitrogen (green) spin. In close proximity of the NV center there are ^{13}C nuclear spins and spin pairs (yellow). Further away, other defect centers such as P1 centers (blue) are found. Other defects and spin species can also be found in the spin environment (white). The part of the spin environment that each chapter of this thesis deals with is indicated.

of nuclear spins that can be detected and controlled with high fidelity[15,47,63], which has lead to initial demonstrations of error-correctable logical qubits[64–67].

To construct larger, distributed quantum networks the NV center has some challenges. The probability to emit a photon in the zero-phonon line (ZPL), a requirement for remote entanglement generation, is relatively low at $\sim 3\%$[68–70]. Embedding the NV center in an optical cavity can help boost this fraction, as well as increase the photon collection efficiency[33]. However, the relative sensitivity of the NV center to electric fields makes it challenging to embed it in a cavity, in particular in photonic crystal cavities where the defect is close to the material surface[33]. This has motivated the search for other defects that are less sensitive to surface charges, such as group-IV colour centers in diamond[33,71] and defects in silicon carbide[72–74].

To make progress towards larger distributed quantum networks, two broad categories of challenges need to be addressed. First, the rate and fidelity of generation of optical entanglement between two distant nodes has to be improved. Second, high-fidelity control of a significant number of spins surrounding the optically active electron spin in a single node is required. This regards both data qubits that can be used for e.g. error correction protocols[44–46], as well as robust quantum memories to store entangled states[61,62,75,76].

The motivation for this thesis mainly regards the latter challenge. We look at the NV center in diamond and in particular at its spin environment, which is complex and dynamic. Understanding it can be a source of new types of qubits as well as a vital ingredient in optimising network node performance. Also, uncovering the spin bath dynamics is of fundamental as well as practical scientific interest. The environment consists of a ^{14}N nuclear spin and ^{13}C nuclear spins, as well as other electron spins, particularly in

the form of nitrogen defects such as the P1 center. In this thesis, we will look at different parts of the spin environment and at the NV center itself, as illustrated in Fig. 1.1. While the experiments focus on the NV center, the ideas and results presented in this thesis can be transferred to other colour centers in diamond and other materials.

In **Chapter 2** we give an overview of the NV center and its optical as well as spin properties. We discuss the different spin species in the environment of an NV center: the ^{14}N nuclear spin, ^{13}C nuclear spins as well as the P1 center. Finally, we discuss initialisation and readout methods for these spins.

In **Chapter 3** we demonstrate initialisation, readout and control of strongly coupled ^{13}C nuclear spin pairs. We measure an inhomogeneous dephasing time of $T_2^* = 1.9(6)$ min. We then elucidate the underlying spin bath physics that makes this possible: a combination of a decoherence-free subspace, clock transition and motional narrowing. Finally, we implement parity measurements to create an entangled state of two spin pairs.

In **Chapter 4** we demonstrate initialisation, control and entanglement of P1 centers surrounding a single NV center in diamond. We use projective measurements to initialise the many degrees of freedom of the P1 centers and leverage these to selectively access multiple P1 centers in the bath. We develop control and single-shot readout of the nuclear and electron spin, which we use to realise an entangled state of two P1 centers.

In **Chapter 5** we show that an electron spin can have a back-action on a bath of P1 centers. This results in a detectable signal of a P1 electron spin pair under dynamical decoupling on the central electron spin. We leverage this back-action to develop full control of a pair of P1 centers. Finally, we use this capability to image the full NV-P1-P1 system.

In **Chapter 6** we characterize the single- and two-qubit gates on the electron-nitrogen system of the NV center. We use gate set tomography to characterize the single- and two-qubit process matrices, obtaining a detailed description of our gates. We use this information to improve the gate fidelities, and we measure single-qubit gate fidelities of 99.999(1)% and two-qubit gate fidelities exceeding 99.9%.

In **Chapter 7** we summarise the main findings from this thesis and discuss avenues for future research, both for the near term and for the long term.

REFERENCES

[1] A. Montanaro, *Quantum algorithms: an overview,* NPJ Quantum Inf. **2**, 1 (2016).

[2] Y. Alexeev *et al., Quantum computer systems for scientific discovery,* PRX Quantum **2**, 017001 (2021).

[3] F. Arute *et al., Quantum supremacy using a programmable superconducting processor,* Nature **574**, 505 (2019).

[4] H.-S. Zhong *et al., Quantum computational advantage using photons,* Science **370**, 1460 (2020).

[5] J. I. Cirac and P. Zoller, *Goals and opportunities in quantum simulation,* Nature Physics **8**, 264 (2012).

[6] I. Buluta and F. Nori, *Quantum Simulators,* Science **326**, 108 (2009).

[7] I. M. Georgescu, S. Ashhab and F. Nori, *Quantum simulation,* Rev. Mod. Phys. **86**, 153 (2014).

[8] E. Altman *et al., Quantum simulators: Architectures and opportunities,* PRX Quantum **2**, 017003 (2021).

[9] N. Gisin, G. Ribordy, W. Tittel and H. Zbinden, *Quantum cryptography,* Rev. Mod. Phys. **74**, 145 (2002).

[10] N. Gisin and R. Thew, *Quantum communication,* Nature Photonics **1**, 165 (2007).

[11] P. W. Shor, *Polynomial-Time Algorithms for Prime Factorization and Discrete Logarithms on a Quantum Computer,* SIAM Review **41**, 303 (1999).

[12] D. J. Bernstein and T. Lange, *Post-quantum cryptography,* Nature **549**, 188 (2017).

[13] V. Scarani *et al., The security of practical quantum key distribution,* Rev. Mod. Phys. **81**, 1301 (2009).

[14] C. L. Degen, F. Reinhard and P. Cappellaro, *Quantum sensing,* Rev. Mod. Phys. **89**, 035002 (2017).

[15] M. Abobeih *et al., Atomic-scale imaging of a 27-nuclear-spin cluster using a quantum sensor,* Nature **576**, 411 (2019).

[16] A. Ajoy, U. Bissbort, M. D. Lukin, R. L. Walsworth and P. Cappellaro, *Atomic-scale nuclear spin imaging using quantum-assisted sensors in diamond,* Phys. Rev. X **5**, 011001 (2015).

[17] M. Kost, J. Cai and M. B. Plenio, *Resolving single molecule structures with nitrogen-vacancy centers in diamond,* Sci. Rep. **5**, 11007 (2015).

[18] V. Perunicic, C. Hill, L. Hall and L. Hollenberg, *A quantum spin-probe molecular microscope,* Nat. Commun. **7**, 12667 (2016).

[19] Z.-Y. Wang, J. F. Haase, J. Casanova and M. B. Plenio, *Positioning nuclear spins in interacting clusters for quantum technologies and bioimaging,* Phys. Rev. B **93**, 174104 (2016).

[20] A. D. Ludlow, M. M. Boyd, J. Ye, E. Peik and P. O. Schmidt, *Optical atomic clocks,* Rev. Mod. Phys. **87**, 637 (2015).

[21] L. Jiang, J. M. Taylor, A. S. Sørensen and M. D. Lukin, *Distributed quantum computation based on small quantum registers,* Phys. Rev. A **76**, 062323 (2007).

[22] J. I. Cirac, A. K. Ekert, S. F. Huelga and C. Macchiavello, *Distributed quantum computation over noisy channels,* Phys. Rev. A **59**, 4249 (1999).

[23] P. Kurpiers *et al.*, *Deterministic quantum state transfer and remote entanglement using microwave photons,* Nature **558**, 264 (2018).

[24] J.-H. Kim, S. Aghaeimeibodi, J. Carolan, D. Englund and E. Waks, *Hybrid integration methods for on-chip quantum photonics,* Optica **7**, 291 (2020).

[25] A. W. Elshaari, W. Pernice, K. Srinivasan, O. Benson and V. Zwiller, *Hybrid integrated quantum photonic circuits,* Nat. Photonics **14**, 285 (2020).

[26] N. H. Wan *et al.*, *Large-scale integration of artificial atoms in hybrid photonic circuits,* Nature **583**, 226 (2020).

[27] J. M. Taylor *et al.*, *Fault-tolerant architecture for quantum computation using electrically controlled semiconductor spins,* Nature Physics **1**, 177 (2005).

[28] L. M. K. Vandersypen *et al.*, *Interfacing spin qubits in quantum dots and donors—hot, dense, and coherent,* npj Quantum Information **3**, 34 (2017).

[29] A. Zwerver *et al.*, *Shuttling an electron spin through a silicon quantum dot array,* PRX Quantum **4**, 030303 (2023).

[30] L.-M. Duan and C. Monroe, *Colloquium: Quantum networks with trapped ions,* Rev. Mod. Phys. **82**, 1209 (2010).

[31] M. Saffman, T. G. Walker and K. Mølmer, *Quantum information with rydberg atoms,* Rev. Mod. Phys. **82**, 2313 (2010).

[32] R. Uppu, L. Midolo, X. Zhou, J. Carolan and P. Lodahl, *Quantum-dot-based deterministic photon–emitter interfaces for scalable photonic quantum technology,* Nature Nanotechnology **16**, 1308 (2021).

[33] M. Ruf, N. H. Wan, H. Choi, D. Englund and R. Hanson, *Quantum networks based on color centers in diamond,* Journal of Applied Physics **130**, 70901 (2021).

[34] A. Tchebotareva *et al.*, *Entanglement between a diamond spin qubit and a photonic time-bin qubit at telecom wavelength,* Phys. Rev. Lett. **123**, 063601 (2019).

[35] D. Lago-Rivera, S. Grandi, J. V. Rakonjac, A. Seri and H. de Riedmatten, *Telecom-heralded entanglement between multimode solid-state quantum memories,* Nature **594**, 37 (2021).

[36] A. Stolk *et al.*, *Telecom-band quantum interference of frequency-converted photons from remote detuned nv centers,* PRX Quantum **3**, 020359 (2022).

[37] B. M. Brubaker *et al.*, *Optomechanical ground-state cooling in a continuous and efficient electro-optic transducer,* Phys. Rev. X **12**, 021062 (2022).

[38] Y. Chu and S. Gröblacher, *A perspective on hybrid quantum opto- and electromechanical systems,* Applied Physics Letters **117**, 150503 (2020).

[39] X. Guo *et al.*, *Distributed quantum sensing in a continuous-variable entangled network,* Nature Physics **16**, 281 (2020).

[40] Z. Eldredge, M. Foss-Feig, J. A. Gross, S. L. Rolston and A. V. Gorshkov, *Optimal and secure measurement protocols for quantum sensor networks,* Phys. Rev. A **97**, 042337 (2018).

[41] T. J. Proctor, P. A. Knott and J. A. Dunningham, *Multiparameter estimation in networked quantum sensors,* Phys. Rev. Lett. **120**, 080501 (2018).

[42] P. C. Humphreys, M. Barbieri, A. Datta and I. A. Walmsley, *Quantum enhanced multiple phase estimation,* Phys. Rev. Lett. **111**, 070403 (2013).

[43] S. Wehner, D. Elkouss and R. Hanson, *Quantum internet: A vision for the road ahead,* Science **362** (2018).

[44] N. H. Nickerson, Y. Li and S. C. Benjamin, *Topological quantum computing with a very noisy network and local error rates approaching one percent,* Nat. Commun. **4**, 1756 (2013).

[45] N. H. Nickerson, J. F. Fitzsimons and S. C. Benjamin, *Freely scalable quantum technologies using cells of 5-to-50 qubits with very lossy and noisy photonic links,* Phys. Rev. X **4**, 041041 (2014).

[46] S. de Bone, R. Ouyang, K. Goodenough and D. Elkouss, *Protocols for creating and distilling multipartite ghz states with bell pairs,* IEEE Trans. Quantum Eng. **1**, 1 (2020).

[47] C. E. Bradley *et al.*, *A ten-qubit solid-state spin register with quantum memory up to one minute,* Phys. Rev. X **9**, 031045 (2019).

[48] D. D. Awschalom, R. Hanson, J. Wrachtrup and B. B. Zhou, *Quantum technologies with optically interfaced solid-state spins,* Nat. Photonics **12**, 516 (2018).

[49] N. Bar-Gill, L. M. Pham, A. Jarmola, D. Budker and R. L. Walsworth, *Solid-state electronic spin coherence time approaching one second,* Nat. Commun. **4**, 1 (2013).

[50] P. C. Maurer *et al.*, *Room-Temperature Quantum Bit Memory Exceeding One Second,* Science **336**, 1283 (2012).

[51] M. H. Abobeih *et al.*, *One-second coherence for a single electron spin coupled to a multi-qubit nuclear-spin environment,* Nat. Commun. **9**, 1 (2018).

[52] H. P. Bartling *et al.*, *Entanglement of spin-pair qubits with intrinsic dephasing times exceeding a minute,* Phys. Rev. X **12**, 011048 (2022).

[53] A. Sipahigil *et al.*, *An integrated diamond nanophotonics platform for quantum-optical networks,* Science **354**, 847 (2016).

[54] L. Robledo *et al.*, *High-fidelity projective read-out of a solid-state spin quantum register,* Nature **477**, 574 (2011).

[55] P. Neumann *et al.*, *Single-shot readout of a single nuclear spin,* Science **329**, 542 (2010).

[56] A. Dréau, P. Spinicelli, J. Maze, J.-F. Roch and V. Jacques, *Single-shot readout of multiple nuclear spin qubits in diamond under ambient conditions,* Phys. Rev. Lett. **110**, 060502 (2013).

[57] G.-Q. Liu *et al.*, *Single-shot readout of a nuclear spin weakly coupled to a nitrogen-vacancy center at room temperature,* Phys. Rev. Lett. **118**, 150504 (2017).

[58] H. Bernien *et al.*, *Heralded entanglement between solid-state qubits separated by three metres,* Nature **497**, 86 (2013).

[59] B. Hensen *et al.*, *Loophole-free bell inequality violation using electron spins separated by 1.3 kilometres,* Nature **526**, 682 (2015).

[60] P. C. Humphreys *et al.*, *Deterministic delivery of remote entanglement on a quantum network,* Nature **558**, 268 (2018).

[61] M. Pompili *et al.*, *Realization of a multinode quantum network of remote solid-state qubits,* Science **372**, 259 (2021).

[62] S. L. N. Hermans *et al.*, *Qubit teleportation between non-neighbouring nodes in a quantum network,* Nature **605**, 663 (2022).

[63] T. Taminiau *et al.*, *Detection and control of individual nuclear spins using a weakly coupled electron spin,* Phys. Rev. Lett. **109**, 137602 (2012).

[64] G. Waldherr *et al.*, *Quantum error correction in a solid-state hybrid spin register,* Nature **506**, 204 (2014).

[65] T. H. Taminiau, J. Cramer, T. van der Sar, V. V. Dobrovitski and R. Hanson, *Universal control and error correction in multi-qubit spin registers in diamond,* Nat. Nanotechnol. **9**, 171 (2014).

[66] J. Cramer *et al.*, *Repeated quantum error correction on a continuously encoded qubit by real-time feedback,* Nat. Commun. **7**, 1 (2016).

[67] M. H. Abobeih *et al.*, *Fault-tolerant operation of a logical qubit in a diamond quantum processor,* Nature **606**, 884 (2022).

[68] G. Davies, *Vibronic spectra in diamond,* Journal of Physics C: Solid state physics **7**, 3797 (1974).

[69] A. Faraon, P. E. Barclay, C. Santori, K.-M. C. Fu and R. G. Beausoleil, *Resonant enhancement of the zero-phonon emission from a colour centre in a diamond cavity,* Nat. Photonics **5**, 301 (2011).

[70] D. Riedel *et al.*, *Deterministic enhancement of coherent photon generation from a nitrogen-vacancy center in ultrapure diamond,* Phys. Rev. X **7**, 031040 (2017).

[71] C. Bradac, W. Gao, J. Forneris, M. E. Trusheim and I. Aharonovich, *Quantum nanophotonics with group iv defects in diamond,* Nat. Commun. **10**, 1 (2019).

[72] R. Nagy *et al.*, *High-fidelity spin and optical control of single silicon-vacancy centres in silicon carbide,* Nat. Commun. **10**, 1 (2019).

[73] D. M. Lukin, M. A. Guidry and J. Vučković, *Integrated quantum photonics with silicon carbide: challenges and prospects,* PRX Quantum **1**, 020102 (2020).

[74] A. Bourassa *et al.*, *Entanglement and control of single nuclear spins in isotopically engineered silicon carbide,* Nat. Mater. **19**, 1319 (2020).

[75] C. E. Bradley *et al.*, *Robust quantum-network memory based on spin qubits in isotopically engineered diamond,* npj Quantum Information **8**, 122 (2022).

[76] N. Kalb, P. C. Humphreys, J. Slim and R. Hanson, *Dephasing mechanisms of diamond-based nuclear-spin memories for quantum networks,* Phys. Rev. A **97**, 062330 (2018).

2

METHODS

In this chapter, we will discuss the basics of the nitrogen vacancy (NV) center and its surroundings. We will look at the optical and spin properties of the NV center itself, the experimental hardware used to address it and the spin environment of the NV center that we aim to detect and control.

2.1. THE NV CENTER IN DIAMOND

The NV center is a defect in the diamond lattice. A substitutional nitrogen atom and an adjacent vacant site replace two carbon atoms. It occurs naturally in diamond, but can also be formed by electron irradiation [1–3] or direct laser writing [4–7]. Alternatively nitrogen can be implanted at a specific location through ion implantation [8–10] at the expense of significant lattice damage deteriorating the NV center's optical properties [11,12].

The NV center is typically in one of two charge states: NV^0 or NV^-. Transitions between the two charge states are induced by optical excitation [13–16] allowing control over the NV charge state, an important prerequisite for quantum control.

In this thesis we focus on the NV^- charge state. We can approximate the NV electron wave function as a linear combination of the neighbouring atomic orbitals under C_{3v} symmetry [17,18]. In Fig. 2.1b these orbitals are shown. There are two doubly-occupied orbitals (a_1', a_1) and two singly-occupied orbitals (e_x, e_y). Upon optical excitation an electron from the a_1 orbital is promoted to either the e_x or e_y orbital. This creates an excited state orbital doublet and spin triplet [17,19]. Importantly, the optical transitions lie within the diamond bandgap [20]. We can thus approximately view the NV center as an isolated, optically addressable atom embedded in a solid-state material.

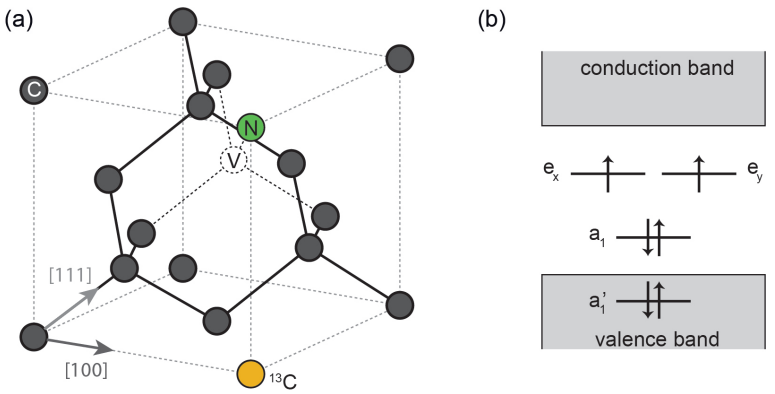

Figure 2.1: **Crystal structure and molecular orbitals of the NV center. (a)** Crystal structure of the NV center within the diamond lattice. A nitrogen atom (green) sits next to a vacant site (white). The spin-1/2 ^{13}C isotope (yellow) has a natural abundance of 1.1%. The rest consists of spinless ^{12}C atoms (grey). **(b)** The molecular orbitals and their ground-state filling for the NV^- charge state. Figures adapted from Pfaff [21], Bernien [22].

2.2. OPTICAL READOUT OF THE NV CENTER

Optical readout of the NV center can be done in two ways: off-resonantly or resonantly. At room temperature, only off-resonant readout is available, but at low temperature (< 10 K) resonant readout becomes a possibility. The difference originates from the suppression of two-phonon Raman processes at low temperatures. While the homogeneous linewidth is broad (~ 15 THz) at room temperature [23–25], it can narrow to the lifetime limited linewidth of 13 MHz at low temperature [23,26]. For typical lateral strain (~ GHz),

spin-selective optical transitions are thus available at low temperatures[27].

2.2.1. ROOM-TEMPERATURE OPTICAL READOUT

At room temperature, optical excitation typically happens via the phonon side band (PSB). This method has been used for the first single spin room temperature experiments with the NV center[28] and is still widely used[25,29,30]. While the excitation is spin-independent, the decay back to the ground state is spin-dependent. Decay directly back to the ground state is accompanied with the emission of a photon. Alternatively, decay happens through an intersystem crossing (ISC) via the singlet states without the emission of a visible photon. The ISC rates are strongly spin-dependent. The decay rate via the $^1A_1$ singlet and metastable $^1E_1$ state preferentially happens for the $m_s = \pm 1$ state[25,31] (Fig. 2.2). The decay from the metastable state to the ground state polarises the spin by preferentially decaying to $m_s = 0$. The spin-dependent decay path implies that more photons are detected for $m_s = 0$ than for $m_s = \pm 1$. However, this spin-dependent photoluminescence contrast vanishes after about 300 ns when the singlet population has decayed to the ground state[25,31,32]. Together with the collection efficiency of the photons, this results in single-shot readout fidelities close to 50%[25,31,32]. Repetitive readout of a nuclear spin containing the electron readout result can be used to improve this number. Readout fidelities exceeding 90% have been demonstrated using this nuclear-assisted readout[33–35]. Alternatively, the spin can be converted to charge by means of spin-selective ionisation to NV^0, so-called spin-to-charge conversion, after which the charge state of the NV center can be read out instead[25,36,37].

2.2.2. LOW-TEMPERATURE OPTICAL READOUT

At low temperature ($\lesssim 10$ K), spin-selective optical transitions are resolvable. We choose distinct optical transitions for initialisation and readout, based on their differences in ISC rates. A_1, E_1 and E_2 are all likely to decay to the singlet state (> 40% probability at 4 K)[38–40]. The decay from the singlet state goes to $m_s = 0$ and $m_s = \pm 1$ with a branching ratio of $1:1$[20,40]. Since the excitation is spin-selective, exciting either one of these three transitions therefore initialises the electron spin in $m_s = 0$ with high fidelity (> 99%)[27,40].

To read out the electron spin, the E_x or E_y transition is used. These have comparatively low ISC rates and therefore cycle between ground and excited state emitting photons[40]. Since E_x, E_y are spin-selective to $m_s = 0$, photons are observed when the spin state is $m_s = 0$ but not when $m_s = \pm 1$. We correlate the observation of a photon with $m_s = 0$ and the observation of no photon with $m_s = \pm 1$. This leads to high-fidelity optical readout of the NV center electron spin state of typically ~ 95%[41–43].

Importantly, the NV optical readout at low temperatures is asymmetric[27]. If a photon is observed, there is an exceedingly high chance (> 99%) the electron state was $m_s = 0$ even when the average readout fidelity is limited to ~ 95%. Conversely, when no photon is detected, there is still a significant chance the pre-measurement state was $m_s = 0$. This asymmetry has important implications for nuclear spin control, in particular for measurement-based initialisation protocols[44,45]. This will be discussed in more detail later in this chapter.

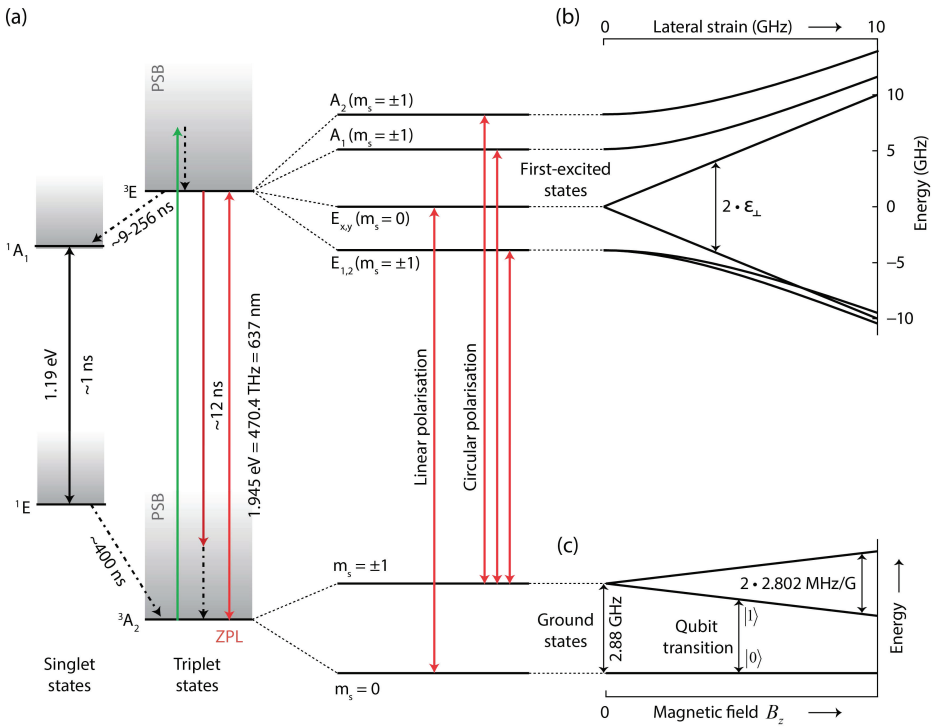

Figure 2.2: **Energy level structure of the NV$^-$ center. (a)** The energies of the transitions between ground and excited states are shown. Excitation can be off-resonantly (green) or resonantly (red). Decay from the first excited state can happen resonantly through the emission of a photon at the zero-phonon line (ZPL) frequency. Or off-resonantly either in combination with a phonon or via an intersystem crossing to the singlet (dashed black lines). **(b)** Effect of lateral strain $\epsilon_\perp$ on the first excited state. In the works presented in this thesis, natural strain is present and no additional electric fields are applied. **(c)** Ground state triplet fine structure. Spin-spin interactions induce a zero-field splitting (ZFS) of $\Delta \sim 2.88$ GHz. The application of a magnetic field along the NV axis splits the $m_s = \pm 1$ levels. Throughout this thesis, the ground state qubit is defined between the $m_s = 0$ and $m_s = -1$ ground state levels of the NV center. Figures adapted from Pfaff[21], Bernien[22], Hensen[19].

2.2.3. CHARGE RESONANCE CHECK

To perform an experiment with the spin-selective transitions resolvable at low temperature, we need to make sure that the lasers are resonant with the optical transitions of the NV center. Charge fluctuations near the NV center can lead to drifts of the transition frequency[46]. Furthermore, photo-ionization can leave the NV in the wrong charge state[13]. Therefore we perform a charge resonance (CR) check[46]. The process is outlined in Fig. 2.3.

The check itself consists of the application of two resonant laser pulses, one at E_x or E_y and one at A_1, E_1 or E_2. If the NV center is in its right charge state and the lasers are resonant, we are continuously cycling between ground and excited state. We thus expect to observe a number of photon counts *cts*. If the number of counts exceeds the threshold *thr*, we begin the experiment. However, if it is lower than the threshold, we do one of two things.

The first case occurs when the counts are lower than the first threshold *thr*, but higher than a second threshold thr_0. Here, not reaching the threshold *thr* is attributed to photon statistics or to the laser pulses being slightly off-resonant. We therefore perform the check again to confirm the laser pulses are resonant. We introduce the second threshold thr_0 to avoid unnecessary reshuffling of the charge environment.

The second case is when the counts are lower than the second threshold thr_0. In this case, we conclude that either the NV center is in the wrong charge state or (one of) the lasers are far off-resonant. To tackle this, we apply a green laser (515 nm). The green laser pulse does two things. First, it leaves the NV center in NV^- with a probability of $\sim 75\%$[13]. Therefore, we use it to repump NV^0 to NV^-. Second, it can reshuffle the charge environment, changing its optical transition frequencies. After the application of a green repump pulse, we perform a new check to confirm whether the NV is now in its right charge state and whether the red lasers are resonant. Alternatively, the NV^- charge state can be prepared using resonant excitation of NV^0 at 575 nm[14,42,47].

The precise values used for *thr* and thr_0 can depend on the type of experiment. It is a balancing act between the single-shot readout fidelity and the experimental rate. If the thresholds are set relatively high, the NV will be more likely to be in the right charge state and the lasers will be better on resonance, but the experimental rate will be slower. For some experiments it is therefore beneficial to lower the thresholds to improve the experimental rate.

2.3. EXPERIMENTAL SETUP

The experiments in this thesis were performed on two different yet similar experimental setups. A schematic is shown in Fig. 2.5. The diamond devices are situated in a closed-cycle cryostat (Montana Cryostation S50) at ~ 4 K. The optics form a confocal microscopy setup with one off-resonant, green laser, two resonant, red lasers and optionally a yellow laser as an alternative method to reinitialize the NV^- charge state. Radio-frequency ($\sim 1-300$ MHz) pulses are generated with an arbitrary waveform generator (AWG) with 1 ns resolution (Tektronix AWG5014C). Microwave ($\sim 1-4$ GHz) pulse shapes are generated by the AWG and mixed with a microwave source (R&S SGS100A). We use single-sideband modulation to control the phase of the microwave pulse. A microcon-

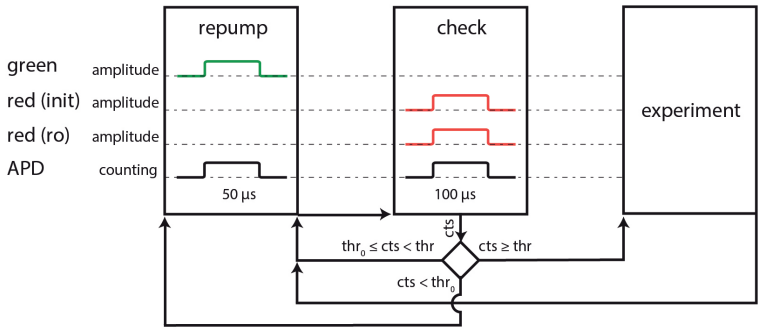

Figure 2.3: **The process of a charge resonance check.** During the check phase, both resonant red lasers are applied. When the NV is in its right charge state, and the lasers are resonant, we expect to observe a number of photon counts *cts* larger than *thr*. Then, the experiment is started. If *cts* is smaller than *thr*, but larger than thr_0, we attribute it to photon statistics and perform the check again. If the counts are lower than thr_0, we use a green laser pulse (515 nm) to reset the charge state and charge environment. Figure adapted from Hensen [19], Hermans [48].

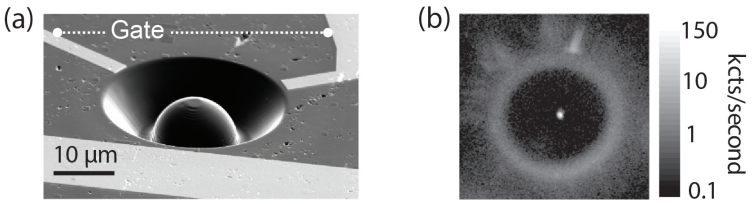

Figure 2.4: **Solid immersion lens on a diamond device. (a)** In the middle of this scanning electron microscope image the solid immersion lens (SIL) is shown. In the front the gold stripline can be seen, which is used to apply both MW and RF signals discussed in this thesis. Above the SIL the gates are indicated, which can be used to tune the optical transitions electrically using the DC Stark effect (not used in this work). **(b)** A scanning confocal microscope image of the SIL under off-resonant, green excitation. The bright spot indicates the detected emission of the NV center. Figure adapted from Bernien [22], Abobeih [49].

troller (ADwin PRO II) is the brain of running any experiment, executing experiments by directing the lasers and AWG. To bring the NV center to a desired magnetic field and to keep it there, we operate computer controllable magnet stages (e.g. Newport UTS100PP) outside of the cryostat containing permanent NdFeB magnets.

2.4. DIAMOND DEVICES

Two different diamond devices were used in this thesis. Common to both, we used a single, naturally occurring NV center in a chemical-vapor-depositioned (CVD) grown diamond (type IIa). Solid immersion lenses (SIL) are fabricated around the NV center with focused ion beam milling (Fig. 2.4) [27]. An aluminium-oxide anti-reflection coating is made on the SIL by atomic layer deposition (ALD) [27].

To apply microwave (MW) and radio-frequency (RF) pulses, a gold stripline is de-

posited close (~ 10 μm) to the SIL (Fig. 2.4). The diamond device is then glued to a printed circuit board (PCB) with silver paste. Bondwires are used to transfer the MW and RF signals from the PCB to the gold on the diamond device.

The first diamond device (Chapter 3) has a <111> crystal orientation and a natural abundance ^{13}C of 1.1 %. The nitrogen concentration is estimated to be less than 5 ppb[44]. The second diamond device (Chapters 4, 5, 6) has a <100> crystal orientation. The ^{13}C concentration is 0.01 %. Additionally, there is a significant nitrogen concentration of ~ 75 ppb[50]. In both devices, natural strain is present and no additional electric fields are applied.

2.5. THE NV CENTER ELECTRON SPIN

The NV center ground state is an electron spin-1 system. Two levels - typically $m_s = 0$ and $m_s = -1$[41,45] - are chosen as the electron spin qubit. Microwave pulses of $\sim 1-4$ GHz are used to perform rotations in this subspace (Chapter 6).

2.5.1. HAMILTONIAN

If we neglect the influence of electric and strain fields, we can write the ground state Hamiltonian of the NV center electron spin as[20,53]:

$$H_e = \Delta_{\text{zfs}} S_z^2 + \gamma_e (\mathbf{B} \cdot \mathbf{S}). \tag{2.1}$$

$\Delta_{\text{zfs}} \approx 2.88$ GHz is the zero-field splitting. It splits the $m_s = 0$ level from $m_s = \pm 1$ due to spin-spin interactions[20,53,54]. The z-direction is defined as the direction of the zero-field splitting. $\mathbf{S} = [S_x, S_y, S_z]$ are the spin-1 operators, $\gamma_e = 2.8024$ MHz/G is the electron gyromagnetic ratio and $\mathbf{B} = [B_x, B_y, B_z]$ is the external magnetic field which leads to Zeeman splitting of the $m_s = \pm 1$ levels. In this thesis, the magnetic field is aligned with the z-axis ($B_x, B_y \sim 0$) or purposely slightly misaligned ($B_z \gg B_x, B_y$).

2.5.2. SPIN RELAXATION

The longitudinal relaxation or T_1 of a qubit is the decay of population out of its computational basis states. At room temperature, two-phonon Raman processes limit the relaxation time of the electron spin to a few ms[30,55]. However, these and other Orbach-type processes are insignificant at our typical operating temperatures of ~ 4 K[55,56]. Therefore the unwanted presence of microwave and optical control fields becomes the main contributor to relaxation. We reduce their leakage through a microwave switch and the use of two, sequential AOMs[44]. This leads to a characteristic relaxation time of $T_1 \sim 1$ hour[44], more than long enough to make its contribution insignificant to the results presented in this thesis.

2.5.3. SPIN COHERENCE

The coherence of a qubit is the loss of phase information when it is in a superposition of its computational basis states. T_2^* refers to the inhomogeneous dephasing time: the spin coherence without the application of any refocusing pulses. For T_2 spin echoes are applied to combat the detrimental effects of the environment.

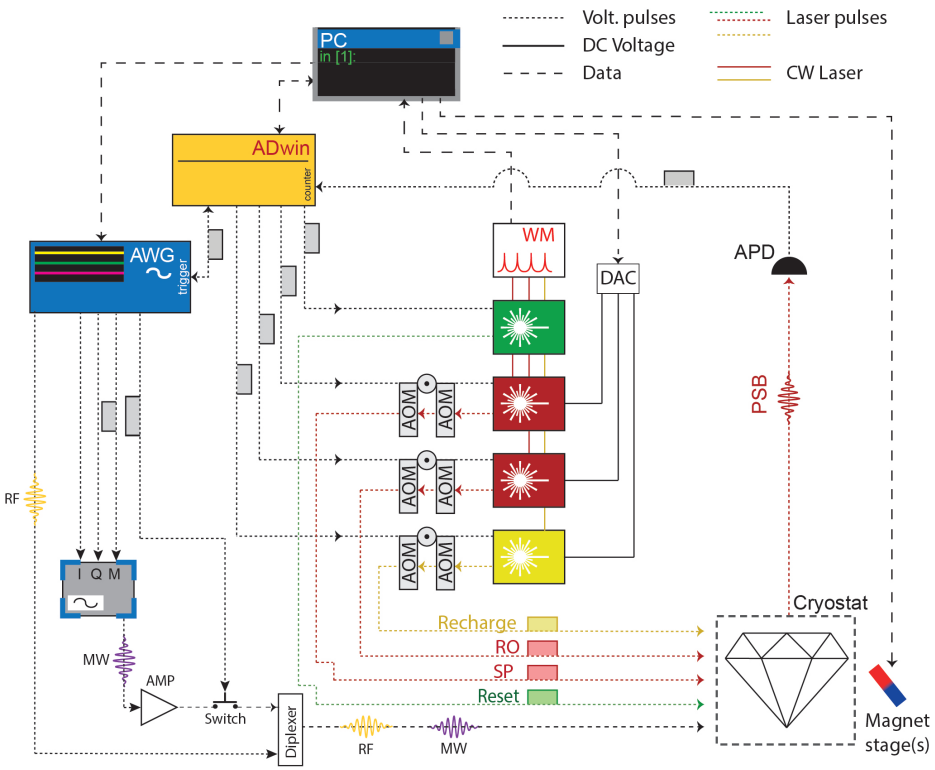

Figure 2.5: **Experimental setup. Control electronics:** A PC programs the control cycle of an experiment on a micro-controller (Jaeger ADwin Pro II). The micro-controller is the 'brain' of the experiment, turning on lasers, registering photon counts and triggering the arbitrary waveform generator (Tektronix AWG 5014, 1 ns resolution) to play pulse sequences. **Microwave & RF electronics:** Microwave (MW) pulses are produced by a vector source (R&S SGS100A). The frequencies, timings, phases and pulse shapes are determined by IQ- and pulse-modulation on the AWG. The MW signal is then amplified by a microwave amplifier (AR 25S1G6). To protect the NV from amplifier noise, we use a fast microwave switch (TriQuint TGS2355-SM, suppression ratio of 40 dB), which is triggered by the AWG. For nuclear spin manipulation, we generate radio-frequency (RF) pulses on the AWG. These are combined with the MW signal through a diplexer. The MW and RF signals then travel to the cryostat, through a bondwire and over the gold stripline on the diamond. **Laser systems:** In this thesis, four lasers are used. A 515 nm laser (Cobolt MLD) is used for charge-resonance reset[46]. Two 637 nm lasers (Toptica DL-pro and New Focus TLB-6704-P) are used for resonant spin initialisation (SP) and readout (RO) respectively. A 575 nm laser (Toptica DL-SHG-pro) can be used for resonant charge reset to NV^-. A wavemeter (HF-Ångstrom WS/U-10U) and PID loop are used to stabilise the resonant laser frequencies to 2 MHz accuracy. We also use two cascaded acousto-optic modulators (AOMs, G&H FibreQ) to achieve >100 dB on/off ratios for the resonant lasers. The AOMs are turned on/off by the micro-controller. A home-built confocal microscope is used to focus the light on and collect it from the NV center. For alignment, we use a 0.9 NA microscope objective (Olympus MPLFLN 100x) controlled by three piezo-electric stages (PI Q-545K038). The phonon-sideband (PSB) emission is then collected on an avalanche photodiode (APD, Laser Components) and registered by the micro-controller. **Magnetic field:** Axial (Ch. 3, 6) and misaligned (Ch. 4, 5) magnetic fields are produced using permanent neodymium magnets, which are mounted on motorised stages (Newport UTS100PP). Figure adapted from Pfaff[21], Kalb[51], Abobeih[49], Bradley[52].

For our system, the inhomogeneous dephasing time is generally limited by the surrounding spin bath, in chief the ^{13}C nuclear spin bath. For natural abundance (1.1% ^{13}C) samples this limits T_2^* to a few μs[44]. The spin background can be removed with isotopic purification, improving the T_2^* by up to two orders of magnitude[50,57,58]. The spin bath evolves slowly on the measurement timescale, because intra-bath couplings are typically limited to Hz[41]. This makes the noise experienced by the NV center quasi-static. The use of dynamical decoupling sequences can efficiently remove the unwanted effects of this type of noise[44,59]. With the application of longer decoupling sequences, the T_2 time can be extended to > 1 s[44], sufficiently long to probe surrounding spins through the NV center.

2.6. NITROGEN SPIN

Every NV center has a host nitrogen spin that is either isotope-14 (99.6 % abundance) or -15 (0.4 % abundance). These are spin-1 or spin-1/2 systems respectively. In the works presented in this thesis, the host nitrogen spin is always ^{14}N and thus spin-1. The Hamiltonian of the ^{14}N spin can be described by[20]:

$$H_n = -QI_z^2 + \gamma_n \mathbf{B}\cdot\mathbf{I}. \tag{2.2}$$

$Q \approx 4.95$ MHz is the quadrupole splitting, which splits the $m_I = 0$ from the $m_I = \pm 1$ levels. The z-direction is defined as the direction of the quadrupole splitting. Due to the symmetry of the NV center, the electron and nitrogen Hamiltonian therefore share the same z-axis. $\gamma_n = 0.3077$ kHz/G is the ^{14}N gyromagnetic ratio and $\mathbf{I} = [I_x, I_y, I_z]$ are the spin-1 operators. The hyperfine interaction with the electron spin is[20]:

$$H_{e-n} = A_\parallel S_z I_z + A_\perp (S_x I_x + S_y I_y). \tag{2.3}$$

Since the electron and nitrogen are both positioned along the z-axis, we can neglect the off-diagonal terms[20]. Due to the large energy mismatch of the electron and ^{14}N spin, the secular approximation can often be made and we obtain:

$$H_{e-n} = A_\parallel S_z I_z, \tag{2.4}$$

where $A_\parallel = 2.18$ MHz. S_z is the electron spin-1 operator and I_z is the nuclear spin-1 operator.

2.7. NV CENTER ENVIRONMENT

Having discussed the internal structure of the NV center, we now turn to its surroundings (Fig. 2.7). There is a plethora of spins to be found including ^{13}C nuclear spins[41,45,60], P1 centers[50,61–63], NV centers[33,64,65], and as-of-yet unidentified spins[66]. In Fig. 2.7 we show a schematic of the spin environment of the NV center.

2.7.1. ^{13}C SPIN

The NV center is embedded in a lattice composed of carbon atoms. At natural abundance, 1.1% of carbon atoms is isotope-13, which is spin-1/2. The other, most abundant

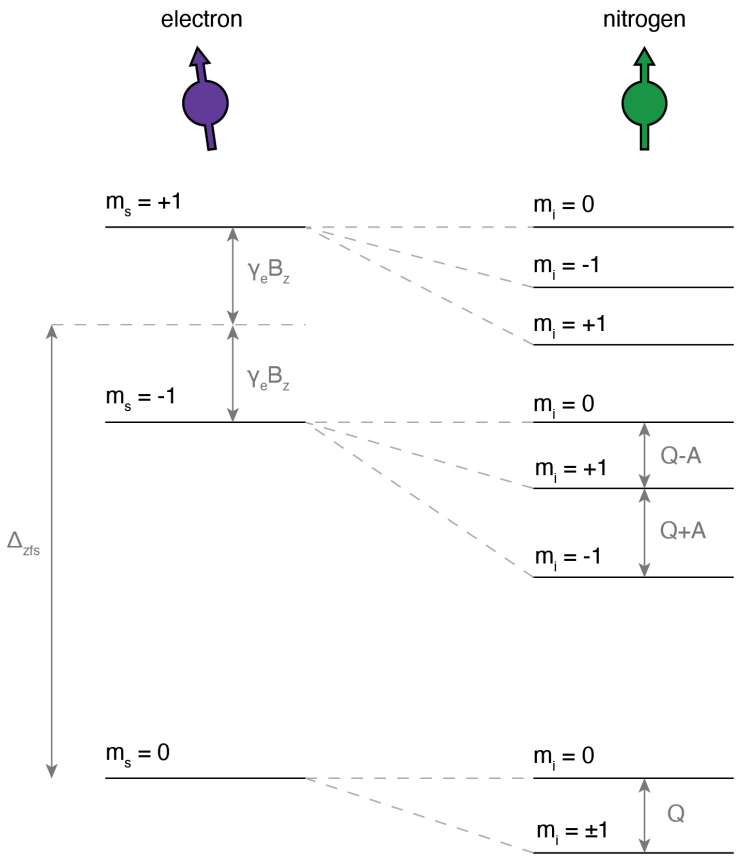

Figure 2.6: **Ground-state electron and nitrogen energy levels.** The electron $m_s = 0$ and $m_s = \pm 1$ levels (left) are split by the zero-field splitting $\Delta_{zfs} \approx 2.88$ GHz. The $m_s = \pm 1$ levels are additionally split through Zeeman splitting. The nitrogen spin-1 (right) has a quadrupole splitting $Q \approx 4.95$ MHz and an additional hyperfine interaction with the electron spin $A = 2.18$ MHz.

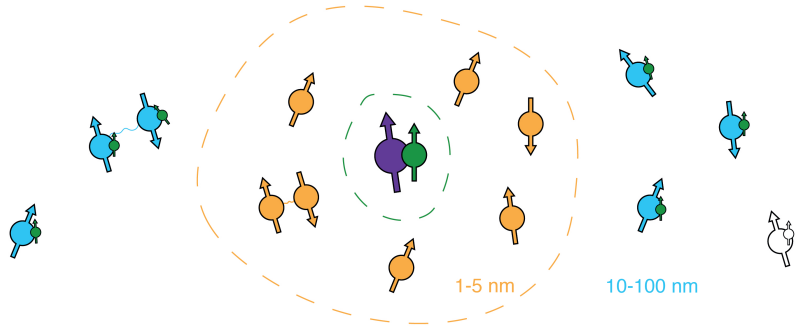

Figure 2.7: **The spin environment of an NV center.** A schematic of the spin environment of the electron spin (purple) and nitrogen spin (green) of the NV center. The first layer is formed by naturally occurring ^{13}C nuclear spins (brown). Further away, we find other electron spins associated to defects, mainly the P1 center electron spin (blue) and nitrogen spin (green). Other NV centers or surface spins (white) can be found, but are not discussed in this thesis.

isotope-12 is spinless. The spin-1/2 ^{13}C nuclear spins that are close-by can be detected and controlled with the NV center electron spin [44,45,67]. Below we will discuss the different methods to control ^{13}C nuclear spins, but first we summarise its characteristics.

Every ^{13}C spin is affected by the external magnetic field through the Zeeman effect. Additionally, a hyperfine interaction with the NV electron spin is present. The hyperfine interaction consists of a dipole-dipole interaction as well as a Fermi contact interaction for close-by nuclear spins [68]. In general, we can write the ^{13}C Hamiltonian and interaction Hamiltonian with the electron spin as:

$$H_c = \gamma_c \mathbf{B} \cdot \mathbf{I}_c, \tag{2.5}$$

$$H_{e-c} = \mathbf{S} \cdot \mathbf{A}_c \cdot \mathbf{I}_c, \tag{2.6}$$

where $\gamma_c = 1.07084$ kHz/G is the ^{13}C nuclear gyromagnetic ratio. $\mathbf{I}_c = (I_{c,x}, I_{c,y}, I_{c,z})$ are the spin-1/2 operators. $\mathbf{A}_c$ is the hyperfine tensor for the electron-nuclear interaction. When the electron energy level splitting is large compared to the electron-nuclear interaction, we can approximate the interaction under the secular approximation as:

$$H_{e-c} = A_\parallel S_z I_{c,z} + A_\perp S_z I_{c,x}, \tag{2.7}$$

where $A_\parallel$ is the parallel component of the hyperfine interaction and $A_\perp = \sqrt{A_{zx}^2 + A_{zy}^2}$ is the perpendicular component with respect to the z-direction.

Since 1.1% of carbon atoms is spin-1/2, the nuclear-nuclear dipolar interaction is also of importance. In general we write this as:

$$H_{c-c} = \mathbf{I}_c^{(i)} \cdot \mathbf{C}_{ij} \cdot \mathbf{I}_c^{(j)}, \tag{2.8}$$

where $\mathbf{C}_{ij}$ is the dipolar interaction tensor between ^{13}C spins i and j. When the external magnetic field is large compared to the nuclear-nuclear interaction, we can approximate

this as:

$$H_{c-c} = X(3I_{c,z}^{(i)}I_{c,z}^{(j)} - \mathbf{I}_c^{(i)} \cdot \mathbf{I}_c^{(j)}), \tag{2.9}$$

$$X = \frac{\mu_0 \gamma_c^2 \hbar}{8\pi |\mathbf{r}_{ij}|^3}(1 - 3\cos^2\theta_{ij}), \tag{2.10}$$

where μ_0 is the vacuum permeability, $|\mathbf{r}_{ij}|$ is the vector between ^{13}C atoms i and j and θ_{ij} is the angle between $\mathbf{r}_{ij}$ and the external magnetic field axis.

For natural abundance of ^{13}C spins, the hyperfine interaction of ^{13}C spins in the vicinity of the NV center (~ 10 kHz) is typically much larger than the nuclear-nuclear interaction (~ 10 Hz) owing to the much larger electron gyromagnetic ratio. As we will see in Chapter 3, the nuclear-nuclear interaction can have some surprising effects.

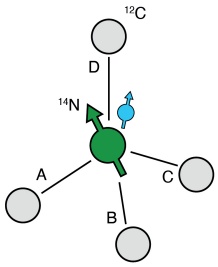

Figure 2.8: **Schematic of a P1 center defect.** P1 center defect in the diamond lattice. A ^{14}N atom replaces a ^{12}C atom in the diamond lattice. The light blue spin indicates the electron spin-1/2 associated with the P1 center defect. The Jahn-Teller axes are indicated by A, B, C and D.

2.7.2. P1 CENTER

P1 centers are a common defect in diamond where a nitrogen atom replaces a single ^{13}C atom in the diamond lattice. Three charge states are known[69,70], but we will focus on the neutral charge state. Its first detection dates back to 1959 in electron paramagnetic resonance experiments[71,72]. These experiments and others[61,62,73] have revealed the spin level structure of the P1 center.

The P1 center has an electron spin-1/2 and typically a ^{14}N nuclear spin-1. Additionally, a Jahn-Teller distortion along one of the four nitrogen-carbon bond axes is present[74,75]. At room temperature, the lifetime of the Jahn-Teller axis is relatively short[76–78]. At low temperature, the lifetime is very long in the dark[50]. However, optical excitation, such as with the green laser (515 nm) used to excite the NV center off-resonantly, quickly scrambles the Jahn-Teller axis[50,79]. The Hamiltonian of the P1 electron spin and ^{14}N nuclear spin is given by:

$$H_{P1} = \gamma_e \mathbf{B} \cdot \mathbf{J} + \gamma_n \mathbf{B} \cdot \mathbf{I} + \mathbf{J} \cdot \mathbf{A}_i \cdot \mathbf{I} + \mathbf{I} \cdot \mathbf{P}_i \cdot \mathbf{I}, \tag{2.11}$$

where γ_e (γ_n) is the electron (nitrogen) gyromagnetic ratio, $\mathbf{B} = (B_x, B_y, B_z)$ is the external magnetic field vector, $\mathbf{J} = (J_x, J_y, J_z)$ ($\mathbf{I} = (I_x, I_y, I_z)$) are the electron spin-1/2 (nuclear

spin-1) operators. **A** and **P** are the electron-nitrogen hyperfine interaction and nuclear quadrupole tensor respectively. The subscript $i \in [A, B, C, D]$ denotes the dependence of the hyperfine and quadrupole tensor on the axis of Jahn-Teller distortion (Chapter 4, 5).

The P1 center electron spin can couple to other defect's electron spins. This mainly regards other P1 centers and the NV center. Since the ^{14}N gyromagnetic ratio is about four orders-of-magnitude smaller than the electron gyromagnetic ratio, we neglect nuclear-nuclear and electron-nuclear interactions between separate defects. Then, we can write the NV-P1 and P1-P1 interactions as:

$$H_{NV-P1} = \mathbf{S} \cdot \mathbf{D}_{NV-P1} \cdot \mathbf{J}, \tag{2.12}$$

$$H_{P1-P1} = \mathbf{J} \cdot \mathbf{D}_{P1-P1} \cdot \mathbf{J}, \tag{2.13}$$

where $\mathbf{D}_{NV-P1}$ ($\mathbf{D}_{P1-P1}$) is the NV-P1 (P1-P1) electron-electron dipolar interaction tensor. This will be discussed in more detail in Chapter 5.

2.8. DETECTION AND CONTROL OF P1 CENTERS

The dipolar coupling between two electron spins can be used to implement gates as has been demonstrated for NV-NV[33,64,65] and NV-P1 systems[50]. In particular, double electron-electron resonance (DEER) has been used to study electron spins with a dipolar coupling smaller than the central electron spin's dephasing time[61,62,66,73,80]. DEER is a technique where the NV center electron spin is decoupled from the surrounding spin bath by a π-pulse. At the same time, part of the spin bath is recoupled by application of a radio-frequency pulse of a particular frequency f (Fig. 2.9, inset). Then, the NV electron's loss of coherence is caused by that particular subset of the surrounding spin bath.

In Figure 2.9 we show the DEER spectrum of a P1 spin bath for a misaligned magnetic field. A P1 center has four Jahn-Teller axes, three possible nitrogen spin states and two possible electron spin states, totalling 24 states. Since the Jahn-Teller axis is stable under application of RF, we obtain a total of 60 possible transitions. The most important are indicated in colour in Figure 2.9. These are electron-flip transitions for which the nitrogen nuclear spin (and Jahn-Teller axis) remain the same.

Due to the misalignment of the magnetic field, the Jahn-Teller axes A, B and C become non-degenerate. We can thus use RF pulses at frequency f to address the P1 centers in that particular Jahn-Teller axis and nitrogen spin state. If there exists a relatively strongly coupled P1 center electron spin for that particular configuration, the electron picks up phase mainly due to the strongly coupled electron spin. We can use such DEER sequences to detect, control and entangle individual P1 centers in the environment of an NV center, as we will show in Chapter 4.

2.9. DETECTION AND CONTROL OF ^{13}C SPINS

In this section, we discuss the various methods to initialise, readout and control single ^{13}C nuclear spins surrounding an NV center. For universal control of the nuclear spins, both single- and two-qubit gates are necessary. An essential ingredient is the electron-nuclear two-qubit gate which is used for initialisation, control and readout. For strongly

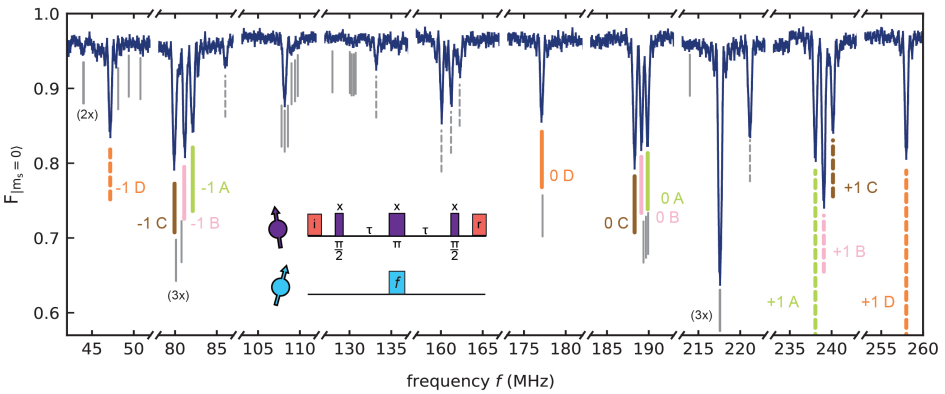

Figure 2.9: **DEER spectroscopy of a P1 spin bath.** The NV center electron spin (purple, inset) is initialised (i) and read out (r) optically. The double electron-electron resonance (DEER) sequence consists of a spin echo on the electron spin while recoupling the spin bath at frequency f. We sweep the frequency f and plot it against the NV electron spin fidelity with $m_s = 0$. Many transitions (grey lines) are observed. In particular, the electron-flipping transitions for fixed nitrogen spin states (-1, 0, +1) and Jahn-Teller axes (A, B, C, D) are indicated (coloured lines). The A, B and C Jahn-Teller axes are non-degenerate because of a misaligned field: $\mathbf{B} = [2.437(2), 1.703(1), 45.5553(5)]$ G. Figure adapted from Degen et al.[50].

coupled spins ($A_\parallel > 1/T^*_{2,e}$ where $T^*_{2,e}$ is the electron spin dephasing time), this gate can be implemented through resonant microwave driving of the electron spin dependent on the nuclear spin state[67,81–83].

However, weakly coupled spins ($A_\parallel < 1/T^*_{2,e}$) are not resolvable in electron spin resonance (ESR) spectra. Thus, a method is needed that extends the electron coherence by decoupling from the spin bath, while coupling to a single, weakly coupled nuclear spin. Such methods have been developed over the past decade in the form of dynamical decoupling sequences[67,84,85].

2.9.1. DYNAMICAL DECOUPLING

To understand how nuclear spin detection and control through dynamical decoupling works, we first turn to the electron-nuclear interaction in Equation 2.7. We can write the ^{13}C spin Hamiltonian separately for the two electron states:

$$H = |0\rangle\langle 0| H_0 + |-1\rangle\langle -1| H_{-1}, \tag{2.14}$$

$$H_0 = \omega_L I_{c,z}, \tag{2.15}$$

$$H_{-1} = (\omega_L - A_\parallel) I_{c,z} + A_\perp I_{c,x}, \tag{2.16}$$

where ω_L is the nuclear spin Larmor frequency. The label 0 (-1) refers to the electron spin state $m_s = 0$ ($m_s = -1$). In the above form, it becomes clear how the nuclear spin evolution depends on the electron spin state. In Fig. 2.10 we show this schematically.

When the electron spin state is $m_s = 0$, the nuclear spin rotation axis is the z-direction with frequency $\omega_L = \gamma_c B_z$. But when the electron-nuclear interaction is turned on in the $m_s = -1$ manifold, the rotation axis tilts away from the z-axis due to the perpendicular hyperfine component $A_\perp$. Both unconditional (single-qubit) and conditional

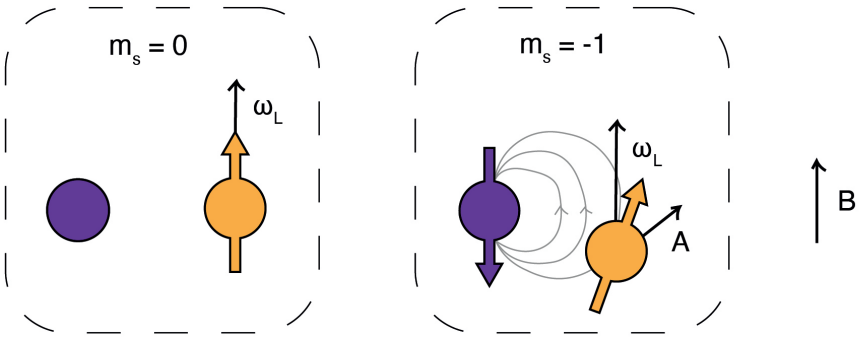

Figure 2.10: **Dependence of the nuclear spin rotation on the electron spin.** When the electron spin is in $m_s = 0$, no hyperfine interaction is present. The nuclear spin thus rotates with the Larmor frequency ω_L along the external magnetic field direction. In $m_s = -1$, the hyperfine interaction with the electron spin is turned on. The nuclear spin rotation axis thus shifts due to the presence of a perpendicular hyperfine component $A_\perp$. This is the essential ingredient for control of nuclear spins with dynamical decoupling.

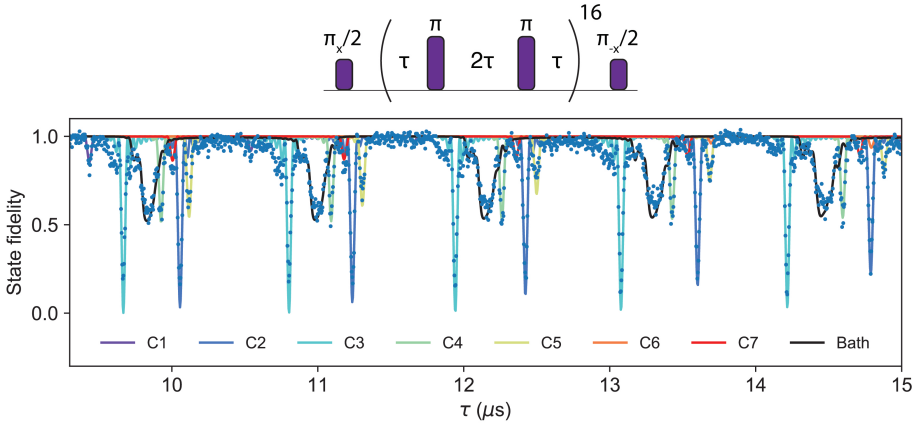

Figure 2.11: **Dynamical decoupling spectroscopy.** (Top) Experimental sequence on the electron spin to obtain a dynamical decoupling spectrum. Before application of the pulse sequence, the electron spin is initialised in $m_s = 0$. (Bottom) Experimentally obtained dynamical decoupling spectrum. The interpulse delay τ is swept for $N = 32$. Multiple ^{13}C nuclear spins result in clear loss of electron coherence, i.e. a dip in the measured state fidelity. The bath is described by 200 randomly generated spins with hyperfine coupling < 10 kHz. Figure adapted from Abobeih et al. [44].

(two-qubit) gates can be obtained by repeatedly flipping between the two rotation axes in the form of a dynamical decoupling sequence[67].

The basic unit of a dynamical decoupling sequence consists of $(\tau - \pi_e - 2\tau - \pi_e - \tau)$ where π_e is a π-pulse on the electron spin and τ is a waiting time. We can write down the unitary evolution of the nuclear spin under this unit as[67]:

$$V_0 = e^{-iH_0\tau} e^{-2iH_{-1}\tau} e^{-iH_0\tau} = e^{-i\phi \mathbf{I}\cdot\hat{\mathbf{n}}_0}, \tag{2.17}$$

$$V_1 = e^{-iH_{-1}\tau} e^{-2iH_0\tau} e^{-iH_{-1}\tau} = e^{-i\phi \mathbf{I}\cdot\hat{\mathbf{n}}_{-1}}, \tag{2.18}$$

where $\hat{\mathbf{n}}_0$ ($\hat{\mathbf{n}}_{-1}$) is the nuclear spin rotation axis when the electron spin is $m_s = 0$ ($m_s = -1$). To achieve a conditional rotation of the nuclear spin dependent on the electron spin we thus require $\hat{\mathbf{n}}_0 \cdot \hat{\mathbf{n}}_{-1} = -1$. This occurs at a value of τ characteristic of a certain value of the electron-nuclear hyperfine coupling. Specifically this condition is met when

$$\tau_k \approx \frac{(2k-1)\pi}{2\omega_L - A_\parallel}, \tag{2.19}$$

with k a nonzero integer[67]. The rotation angle ϕ is then determined by the number of applications of this dynamical decoupling unit.

Typically, the environment surrounding the NV center electron spin consists of many ^{13}C nuclear spins. We can thus sweep the interpulse delay τ to detect different nuclear spins. To that end the electron spin is initialised in a superposition. A dynamical decoupling sequence with interpulse delay τ and N pulses is then applied. The electron spin loses coherence when τ is resonant with one of the environmental spins, obtaining a dip in electron coherence (Fig. 2.11).

We can describe the probability to find the electron in the initial superposition as[44]

$$P = (M+1)/2, \tag{2.20}$$

$$M = \prod_i M_i, \tag{2.21}$$

$$M_i = \mathrm{Re}\left[\mathrm{Tr}\left[V_{0,i}^{N/2}\left(V_{1,i}^{N/2}\right)^\dagger\right]\right], \tag{2.22}$$

where M_i is the signal originating from nuclear spin i.

The data in Fig. 2.11 can be fit to obtain the hyperfine parameters of the nuclear spins[44,86]. More advanced deep learning techniques can be applied to the same effect[87,88]. Alternatively, direct measurements of the nuclear spin frequencies can be performed from which the hyperfine parameters can be distilled[41,89]. We have used these methods in combination with nuclear-nuclear interactions to image 27 nuclear spins in the environment surrounding the electron spin[41].

2.9.2. DYNAMICAL DECOUPLING WITH RADIO-FREQUENCY DRIVING (DDRF)

Recently, a new technique has been developed to obtain an electron-nuclear two-qubit interaction through direct, radio-frequency (RF) driving of the nuclear spin[45]. By combining the nuclear spin driving with dynamical decoupling of the electron spin, we both

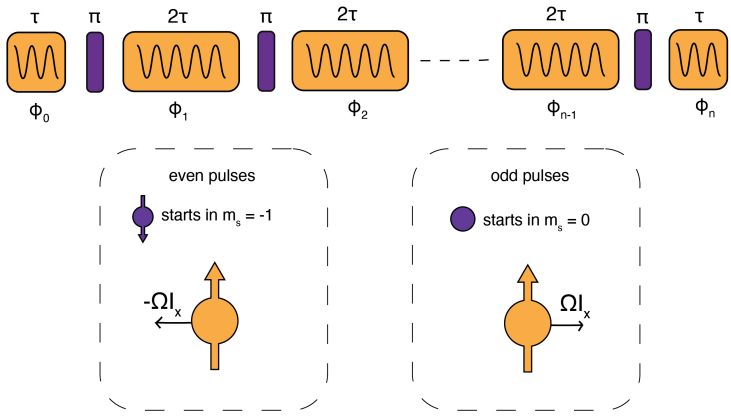

Figure 2.12: **The DDRF pulse sequence.** (Top) The pulse sequence consists of radio-frequency (RF) pulses to drive the nuclear spin combined with dynamical decoupling on the electron spin. The phase of subsequent RF pulses ϕ_i is updated to account for the free evolution of the nuclear spin. To make the gate conditional on the electron spin, each odd RF pulse gets a π phase shift. (Bottom) Schematic of the driving of the nuclear spin depending on the initial electron state for the conditional DDRF gate. The nuclear spin rotates around x ($-x$) when the electron starts in $m_s = 0$ ($m_s = -1$).

preserve the electron coherence and we can drive the nuclear spin either independent of (single-qubit gate) or dependent on (two-qubit gate) the initial electron spin state. Here, we outline the basics of this technique.

First, we discuss the application of an RF pulse on the nuclear spin. We consider an RF pulse with Rabi frequency Ω, phase ϕ and frequency ω. To control a specific nuclear spin, we set the frequency $\omega = \omega_1$, where ω_1 is the nuclear spin frequency when the electron is in $m_s = -1$. For simplicity, we assume that we can neglect nuclear spin driving when the electron is in $m_s = 0$ and we assume $A_\perp = 0$. These conditions hold for a nuclear spin with a relatively large $A_\parallel$ and a large magnetic field ($\gamma_c B \gg A_\parallel, A_\perp$) respectively. In the rotating frame of the RF frequency, we can then write the Hamiltonian as[45]:

$$H = |0\rangle\langle 0|\,(\omega_L - \omega_1)\,I_z \tag{2.23}$$

$$+\,|1\rangle\langle 1|\,\Omega(\cos(\phi)I_x + \sin(\phi)I_y), \tag{2.24}$$

where $|0\rangle$ ($|1\rangle$) is the electron spin projection. When the electron is in $m_s = 0$, the RF is off-resonant and the nuclear spin simply rotates around z. However, when the electron is in $m_s = -1$, the RF is resonant and the nuclear spin undergoes a rotation around an axis determined by the RF phase ϕ.

Now, we add dynamical decoupling to the electron spin. This results in a sequence as shown in Fig. 2.12. We number the pulses from 0 to n, indicated by the subscript of their phases. When the electron starts in $m_s = -1$ ($m_s = 0$), the even (odd) pulses are resonant, since the RF is resonant when the electron is in $m_s = -1$. By setting different rotation

axes for the even/odd pulses through their phase ϕ, we can construct both single- and two-qubit gates.

Since the RF pulses are now interspersed with dynamical decoupling pulses, we need to account for the free evolution of the nuclear spin between subsequent RF pulses. We thus update the RF phase by $\phi_n = (\omega_L - \omega_1)n\tau$ where n is the pulse number. By accounting for the nuclear spin evolution, the rotation of even and odd pulses is effectively around the same axis. To turn this into a conditional electron-nuclear operation, the nuclear spin evolution should depend on the electron spin state. We can therefore add a π phase shift to all odd pulses:

$$\phi_n = \begin{cases} (\omega_L - \omega_1)n\tau, & n \text{ even} \\ (\omega_L - \omega_1)n\tau + \pi, & n \text{ odd} \end{cases} \tag{2.25}$$

In this way, we obtain the interaction presented in Fig. 2.12 where the rotation axis is $-x$ when the electron is in $m_s = -1$ and $+x$ when the electron is in $m_s = 0$. By removing the π phase shift, we obtain a nuclear spin rotation independent of the initial electron spin state.

The generalised controlled interaction obtained with the DDRF gate is [45]

$$U = |0\rangle\langle 0| \otimes R_\phi(N\Omega\tau) \tag{2.26}$$

$$+ |1\rangle\langle 1| \otimes R_\phi(-N\Omega\tau). \tag{2.27}$$

The maximally entangling gate is obtained when $N\Omega\tau = \pi/2$. Choosing the rotation axis to be the x-axis, we can rewrite this to

$$U = |0\rangle\langle 0| \otimes R_x(\pi/2) + |1\rangle\langle 1| \otimes R_x(-\pi/2) = R_x^{(e,n)}(\pm\pi/2). \tag{2.28}$$

This can be related to a CNOT by local operations:

$$\text{CNOT} = R_x^{(e,n)}(\pm\pi/2)R_z^{(e)}(-\pi/2)R_x^{(n)}(-\pi/2), \tag{2.29}$$

where e, n refer to the electron and nuclear spin respectively. Note that the relation between a CNOT and the dynamical decoupling two-qubit gate encountered in the previous section is analogous to the one derived here.

2.9.3. COMPARISON OF DD AND DDRF

We have discussed two different approaches to constructing a $R_x^{(e,n)}(\pm\pi/2)$ gate in the previous section. One is based on dynamical decoupling (DD) and the other is based on combining DD with RF driving of the nuclear spin (DDRF). Here, we highlight some of the important differences and trade-offs between the two schemes.

First, the perpendicular hyperfine coupling $A_\perp$ is essential for DD, but not for DDRF. Namely, the DD scheme relies on the different nuclear rotation axes between $m_s = 0$ and $m_s = -1$ (Fig. 2.10). At high magnetic fields ($\gtrsim 2$ kG) the relative effect of $A_\perp$ diminishes and the nuclear rotation axes are more similar. The DDRF scheme does not require the presence of $A_\perp$ since the nuclear spins are driven directly by radio-frequency pulses. Its presence even reduces the two-qubit gate fidelity [45]. For the DDRF scheme, moving to a high magnetic field is therefore desired as it makes the effect of $A_\perp$ smaller.

Second, DDRF is a more general scheme than DD. For spin-1/2 defects, DD is only second-order sensitive to the hyperfine interaction $A_\perp$ [90], whereas DDRF functions analogously as presented above. There is a complication in applying DDRF to spin-1/2 systems in that nuclear spins do not bunch up at the Larmor frequency ω_L anymore. Therefore, unwanted driving of nuclear spins is more likely to happen during DDRF. The application of DDRF to spin-1/2 systems still has to be demonstrated experimentally.

Third, the DD scheme's specificity lies in the choice of τ. For DDRF, it lies in the chosen RF frequency and phase-update ϕ_n. In principle the choice of τ in DDRF is free. Importantly though, τ has to be chosen such that the dynamical decoupling sequence of DDRF does not rotate any nuclear spins.

Finally, DDRF does add additional complexity to the experimental setup. In particular, the application of RF can heat up the diamond device [45]. This can result in the deterioration of the optical single-shot readout at low temperatures.

In any real experiment, a combination of DD and DDRF is likely to be most suitable [45]. Each nuclear spin can then be addressed by its most optimal gate. Nuclear spins with a relatively large $A_\perp$ are likely best addressed by DD, whereas nuclear spins with a smaller $A_\perp$ are best addressed by DDRF. At high magnetic fields ($\gtrsim$ 2 kG) DDRF likely becomes more favourable. Future work on optimising nuclear spin gate fidelities will shine more light on what type of gate is optimal under what conditions.

2.9.4. INITIALISATION AND READOUT OF NUCLEAR SPINS

With dynamical decoupling or DDRF we can apply a $R_x^{(e,n)}(\pm\pi/2)$ gate between the electron and nuclear spin. The electron spin can be initialised optically in $m_s = 0$ (Sec. 2.2). However, the nuclear spin has to be initialised through the electron spin. Here, we can take two approaches.

The first initialisation method is measurement-based initialisation (MBI) (Fig. 2.13) [44,45,67]. Here, we apply two electron single-qubit gates and an electron-nuclear two-qubit gate to obtain the state:

$$\frac{1}{2}\Big(|0\rangle\langle 0|_e \otimes |x\rangle\langle x|_n + |1\rangle\langle 1|_e \otimes |-x\rangle\langle -x|_n\Big). \tag{2.30}$$

When we read out the electron spin, we thus project the nuclear spin in either $|x\rangle$ or $|-x\rangle$. As outlined in Section 2.2, it is vital for MBI that we only observe a photon when the underlying spin state is $m_s = 0$ with high probability (> 99%). This leads to high-fidelity initialisation of the nuclear spin in $|x\rangle$. When no photon is obtained, there is a non-negligible chance the electron was in $m_s = 0$. This would mean a significant reduction in initialisation fidelity. We thus condition MBI on obtaining a photon during the electron readout.

Alternatively, we apply an additional electron-nuclear gate $R_y^{(e,n)}(\pm\pi/2)$ to Equation 2.30. Then, we initialise the nuclear spin regardless of the electron spin state:

$$\frac{1}{2}\Big(|0\rangle\langle 0|_e \otimes |0\rangle\langle 0|_n + |1\rangle\langle 1|_e \otimes |0\rangle\langle 0|_n\Big). \tag{2.31}$$

This is nuclear spin initialisation based on a deterministic SWAP gate: the electron spin state is swapped to the nuclear spin [45]. Afterwards, we optically reinitialise the electron

spin in $m_s = 0$. The advantage of SWAP initialisation is in its deterministic nature. However, this comes at the expense of using an additional two-qubit gate, potentially reducing the initialisation fidelity.

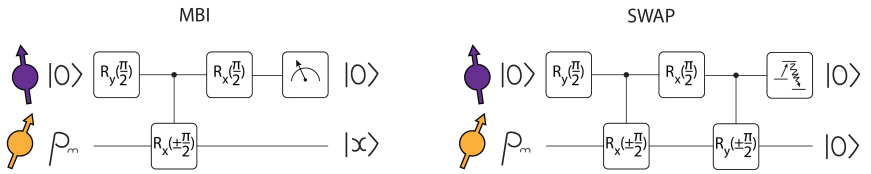

Figure 2.13: **Quantum circuits for nuclear spin initialisation.** (Left) Circuit for measurement-based initialisation (MBI). The nuclear spin is initialised in $|x\rangle$ upon measuring a photon, which projects the electron spin in $m_s = 0$. (Right) Circuit for SWAP initialisation. By adding an additional two-qubit gate compared to MBI, the initialisation can be made deterministic. At the end of the sequence, we reset the electron spin to $m_s = 0$.

REFERENCES

[1] M. Ruf *et al., Optically coherent nitrogen-vacancy centers in micrometer-thin etched diamond membranes,* Nano Lett. **19**, 3987 (2019).

[2] D. Twitchen *et al., Electron paramagnetic resonance (epr) and optical absorption studies of defects created in diamond by electron irradiation damage at 100 and 350 k,* Physica B Condens. **273**, 628 (1999).

[3] B. Campbell and A. Mainwood, *Radiation damage of diamond by electron and gamma irradiation,* Phys. Status Solidi A **181**, 99 (2000).

[4] Y.-C. Chen *et al., Laser writing of coherent colour centres in diamond,* Nat. Photonics **11**, 77 (2017).

[5] Y.-C. Chen *et al., Laser writing of individual nitrogen-vacancy defects in diamond with near-unity yield,* Optica **6**, 662 (2019).

[6] J. M. Smith, S. A. Meynell, A. C. B. Jayich and J. Meijer, *Colour centre generation in diamond for quantum technologies,* Nanophotonics **8**, 1889 (2019).

[7] C. Stephen *et al., Deep three-dimensional solid-state qubit arrays with long-lived spin coherence,* Phys. Rev. Appl. **12**, 064005 (2019).

[8] D. Antonov *et al., Statistical investigations on nitrogen-vacancy center creation,* Applied Physics Letters **104**, 012105 (2014).

[9] B. Naydenov *et al., Enhanced generation of single optically active spins in diamond by ion implantation,* Applied Physics Letters **96**, 163108 (2010).

[10] F. Fávaro de Oliveira *et al., Tailoring spin defects in diamond by lattice charging,* Nature Communications **8**, 15409 (2017).

[11] M. Kasperczyk *et al., Statistically modeling optical linewidths of nitrogen vacancy centers in microstructures,* Phys. Rev. B **102**, 075312 (2020).

[12] S. B. van Dam *et al., Optical coherence of diamond nitrogen-vacancy centers formed by ion implantation and annealing,* Phys. Rev. B **99**, 161203 (2019).

[13] N. Aslam, G. Waldherr, P. Neumann, F. Jelezko and J. Wrachtrup, *Photo-induced ionization dynamics of the nitrogen vacancy defect in diamond investigated by single-shot charge state detection,* New J. Phys. **15**, 013064 (2013).

[14] S. Baier *et al., Orbital and spin dynamics of single neutrally-charged nitrogen-vacancy centers in diamond,* Phys. Rev. Lett. **125**, 193601 (2020).

[15] G. Waldherr *et al., Dark states of single nitrogen-vacancy centers in diamond unraveled by single shot nmr,* Phys. Rev. Lett. **106**, 157601 (2011).

[16] M. S. Barson, E. Krausz, N. B. Manson and M. W. Doherty, *The fine structure of the neutral nitrogen-vacancy center in diamond,* Nanophotonics **8**, 1985 (2019).

[17] M. W. Doherty, N. B. Manson, P. Delaney and L. C. Hollenberg, *The negatively charged nitrogen-vacancy centre in diamond: the electronic solution,* New J. Phys. **13**, 025019 (2011).

[18] J. R. Maze *et al.*, *Properties of nitrogen-vacancy centers in diamond: the group theoretic approach,* New J. Phys. **13**, 025025 (2011).

[19] B. J. Hensen, *Quantum nonlocality with spins in diamond,* Ph.D. Thesis, TUDelft (2016).

[20] M. W. Doherty *et al.*, *The nitrogen-vacancy colour centre in diamond,* Phys. Rep. **528**, 1 (2013).

[21] W. Pfaff, *Quantum measurement and entanglement of spin quantum bits in diamond,* Ph.D. Thesis, TUDelft (2013).

[22] H. Bernien, *Control, measurement and entanglement of remote quantum spin registers in diamond,* Ph.D. Thesis, TUDelft (2014).

[23] K.-M. C. Fu *et al.*, *Observation of the dynamic jahn-teller effect in the excited states of nitrogen-vacancy centers in diamond,* Phys. Rev. Lett. **103**, 256404 (2009).

[24] R. Albrecht, A. Bommer, C. Deutsch, J. Reichel and C. Becher, *Coupling of a single nitrogen-vacancy center in diamond to a fiber-based microcavity,* Phys. Rev. Lett. **110**, 243602 (2013).

[25] D. A. Hopper, H. J. Shulevitz and L. C. Bassett, *Spin readout techniques of the nitrogen-vacancy center in diamond,* Micromachines **9**, 437 (2018).

[26] P. Tamarat *et al.*, *Stark shift control of single optical centers in diamond,* Phys. Rev. Lett. **97**, 083002 (2006).

[27] L. Robledo *et al.*, *High-fidelity projective read-out of a solid-state spin quantum register,* Nature **477**, 574 (2011).

[28] A. Gruber *et al.*, *Scanning confocal optical microscopy and magnetic resonance on single defect centers,* Science **276**, 2012 (1997).

[29] P. Neumann *et al.*, *Multipartite entanglement among single spins in diamond,* science **320**, 1326 (2008).

[30] T. H. Taminiau, J. Cramer, T. van der Sar, V. V. Dobrovitski and R. Hanson, *Universal control and error correction in multi-qubit spin registers in diamond,* Nat. Nanotechnol. **9**, 171 (2014).

[31] M. Steiner, P. Neumann, J. Beck, F. Jelezko and J. Wrachtrup, *Universal enhancement of the optical readout fidelity of single electron spins at nitrogen-vacancy centers in diamond,* Phys. Rev. B **81**, 035205 (2010).

[32] A. Gupta, L. Hacquebard and L. Childress, *Efficient signal processing for time-resolved fluorescence detection of nitrogen-vacancy spins in diamond,* J. Opt. Soc. Am. B **33**, B28 (2016).

[33] P. Neumann *et al., Single-shot readout of a single nuclear spin,* Science **329**, 542 (2010).

[34] A. Dréau, P. Spinicelli, J. Maze, J.-F. Roch and V. Jacques, *Single-shot readout of multiple nuclear spin qubits in diamond under ambient conditions,* Phys. Rev. Lett. **110**, 060502 (2013).

[35] G.-Q. Liu *et al., Single-shot readout of a nuclear spin weakly coupled to a nitrogen-vacancy center at room temperature,* Phys. Rev. Lett. **118**, 150504 (2017).

[36] D. A. Hopper, J. D. Lauigan, T.-Y. Huang and L. C. Bassett, *Real-time charge initialization of diamond nitrogen-vacancy centers for enhanced spin readout,* Phys. Rev. Appl. **13**, 024016 (2020).

[37] B. J. Shields, Q. P. Unterreithmeier, N. P. de Leon, H. Park and M. D. Lukin, *Efficient readout of a single spin state in diamond via spin-to-charge conversion,* Phys. Rev. Lett. **114**, 136402 (2015).

[38] M. L. Goldman *et al., Phonon-induced population dynamics and intersystem crossing in nitrogen-vacancy centers,* Phys. Rev. Lett. **114**, 145502 (2015).

[39] M. L. Goldman *et al., State-selective intersystem crossing in nitrogen-vacancy centers,* Phys. Rev. B **91**, 165201 (2015).

[40] N. Kalb, P. C. Humphreys, J. Slim and R. Hanson, *Dephasing mechanisms of diamond-based nuclear-spin memories for quantum networks,* Phys. Rev. A **97**, 062330 (2018).

[41] M. Abobeih *et al., Atomic-scale imaging of a 27-nuclear-spin cluster using a quantum sensor,* Nature **576**, 411 (2019).

[42] M. Pompili *et al., Realization of a multinode quantum network of remote solid-state qubits,* Science **372**, 259 (2021).

[43] S. L. N. Hermans *et al., Qubit teleportation between non-neighbouring nodes in a quantum network,* Nature **605**, 663 (2022).

[44] M. H. Abobeih *et al., One-second coherence for a single electron spin coupled to a multi-qubit nuclear-spin environment,* Nat. Commun. **9**, 1 (2018).

[45] C. E. Bradley *et al., A ten-qubit solid-state spin register with quantum memory up to one minute,* Phys. Rev. X **9**, 031045 (2019).

[46] H. Bernien *et al., Heralded entanglement between solid-state qubits separated by three metres,* Nature **497**, 86 (2013).

[47] S. L. N. Hermans *et al., Qubit teleportation between non-neighbouring nodes in a quantum network,* Nature **605**, 663 (2022).

[48] S. Hermans, *Quantum networks using spins in diamond,* Ph.D. Thesis, TUDelft (2022).

[49] M. Abobeih, *From atomic-scale imaging to quantum fault-tolerance with spins in diamond,* Ph.D. Thesis, TUDelft (2021).

[50] M. Degen *et al.*, *Entanglement of dark electron-nuclear spin defects in diamond,* Nat. Commun. **12**, 1 (2021).

[51] N. Kalb, *Diamond-based quantum networks with multi-qubit nodes,* Ph.D. Thesis, TUDelft (2018).

[52] C. Bradley, *Order from disorder: Control of multi-qubit spin registers in diamond,* Ph.D. Thesis, TUDelft (2021).

[53] M. Doherty *et al., Theory of the ground-state spin of the nv- center in diamond,* Phys. Rev. B **85**, 205203 (2012).

[54] V. Ivády, I. A. Abrikosov and A. Gali, *First principles calculation of spin-related quantities for point defect qubit research,* NPJ Comput. Mater. **4**, 1 (2018).

[55] A. Jarmola, V. Acosta, K. Jensen, S. Chemerisov and D. Budker, *Temperature-and magnetic-field-dependent longitudinal spin relaxation in nitrogen-vacancy ensembles in diamond,* Phys. Rev. Lett. **108**, 197601 (2012).

[56] S. Takahashi, R. Hanson, J. van Tol, M. S. Sherwin and D. D. Awschalom, *Quenching spin decoherence in diamond through spin bath polarization,* Phys. Rev. Lett. **101**, 047601 (2008).

[57] C. E. Bradley *et al.*, *Robust quantum-network memory based on spin qubits in isotopically engineered diamond,* npj Quantum Information **8**, 122 (2022).

[58] M. Blok, *Quantum measurement and real-time feedback with a spin-register in diamond,* Ph.D. Thesis, TUDelft (2015).

[59] N. Bar-Gill, L. M. Pham, A. Jarmola, D. Budker and R. L. Walsworth, *Solid-state electronic spin coherence time approaching one second,* Nat. Commun. **4**, 1 (2013).

[60] K. Cujia, J. M. Boss, K. Herb, J. Zopes and C. L. Degen, *Tracking the precession of single nuclear spins by weak measurements,* Nature **571**, 230 (2019).

[61] H. S. Knowles, D. M. Kara and M. Atatüre, *Demonstration of a coherent electronic spin cluster in diamond,* Phys. Rev. Lett. **117**, 100802 (2016).

[62] H. S. Knowles, D. M. Kara and M. Atatüre, *Observing bulk diamond spin coherence in high-purity nanodiamonds,* Nature Materials **13**, 21 (2014).

[63] C. Belthangady *et al.*, *Dressed-state resonant coupling between bright and dark spins in diamond,* Physical Review Letters **110**, 1 (2013).

[64] F. Dolde *et al.*, *Room-temperature entanglement between single defect spins in diamond,* Nat. Phys. **9**, 139 (2013).

[65] F. Dolde *et al.*, *High-fidelity spin entanglement using optimal control,* Nat. Commun. **5**, 3371 (2014).

[66] E. L. Rosenfeld, L. M. Pham, M. D. Lukin and R. L. Walsworth, *Sensing coherent dynamics of electronic spin clusters in solids,* Phys. Rev. Lett. **120**, 243604 (2018).

[67] T. Taminiau *et al.*, *Detection and control of individual nuclear spins using a weakly coupled electron spin,* Phys. Rev. Lett. **109**, 137602 (2012).

[68] A. P. Nizovtsev *et al.*, *Non-flipping 13c spins near an nv center in diamond: hyperfine and spatial characteristics by density functional theory simulation of the c510 [nv] h252 cluster,* New J. Phys. **20**, 023022 (2018).

[69] R. Ulbricht *et al.*, *Single substitutional nitrogen defects revealed as electron acceptor states in diamond using ultrafast spectroscopy,* Physical Review B - Condensed Matter and Materials Physics **84**, 1 (2011).

[70] P. Deák, B. Aradi, M. Kaviani, T. Frauenheim and A. Gali, *Formation of NV centers in diamond: A theoretical study based on calculated transitions and migration of nitrogen and vacancy related defects,* Physical Review B - Condensed Matter and Materials Physics **89**, 1 (2014).

[71] W. V. Smith, P. P. Sorokin, I. L. Gelles and G. J. Lasher, *Electron-spin resonance of nitrogen donors in diamond,* Phys. Rev. **115**, 1546 (1959).

[72] R. Cook and D. H. Whiffen, *Electron nuclear double resonance study of a nitrogen centre in diamond,* Proc. Math. Phys. Eng. Sci. **295**, 99 (1966).

[73] G. De Lange *et al.*, *Controlling the quantum dynamics of a mesoscopic spin bath in diamond,* Scientific Reports **2**, 1 (2012).

[74] S. J. Breuer and P. R. Briddon, *Energy barrier to reorientation of the substitutional nitrogen in diamond,* Phys. Rev. B **53**, 7819 (1996).

[75] H. A. Jahn, E. Teller and F. G. Donnan, *Stability of polyatomic molecules in degenerate electronic states - I—Orbital degeneracy,* Proceedings of the Royal Society of London. Series A - Mathematical and Physical Sciences **161**, 220 (1937).

[76] I. M. Zaritskii, V. Bratus, V. S. Vikhnin and A. A. Konchits, *Spin-lattice relaxation of the Jahn-Teller nitrogen center in diamond,* Sov. Phys. Solid State **18**, 1883 (1976).

[77] L. Shulman, M. Zaritskii and G. Podzyarei, *Reorientation of the jahn-teller distortion in nitrogen impurity centers in diamond,* Sov. Phys. Solid State **8**, 1842 (1967).

[78] C. A. J. Ammerlaan and E. A. Burgemeister, *Reorientation of nitrogen in type-Ib diamond by thermal excitation and tunneling,* Phys. Rev. Lett. **47**, 954 (1981).

[79] F. J. Heremans, G. D. Fuchs, C. F. Wang, R. Hanson and D. D. Awschalom, *Generation and transport of photoexcited electrons in single-crystal diamond,* Applied Physics Letters **94**, 152102 (2009).

[80] A. Cooper, W. K. C. Sun, J. C. Jaskula and P. Cappellaro, *Identification and Control of Electron-Nuclear Spin Defects in Diamond,* Physical Review Letters **124**, 83602 (2020).

[81] G. Waldherr *et al., Quantum error correction in a solid-state hybrid spin register,* Nature **506**, 204 (2014).

[82] L. Childress *et al., Coherent dynamics of coupled electron and nuclear spin qubits in diamond,* Science **314**, 281 (2006).

[83] M. G. Dutt *et al., Quantum register based on individual electronic and nuclear spin qubits in diamond,* Science **316**, 1312 (2007).

[84] N. Zhao *et al., Sensing single remote nuclear spins,* Nat. Nanotechnol. **7**, 657 (2012).

[85] S. Kolkowitz, Q. P. Unterreithmeier, S. D. Bennett and M. D. Lukin, *Sensing distant nuclear spins with a single electron spin,* Phys. Rev. Lett. **109**, 137601 (2012).

[86] J. Cramer, *Quantum error correction with spins in diamond,* Ph.D. Thesis, TUDelft (2016).

[87] K. Jung *et al., Deep learning enhanced individual nuclear-spin detection,* NPJ Quantum Inf. **7**, 1 (2021).

[88] H. Oh *et al., Algorithmic decomposition for efficient multiple nuclear spin detection in diamond,* Sci. Rep. **10**, 1 (2020).

[89] J. Zopes *et al., Three-dimensional localization spectroscopy of individual nuclear spins with sub-angstrom resolution,* Nat. Commun. **9**, 4678 (2018).

[90] S. Maity *et al., Mechanical control of a single nuclear spin,* Phys. Rev. X **12**, 011056 (2022).

3

ENTANGLEMENT OF SPIN-PAIR QUBITS WITH INTRINSIC DEPHASING TIMES EXCEEDING A MINUTE

H.P. Bartling, M.H. Abobeih, B. Pingault, M.J. Degen, S.J.H. Loenen, C. E. Bradley, J. Randall, M. Markham, D.J. Twitchen, T.H. Taminiau

Understanding and protecting the coherence of individual quantum systems is a central challenge in quantum science and technology. Over the last decades, a rich variety of methods to extend coherence have been developed. A complementary approach is to look for naturally occurring systems that are inherently protected against decoherence. Here, we show that pairs of identical nuclear spins in solids form intrinsically long-lived qubits. We study three carbon-13 pairs in diamond and realize high-fidelity measurements of their quantum states using a single NV center in their vicinity. We then reveal that the spin pairs are robust to external perturbations due to a combination of three phenomena: a decoherence-free subspace, a clock transition, and a variant on motional narrowing. The resulting inhomogeneous dephasing time is $T_2^* = 1.9(6)$ minutes, the longest reported for individually controlled qubits. Finally, we develop complete control and realize an entangled state between two spin pairs through projective parity measurements. These long-lived qubits are abundantly present in diamond and other solids, and provide new opportunities for ancilla-enhanced quantum sensing and for robust memory qubits for quantum networks.

The results of this chapter have been published in Phys. Rev. X **12**, 011048 (2022).

3.1. INTRODUCTION

Solid-state spins provide a versatile platform for investigating quantum physics and realizing quantum technologies[1–28]. A central challenge is to protect spin qubits from decoherence due to their environment. Various methods to extend coherence times have been developed for spin ensembles[2,7–9], as well as individually controlled spin qubits[1,3–6,10,11,16,17]. These methods include the precise tuning of magnetic fields to create magnetic-field insensitive clock transitions[7,9,10,29,30], decoherence-free subspaces to protect against correlated noise[5,10,19,30], dynamical decoupling to mitigate slowly varying noise[2–4,8,9,11,31], real-time Hamiltonian estimation[6], quantum error correction[16,17,32], and isotopic purification to remove the spin background[2,3,8].

Here, we take a different approach: we look for naturally occurring qubits that are inherently protected against decoherence. We investigate pairs of identical interacting nuclear spins[33]. Such spin pairs are naturally and abundantly present in solids like diamond, silicon, silicon-carbide, germanium, graphene and MoS_2[11,13,14,21,22]. Traditionally, the dynamics of such spin pairs have been regarded as a primary noise source for solid-state spin qubits[7,11,21,22,34]. In contrast, we show that spin pairs themselves provide individually controllable and decoherence-protected quantum systems. First, we develop high-fidelity initialisation and single-shot readout of multiple spin-pair qubits. Then, we investigate their coherence and show that they are inherently protected by a combination of a decoherence-free subspace, a clock transition, and a variant on motional narrowing. Finally, we highlight the potential of these spin pairs as qubits by creating an entangled state of two spin pairs through sequential non-destructive parity measurements.

3.2. SPIN PAIRS

The system that we investigate is illustrated in Fig. 3.1a. We consider three pairs of coupled ^{13}C nuclear spins in the vicinity of an NV center in a diamond at 3.7 K. The NV center provides a controllable electron spin with long coherence times that can be initialised and measured optically[2,4,11,14,16–18]. Because the NV spin creates a switchable local magnetic-field gradient over each pair, it can be used to sense and manipulate the spin pairs[11,13,14], despite their excellent protection from external influences.

A spin-1/2 pair is described by four states: $|\uparrow\uparrow\rangle$, $|\uparrow\downarrow\rangle$, $|\downarrow\uparrow\rangle$ and $|\downarrow\downarrow\rangle$. We focus on the dynamics in the antiparallel subspace and define a pseudo-spin spanned by $|\Uparrow\rangle = |\uparrow\downarrow\rangle$ and $|\Downarrow\rangle = |\downarrow\uparrow\rangle$[11,13,14]. The pseudo-spin Hamiltonian is (Sec. 3.9.3):

$$H = X\hat{I}_x + m_s Z\hat{I}_z, \tag{3.1}$$

in which $\hat{I}_z$ and $\hat{I}_x$ are spin–1/2 operators. X is the dipolar coupling between the ^{13}C spins, which creates the evolution $|\Uparrow\rangle \leftrightarrow |\Downarrow\rangle$ (flip-flops). $m_s = \{-1, 0, +1\}$ is the NV spin projection and Z is the difference between the two NV-^{13}C hyperfine couplings (Sec. 3.9.3).

Pair A and pair B are nearest-neighbour pairs oriented along the external magnetic field with $X_A = X_B = 2080.9900(3)$ Hz, $Z_A = 130(1)$ Hz and $Z_B = 91(2)$ Hz (see measurements below). Pair C has a larger spatial separation between the spins resulting

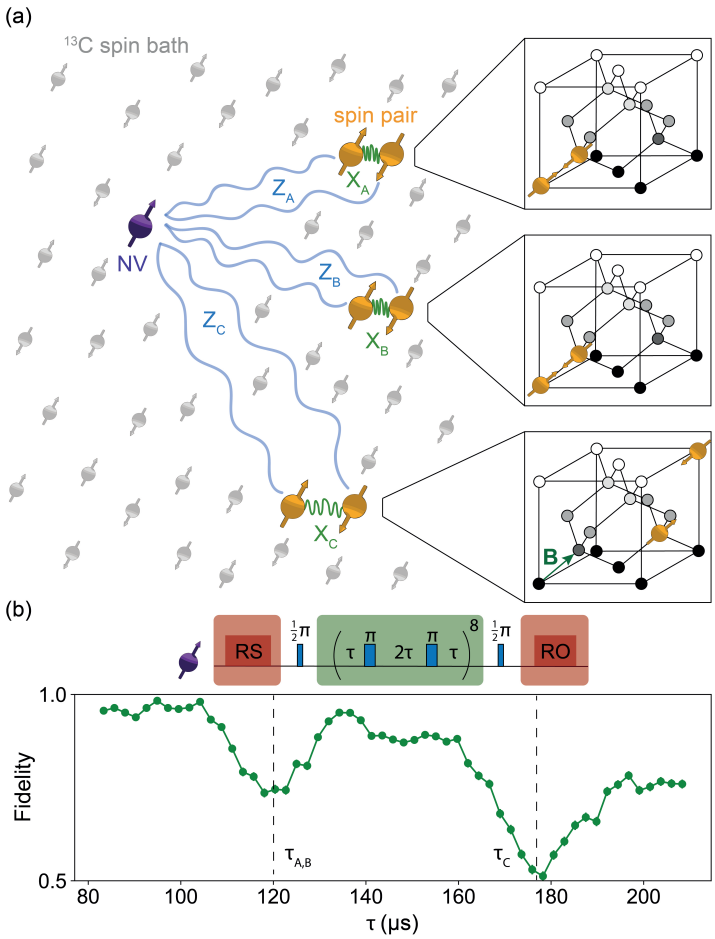

Figure 3.1: **System and basic spectroscopy. a.** We study three ^{13}C spin pairs (A, B and C) in a diamond. The pairs are detected and controlled using a nearby NV center. The insets show the spatial configuration of the pairs. Pair A and B are nearest-neighbour pairs oriented along the external magnetic field B_z. For pair C we show one of the three possible orientations (Sec. 3.9.8). The main source of decoherence is the surrounding bath of ^{13}C spins (1.1% abundance). **b.** Sensing the pair pseudo-spins [11,13,14]. The NV electron spin is prepared in a superposition and a periodic sequence of π pulses is applied. If the interpulse delay is resonant with the dynamics of a pair, a loss of electron coherence is observed. We set $\tau = m2\pi/\omega_L$ with m an integer and ω_L the ^{13}C Larmor frequency to avoid interactions with individual ^{13}C spins [11,14]. The vertical lines mark the values for τ used in this work for the three pairs ($\tau_A = \tau_B = 120.330$ μs and $\tau_C = 177.026$ μs). The NV spin is prepared (RS) and read out (RO) optically (Sec. 3.9.1). The error bars represent one standard deviation.

in X_C = 188.33(2) Hz, and Z_C = 2802(2) Hz. In the following, we develop initialisation, control and measurement for pairs A and B, for which $X \gg Z$ (see Sec. 3.9.4 for pair C control, for which $Z \gg X$).

Previous work has demonstrated that the pseudo-spin of pairs can be detected through decoupling sequences that toggle the $m_s Z \hat{I}_z$ term by periodically inverting the NV electron spin (Fig. 3.1b)[11,13,14]. For an interpulse delay of $2\tau = \pi/\omega_r$, with $\omega_r = \sqrt{X^2 + (Z/2)^2}$, the sequence is resonant with the pseudo-spin dynamics and the effective NV-pair interaction is of the form $\hat{S}_z \hat{I}_z$, with $\hat{S}_z$ the spin operator for the NV electron spin[11,13,14]. The NV center thus accumulates a phase that depends on the z-projection of the pseudo-spin. We use the NV center as a sensor to detect the spin pairs in its environment by sweeping τ (Fig. 3.1b)[11,13,14] and find the resonances for pair A and B (τ = 120.330 μs) and pair C (τ = 177.026 μs).

3.3. INITIALISATION AND READOUT

We start by developing projective single-shot measurements. Unlike all previous work, which was limited to manipulating mixed states of the parallel and antiparallel subspaces[11], these measurements enable us to initialise and measure the complete state of the spin pairs with high contrast.

Our method is based on repeated non-destructive measurements and illustrated in Fig. 3.2. Each repetition comprises an interaction period between the NV and the pair pseudo-spin before optical readout. During the interaction the NV electron spin accumulates a positive (negative) phase if a pair is in $|\Uparrow\rangle$ ($|\Downarrow\rangle$). For a pair in the parallel subspace ($|\uparrow\uparrow\rangle$ or $|\downarrow\downarrow\rangle$), the NV spin does not accumulate any phase. We choose τ such that pairs A and B interact with the NV spin simultaneously. Therefore, the NV spin accumulates a phase that depends on which of the 16 possible states the two pairs are in (Fig. 3.2c). By repeatedly applying this sequence, we realize a projective measurement that can distinguish multiple states in a single shot and with high contrast.

We construct two types of measurements by setting different interaction times and NV readout axes (Fig. 3.2a,b). The 'spin' measurement distinguishes the four pseudo-spin states ($|\Uparrow\Uparrow\rangle, |\Uparrow\Downarrow\rangle, |\Downarrow\Uparrow\rangle, |\Downarrow\Downarrow\rangle$; Fig. 3.2a,c). The 'parity' measurement only distinguishes the pseudo-spin parity of the two pairs ($\{|\Uparrow\Uparrow\rangle, |\Downarrow\Downarrow\rangle\}$: even parity versus $\{|\Uparrow\Downarrow\rangle, |\Downarrow\Uparrow\rangle\}$: odd parity; Fig. 3.2b,d). Because the pseudo-spins evolve as $|\Uparrow\rangle \leftrightarrow |\Downarrow\rangle$ with a frequency $\sim X$ during the NV spin readout, each repetition must be timed to align the measurement axes. This synchronization of repeated non-destructive measurements to the system evolution is similar to the case of repeated measurements on individual spins, e.g. in the context of quantum algorithms[16,23], atomic frequency locking and quantum Zeno dynamics[24], and weak measurement sequences[25,26].

We combine these sequences to realize high-fidelity initialisation and measurement (Fig. 3.2e). We first apply the parity measurement sequence (20 repetitions) to herald preparation in an even parity state, and to exclude the cases for which one or both pairs are in their parallel subspace. Then, we apply a spin measurement (30 repetitions) to herald either $|\Uparrow\Uparrow\rangle$ or $|\Downarrow\Downarrow\rangle$. Finally, we measure the pseudo-spin state with another spin measurement (30 repetitions). The resulting conditional histograms show well-isolated distributions (Fig. 3.2f) and an optimization of the measurement decision threshold (Fig.

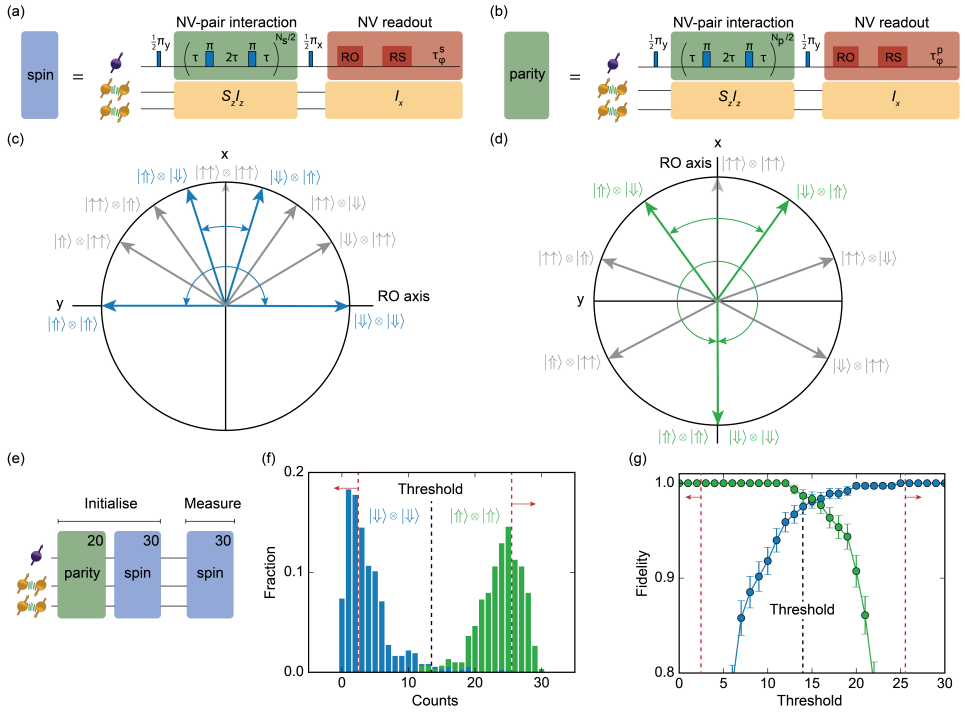

Figure 3.2: **Projective spin and parity measurements for pairs A and B. a.** Sequence to measure the pseudo-spin states. The NV electron spin starts in $m_s = 0$. The $\hat{S}_z \hat{I}_z$ interaction sequence ($\tau = 120.330$ µs and $N_s = 14$) maps the state of the two pairs onto the NV spin. The NV spin is subsequently read out (RO) and reset (RS) to $m_s = 0$. We synchronize subsequent repetitions by calibrating a waiting time $\tau_\phi^s = 323.5$ µs to compensate for the $\hat{I}_x$ evolution during NV readout. This ensures that the full sequence duration is a multiple of $1/X$. **b.** Sequence to measure the pseudo-spin parity ($N_p = 20$, Sec. 3.9.12). We set $\tau_\phi^p = 81$ µs to synchronize subsequent measurements (sequence duration a multiple of $1/(2X)$). **c.** XY-plane of the NV Bloch sphere showing the possible phases accumulated in the spin measurement. The NV spin starts along x and picks up a positive (negative) phase for a pair in $|\Uparrow\rangle$ ($|\Downarrow\rangle$) and no phase for a pair in a parallel state ($|\uparrow\uparrow\rangle$ or $|\downarrow\downarrow\rangle$). Reading out along the y-axis distinguishes the 4 pseudo-spin states (blue). Note that $|\downarrow\downarrow\rangle$ (not shown) gives the same result as $|\uparrow\uparrow\rangle$. **d.** XY-plane of the NV Bloch sphere under parity readout. The initial state (x-axis) and the readout axis (x-axis) are identical so that the parity of pair A and B is measured. **e.** Measurement sequence to calibrate single-shot readout and initialisation. The top right of each block indicates the number of repetitions. The optimal number of spin readouts is 30 (Sec. 3.9.11). **f.** Conditional histograms for 30 spin readouts after initialisation in $|\Uparrow\rangle|\Uparrow\rangle$ (green) and $|\Downarrow\rangle|\Downarrow\rangle$ (blue). The initialisation conditions for the 30 preceding spin readouts are indicated in red. **g.** Combined initialisation and readout fidelity for $|\Uparrow\rangle|\Uparrow\rangle$ (green) and $|\Downarrow\rangle|\Downarrow\rangle$ (blue) for 30 spin readouts. We find an optimum of $F = 98.1(5)\%$ for a decision threshold of 14 out of 30. The error bars represent one standard deviation.

3.2g) yields a combined initialisation and readout fidelity of 98.1(5)%. We refer to the Supplementary Materials for the full optimization procedure.

3.4. COHERENCE OF PAIR A, B

We use the developed high-contrast measurements to investigate the coherence of pair A and B. First, we perform a free-evolution experiment with the NV spin in $m_s = -1$ (Fig. 3.3a), for which the NV-pair coupling is on. Because the pseudo-spin precession frequency $\sqrt{X^2 + Z^2}$ is different for the pairs ($Z_A \neq Z_B$), this measurement reveals the presence of the two pairs and characterizes their couplings Z to the NV. The two frequencies observed give $Z_A = 130(1)$ Hz and $Z_B = 91(2)$ Hz (Sec. 3.9.2). We obtain the dephasing times from a Fourier transform (Fig. 3.3a): $T^*_{2,A} = 0.26(2)$ s and $T^*_{2,B} = 0.39(6)$ s (Sec. 3.9.2). These values are one to two orders of magnitude larger than for individual ^{13}C spins in the same sample[4].

Second, we perform the same experiment with the NV spin in $m_s = 0$, so that the coupling to the NV is effectively turned off. Now both pairs precess with frequency $X_A = X_B = 2080.9900(3)$ Hz (Fig. 3.3b) and a coherent oscillation that extends past 70 s is observed. To extract the dephasing time, we measure the oscillation amplitude at various times (Fig. 3.3c). The resulting decay yields $T^*_2 = 1.9(6)$ minutes, a four order-of-magnitude improvement over an individual spin[4] and the longest inhomogeneous dephasing time reported for any individually controllable quantum system[29].

3.5. DECOHERENCE MECHANISMS

We now elucidate the mechanisms which lead to these remarkable coherence properties. We add a magnetic-field noise term $\Delta Z(t)$ to the pseudo-spin Hamiltonian:

$$H = X\hat{I}_x + (m_s Z + \Delta Z(t))\hat{I}_z. \tag{3.2}$$

The first mechanism which enhances the coherence is the decoherence-free subspace[30,35] formed by the pseudo-spin states. Because the spins are identical, $\Delta Z(t)$ is given by the fluctuations of the magnetic field *difference* between the two spins. The atomic distance between the spins ensures near-complete immunity to noise from distant sources, such as the external magnetic field and the control signals. The main source of noise is the surrounding ^{13}C spin bath. Hence, $\Delta Z(t)$ can be approximated as a Gaussian distribution with a correlation time τ_c[36,37] and variance $b^2 = \frac{1}{4}\sum_k (A_k^{(1)} - A_k^{(2)})^2$, where $A_k^{(1)}$ ($A_k^{(2)}$) is the dipolar coupling of bath spin k to the first (second) spin of the pair. We calculate the typical effective noise strength $b \sim 10$ Hz by numerically simulating many spin-bath configurations. This is a noise reduction by a factor ~ 2 due to the decoherence-free subspace (Sec. 3.9.6).

We first analyze the case of the NV electron spin in $m_s = -1$ (Fig. 3.3a), which enables us to extract the strength of the noise due to the spin bath. Because $X \gg Z \gg \Delta Z(t)$, the Hamiltonian can be approximated as (Sec. 3.9.9)

$$H = (\omega_{-1} + \frac{Z}{\omega_{-1}}\Delta Z(t))\hat{I}_x, \tag{3.3}$$

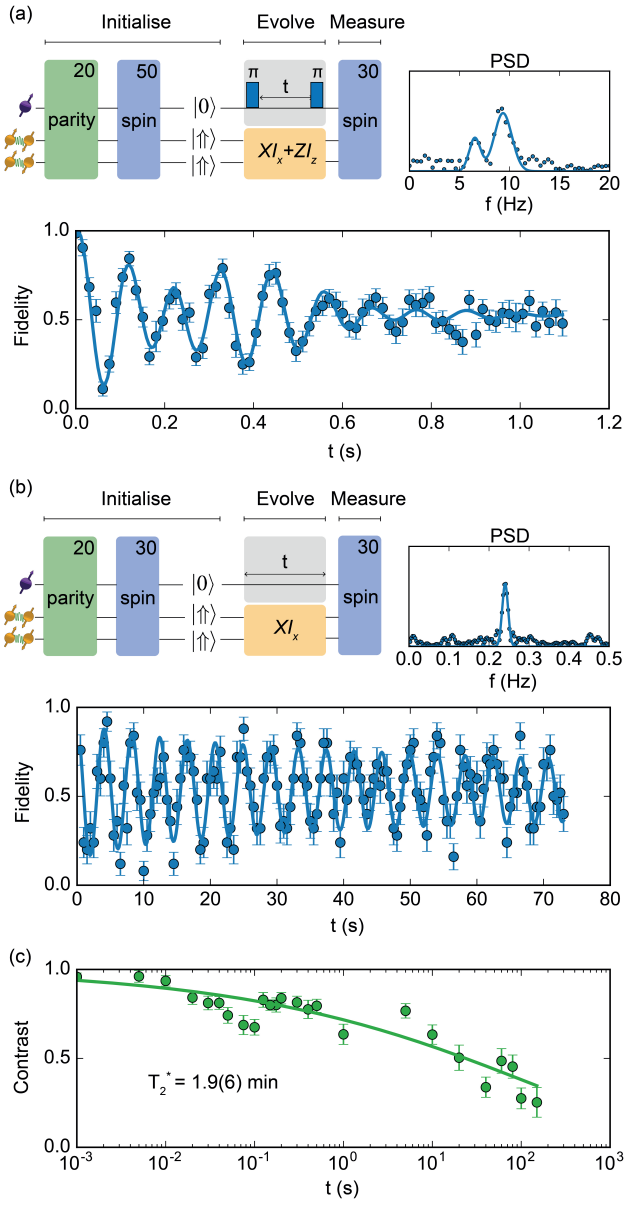

Figure 3.3: **Coherence of pair A and B. a.** Ramsey measurement with the NV in $m_s = -1$. (Top left) Experimental sequence. (Top right) Fourier transform of the signal indicating two frequencies. From the data we obtain the coupling of the pairs to the NV: $Z_A = 130(1)$ Hz and $Z_B = 91(2)$ Hz. **b.** Ramsey measurement with the NV in $m_s = 0$. (Top left) Experimental sequence. (Top right) Fourier transform indicating a single frequency. From the data we obtain $X = 2080.9900(3)$ Hz. For a and b a detuning has been applied (Sec. 3.9.2). **c.** Each data point corresponds to the amplitude of a Ramsey measurement in $m_s = 0$. A fit yields $T_2^* = 1.9(6)$ min, see Section 3.9.2. The data deviates from a simple exponential decay, indicating that processes beyond pure dephasing contribute to decoherence (Sec. 3.9.9). The error bars represent one standard deviation.

with $\omega_{-1} = \sqrt{X^2 + Z^2}$. Additionally, the NV spin creates a field gradient that suppresses spin flip-flops in the bath (a frozen core[4,9]). Therefore, the noise can be treated as quasi-static and the signal decay is Gaussian[36], as experimentally observed (Fig. 3.3a). The dephasing time is given by[36]

$$T_2^* = \frac{\omega_{-1}}{Z}\frac{\sqrt{2}}{b}. \tag{3.4}$$

In this case, the coherence is enhanced by a factor $\frac{\omega_{-1}}{Z} \approx 20$ in addition to the enhancement by the decoherence-free subspace. Finally, inserting the measured dephasing times into Eq. 3.4 yields noise strengths $b_A = 13.9(2)$ Hz and $b_B = 12.5(4)$ Hz. These values are consistent with the inter-pair distance and ^{13}C concentration (Sec. 3.9.6).

Second, we analyze the case with the NV electron spin in $m_s = 0$ (Fig. 3.3b). Because $X \gg \Delta Z(t)$, the Hamiltonian can be approximated as (Sec. 3.9.9)[37]

$$H = X\hat{I}_x + \frac{\Delta Z^2(t)}{2X}\hat{I}_x. \tag{3.5}$$

The eigenenergies are now first-order insensitive to $\Delta Z(t)$ as the spin pair forms a clock transition due to the coupling X, a second mechanism that enhances coherence. Note that the clock transition in this system does not require a specific magnetic field value, as the simultaneous decoherence-free subspace removes the dependence on global magnetic fields.

The decoherence-free subspace and clock transition alone cannot yet explain the observed $m_s = 0$ dephasing time. In particular, for quasi-static or slow noise the coherence would be limited to ~ 10 s (Sec. 3.9.9). However, the increased coherence, in combination with the lack of a frozen core for $m_s = 0$, unlocks a new regime in which the nuclear-spin bath fluctuations become relatively fast ($\tau_c \ll X/b^2$). A mathematically equivalent Hamiltonian was analysed theoretically by Dobrovitski et al.[37]. The resulting time constant is

$$T_2^* = \frac{4X^2}{b^4\tau_c}. \tag{3.6}$$

The dependence on the correlation time τ_c reveals a third mechanism, similar to motional narrowing[37], that further enhances the coherence. Inserting the parameters obtained from the $m_s = -1$ measurement and a typical value for $\tau_c \sim 0.1$ s[16], inhomogeneous dephasing times of ~ 100 s are predicted. Together these three mechanisms thus provide an explanation for the observed dephasing times.

3.6. COHERENCE OF PAIR C

To further analyse the different physical regimes that play a role, we investigate pair C (Fig. 3.1). Because $Z \gg X$, the dynamics are different and the clock transition can be switched on ($m_s = 0$) and off ($m_s = -1$) (Sec. 3.9.9). We develop complete control, initialisation and single-shot readout of such pairs in Section 3.9.4.

For evolution under $m_s = 0$, the situation is similar to pairs A and B. We find $T_2^* = 0.6(1)$ s, which is reduced compared to pairs A and B because the smaller coupling X makes the clock transition less effective (Sec. 3.9.4). Additionally, similar values obtained

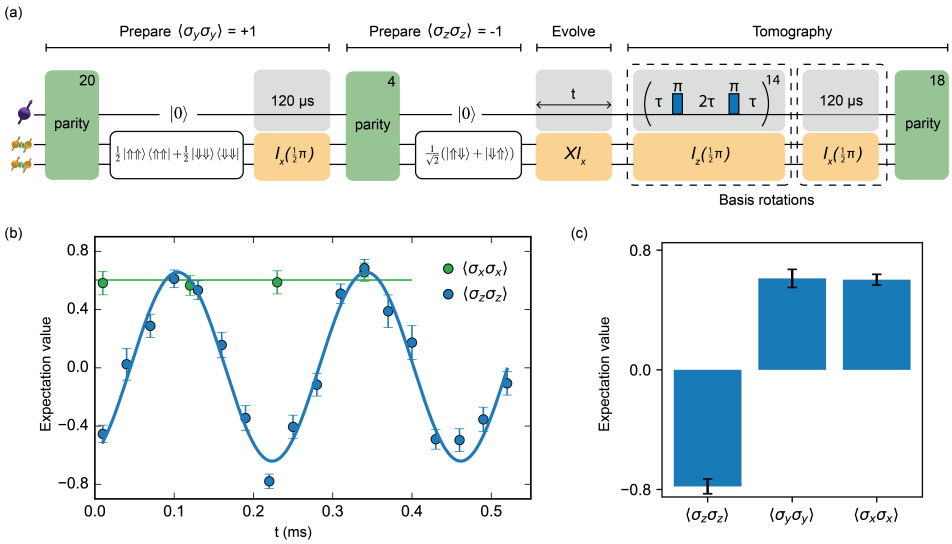

Figure 3.4: **Entanglement of pair A and B. a.** Experimental sequence. We prepare the entangled state $\frac{1}{\sqrt{2}}(|\Uparrow\Downarrow\rangle + |\Downarrow\Uparrow\rangle)$ by consecutively measuring $\langle\sigma_y\sigma_y\rangle$ and $\langle\sigma_z\sigma_z\rangle$. We herald on the +1 (> 14/20 counts) and -1 (< 1/4 counts) outcomes in the initialisation steps. Final operators are measured through optional basis rotations (dashed boxes) and a $\langle\sigma_z\sigma_z\rangle$ parity measurement. $I_{x/z}(\phi)$ stands for a rotation around x/z by an angle ϕ. **b.** Parity oscillations show a frequency of 4.20(4) kHz ($\sim 2X$). For $\langle\sigma_x\sigma_x\rangle$ no oscillation is observed as the pseudo-spin eigenstates are along x. **c.** Measurement of the three nonzero operators of the entangled state. The state fidelity is $F = (1 - \langle\sigma_z\sigma_z\rangle + \langle\sigma_y\sigma_y\rangle + \langle\sigma_x\sigma_x\rangle)/4 = 75(2)\%$. We use $t = 225$ µs for measuring $\langle\sigma_z\sigma_z\rangle$ and $t = 105$ µs for $\langle\sigma_y\sigma_y\rangle$. The results have not been corrected for readout infidelity and the error bars represent one standard deviation.

for spin echo ($T_2 = 0.7(1)$ s) and relaxation measurements ($T_1 = 0.9(2)$ s) indicate that relaxation plays a role in limiting the coherence (Sec. 3.9.9). For $m_s = -1$, a frozen core is formed and the clock transition is turned off, so that the noise $\Delta Z(t)$ affects the eigenfrequencies linearly. We find $T_2^* = 18(1)$ ms with Gaussian decay, indicating quasi-static noise[36], which is consistent with spin echo ($T_2 = 0.3(2)$ s $\gg T_2^*$) and relaxation measurements ($T_1 \gg 1$ s) (Sec. 3.9.4). In this case, there is no significant coherence protection and the results are similar to individual ^{13}C spins[4].

3.7. ENTANGLING TWO SPIN-PAIR QUBITS

Finally, we demonstrate the potential of the spin pairs as qubits by demonstrating an entangled state of pair A and pair B. We create entanglement through subsequent projective measurements of the $\sigma_y\sigma_y$ and $\sigma_z\sigma_z$ pseudo-spin parity (Fig. 3.4a). We herald on outcomes $\langle\sigma_y\sigma_y\rangle = +1$ and $\langle\sigma_z\sigma_z\rangle = -1$, so that the resulting state is $\frac{1}{\sqrt{2}}(|\Uparrow\Downarrow\rangle + |\Downarrow\Uparrow\rangle)$. This state is a 4-spin entangled state $\frac{1}{\sqrt{2}}(|\uparrow\downarrow\downarrow\uparrow\rangle + |\downarrow\uparrow\uparrow\downarrow\rangle)$ that encodes two qubits of information in two long-lived pseudo-spin states.

To characterize the resulting state we first measure parity oscillations by varying the evolution time t (Fig. 3.4a). The observed frequency is 4.20(4) kHz, which equals $2X$, as

expected (Fig. 3.4b). To determine the state fidelity, we measure the pseudo-spin parity operators $\langle\sigma_x\sigma_x\rangle$, $\langle\sigma_y\sigma_y\rangle$ and $\langle\sigma_z\sigma_z\rangle$. We realize the required single-qubit rotations through waiting times (for x-rotations) and dynamical decoupling sequences with the NV spin in an eigenstate (for z-rotations) (Fig. 3.4a). Figure 3.4c shows the resulting expectation values, which yield a fidelity $F = 0.75(2)$, confirming entanglement ($F > 0.5$)[38]. This result highlights the high-fidelity initialisation, control, and non-destructive measurements realized.

3.8. CONCLUSION

In conclusion, we have developed complete control over multiple nuclear-spin pairs. These spin pairs provide inherently long-lived quantum states due to a combination of three physical phenomena: a decoherence-free subspace, a clock transition and a variant of motional narrowing. This inherent coherence protection makes spin pairs promising systems for a variety of applications, such as robust memories for optically connected quantum networks[18–20,39] and memory-enhanced sensing[40–45].

For quantum networks, the long coherence time and small effective coupling to the NV electron spin (a few Hz) might enable faithful storage of quantum states during the probabilistic generation of NV-NV entanglement through optical channels. Such a robust memory is a key requirement for progressing towards larger-scale networks based on defect spins[19,39,46]. For sensing, a hybrid system consisting of a sensitive quantum sensor (e.g. the NV electron spin) in conjunction with a robust quantum memory can increase sensitivity and enhance sensor properties[40–45].

Furthermore, the presented methods might be extended to electron spin pairs, where greater control speeds are possible, and provide new opportunities for the magnetic imaging of spin systems through spin-spin interactions[12]. Further improved control over the spin pairs might be realized by using tailored decoupling sequences[47–54]. Such long-lived nuclear spin pairs are available for most NV centers (Sec. 3.9.8) and are present in a variety of other materials. Therefore, our results reveal a new, promising, and abundantly available resource for quantum science and technology.

3.9. SUPPLEMENTARY MATERIALS

3.9.1. SAMPLE AND SETUP

The experiments are performed on a naturally occurring NV center in a cryogenic confocal microscope (3.7 K). The diamond was homoepitaxially grown using chemical vapor deposition and cleaved along the ⟨111⟩ axis (Element Six). There is a natural abundance (1.1%) of ^{13}C. The NV centre was selected on the absence of strongly coupled ^{13}C spins exceeding ~ 500 kHz hyperfine coupling, but without any other criteria on the spin environment or spin pairs.

The NV electron spin has a dephasing time of $T_2^* = 4.9(2)$ μs and a spin echo time of $T_2 = 1.182(5)$ ms. The electron relaxation ($T_1 > 1$ h) at this temperature is negligible[11]. We measure the NV spin state in a single shot using spin-selective optical readout[16]. The readout fidelities are 0.905(2) (0.986(2)) for the $m_s = 0$ ($m_s = -1$) state with an average

fidelity of $F = 0.946(1)$. The dynamical decoupling sequences follow the XY8-scheme to mitigate pulse errors[55]. The NV studied in this work is the same NV studied in Abobeih et al.[12]. However the ^{13}C spins that constitute the pairs studied in this work are not part of the 27 spins that were found in reference[12].

3.9.2. DATA ANALYSIS

FIT FUNCTIONS

The Ramsey data in Fig. 3.3a ($m_s = -1$) is fitted to

$$F(t) = a + \exp\big(-(t/T)^n\big)[A\cos\big(2\pi f_A t + \phi_A\big) + B\cos\big(2\pi f_B t + \phi_B\big)]. \tag{3.7}$$

We obtain $T = 0.53(4)$ s, $n = 2.1(4)$, $f_A = 9.07(6)$ Hz and $f_B = 7.0(1)$ Hz (measured with a 10 Hz detuning with respect to 2086 Hz). Using $f = \sqrt{X^2 + Z^2}$ and $X = 2080.9900(3)$ Hz, the values for f_A and f_B yield $Z_A = 130(1)$ Hz and $Z_B = 91(2)$ Hz. The observed shape of the decay ($n = 2.1(4)$) is in agreement with the predicted Gaussian ($n = 2$) decay for quasi-static noise (Sec. 3.9.9).

To extract the dephasing times we fit the Fourier transform in Fig. 3.3a to

$$F(f) = a + A\exp\big(-(f + f_A)^2/2\sigma_A^2\big) + B\exp\big(-(f + f_B)^2/2\sigma_B^2\big). \tag{3.8}$$

We find $\sigma_A = 0.88(6)$ Hz and $\sigma_B = 0.57(9)$ Hz which gives $T^*_{2,A} = 1/(\sqrt{2}\pi\sigma_A) = 0.26(2)$ s and $T^*_{2,B} = 0.39(6)$ s.

The Ramsey data in Fig. 3.3b ($m_s = 0$) is fitted to

$$F(t) = \exp\big(-(t/T)^n\big)\cos\big(2\pi f t + \phi\big). \tag{3.9}$$

We obtain $T = 98(44)$ s, $n = 0.5(4)$ and $f = 0.2400(3)$ Hz (measured with a 0.25 Hz detuning with respect to 2081 Hz). Therefore we obtain $X = 2080.9900(3)$ Hz. Note that the precise value obtained for X deviates from simple theoretical estimates and is analyzed in Section 3.9.15. The Fourier transform is fitted to

$$F(f) = a + A\exp\big(-(f + f_0)^2/2\sigma_0^2\big). \tag{3.10}$$

We obtain $f_0 = 0.2402(3)$ Hz and $\sigma_0 = 0.0074(3)$ Hz.

The data in Fig. 3.3c is fitted to $\exp(-(t/T)^n)$ obtaining $T = 1.9(6)$ min and $n = 0.23(4)$. Note that n deviates from the simple exponential decay ($n = 1$) associated to equation (6), indicating that other effects beyond pure dephasing contribute to the decoherence (Sec. 3.9.9).

The data in Fig. 3.3 as well as the data in Fig. 3.7 is corrected for NV ionisation.

ERROR ANALYSIS

All error bars on data points represent one standard deviation. The error on data involving single-shot readout of (the parity of) nuclear spin pairs is given by a binomial error:

$$\sigma = \sqrt{\frac{p(1-p)}{n}} \tag{3.11}$$

where p is the success probability in a Bernoulli process and n is the number of trials. When a data point consists of m independent data sets the individual errors are added in quadrature:

$$\sigma = \frac{1}{m}\sqrt{\sum_i \sigma_i^2} \tag{3.12}$$

In Fig. 3.3c the error bars are instead given by the fit error on the amplitude of the underlying Ramsey measurements.

3.9.3. PSEUDO-SPIN HAMILTONIAN

The Hamiltonian for two ^{13}C spins in the vicinity of an NV center in the interaction picture with respect to the electron energy splitting and under the secular approximation can be written as:

$$\begin{aligned} H = {} & \omega_L I_z^{(1)} + \omega_L I_z^{(2)} + m_s \mathbf{A}^{(1)} \cdot \mathbf{I}^{(1)} \\ & + m_s \mathbf{A}^{(2)} \cdot \mathbf{I}^{(2)} + H_D. \end{aligned} \tag{3.13}$$

where $\omega_L = \gamma_c B$ is the ^{13}C spin Larmor frequency, with γ_c the ^{13}C gyromagnetic ratio. B is the magnetic field along the NV-axis. $\mathbf{I}^{(i)}$ are the spin-$\frac{1}{2}$ operators acting on spin i, $m_s = \{-1, 0, +1\}$ are the NV electron spin states and $\mathbf{A}^{(i)} = [A_x, A_y, A_z]$ is the NV-^{13}C hyperfine interaction vector of spin i. H_D is the dipolar interaction between two ^{13}C spins. Throughout the paper, all units in equations (X, Z, b, etc.) are in angular frequency. For a large magnetic field compared to the dipolar (X) and hyperfine couplings ($A^{(1)}, A^{(2)}$) H_D can be written as:

$$H_D = X(3I_z^{(1)} I_z^{(2)} - \mathbf{I}^{(1)} \cdot \mathbf{I}^{(2)}) \tag{3.14}$$

$$X = \frac{\mu_0 \gamma_c \gamma_c \hbar}{8\pi |\mathbf{r}_{12}|^3}(1 - 3\cos^2\theta_{12}), \tag{3.15}$$

where μ_0 is the vacuum permeability, $\mathbf{r}_{12}$ is the vector between the two ^{13}C atoms and θ_{12} the angle between the magnetic field axis and the pair axis. Since $\omega_L = \gamma_c B = 432.140$ kHz is large compared to the dipolar (X) and hyperfine couplings ($A^{(1)}, A^{(2)}$), the antiparallel states $|\uparrow\downarrow\rangle$ and $|\downarrow\uparrow\rangle$ form an isolated subspace in which we define a pseudo-spin $\frac{1}{2}$ as $|\Uparrow\rangle = |\uparrow\downarrow\rangle$ and $|\Downarrow\rangle = |\downarrow\uparrow\rangle$ [11,13,14,34]. The Hamiltonian in this subspace is given by [13,34]

$$H = X\hat{I}_x + m_s Z \hat{I}_z. \tag{3.16}$$

Z originates from the difference of the hyperfine couplings of the two spins to the NV electron spin, and is given by [34]

$$Z = Z_\parallel + Z_\perp = A_\parallel^{(1)} - A_\parallel^{(2)} + \frac{(A_\perp^{(1)})^2 - (A_\perp^{(2)})^2}{\gamma_c B}, \tag{3.17}$$

where $A_\parallel^{(i)} = A_z^{(i)}$ and $A_\perp^{(i)} = \sqrt{(A_x^{(i)})^2 + (A_y^{(i)})^2}$ for spin i of the pair.

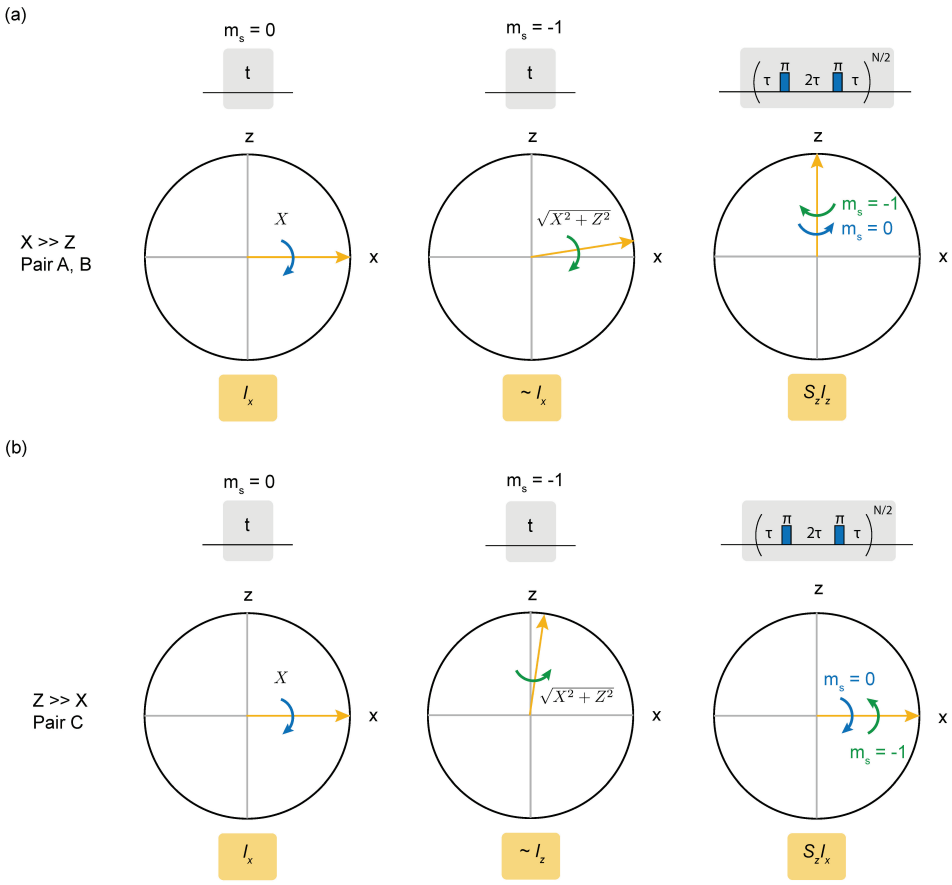

Figure 3.5: **Overview of pair pseudo-spin dynamics during various sequences on the NV electron spin. a.** Pseudo-spin dynamics of pairs with $X \gg Z$ (pair A, B). The top row indicates the sequence performed on the NV electron spin, the middle row the corresponding pair dynamics in the XZ-plane of the pseudo-spin Bloch sphere and the bottom row indicates the effective pseudo-spin Hamiltonian term under that sequence. For the left two columns the rotation frequencies are given inside the Bloch spheres. From left to right the sequences are free evolution in $m_s = 0$ and $m_s = -1$, and a dynamical decoupling sequence with τ resonant, i.e. $2\tau = \pi/\sqrt{X^2 + (Z/2)^2}$. Rotations that are unconditional on the NV electron spin state can be obtained by setting $\tau = \pi/\sqrt{X^2 + (Z/2)^2}$ (unconditional z-rotation) and by setting τ far off-resonant (unconditional x-rotation), but these are not shown or used here. Note that the z-rotation frequency depends on the hyperfine field difference Z, so that pair A and B can, in principle, be controlled individually. **b.** Pseudo-spin dynamics of pairs with $Z \gg X$ (pair C). Like above, z- and x-rotations that are unconditional on the NV electron-spin state can be obtained by setting different values for τ (not shown). Together these operations enable universal control of the system consisting of the three pseudo-spins and the NV center.

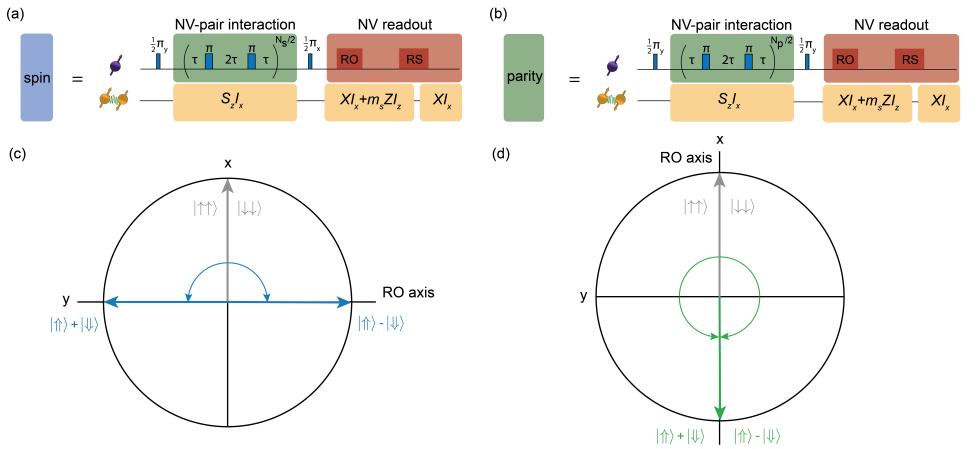

Figure 3.6: **Projective spin and parity measurements for Pair C. a.** Sequence to measure the spin state of pair C. The NV starts in $m_s = 0$. Because $Z \gg X$, the effective interaction between the NV spin and pseudo-spin is $\hat{S}_z \hat{I}_x$. During the NV readout (RO) and reset (RS), the NV can spend an unknown time in $m_s = -1$ which causes dephasing of the pair spin. Additionally pair C undergoes a deterministic z-rotation for any known time spent in $m_s = -1$. To minimize these effects, we use a fast readout and reset. $N_s = 8$. **b.** Sequence to measure the parity of the two spins that make up pair C. Note that in this case the timing of the sequence is unimportant, as evolution in $m_s = -1$ or $m_s = 0$ does not change the parity. $N_p = 14$. **c.** XY-plane of the NV Bloch sphere during the NV-pair interaction in a. The NV picks up a positive or negative phase depending on the x-projection of the pair pseudo-spin and no phase when the pair is in the parallel subspace. **d.** XY-plane of the NV Bloch sphere during the NV-pair interaction in b.

3.9.4. PAIR C CONTROL, COHERENCE AND RELAXATION

Pair C has a dipolar coupling $X = 188.33(2)$ Hz and a hyperfine difference $Z = 2802(2)$ Hz. Therefore, $Z \gg X$, in contrast to pairs A and B for which $X \gg Z$. This changes the dynamics in two ways. First, for $m_s = -1$, Z is the dominant term in the pair frequency $\omega_{-1} = \sqrt{X^2 + Z^2}$ and thus sets the location of the resonance in Fig. 3.1b. Second, the effective NV-pair interaction during the dynamical decoupling sequence becomes $\hat{S}_z \hat{I}_x$ [11] (Fig. 3.5).

We implement two types of projective measurements on pair C (see Fig. 3.6). The spin measurement sequence distinguishes the pseudo-spin states $\frac{1}{\sqrt{2}}(|\Uparrow\rangle \pm |\Downarrow\rangle)$. The parity measurement sequence distinguishes between the parallel ($|\uparrow\uparrow\rangle$,$|\downarrow\downarrow\rangle$) and antiparallel ($|\Uparrow\rangle$,$|\Downarrow\rangle$) subspaces of the pair. We obtain high-fidelity initialisation and readout by repeatedly applying these sequences (Sections 3.9.13, 3.9.14).

For spin pairs with $Z \gg X$, the timing of repetitions is complicated by the fact that the $m_s = 0$ and $m_s = -1$ evolution frequencies and eigenstates differ significantly. Here, we mitigate this by minimizing the NV readout time (RO, ~ 5 µs) and applying a fast reset of the NV spin (RS), so that the potential time spent in $m_s = -1$ is small. Because the states that the measurement projects onto ($\frac{1}{\sqrt{2}}(|\Uparrow\rangle \pm |\Downarrow\rangle)$) are eigenstates of the $m_s = 0$ evolution, there is no timing requirement after resetting the NV and we simply concatenate subsequent measurements.

For pairs A and B ($X \gg Z$), we use free evolution and dynamical decoupling sequences to realize universal single-qubit control for the pseudo-spins (Fig. 3.4; Fig. 3.5). For pair C ($Z \gg X$) all single-qubit operations can be obtained by letting the system evolve freely. Evolution with the NV electron spin in $m_s = 0$ implements a rotation around the x-axis, and evolution under $m_s = -1$ realizes a rotation around the z-axis. Note that the z-axis rotation is approximate as Z is finite. In principle, this can be corrected for but this is not done here. We use the pair C control to measure the pseudo-spin dephasing time T_2^*, the spin echo time T_2 and the relaxation time T_1 in both NV electron spin states, see Fig. 3.7.

3.9.5. SPECTROSCOPY AND CONTROL OF THE FULL HILBERT SPACE

Most of the work presented is focused on initialising, controlling and measuring the states in the antiparallel subspace of spin pairs, i.e. $|\uparrow\downarrow\rangle$ and $|\downarrow\uparrow\rangle$. In Fig. 3.8, we demonstrate that the entire Hilbert space of the spin pairs can be controlled by RF driving the single-spin-flip transitions of pair C.

The single-spin transition frequencies are $\omega_1 = 429.314(5)$ kHz and $\omega_2 = 432.122(7)$ kHz (Fig. 3.8a). Since the frequency of a single-spin transition in $m_s = -1$ is $\omega \approx \omega_L - A_\parallel$, this yields $A_\parallel^{(1)} = 2826(5)$ Hz and $A_\parallel^{(2)} = 18(7)$ Hz. Note that these values assume that $A_\perp$ is of similar magnitude, so that it can be neglected. The frequencies observed are consistent with the characteristic ^{13}C frequencies ($\omega_L = 432.140$ kHz), further corroborating our assignment of ^{13}C-^{13}C pairs as the source of the signals.

These results also demonstrate selective initialisation, control and measurement of an individual carbon spin with negligible coupling to the NV by using its coupling to neighbouring spins. Spin 2 couples negligibly to the NV (18(7) Hz), so that it overlaps in precession frequency with most of the spin bath. Nevertheless, it can be initialised and controlled selectively by using the NV to directly detect its flip-flops with spin 1 (i.e. pseudo-spin dynamics).

3.9.6. DECOHERENCE-FREE SUBSPACE AND SPIN BATH NOISE

The noise $\Delta Z(t)$ on a spin pair originates from the surrounding ^{13}C spins. As a pair is only sensitive to field gradients (a decoherence-free subspace), distant external noise sources can generally be neglected. There are k bath spins that each create a field difference $A_k^{(1)} - A_k^{(2)}$ on the pair (Fig. 3.9a). We model $\Delta Z(t)$ as an Ornstein-Uhlenbeck process with a variance $b^2 = \frac{1}{4}\sum_k (A_k^{(1)} - A_k^{(2)})^2$. The question that we address in this section is what b is for typical spin baths.

We numerically generate 10^5 different baths (1.1% ^{13}C abundance) surrounding a pair (Fig. 3.9b,c) or a single spin (Fig. 3.9d) in a volume of $15 \times 15 \times 15$ unit cells. For each bath we calculate $b^2 = \frac{1}{4}\sum_k (A_k^{(1)} - A_k^{(2)})^2$ but exclude spins with $\left|A_k^{(1)}\right| > 50$ Hz or $\left|A_k^{(2)}\right| > 50$ Hz, i.e. we exclude strongly coupled spins for which the system would not be a well-defined spin pair anymore. The expectation is that the closer the spins of the pair are, the more correlated the noise and the smaller b is.

The result for a nearest neighbour pair oriented along the magnetic field (like pair A or B) is shown in Fig. 3.9b. We find a mean of 10 Hz and a standard deviation of 4 Hz. For

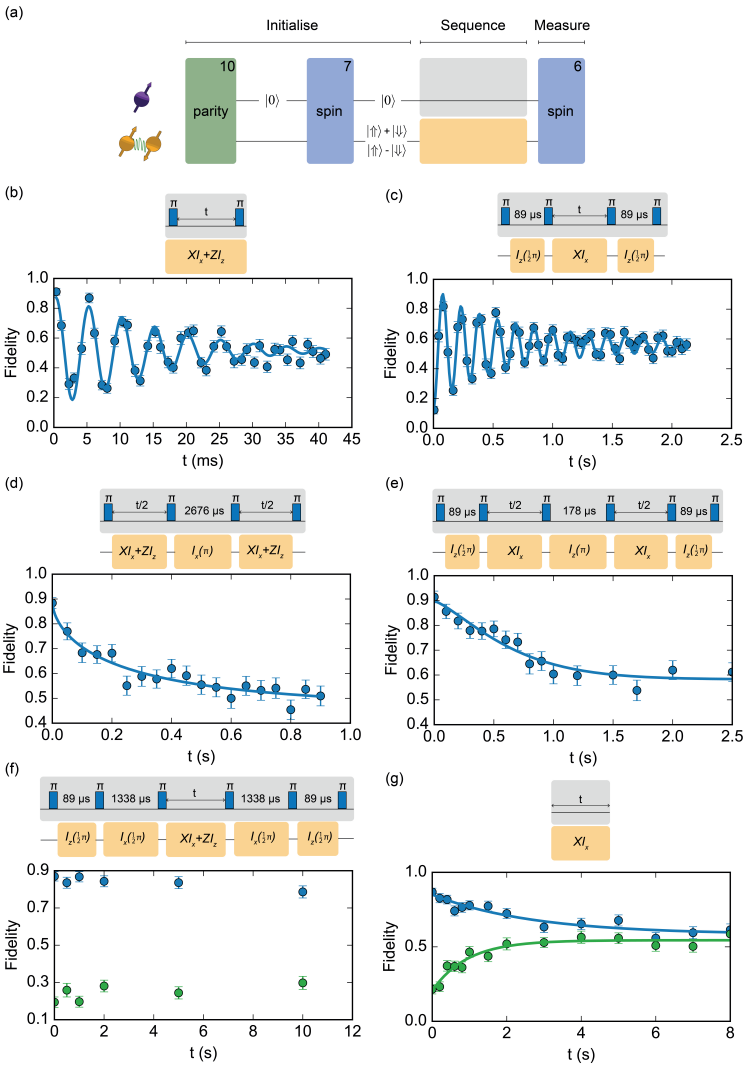

Figure 3.7: **Coherence and relaxation of pair C. a.** Measurement sequence. First, we use 10 parity readouts to herald the pair in the antiparallel subspace (condition > 7/10). Then, we use 7 spin readouts to initialise the pair in $\frac{1}{\sqrt{2}}(|\Uparrow\rangle + |\Downarrow\rangle)$ (> 4/7, blue data) or $\frac{1}{\sqrt{2}}(|\Uparrow\rangle - |\Downarrow\rangle)$ (< 3/7, green data). The various evolution sequences are given as insets in panels b-g. Finally, 6 spin readouts are used to readout the spin state. Panels b,c are fitted to $F(t) = a + Ae^{-(t/T)^n}\cos(2\pi f t + \phi)$ and panels d,e,g to $F(t) = a + Ae^{-(t/T)^n}$. **b.** Ramsey measurement in $m_s = -1$. $T_2^* = 0.018(1)$ s, $n = 1.4(2)$ and $f = 2808(1)$ Hz (measured with a 200 Hz detuning with respect to 2807 Hz). **c.** Ramsey measurement in $m_s = 0$. $T_2^* = 0.6(1)$ s, $n = 0.7(1)$ and $f = 188.33(2)$ Hz (measured with a 5 Hz detuning with respect to 186.8 Hz). **d.** Spin echo measurement in $m_s = -1$. $T_2 = 0.3(2)$ s and $n = 0.6(2)$. **e.** Spin echo measurement in $m_s = 0$. $T_2 = 0.7(1)$ s and $n = 1.3(3)$. **f.** Relaxation measurement in $m_s = -1$. $T_1 \gg 1$ s. **g.** Relaxation measurement in $m_s = 0$. $T_1 = 3.6(7)$ s and $n = 0.8(2)$ for the blue data ($\frac{1}{\sqrt{2}}(|\Uparrow\rangle + |\Downarrow\rangle)$). $T_1 = 0.9(2)$ s and $n = 1.0(2)$ for the green data ($\frac{1}{\sqrt{2}}(|\Uparrow\rangle - |\Downarrow\rangle)$). The relaxation times are different for the two eigenstates, indicating a mechanism that depends on whether the state is a singlet or triplet.

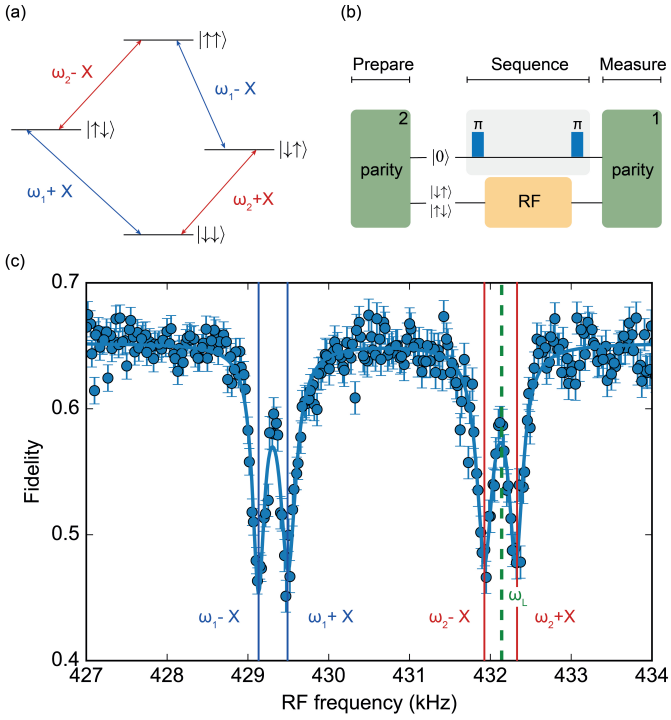

Figure 3.8: **Spectroscopy and control of the complete pair Hilbert space. a.** Level diagram for pair C with the electron spin in $m_s = -1$. ω_1 (ω_2) is the frequency associated to the first (second) spin of the pair with the NV in $m_s = -1$. **b.** Sequence to reveal the transitions between the subspaces. First, the pair is initialised in the antiparallel subspace through a parity measurement, then an RF pulse with variable frequency with the NV in $m_s = -1$ is applied, and finally the subspace population is measured using another parity measurement. If the frequency of the RF pulse is resonant with a single-spin transition, the spin pair changes its subspace. **c.** Measurement result. Four transitions are observed corresponding to the marked transitions in a. The green dashed line corresponds to the bare Larmor frequency $\omega_L = 432.140$ kHz. We fit the data to four Lorentzians and extract $\omega_1 = 429.314(5)$ kHz, $\omega_2 = 432.122(7)$ kHz. For the left (right) dips we also obtain $X = 184(3)$ (194(4)) Hz. These results corroborate the assignment of the signals to ^{13}C pairs and enable complete control over the full pair state.

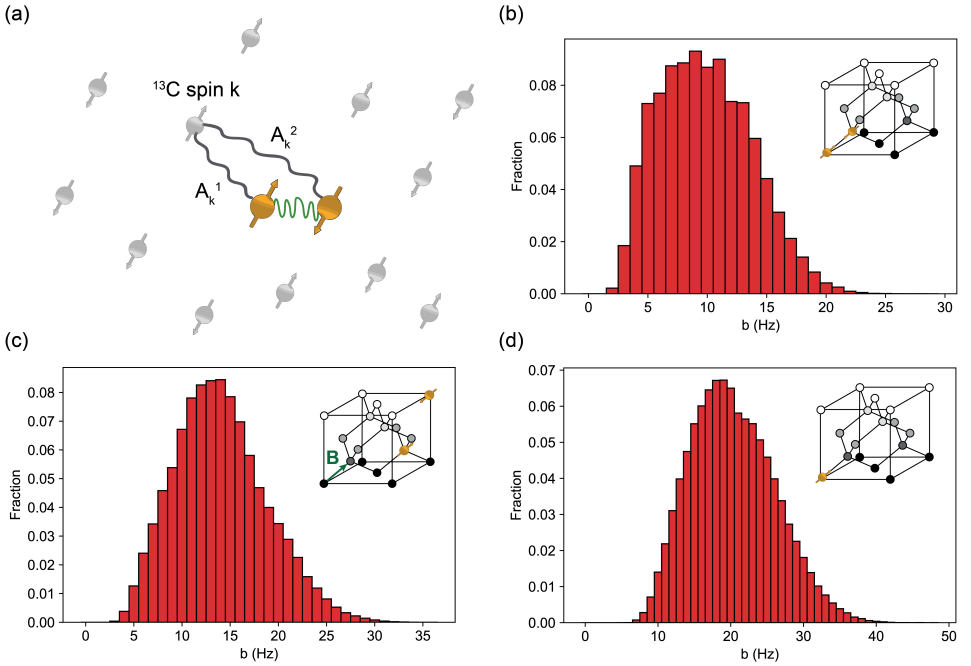

Figure 3.9: **Distributions of the noise strength b for typical baths. a.** Schematic of the situation. A pair is surrounded by k bath spins that each create a magnetic field difference $A_k^{(1)} - A_k^{(2)}$ on the pair. Assuming Gaussian noise, we obtain b from $b^2 = \frac{1}{4}\sum_k (A_k^{(1)} - A_k^{(2)})^2$. **bcd.** Distribution of b for 10^5 generated baths for the parameters of pair A and B (b), for the parameters of pair C (c) and for a single spin (d). Strongly coupled spins ($\left|A_k^{(1)}\right| > 50$ Hz or $\left|A_k^{(2)}\right| > 50$ Hz) have been excluded.

the parameters of pair C (Fig. 3.9c) we find a mean of 14 Hz and a standard deviation of 5 Hz. Lastly for an individual ^{13}C spin (Fig. 3.9d) we find a mean of 20 Hz and a standard deviation of 6 Hz. A decrease in the effective noise is observed for the pairs compared to an individual spin. Furthermore, the closer the pair spins are, the smaller the effective noise is.

3.9.7. DECOHERENCE-FREE SUBSPACE AND EXTERNAL NOISE

The decoherence-free subspace makes pairs nearly immune to noise from distant sources. In this section we consider the effect of two such external sources. For single ^{13}C spins in the same sample typical inhomogeneous dephasing times of 10 ms are observed[4], which sets a bound on the noise strength. If we take the extreme case that all noise comes from an external source, i.e. not from the spin bath, this gives an upper limit of the noise magnitude $b = 1/\sqrt{2}\pi T_2^* = 22.5$ Hz. Since we are interested in an order of magnitude estimate, we take $b \sim 10^2$ Hz, corresponding to magnetic field fluctuations of $\delta B \sim 10^{-5}$ T. Now we consider that these fluctuations originate from either the on-chip MW line that we use to apply microwaves or from the external magnets that we use to apply a magnetic field.

MICROWAVE LINE

We approximate the microwave line as an infinite wire that generates a field at a distance r from the wire of magnitude $B(r) = \mu_0 I/2\pi r$ where μ_0 is the vacuum permeability and I the current through the wire. Given $r \sim 10$ μm and $\delta B \sim 10^{-5}$ T, we obtain $I = 2\pi r \delta B/\mu_0 \sim 10^{-4}$ A. Now we turn to the effect of this noise on a decoherence-free subspace formed by a ^{13}C pair. The positions of the pair spins are $r_a = 10$ μm and $r_b = 10$ μm + a_0 where for a_0 we take a conservative value of $\sim 10^{-9}$ m. Given $I = 10^{-4}$ A, the MW line would add a field difference to the decoherence-free subspace of $\Delta B = B(r_a) - B(r_b) = \frac{\mu_0 I}{2\pi}(\frac{1}{r_a} - \frac{1}{r_b}) \sim 10^{-10}$ T. That corresponds to $\sim 10^{-3}$ Hz which has a negligible effect on the coherence.

MAGNET

The external magnetic field comes from a cylindrical permanent magnet. We calculate the effect of that field (~ 0.04 T) on the decoherence-free subspace of a pair. From the above we know that the maximum field fluctuations are on the order of $\delta B \sim 10^{-5}$ T. We consider a magnet with an NV-magnet distance $r \sim 10^{-2}$ m, the radius of the magnet $R = 5$ mm, the length $L = 5$ mm and the remanence field $B_r = 1.5$ T. To calculate the magnetic field at r we use

$$B(r) = \frac{B_r}{2}\left(\frac{L+r}{\sqrt{R^2+(L+r)^2}} - \frac{r}{\sqrt{R^2+r^2}}\right) \tag{3.18}$$

At $r \sim 10^{-2}$ m the magnetic field is ~ 0.04 T. The expected effect of the permanent field on the decoherence-free subspace is then $B(r_a) - B(r_b) \sim 10^{-8}$ T or 10^{-1} Hz. We have used $r_a = 1$ cm and $r_b = 1$ cm + a_0 where for a_0 we take a conservative value of 10^{-9} m. This is a constant field difference (c.f. Z) added to the pair. However, the field fluctuations are $\delta B \sim 10^{-5}$ T, more than three orders of magnitude less than the permanent field of ~ 0.04 T. The influence of δB on the decoherence-free subspace is therefore < 1 mHz which has a negligible effect on the coherence.

X (Hz)	occurrence	**r** (in units $a_0/4$)
2062	1	[1,1,1]
687	3	[-1,1,-1]
237	12	[±2,±2,0] and [∓2,±2,0]
187	3	[-1,-1,-3]
134	3	[1,1,-3]
102	3	[1,3,3]
76.38	1	[-3,-3,-3]
75.95	6	[±4,±2,±2]
61	6	[-3,-1,3]
46	6	[∓4,±2,±2]

Table 3.1: The occurrence of a given coupling X when fixing one of the ^{13}C spins of the pair and moving the other around the lattice. The vector between the two ^{13}C spins of the pair is given for each X coupling in units of $a_0/4$ where a_0 is the lattice constant of diamond. All permutations of the entries of **r** give the same coupling X.

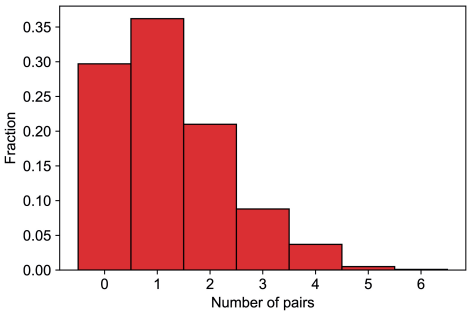

Figure 3.10: **Expected number of nearest neighbour pairs per NV**. The expected number of pairs with $50 < Z < 500$ Hz for a volume of $15 \times 15 \times 15$ unit cells surrounding an NV center. We estimate that pairs with a Z within the indicated region to be controllable with high fidelity. When Z is larger, it becomes comparable to X and the control methods presented in this paper do not hold anymore. When Z is much smaller, more pulses are required in the dynamical decoupling sequence resulting in more electron dephasing, and resolving the pair from the background bath of pairs becomes more challenging.

3.9.8. EXPECTED NUMBER OF NEAREST-NEIGHBOUR PAIRS PER NV

In this section we address how many nearest neighbour pairs with similar Z as pair A and B one would expect surrounding a typical NV center. To that end we generate 10^4 different ^{13}C baths with 1.1% abundance surrounding an NV center in a volume of $15 \times 15 \times 15$ diamond unit cells. For every generated bath, we look for the nearest neighbour pairs along the magnetic field axis and calculate the hyperfine field difference Z due to the NV, assuming a dipolar NV-^{13}C interaction. Then we estimate a controllable region of $50 < Z < 500$ Hz. The upper bound comes from the required condition $X \gg Z$ and the (approximate) lower bound is a limit due to the detrimental effect of electron dephasing for a large number of dynamical decoupling pulses. Additionally for smaller Z resolving a pair from the background bath of pairs with small Z is expected to be challenging. For every generated bath, we determine how many pairs satisfy this condition and plot the result in Fig. 3.10. The expected number of such nearest neighbour pairs per NV is 1 ± 1. Moreover, more than 70% of simulated NVs host at least one nearest-neighbour pair, indicating that such pairs can commonly be found.

In the above we only consider nearest-neighbour pairs along the magnetic field axis. Other pairs with smaller X and larger Z can also be detected and controlled (pair C, see Sec. 3.9.4). In Table 3.1 we show the ten largest values of X with their corresponding occurrence and vector $\mathbf{r}$ between the two ^{13}C spins.

3.9.9. SPIN-PAIR COHERENCE REGIMES

In this section we provide the derivations for the spin-pair coherence alongside a more detailed discussion. The key idea is that different physical regimes are accessed depending on the NV electron-spin state and the spin-pair parameters. In particular, the analysis shows that the long coherence times observed for the $m_s = 0$ state are made possible by a unique combination of a decoherence-free subspace, a clock transition and a variant of motional narrowing.

We first focus on interactions and noise that cause dephasing or relaxation within the pseudo-spin subspace. Potential relaxation out of the pseudo-spin subspace, for example due to flip-flops with the surrounding bath spins, is discussed separately below. The Hamiltonian for a pair in the pseudo-spin subspace (spanned by $|\Uparrow\rangle = |\uparrow\downarrow\rangle$ and $|\Downarrow\rangle = |\downarrow\uparrow\rangle$), including a magnetic-field noise term $\Delta Z(t)$, is

$$H = X\hat{I}_x + (m_s Z + \Delta Z(t))\hat{I}_z, \tag{3.19}$$

where X is the dipolar coupling between the two ^{13}C spins, $m_s = \{0, -1\}$ the electron state ($m_s = +1$ is not populated during the experiments) and Z is due to the hyperfine field gradient induced by the electron spin. Because the two spins are identical, the pseudo-spin forms a decoherence-free subspace. It is therefore only sensitive to field gradients. Noise from distant sources, such as fluctuations of the applied magnetic field (distance to the closest magnet: ~ 1 cm) and noise from the control electronics on the on-chip stripline (distance: ~ 10 μm) has negligible influence on the pseudo-spin dynamics, see Section 3.9.7. Therefore, the surrounding ^{13}C bath is the main source of noise and the origin of $\Delta Z(t)$.

The interaction between two central spins and a bath can be described as

$$H_{int} = I_z^{(1)} \sum_k A_k^{(1)} I_z^{(k)} + I_z^{(2)} \sum_k A_k^{(2)} I_z^{(k)} + H_B, \tag{3.20}$$

where $A_k^{(1)}$ ($A_k^{(2)}$) is the dipolar coupling of bath spin k to spin 1 (2) of the pair and $I_z^{(i)}$ the nuclear spin-1/2 z-operator on spin i. H_B describes the intrabath coupling. We rewrite this interaction as

$$H_{int} = \frac{1}{2}\Big(\sum_k A_k^{(1)} + \sum_k A_k^{(2)}\Big)\Big(I_z^{(1)} + I_z^{(2)}\Big)I_z^{(k)} + \frac{1}{2}\Big(\sum_k A_k^{(1)} - \sum_k A_k^{(2)}\Big)\Big(I_z^{(1)} - I_z^{(2)}\Big)I_z^{(k)} + H_B.$$

Only the latter term $\Big(I_z^{(1)} - I_z^{(2)}\Big)I_z^{(k)}$ affects the pseudo-spin of the pair. In the pseudo-spin subspace we then obtain

$$H_{int} = \sum_k (A_k^{(1)} - A_k^{(2)})\hat{I}_z I_z^{(k)} + H_B, \tag{3.21}$$

where $\hat{I}_z$ is the pseudo-spin operator and the sum is over all k bath spins. The pair forms a decoherence-free subspace: only the difference in coupling of a bath spin k causes noise on the pseudo-spin of the pair. For a single spin $A_k^{(2)} = 0$ and $\hat{I}_z$ becomes the single-spin operator I_z.

Following analyses by Anderson et al.[36] and Klauder et al.[56], we now take a classical approach to the noise in the pseudo-spin subspace. We model $\Delta Z(t)$ as an Ornstein-Uhlenbeck process with correlation function $\langle \Delta Z(t)\Delta Z(0)\rangle = b^2 \exp(-t/\tau_c)$ where τ_c is the correlation time of the bath due to the intra-bath dynamics H_B and $b^2 = \frac{1}{4}\sum_k (A_k^{(1)} - A_k^{(2)})^2$ is the variance of the noise.

We calculate the distributions for b numerically (Sec. 3.9.6). For nearest-neighbour pairs (like pairs A and B), we find a typical $b \sim 10$ Hz. For the parameters of pair C we find a larger value $b \sim 15$ Hz, consistent with the larger distance between the spins leading to less correlated noise and a less effective decoherence-free subspace. As a reference, for an individual ^{13}C spin one has $b \sim 20$ Hz. For the correlation time when the NV spin is in $m_s = 0$, a typical value $\tau_c = 0.1$ s can be estimated from previous experiments[16].

PAIR C AND $m_s = -1$: NO CLOCK TRANSITION, A FROZEN CORE, QUASI-STATIC NOISE

For pair C we have $Z \gg X$. For the NV in $m_s = -1$, the effect of the coupling X becomes negligible, so that equation (S1) can be approximated as

$$H \approx (-Z + \Delta Z(t))\hat{I}_z. \tag{3.22}$$

In this case, $\Delta Z(t)$ directly and linearly modifies the eigenenergies. There is no coherence protection related to a clock transition. Additionally, in the $m_s = -1$ state, the NV magnetic field gradient creates a frozen core, in which nuclear spin flip-flops are suppressed[4,9]. As a result, the dephasing time (T_2^*) is short compared to the correlation time of the noise τ_c, and $\Delta Z(t)$ can be described as quasi-static.

This regime leads to a Gaussian decay of $\exp\left(-b^2\tau^2/2\right)$ with $T_2^* = \frac{\sqrt{2}}{b}$ [36]. Therefore, we can extract b from the experimental data. The measured T_2^* time of 18(1) ms yields $b_C = 12.5(7)$ Hz, consistent with the expected distribution for the inter-pair distance of pair C (Sec. 3.9.6). The hypothesis that the noise can be treated as quasi-static is further corroborated by the fact that a large increase in coherence is observed for a spin echo ($T_2 = 0.3(2)$ s, Fig. 3.7d).

In summary, for pair C and $m_s = -1$, we probe a regime where the clock transition is turned off, the decoherence-free subspace has a reduced influence (larger inter-pair distance) and the bath noise can be treated as quasi-static (frozen core and $T_2^* \ll \tau_c$). This regime and the resulting T_2^* is similar as for an individual nuclear spin in the same environment[4]. No significant enhancement of coherence is obtained for the spin pair.

PAIR A, B AND $m_s = -1$: A DETUNED CLOCK TRANSITION, A FROZEN CORE, QUASI-STATIC NOISE

For pair A, B we have $X \gg Z$. Additionally we typically have a situation in which $X \gg Z \gg \Delta Z(t)$. Taking only terms that contribute to dephasing, we can therefore approximate the Hamiltonian with the NV in $m_s = -1$ using a Taylor series expansion as

$$H = \omega_{-1}\hat{I}_x + \frac{Z}{\omega_{-1}}\Delta Z(t)\hat{I}_x, \tag{3.23}$$

where $\omega_{-1} = \sqrt{X^2 + Z^2}$. Similarly to the case of pair C, we expect a Gaussian decay shape, but now with $T_2^* = \frac{\omega_{-1}}{Z}\frac{\sqrt{2}}{b}$. While the coupling X now creates a clock transition, the system is detuned from the ideal point, because $Z \gg \Delta Z(t)$. As a result, the effect of the noise is reduced by a factor $\frac{\omega_{-1}}{Z} \approx 20$, consistent with the increase of T_2^* of pair A and B compared to pair C.

The experimental data contains the decay of both pair A and B that are generally not equal. We extract two decay times from the Gaussian fit of the Fourier transform (Fig. 3.3a), obtaining $T_{2,A}^* = 0.26(2)$ s and $T_{2,B}^* = 0.39(6)$ s. For pair A with $Z_A = 130(1)$ this corresponds to $b_A = 13.9(2)$ Hz and for pair B with $Z_B = 91(2)$ Hz this corresponds to $b_B = 12.5(4)$ Hz. The values agree with typical values for b (Sec. 3.9.6).

In conclusion, in this case we probe a regime where the pair interaction X creates a clock transition (as $X \gg Z$), but the system is detuned because $Z \gg \Delta Z(t)$. Additionally, the NV electron spin creates a frozen core and the noise can thus be treated as quasi-static. The resulting dephasing time is enhanced by a factor $\sqrt{X^2 + Z^2}/Z$.

PAIR A, B AND $m_s = 0$: CLOCK TRANSITION, MOTIONAL NARROWING

In $m_s = 0$, the noise cannot be treated as quasi-static anymore, because flip-flops between ^{13}C spins occur more frequently. We therefore have to take into account the correlation time τ_c of the bath as well as its strength b. The Hamiltonian for a pair in the pseudo-spin subspace in $m_s = 0$ is

$$H = X\hat{I}_x + \Delta Z(t)\hat{I}_z. \tag{3.24}$$

For pair A, B it holds that $X \gg \Delta Z(t)$ for typical values of $\Delta Z(t)$ (Sec. 3.9.6). We initially assume that the bath has no significant frequency components leading to direct transitions between the pair eigenstates ($X \gg 1/\tau_c$), but will come back to this effect at the end of the section. Then, following the analysis by Dobrovitski et al.[37], we can approximate the Hamiltonian as

$$H = X\hat{I}_x + \frac{\Delta Z^2(t)}{2X}\hat{I}_x, \tag{3.25}$$

with $\Delta Z(t)$ a Gaussian distribution with variance $b^2 = \frac{1}{4}\sum_k (A_k^{(1)} - A_k^{(2)})^2$. The system now forms an effective clock transition and the noise term $\Delta Z(t)$ enters quadratically in the Hamiltonian.

This model can be solved analytically for the expectation value $\langle S_z \rangle$ of the pair pseudo-spin[37]:

$$\begin{aligned} \langle S_z(t)\rangle &= \frac{1}{2}\mathrm{Re}[M(t)\exp(iXt)] \\ [M(t)]^{-2} &= \exp(-Rt)[\cosh(Pt) + (R/P)\sinh(Pt)] - i\frac{b^2}{XP}\exp(-Rt)\sinh(Pt) \end{aligned} \tag{3.26}$$

where $P = \sqrt{R^2 - 2ib^2R/X}$ and $R = 1/\tau_c$ where τ_c is the correlation time of the bath.

Equation (3.26) holds generally, but it is possible to consider three different regimes separately. These regimes are defined by the rate of the noise bath fluctuations R compared to the effective coupling to the noise bath of $b^2/2X$. First, we consider a quasi-static bath. This leads to a non-exponential decay of the form[37,57]

$$M(t) = \left(1 + \left(\frac{b^2 t}{X}\right)^2\right)^{-\frac{1}{4}}. \tag{3.27}$$

Second, the noise bath can be 'slow' compared to the coupling strength to the noise: $R \ll b^2/X$. For short times, during which the bath is static, the decay follows equation (3.27). For longer times, during which slow bath dynamics have to be taken into account, the decay is of the form[37]

$$M(t) = \exp\left(-bt\sqrt{R/4X}\right). \tag{3.28}$$

Third, the bath dynamics can be fast compared to the magnitude of the noise: $R \gg b^2/X$. In this regime we can approximate the solution in equation (3.26) as[37]

$$M(t) = \exp\left(i\frac{b^2 t}{2X} - \frac{b^4 t}{4X^2 R}\right). \tag{3.29}$$

The expected decay time of the Ramsey experiment is $T_2^* = \frac{4X^2R}{b^4}$. In this regime the pair coherence benefits from an effect that is similar to motional narrowing[37]: T_2^* linearly increases with the rate of fluctuations R. The result differs from the standard case of motional narrowing in that there is an additional frequency shift of $b^2/2X$[37].

We now discuss which of these regimes governs the coherence of pair A and B. As shown in the previous section $b_A = 13.9(2)$ Hz and $b_B = 12.5(4)$ Hz. From the main text we know $X = 2080.9900(3)$ Hz (Fig. 3.3b). First we consider the expected dephasing times for slow baths. Equation (3.26) is plotted in Fig. 3.11 for pair A ($b_A = 13.9(2)$ Hz) with a correlation time of $\tau_c = 10$ s. From Fig. 3.11 it is clear that a slow bath cannot explain the long inhomogeneous dephasing time observed in the main text ($T_2^* = 1.9(6)$ min, Fig. 3.3c).

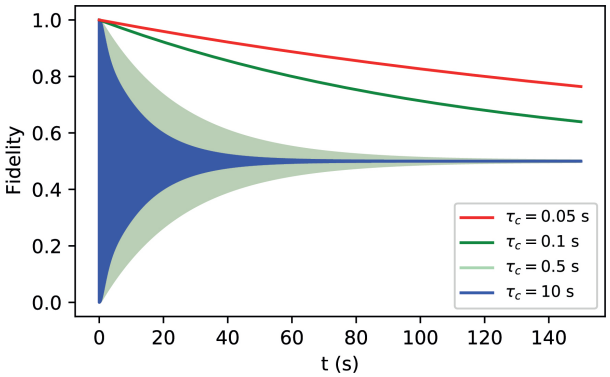

Figure 3.11: **Dephasing-limited signals and envelopes for fast and slow baths.** The results for $\tau_c = 10$ s and $\tau_c = 0.5$ s are calculated from equation (3.26). For $\tau_c = 0.1$ s and $\tau_c = 0.05$ s equation (3.29) holds and we therefore calculate the dephasing-limited envelope from equation (3.29). We have used $X = 2080.9900$ Hz and $b = 13.9$ Hz.

Because typical measured relaxation times T_1 for individual ^{13}C spins indicate $\tau_c = 0.1-0.3$ seconds[16], one would indeed expect that the bath noise enters a fast regime: the fast bath condition $R \gg b^2/X$ is satisfied for bath correlation times of $\tau_c \lesssim 0.5$ s.

The envelopes for a fast bath are shown in Fig. 3.11. These results show that significantly longer dephasing times are expected in this regime compared to the slow bath regime. We conclude that the measured $T_2^* = 1.9(6)$ min can only be explained in this fast bath regime where an effect similar to motional narrowing further enhances the inhomogeneous dephasing time.

Since the coupling to the noise of pair A (b_A) and B (b_B) were determined above, the bath fluctuation rate can be estimated under the assumption that dephasing is limiting. Using $T_2^* = 1.9(6)$ min and $X = 2080.9900(3)$ Hz we obtain $R_A = 10(2)$ Hz and $R_B = 6(2)$ Hz. These values are consistent with previously measured values for T_1 of individual ^{13}C spins with the NV electron spin in $m_s = 0$[16].

Finally, we consider relaxation as a potential mechanism limiting the dephasing

time. Spectral components around frequency X could lead to direct transitions between the antiparallel pair eigenstates $([|\Uparrow\rangle + |\Downarrow\rangle]/\sqrt{2} \leftrightarrow [|\Uparrow\rangle - |\Downarrow\rangle]/\sqrt{2})$. In the regime of a fast bath this can be treated analytically and introduces a factor that multiplies equation (3.26) by $\exp\left(-b^2Rt/2X^2\right)$[37]. If this type of relaxation is dominant we would obtain $T_2^* = \frac{2X^2}{b^2R}$. The identified values for b_A, b_B, X and T_2^* give $R_A = 400(75)$ Hz and $R_B = 500(100)$ Hz, which is inconsistent with previously measured single ^{13}C spin T_1 values[16] and with the typical ^{13}C-^{13}C couplings for this ^{13}C concentration. We conclude that such relaxation within the pseudo-spin subspace is unlikely to contribute to the observed coherence curves.

In summary, the long observed dephasing times for pair A, B are the result of three different physical effects working together. First, the effective noise b is reduced because correlated noise does not affect the spin pair, i.e. the pair forms a decoherence-free subspace (DFS). Second, since $X \gg \Delta Z(t)$, the pair pseudo-spin forms a clock transition (equation (3.25)). It is therefore only second-order sensitive to noise following $\Delta Z^2(t)/2X$. Third, the DFS and clock transition alone are not sufficient to explain a dephasing time of 1.9(6) min. Only in the regime of a fast bath, in which the pair benefits from an effect similar to motional narrowing, can such dephasing times be realized.

PAIR A, B AND $m_s = 0$: OTHER DECOHERENCE MECHANISMS

Above, we show how a combination of three effects strongly suppresses dephasing for the spin pairs. This strong suppression of dephasing is a necessary condition to obtain the long T_2^* times observed. However, it does not imply that the obtained T_2^* times and decay curves are explained by and purely limited by dephasing. Indeed, the decay envelope observed for pairs A and B (Fig. 3.3c) deviates from the simple exponential decay obtained in equation (3.29). In particular, the fit yields a decay curve following $e^{-(t/T_2^*)^n}$ with $n = 0.23(4)$ (Sec. 3.9.2) and the data suggests additional features in the decay shape that are not captured by the fit curve. These observations indicate that other mechanisms, like coherent interactions with the bath or relaxation of the pair spins due to flip-flops with the bath spins are contributing to decoherence. Such effects strongly depend on the microscopic environment of the pairs and are challenging to treat generally. Future research could aim to understand the microscopic environment of the pairs and determine the mechanisms limiting the observed coherence times.

PAIR C AND $m_s = 0$

The analysis for pair C is analogous to the above analysis. However, there is an important difference between pair A, B and pair C. Namely, the dipolar coupling X is an order of magnitude smaller for pair C. Since the effective noise strength for pair C ($b_C = 12.5(7)$ Hz) is similar to the noise for pair A ($b_A = 13.9(2)$ Hz) and pair B ($b_B = 12.5(4)$ Hz), the approximation of a fast bath cannot be easily made. Therefore we are in an intermediate regime where the full expression in equation (3.26) describes the dephasing. The pair C coherence in $m_s = 0$ therefore still benefits from the decoherence-free subspace and clock transition, but to a lesser degree from motional narrowing.

PAIR C: SPIN ECHO T_2, RELAXATION TIME T_1

For pair C, spin echo (T_2) and relaxation (T_1) measurements in both electron states were taken (Fig. 3.7). When the NV electron spin is in $m_s = -1$, the NV spin creates a hyperfine

field gradient that slows down spin flip-flops in the bath (a frozen core[4,9]). The noise a ^{13}C pair experiences is therefore expected to be quasi-static. Given quasi-static noise, a spin echo is expected to increase coherence. This is in agreement with the marked increase in coherence time: $T_2 = 0.3(2)$ s (Fig. 3.7d). Similarly, the frozen core also suppresses flip-flops involving one of the ^{13}C spins of the pair, leading to long relaxation times. For pair C we do indeed find a relaxation time $T_1 \gg 1$ s, comparable to that of single ^{13}C spins[4].

When the NV electron spin is in $m_s = 0$, ^{13}C spins are no longer detuned and flip-flops can become limiting for spin coherence. For pair C we find a spin echo time of $T_2 = 0.7(1)$ s. The relaxation time is $T_1 = 0.9(2)$ s or $T_1 = 3.6(7)$ s depending on the initial state. This suggests that the relaxation mechanism is dependent on initialisation in the singlet $((|\Uparrow\rangle - |\Downarrow\rangle)/\sqrt{2})$ or triplet state $((|\Uparrow\rangle + |\Downarrow\rangle)/\sqrt{2})$. Furthermore these results indicate that the coherence of pair C may be limited by relaxation.

3.9.10. PAIR INITIALISATION AND READOUT CALIBRATION

In this section we describe the optimization of the parameters used for initialisation and single-shot measurements. The most important trade-off lies in the number of repetitions of the measurement sequences. On the one hand, increasing the number of repetitions improves the fidelity because the different states can be distinguished better and the effect of the NV electron spin dephasing is diminished. On the other hand, the pair spin state decoheres during the measurement, limiting the maximum number of repetitions. Therefore, there is an optimum in the number of repetitions and the corresponding decision thresholds used.

We first describe our approach to optimize the parameters in general. We will call the two states that we want to optimally distinguish $|a\rangle$ and $|b\rangle$. In an initialisation step, we generally use k repetitions and we record the number of counts ($m_s = 0$ outcomes) as $N(k)$. This initialisation step is then defined by $N(k) > N_a$ and $N(k) < N_b$ where N_a and N_b are the thresholds set (red lines in Fig. 3.2f,g). In case there is a two-step initialisation process (see e.g. Fig. 3.2e) we denote the number of counts in the first step as $N(p)$ with condition $N(p) > N_0$ where N_0 is the threshold set. In the readout step, we use m repetitions and obtain $N(m)$ counts. Two histograms are obtained (see e.g. Fig. 3.2f), one corresponding to each initialised state. To optimally distinguish these states, we sweep a threshold T (see e.g. Fig. 3.2g) and obtain the combined initialisation and readout fidelity as

$$\begin{aligned} F = \frac{F_{|a\rangle} + F_{|b\rangle}}{2} &= \frac{1}{2} P(N(m) \geq T | N(k) > N_a \wedge N(p) > N_0) \\ &+ \frac{1}{2} P(N(m) < T | N(k) < N_b \wedge N(p) > N_0). \end{aligned} \tag{3.30}$$

We then optimize the fidelity for the number of repetitions m, the measurement decision threshold T, and the initialisation thresholds N_a, N_b and if applicable N_0. For the initialisation, the number of repetitions k is not as important. The main trade-off now lies in the initialisation thresholds: we pick values that balance the resulting fidelity and the success probability (experimental rate). Namely, the stricter the threshold is, the higher the fidelity but the lower the experimental rate.

3.9.11. CALIBRATION OF THE SPIN MEASUREMENT FOR PAIR A AND B

For pair A and B we calibrate the spin measurement to optimally distinguish $|a\rangle = |\Uparrow\rangle|\Uparrow\rangle$ and $|b\rangle = |\Downarrow\rangle|\Downarrow\rangle$. The sequence is shown in Fig. 3.12a. First, we initialise the parity of pair A and B with $p = 20$ repetitions and a threshold of $N_0 = 12$. To initialise the two states of interest we then use $k = 30$ spin readouts and set thresholds of $N_a = 25$ and $N_b = 3$ counts.
For a varying number of readouts m we now determine the optimal threshold and corresponding fidelity as in Fig. 3.2g in the main text. In Fig. 3.12b, we plot the average fidelity and corresponding optimal threshold for a varying number of readouts. The optimum is at $m = 40$ readouts with a threshold of $T = 19$. We obtain a combined initialisation and readout fidelity of $F = 98.4(5)\%$. For the results in the main text we use $m = 30$ and $T = 14$ which gives, within error, the same fidelity ($F = 98.1(5)\%$).

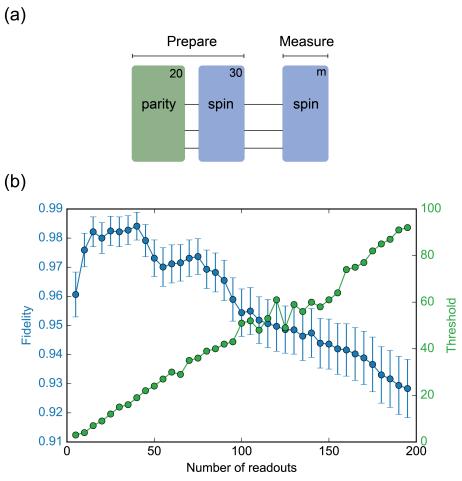

Figure 3.12: **Spin measurement calibration for pair A and B. a.** The sequence used to calibrate the spin readout. First we select on > 14/20 counts in 20 parity readouts to initialise the pairs in $\frac{1}{2}|\Uparrow\rangle|\Uparrow\rangle\langle\Uparrow|\langle\Uparrow| + \frac{1}{2}|\Downarrow\rangle|\Downarrow\rangle\langle\Downarrow|\langle\Downarrow|$. Then we either initialise the pairs in $|\Uparrow\rangle|\Uparrow\rangle$ (> 25/30) or $|\Downarrow\rangle|\Downarrow\rangle$ (< 3/30) with 30 spin readouts. Finally the spin is read out using m spin readouts. **b.** We vary the number of readouts m and find the optimal threshold for each m. The average fidelity (equation (3.30)) is plotted against the number of readouts m and the corresponding optimal threshold is indicated for that number of readouts. The initial increase of fidelity with the number of repetitions originates from the limiting effect of dephasing of the NV electron spin during the interaction sequence. For a small number of repetitions, this dephasing limits the measurement fidelity. But with more repetitions the conditional histograms (Fig. 3.2f) separate and NV electron dephasing plays a limited role. For a large number of repetitions a slow decay in the fidelity is observed, which is due to decoherence of the pair spin during the measurement sequence.

3.9.12. CALIBRATION OF THE PARITY MEASUREMENT FOR PAIR A AND B

For pair A and B the parity measurement is optimized to distinguish the pair parity. To calibrate the measurement, we use the states $|a\rangle = \frac{1}{2}|\Uparrow\rangle|\Uparrow\rangle\langle\Uparrow|\langle\Uparrow| + \frac{1}{2}|\Downarrow\rangle|\Downarrow\rangle\langle\Downarrow|\langle\Downarrow|$ and $|b\rangle = \frac{1}{2}|\Uparrow\rangle|\Downarrow\rangle\langle\Uparrow|\langle\Downarrow| + \frac{1}{2}|\Downarrow\rangle|\Uparrow\rangle\langle\Downarrow|\langle\Uparrow|$. To prepare these two states, we use a two-step ini-

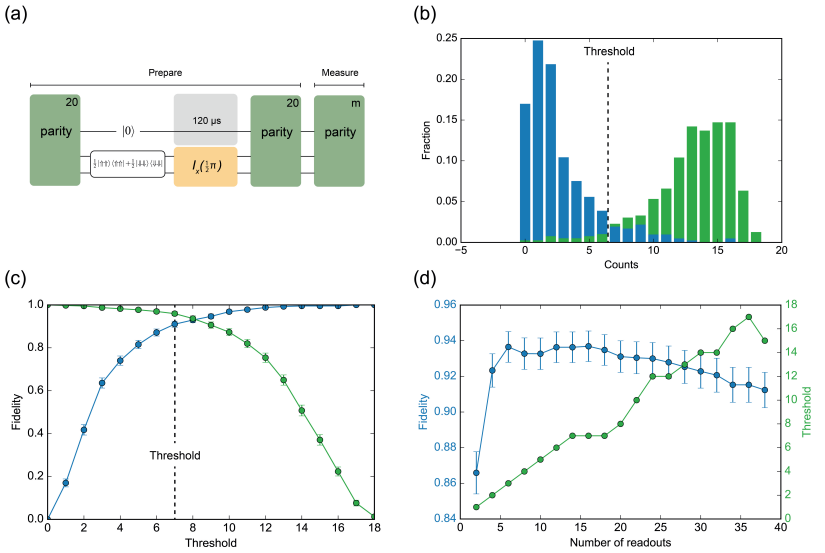

Figure 3.13: **Parity measurement calibration of pair A and B a.** The sequence used to calibrate the pair A and B parity measurement. We select on $> 14/20$ counts in the first 20 readouts and apply a $\pi/2$ around x to obtain a mixed state in the antiparallel subspace. Then another 20 parity readouts are used to initialise pair A and B in even parity ($> 15/20$) or odd parity ($< 2/20$) states. Finally m parity readouts are performed that we aim to calibrate. **b.** Conditional histograms for $|a\rangle$ (green) and $|b\rangle$ (blue) for $m = 18$ readouts. The optimal threshold of $T = 7$ is indicated. **c.** Combined initialisaton and readout fidelity of the individual states $|a\rangle$ (green) and $|b\rangle$ (blue) for $m = 18$ readouts. **d.** We vary the number of readouts m and find the optimal threshold for each m. The average fidelity (equation (3.30)) is plotted against the number of readouts m and the corresponding optimal threshold is indicated for that number of readouts.

tialisation (Fig. 3.13a). First, we use $p = 20$ parity initialisations with a threshold $N_0 = 14$ to obtain $|a\rangle$. Then we apply a $\pi/2$ pulse around x to obtain a fully mixed state in the antiparallel subspace ($\{|\Uparrow\Uparrow\rangle, |\Uparrow\Downarrow\rangle, |\Downarrow\Uparrow\rangle, |\Downarrow\Downarrow\rangle\}$). This first step of the initialisation has reduced the Bloch sphere in Fig. 3.2d to just contain antiparallel states (the pseudo-spin states), improving subsequent initialisation steps. The second step of the initialisation uses $k = 20$ readouts with initialisation thresholds of $N_a = 15$ and $N_b = 2$. We set the number of decoupling elements for the parity sequence to $N_p = 20$ in Fig. 3.2b. This is less than twice the decoupling elements for the spin sequence ($N_s = 14$ in Fig. 3.2a). The optimal interaction time is smaller than a π-rotation due to the loss of NV electron spin coherence with increasing N_p.

In Fig. 3.13b the histograms for $|a\rangle$ (green) and $|b\rangle$ (blue) are shown for $m = 18$ readouts. We use equation (3.30) to obtain the fidelity of the individual states (Fig. 3.13c) and the average fidelity while sweeping the threshold T. This process is repeated for a varying number of readouts m. In Fig. 3.13d the average fidelity is shown as a function of the number of readouts m. The optimum is found for $m = 16$ readouts with a threshold $T = 7$. We obtain a combined initialisation and readout fidelity of $F = 93.7(9)\%$. For the results in the main text we use $m = 18$ and $T = 7$ which gives, within error, the same fidelity.

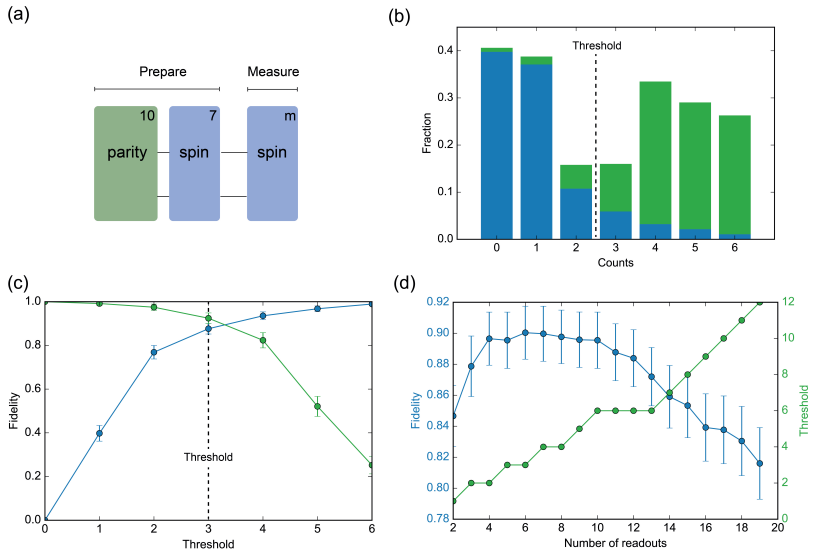

Figure 3.14: **Spin readout calibration of pair C. a.** The sequence used to calibrate the pair C spin readout. We select on $> 9/10$ in the 10 parity readouts to obtain a mixed state in the antiparallel subspace. Then we initialise $\frac{1}{\sqrt{2}}(|\Uparrow\rangle + |\Downarrow\rangle)$ $(> 6/7)$ or $\frac{1}{\sqrt{2}}(|\Uparrow\rangle - |\Downarrow\rangle)$ $(< 1/7)$. Finally we do m spin readouts that we calibrate to optimally distinguish these states. **b.** Conditional histograms for $\frac{1}{\sqrt{2}}(|\Uparrow\rangle + |\Downarrow\rangle)$ (green) and $\frac{1}{\sqrt{2}}(|\Uparrow\rangle - |\Downarrow\rangle)$ (blue). The optimal threshold of $T = 3$ is indicated. **c.** Combined initialisation and readout fidelity of $\frac{1}{\sqrt{2}}(|\Uparrow\rangle + |\Downarrow\rangle)$ (green) and $\frac{1}{\sqrt{2}}(|\Uparrow\rangle - |\Downarrow\rangle)$ (blue) for $m = 6$ readouts. **d.** The average fidelity (equation (3.30)) is plotted as a function of the number of readouts m and the corresponding optimal threshold for the given number of readouts.

3.9.13. CALIBRATION OF THE SPIN MEASUREMENT FOR PAIR C

For pair C we optimize the spin readout to optimally distinguish $|a\rangle = \frac{1}{\sqrt{2}}(|\Uparrow\rangle + |\Downarrow\rangle)$ and $|b\rangle = \frac{1}{\sqrt{2}}(|\Uparrow\rangle - |\Downarrow\rangle)$ (Fig. 3.6). To initialise these states, we first initialise the pair in the antiparallel subspace and then initialise the spin state (Fig. 3.14a). We set $N_0 = 9$ in the $p = 10$ parity readouts and set $N_a = 6$ and $N_b = 1$ for the $k = 7$ spin readouts.

In Fig. 3.14b the histograms for $|a\rangle$ (green) and $|b\rangle$ (blue) are shown for $m = 6$ readouts. We calculate the combined initialised and readout fidelity of $|a\rangle$ and $|b\rangle$ using equation (3.30) for varying thresholds T (Fig. 3.14c). In Fig. 3.14d we vary the number of readouts m and plot it against the average fidelity. The indicated threshold is the one that gives the maximum average fidelity. The optimum is found for $m = 6$ with a threshold $T = 3$. We obtain a combined initialisation and readout fidelity of 90(2)%.

3.9.14. CALIBRATION OF THE PARITY MEASUREMENT FOR PAIR C

For pair C, the parity measurement distinguishes between the parallel and the antiparallel subspace (Fig. 3.6). We calibrate the parity measurement to optimally distinguish $|a\rangle = \frac{1}{2}|\Uparrow\rangle\langle\Uparrow| + \frac{1}{2}|\Downarrow\rangle\langle\Downarrow|$ and $|b\rangle = \frac{1}{2}|\uparrow\uparrow\rangle\langle\uparrow\uparrow| + \frac{1}{2}|\downarrow\downarrow\rangle\langle\downarrow\downarrow|$. To initialise the subspace we use

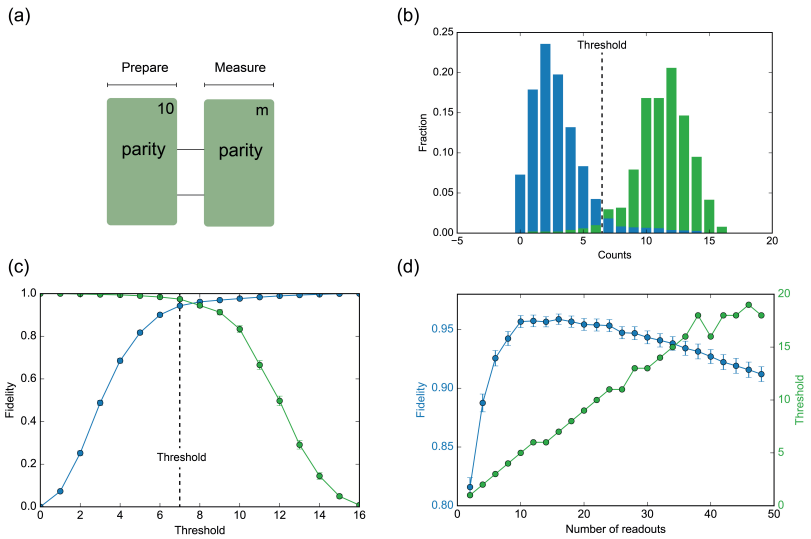

Figure 3.15: **Parity readout calibration of pair C a.** The sequence used to calibrate the pair C parity readout. We initialise the pair in the antiparallel (> 9/10) or parallel (< 1/10) subspace. Then we do m parity readouts that are calibrated to optimally distinguish the subspaces. **b.** Conditional histograms for the antiparallel (green) and parallel (blue) subspace for $m = 16$ readouts. The optimal threshold of $T = 7$ is indicated. **c.** Combined initialisation and readout fidelity of the antiparallel (green) and parallel (blue) subspace for $m = 16$ readouts. **d.** The average fidelity (equation (3.30)) is plotted as a function of the number of readouts m and the corresponding optimal threshold for the given number of readouts.

$k = 10$ parity readouts and set $N_a = 9$ and $N_b = 1$ (Fig. 3.15a).

In Fig. 3.15b the histograms for $|a\rangle$ (green) and $|b\rangle$ (blue) are shown for $m = 16$ readouts. We calculate the combined initialisation and readout fidelity of $|a\rangle$ and $|b\rangle$ using equation (3.30) for varying thresholds T (Fig. 3.15c). In Fig. 3.15d we vary the number of readouts m and plot it against the average fidelity. The indicated threshold is the one that gives the maximum average fidelity. The optimum is found for $m = 16$ with a threshold $T = 7$. We obtain a combined initialisation and readout fidelity of 95.9(4)%.

3.9.15. VALUE OF THE DIPOLAR COUPLING X

The dipolar coupling X between two carbon spins is given by[34]

$$X = \frac{\mu_0 \gamma_c^2 \hbar}{8\pi r^3}(1 - 3\cos^2\theta) \tag{3.31}$$

as defined in Section 3.9.3, with $\gamma_c = 67.2828 \cdot 10^6$ rad s^{-1} T^{-1} and $\mu_0 = 4\pi \cdot 10^{-7}$ H/m. A nearest neighbour pair along the field, such as pair A and B, has $\mathbf{r} = \frac{a_0}{4}[1,1,1]$ where $a_0 = 3.5668$ Å is the lattice constant of diamond at 3.7 K[58]. Consequently $\theta = 0$ and we obtain $X = 2062.37$ Hz. This is significantly different from the observed value of $X = 2080.9900(3)$ Hz. For pair C the theoretically predicted value is $X = 186.92$ Hz

whereas the observed value is $X = 188.33(2)$ Hz. Notably pair A and B have the same or very similar X values, suggesting a mechanism that is not dependent on the local environment. Furthermore, the observed change in X for pair A, B and C is consistent with a reduction of the lattice constant by ~ 0.01 Å. In this section, we analyze several mechanisms that could affect the value of X.

STRAIN

The E_x and E_y optical transitions for the NV considered in this work are split by ~ 4 GHz, implying a strain of $\delta = 2$ GHz[11]. This is transversal strain with respect to the NV-axis. Axial strain is aligned with the pair A, B axis. We take a typical strain-induced splitting on the order of ~ 10 GHz and perform an order of magnitude estimate. 1 GPa of external stress corresponds to a 10^3 GHz splitting[59,60], so ~ 10 GHz corresponds to 0.01 GPa. Taking a Young's modulus of $\sim 10^3$ GPa we obtain a deformation of $\sim 10^{-5}$. If the axial strain is comparable to the transversal strain, strain cannot explain the observed increase in X, since the required reduction in the lattice constant is on the order of $\sim 10^{-3}$. However, a precise value for the axial strain is not known and we can therefore not rule out this mechanism.

EFFECT OF ^{13}C ISOTOPE

Pair A and B each consist of two ^{13}C spins surrounded by mostly ^{12}C spins, because of the natural ^{13}C abundance of 1.1%. The value for a_0 used to get to $X = 2062$ Hz does not take into account variations in the ^{13}C abundance. It has been shown that the diamond lattice constant decreases upon increasing the ^{13}C abundance[61]. This suggests that local variations in the diamond lattice constant due to ^{13}C might play a role in the observed value of X. Additional research is required to be able to quantitatively compare this microscopic effect to the measured values.

FREQUENCY SHIFTS DUE TO THE ^{13}C BATH

From equation (3.29) we find that the observed frequency in $m_s = 0$ is actually $X + \frac{b^2}{2X}$. The noise contribution $\delta f = \frac{1}{2\pi}\frac{b^2}{2X}$ is relatively small and therefore we quote the observed value as X in the main text. However, we can estimate the noise term using the values of $b_A = 13.9(2)$ Hz and $b_B = 12.5(4)$, obtained from the T_2^* measurement with the NV electron spin in $m_s = -1$. Thus $\delta f_A = 0.046(1)$ Hz and $\delta f_B = 0.038(2)$ Hz. Notably, the difference is 0.009(3) Hz. It is therefore possible that the long T_2^* measurements presented in the main text are affected by this frequency difference. However the frequency changes due to the noise $\frac{b^2}{2X}$ are too small to explain the difference between expected and measured value of X.

ELECTRON-MEDIATED COUPLING

The coupling strength measured can also be modified due to the presence of the electron spin especially in the presence of a misaligned magnetic field[12]. To study the electron-mediated coupling effects on the measured coupling strength, we consider the Hamiltonian describing a system of an NV center and a pair of coupled ^{13}C spins with dipolar coupling $X = 2062.37$ Hz. We numerically solve the full system Hamiltonian (i.e. not considering the pseudo-spin model) to obtain the eigenenergies of the system, from which

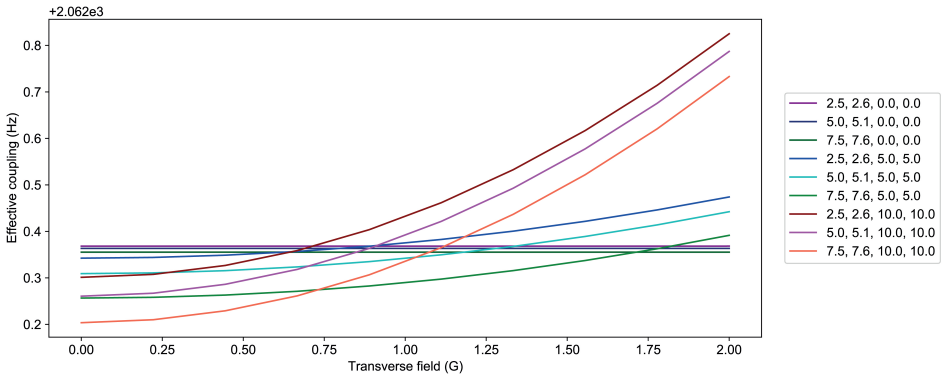

Figure 3.16: **Electron-mediated effects on the measured coupling strength X.** Numerical simulations showing the obtained effective coupling strength as a function of the transverse magnetic field strength. We show some examples with different combinations of hyperfine couplings between the NV center and the two ^{13}C spins of the pair. Note that, based on a detailed previous characterization of the nearby environment of this NV center [12] that did not show evidence of these pairs, the actual hyperfine parameters for pairs A and B are expected to be significantly smaller than the largest examples used here. The figure legend shows respectively $A_{\parallel}^{(1)}$, $A_{\parallel}^{(2)}$, and $A_{\perp}^{(1)}$, $A_{\perp}^{(2)}$ in kHz. For our magnetic field alignment, the transverse field is expected to be well below 1 Gauss [12], and therefore we conclude that the electron mediated effects in our case are very small (< 0.5 Hz).

we calculate the effective coupling strength. Figure 3.16 shows the obtained effective coupling strength as a function of the transversal magnetic field strength (which reflects how well the field is aligned with the NV axis). We consider some examples with different combinations of hyperfine couplings to the NV center ($A_{\parallel}$ and $A_{\perp}$) of the two ^{13}C spins making up the pair. The maximum values are significantly higher than expected for pairs A and B. For our magnetic field alignment, the perpendicular field is expected to be well below 1 Gauss [12], and therefore we conclude that the electron mediated effects in our case are very small (< 0.5 Hz). Electron-mediated effects are thus very unlikely to explain the difference in the expected and observed value of X.

AUTHOR CONTRIBUTIONS

H.P.B. played a leading role in all the aspects of the work, with support from all authors.

REFERENCES

[1] K. C. Miao *et al.*, *Universal coherence protection in a solid-state spin qubit,* Science **369**, 1493 (2020).

[2] N. Bar-Gill, L. M. Pham, A. Jarmola, D. Budker and R. L. Walsworth, *Solid-state electronic spin coherence time approaching one second,* Nat. Commun. **4**, 1743 (2013).

[3] J. T. Muhonen *et al.*, *Storing quantum information for 30 seconds in a nanoelectronic device,* Nat. Nanotechnol. **9**, 986 (2014).

[4] C. E. Bradley *et al.*, *A ten-qubit solid-state spin register with quantum memory up to one minute,* Phys. Rev. X **9**, 031045 (2019).

[5] M. D. Shulman *et al.*, *Demonstration of entanglement of electrostatically coupled singlet-triplet qubits,* Science **336**, 202 (2012).

[6] M. D. Shulman *et al.*, *Suppressing qubit dephasing using real-time Hamiltonian estimation,* Nat. Commun. **5**, 5156 (2014).

[7] G. Wolfowicz *et al.*, *Atomic clock transitions in silicon-based spin qubits,* Nat. Nanotechnol. **8**, 561 (2013).

[8] K. Saeedi *et al.*, *Room-temperature quantum bit storage exceeding 39 minutes using ionized donors in silicon-28,* Science **342**, 830 (2013).

[9] M. Zhong *et al.*, *Optically addressable nuclear spins in a solid with a six-hour coherence time,* Nature **517**, 177 (2015).

[10] Y. Bae *et al.*, *Enhanced quantum coherence in exchange coupled spins via singlet-triplet transitions,* Sci. Adv. **4**, 1 (2018).

[11] M. H. Abobeih *et al.*, *One-second coherence for a single electron spin coupled to a multi-qubit nuclear-spin environment,* Nat. Commun. **9**, 1 (2018).

[12] M. H. Abobeih *et al.*, *Atomic-scale imaging of a 27-nuclear-spin cluster using a quantum sensor,* Nature **576**, 411 (2019).

[13] N. Zhao, J. L. Hu, S. W. Ho, J. T. Wan and R. B. Liu, *Atomic-scale magnetometry of distant nuclear spin clusters via nitrogen-vacancy spin in diamond,* Nat. Nanotechnol. **6**, 242 (2011).

[14] F. Shi *et al.*, *Sensing and atomic-scale structure analysis of single nuclear-spin clusters in diamond,* Nat. Phys. **10**, 21 (2013).

[15] C. L. Degen, F. Reinhard and P. Cappellaro, *Quantum sensing,* Reviews of Modern Physics **89**, 1 (2017).

[16] J. Cramer *et al.*, *Repeated quantum error correction on a continuously encoded qubit by real-time feedback,* Nature Communications **7**, 11526 (2016).

[17] G. Waldherr *et al., Quantum error correction in a solid-state hybrid spin register,* Nature **506**, 204 (2014).

[18] B. Hensen *et al., Loophole-free Bell inequality violation using electron spins separated by 1.3 kilometres,* Nature **526**, 682 (2015).

[19] A. Reiserer *et al., Robust quantum-network memory using decoherence-protected subspaces of nuclear spins,* Phys. Rev. X **6**, 021040 (2016).

[20] M. Pompili *et al., Realization of a multinode quantum network of remote solid-state qubits,* Science **372**, 259 (2021).

[21] H. Seo *et al., Quantum decoherence dynamics of divacancy spins in silicon carbide,* Nat. Commun. **7**, 1 (2016).

[22] M. Ye, H. Seo and G. Galli, *Spin coherence in two-dimensional materials,* npj Comput. Mater **5**, 44 (2019).

[23] G. Q. Liu *et al., Single-Shot Readout of a Nuclear Spin Weakly Coupled to a Nitrogen-Vacancy Center at Room Temperature,* Phys. Rev. Lett. **118**, 150504 (2017).

[24] N. Kalb *et al., Experimental creation of quantum Zeno subspaces by repeated multi-spin projections in diamond,* Nat. Commun. **7**, 1 (2016).

[25] K. S. Cujia, J. M. Boss, K. Herb, J. Zopes and C. L. Degen, *Tracking the precession of single nuclear spins by weak measurements,* Nature **571**, 230 (2019).

[26] M. Pfender *et al., High-resolution spectroscopy of single nuclear spins via sequential weak measurements,* Nat. Commun. **10**, 594 (2019).

[27] S. Chen, M. Raha, C. M. Phenicie, S. Ourari and J. D. Thompson, *Parallel single-shot measurement and coherent control of solid-state spins below the diffraction limit,* Science **370**, 592 (2020).

[28] A. Ruskuc, C.-J. Wu, J. Rochman, J. Choi and A. Faraon, *Nuclear spin-wave quantum register for a solid-state qubit,* Nature **602**, 408 (2022).

[29] T. P. Harty *et al., High-fidelity preparation, gates, memory, and readout of a trapped-ion quantum bit,* Phys. Rev. Lett. **113**, 220501 (2014).

[30] C. Langer *et al., Long-lived qubit memory using atomic ions,* Physical Review Letters **95**, 060502 (2005).

[31] P. Wang *et al., Single ion qubit with estimated coherence time exceeding one hour,* Nature Communications **12** (2021).

[32] B. M. Terhal, *Quantum error correction for quantum memories,* Rev. Mod. Phys. **87**, 307 (2015).

[33] *Note that (near-)identical spin pairs are also explored in liquid-state ensemble NMR, for example for long-lived singlet states and spin polarisation through para-hydrogen*[62–64]*. .*

[34] N. Zhao, S. W. Ho and R. B. Liu, *Decoherence and dynamical decoupling control of nitrogen vacancy center electron spins in nuclear spin baths,* Phys. Rev. B **85**, 115303 (2012).

[35] D. A. Lidar, I. L. Chuang and K. B. Whaley, *Decoherence-free subspaces for quantum computation,* Physical Review Letters **81**, 2594 (1998).

[36] P. W. Anderson and P. R. Weiss, *Exchange narrowing in paramagnetic resonance,* Rev. Mod. Phys. **25** (1953).

[37] V. V. Dobrovitski, A. E. Feiguin, R. Hanson and D. D. Awschalom, *Decay of Rabi oscillations by dipolar-coupled dynamical spin environments,* Phys. Rev. Lett. **102**, 237601 (2009).

[38] O. Gühne and G. Tóth, *Entanglement detection,* Physics Reports **474**, 1 (2009).

[39] C. E. Bradley *et al.*, *Robust quantum-network memory based on spin qubits in isotopically engineered diamond,* npj Quantum Information **8**, 122 (2022).

[40] T. Unden *et al.*, *Quantum metrology enhanced by repetitive quantum error correction,* Phys. Rev. Lett. **116**, 230502 (2016).

[41] V. Vorobyov *et al.*, *Quantum Fourier transform for nanoscale quantum sensing,* npj Quantum Information **7**, 124 (2021).

[42] M. Pfender *et al.*, *Nonvolatile nuclear spin memory enables sensor-unlimited nanoscale spectroscopy of small spin clusters,* Nature Communications **8** (2017).

[43] Y. Matsuzaki *et al.*, *Hybrid quantum magnetic-field sensor with an electron spin and a nuclear spin in diamond,* Physical Review A **94**, 052330 (2016).

[44] S. Zaiser *et al.*, *Enhancing quantum sensing sensitivity by a quantum memory,* Nature Communications **7** (2016).

[45] A. Ajoy, U. Bissbort, M. D. Lukin, R. L. Walsworth and P. Cappellaro, *Atomic-scale nuclear spin imaging using quantum-assisted sensors in diamond,* Phys. Rev. X **5**, 011001 (2015).

[46] N. H. Nickerson, Y. Li and S. C. Benjamin, *Topological quantum computing with a very noisy network and local error rates approaching one percent,* Nature Communications **4**, 1756 (2013).

[47] J. F. Haase, Z. Y. Wang, J. Casanova and M. B. Plenio, *Soft quantum control for highly selective interactions among joint quantum systems,* Physical Review Letters **121**, 050402 (2018).

[48] J. Casanova, Z. Y. Wang, J. F. Haase and M. B. Plenio, *Robust dynamical decoupling sequences for individual-nuclear-spin addressing,* Physical Review A **92**, 042304 (2015).

[49] T. K. Unden, D. Louzon, M. Zwolak, W. H. Zurek and F. Jelezko, *Revealing the emergence of classicality using nitrogen-vacancy centers,* Physical Review Letters **123**, 140402 (2019).

[50] B. Tratzmiller, J. F. Haase, Z. Wang and M. B. Plenio, *Parallel selective nuclear-spin addressing for fast high-fidelity quantum gates,* Physical Review A **103**, 012607 (2021).

[51] S. S. Hegde, J. Zhang and D. Suter, *Efficient quantum gates for individual nuclear spin qubits by indirect control,* Physical Review Letters **124**, 220501 (2020).

[52] N. Zhao, J. Wrachtrup and R. B. Liu, *Dynamical decoupling design for identifying weakly coupled nuclear spins in a bath,* Physical Review A **90**, 032319 (2014).

[53] Z. Y. Wang, J. Casanova and M. B. Plenio, *Delayed entanglement echo for individual control of a large number of nuclear spins,* Nature Communications **8** (2017).

[54] J. Casanova, Z. Y. Wang and M. B. Plenio, *Arbitrary nuclear-spin gates in diamond mediated by a nitrogen-vacancy-center electron spin,* Physical Review A **96**, 032314 (2017).

[55] T. Gullion, D. B. Baker and M. S. Conradi, *New, compensated Carr-Purcell sequences,* Journal of Magnetic Resonance (1969) **89**, 479 (1990).

[56] J. R. Klauder and P. W. Anderson, *Spectral diffusion decay in spin resonance experiments,* Phys. Rev. **125**, 912 (1962).

[57] V. V. Dobrovitski, H. A. De Raedt, M. I. Katsnelson and B. N. Harmon, *Quantum Oscillations without Quantum Coherence,* Phys. Rev. Lett. **90**, 4 (2003).

[58] S. Stoupin and Y. V. Shvyd'ko, *Thermal expansion of diamond at low temperatures,* Phys. Rev. Lett. **104**, 085901 (2010).

[59] G. Davies, M. F. Hamer and W. C. Price, *Optical studies of the 1.945 ev vibronic band in diamond,* Proceedings of the Royal Society of London. A. Mathematical and Physical Sciences **348**, 285 (1976).

[60] A. Batalov *et al., Low temperature studies of the excited-state structure of negatively charged nitrogen-vacancy color centers in diamond,* Physical Review Letters **102**, 195506 (2009).

[61] H. Holloway, K. C. Hass, M. A. Tamor, T. R. Anthony and W. F. Banholzer, *Isotopic dependence of the lattice constant of diamond,* Physical Review B **44**, 7123 (1991).

[62] K. F. Sheberstov *et al., Excitation of singlet-triplet coherences in pairs of nearly-equivalent spins,* Physical Chemistry Chemical Physics **21**, 6087 (2019).

[63] J. A. Jones, *Quantum computing with NMR,* Progress in Nuclear Magnetic Resonance Spectroscopy **59**, 91 (2011).

[64] G. Pileio, ed., *Long-lived Nuclear Spin Order* (The Royal Society of Chemistry, 2020).

4

ENTANGLEMENT OF DARK ELECTRON-NUCLEAR SPIN DEFECTS IN DIAMOND

M.J. Degen*, S.J.H. Loenen*, H.P. Bartling, C.E. Bradley, A.L. Meinsma, M. Markham, D.J. Twitchen, T.H. Taminiau

A promising approach for multi-qubit quantum registers is to use optically addressable spins to control multiple dark electron-spin defects in the environment. While recent experiments have observed signatures of coherent interactions with such dark spins, it is an open challenge to realize the individual control required for quantum information processing. Here we demonstrate the heralded initialisation, control and entanglement of individual dark spins associated to multiple P1 centers, which are part of a spin bath surrounding a nitrogen-vacancy center in diamond. We realize projective measurements to prepare the multiple degrees of freedom of P1 centers - their Jahn-Teller axis, nuclear spin and charge state - and exploit these to selectively access multiple P1s in the bath. We develop control and single-shot readout of the nuclear and electron spin, and use this to demonstrate an entangled state of two P1 centers. These results provide a proof-of-principle towards using dark electron-nuclear spin defects as qubits for quantum sensing, computation and networks.

*Equally contributing authors.

The results of this chapter have been published in Nature Comm. **12**, 3470 (2021). The Supplementary Materials are not included in this thesis, but can be found online.

4.1. INTRODUCTION

Optically active defects in solids provide promising qubits for quantum sensing[1], quantum-information processing[2–4], quantum simulations[5,6] and quantum networks[7–9]. These defects, including the nitrogen-vacancy (NV) and silicon-vacancy (SiV) centers in diamond and various defects in silicon-carbide[10–12], combine long spin coherence times[4,13–18], high-quality control and readout[2–4,14,19–21], and a coherent optical interface[7–9,15,19,22].

Larger-scale systems can be realized by entangling multiple defects together through long-range optical network links[7–9] and through direct magnetic coupling, as demonstrated for a pair of ion-implanted NV centers[23,24]. The number of available spins can be further extended by controlling nuclear spins in the vicinity. Multi-qubit quantum registers[4,24–27], quantum error correction[2,3], enhanced sensing schemes[28], and entanglement distillation[29] have been realized using nuclear spins.

The ability to additionally control dark electron-spin defects that cannot be directly detected optically would open new opportunities. Examples are studying single defect dynamics[30], extended quantum registers, enhanced sensing protocols[28,31,32] and spin chains for quantum computation architectures[33–36]. Two pioneering experiments reported signals consistent with an NV center coupled to a single P1 center (a dark substitutional nitrogen defect)[37,38], but the absence of the expected P1 electron-spin resonance signal[39] and later results revealing identical signals due to NV-^{13}C couplings in combination with an excited state anti-crossing[40], make these assignments inconclusive. Recent experiments have revealed signatures of coherent interactions between NV centers and individual dark electron-spin defects, including P1 centers[41–43], N2 centers[44] and not-yet-assigned defects[31,45–49]. Those results have revealed the prospect of using dark spin defects as qubits. However, high-quality initialisation, measurement and control of multi-qubit quantum states is required to exploit such spins as a quantum resource.

Here we demonstrate the control and entanglement of individual P1 centers that are part of a bath surrounding an NV center in diamond (Fig. 4.1a). A key property of the P1 center is that, in addition to its electron spin, it exhibits three extra degrees of freedom: the Jahn-Teller axis, a nuclear spin, and the charge state[50–52]. Underlying our selective control of individual centers is the heralded preparation of specific configurations of these additional degrees of freedom for multiple P1 centers through projective measurements. In contrast, all previous experiments averaged over these additional degrees of freedom[41,42,53]. We use this capability to develop initialisation, single-shot readout and control of the electron and nuclear spin states of multiple P1s, and investigate their spin relaxation and coherence times. Finally, we demonstrate the potential of these dark spins as a qubit platform by realizing an entangled state between two P1 electron spins through their direct magnetic-dipole coupling.

4.2. A SPIN BATH WITH MULTIPLE DEGREES OF FREEDOM

We consider a bath of P1 centers surrounding a single NV center at 3.3 K (Fig. 4.1a). The diamond is isotopically purified with an estimated ^{13}C concentration of 0.01%. The

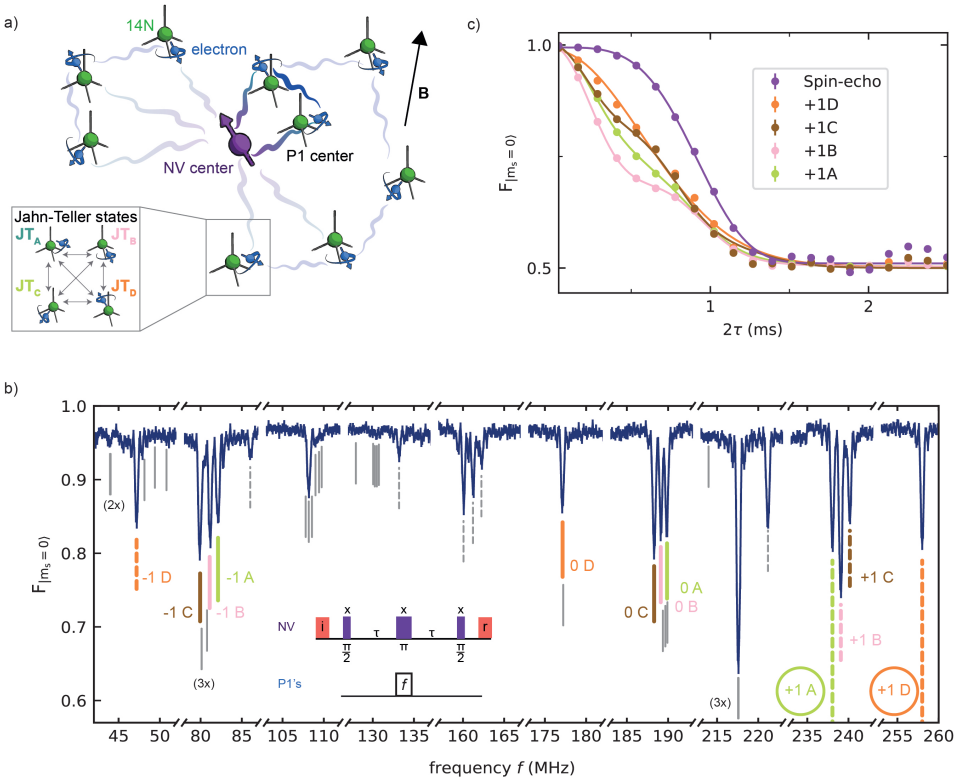

Figure 4.1: **DEER spectroscopy of a P1 spin bath. a)** We study a bath of P1 centers surrounding a single NV center. The state of each P1 center is defined by an electron spin (blue), a ^{14}N nuclear spin (green), and one of four JT axis, which can vary over time (see inset). **b)** DEER spectrum obtained by varying the frequency f (see inset). The NV is initialized in $m_s = 0$ via optical spin-pumping (i) and optically read out (r) at the end of the sequence (Methods). $F_{|m_s=0\rangle}$ is the fidelity of the final NV state with $m_s = 0$. The 12 main P1 electron-spin transitions are labelled by their nitrogen nuclear spin state and JT axis (colored lines). 11 isolated transitions (dashed lines) are used to fit the P1 Hamiltonian and all predicted transition frequencies are indicated (solid lines). In this work, we mainly use the circled transitions corresponding to $|+1,\mathrm{D}\rangle$ and $|+1,\mathrm{A}\rangle$. **c)** We apply a calibrated π pulse (Rabi frequency $\Omega = 250$ kHz) at a fixed frequency f, to selectively couple to P1 centers in the $|+1,i\rangle$ state ($i \in \{\mathrm{A,B,C,D}\}$) and vary the interaction time 2τ (see inset in b). From the fits we obtain a dephasing time $T_{2,\mathrm{DEER}}$ of 0.767(6), 0.756(7), 0.802(6) and 0.803(5) ms for the $|+1,i\rangle$ state with i corresponding to A,B,C and D respectively. A spin-echo (no pulse on P1 centers) is added for reference from which we obtain $T_{2,\mathrm{NV}} = 0.992(4)$ ms. Error bars are one standard deviation (Methods), with a typical value 4×10^{-3}, which is smaller than the data points. See Methods for the fit functions.

P1 concentration is estimated to be ~ 75 ppb (see Supplementary Note 5[54]). Three P1 charge states are known[51,52]. The experiments in this work detect the neutral charge state and do not generate signal for the positive and negative charge states. In addition to an electron spin ($S = 1/2$), the P1 center exhibits a ^{14}N nuclear spin ($I = 1$, 99.6% natural abundance) and a Jahn-Teller (JT) distortion, which results in four possible symmetry axes due to the elongation of one of the four N-C bonds[55]. Both the ^{14}N state and the JT axis generally fluctuate over time[56–58]. The Hamiltonian for a single neutrally-charged P1 defect in one of the four JT axis $i \in$ {A,B,C,D} is[50]:

$$H_{\mathbf{i},\mathrm{P1}} = \gamma_e \mathbf{B}\cdot\mathbf{S} + \gamma_n \mathbf{B}\cdot\mathbf{I} + \mathbf{I}\cdot\hat{\mathbf{P}}_\mathbf{i}\cdot\mathbf{I} + \mathbf{S}\cdot\hat{\mathbf{A}}_\mathbf{i}\cdot\mathbf{I}, \tag{4.1}$$

where γ_e (γ_n) is the electron (^{14}N) gyromagnetic ratio, $\mathbf{B}$ the external magnetic field vector, $\mathbf{S}$ and $\mathbf{I}$ are the electron spin-1/2 and nuclear spin-1 operator vectors, and $\hat{\mathbf{A}}_\mathbf{i}$ ($\hat{\mathbf{P}}_\mathbf{i}$) the hyperfine (quadrupole) tensor. We label the ^{14}N ($m_I \in \{-1, 0, +1\}$) and JT states as $|m_I, i\rangle$, and the electron spin states as $|\uparrow\rangle$ and $|\downarrow\rangle$. For convenience, we use the spin eigenstates as labels, while the actual eigenstates are, to some extent, mixtures of the ^{14}N and electron spin states.

We probe the bath surrounding the NV by double electron-electron resonance (DEER) spectroscopy[41,42,45,47,53]. The DEER sequence consists of a spin echo on the NV electron spin, which decouples it from the environment, plus a simultaneous π-pulse that selectively recouples resonant P1 centers. Figure 4.1b reveals a complex spectrum. The degeneracy of three of the JT axes is lifted by a purposely slightly tilted magnetic field with respect to the NV axis ($\theta \approx 4°$). In combination with the long P1 dephasing time ($T_2^* \sim$ 50 µs, see below) this enables us to resolve all 12 main P1 electron-spin transitions – for four JT axes and three ^{14}N states – and selectively address at least one transition for each JT axis.

Several additional transitions are visible due to mixing of the electron and nuclear spin in the used magnetic field regime ($\gamma_e|\mathbf{B}| \sim A_\parallel, A_\perp$). We select 11 well-isolated transitions to fit the P1 Hamiltonian parameters and obtain $\{A_\parallel, A_\perp, P_\parallel\}$ = {114.0264(9), 81.312(1), -3.9770(9)} MHz and $\mathbf{B}$ = {2.437(2), 1.703(1), 45.5553(5)} G (Supplementary Note 4[54]), closely matching ensemble ESR measurements[59]. The experimental spectrum is well described by the 60 P1 transitions for these parameters. No signal is observed at the bare electron Larmor frequency (≈ 128 MHz), confirming that the P1 centers form the dominant electron spin bath.

To probe the coupling strength of the P1 bath to the NV, we sweep the interaction time in the DEER sequences (Fig. 4.1c). The curves for the different $|+1, i\rangle$ states show oscillatory features, providing a first indication of an underlying microscopic structure of the P1 bath. However, like all previous experiments[41,42,53], these measurements are a complex averaging over ^{14}N, JT and charge states for all the P1 centers, which obscures the underlying structure and hinders control over individual spins.

4.3. DETECTING AND PREPARING SINGLE P1 CENTERS

To investigate the microscopic structure of the bath we repeatedly apply the DEER sequence and analyze the correlations in the measurement outcomes[30]. Figure 4.2a shows

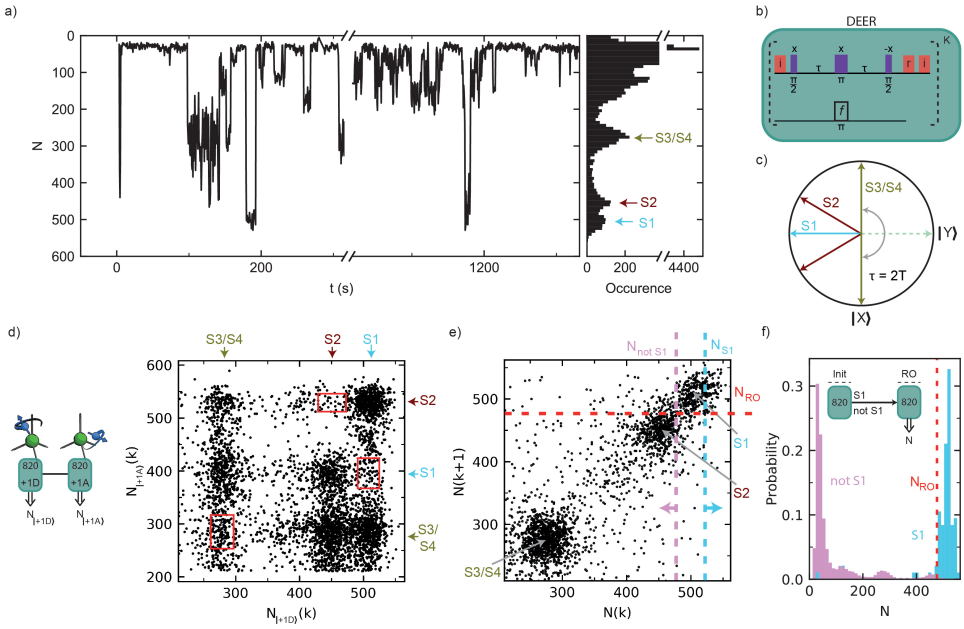

Figure 4.2: **Detection and preparation of single P1 centers. a)** Typical time trace for the DEER signal for $|+1,\mathrm{D}\rangle$. N is the total number of $m_s = 0$ NV readout outcomes in $K = 820$ repetitions of the sequence (see (b)). The discrete jumps and corresponding peaks in the histogram of the full time trace (~ 6 h, right) indicate that several individual P1s are observed (S1, S2 and S3/S4). **b)** Sequence for K repeated DEER measurements. Note that the phase of the final $\pi/2$ pulse is along -x and thus the signal is inverted as compared to Fig. 4.1b. Optical initialisation (i) and readout (r) of the NV electron are indicated with red pulses. **c)** XY-plane of the NV-spin Bloch sphere before the second $\pi/2$ pulse of a DEER measurement, with the NV initialised along +z at the start. The NV spin picks up phase depending on which nearby P1 centers are in the targeted $|+1,\mathrm{D}\rangle$ state. Because the NV spin is effectively measured along the y-axis, this sequence is insensitive to the P1 electron spin state. We discuss the case of two P1 centers simultaneously in the same state, which happens with a small probability and yields a distinct signal, in Supplementary Note 2C[54]. **d)** Cross-correlation of two consecutive DEER measurements for $|+1,\mathrm{D}\rangle$ (K=820) and $|+1,\mathrm{A}\rangle$ (K=820). Three areas (red boxes, Supplementary Note 8[54]) show an anti-correlation associated to S1, S2, and S3/S4, in agreement with the assignment of discrete P1 centers. Left: sequence for the two consecutive DEER measurements (green blocks). Double lined arrows indicate measurement outcomes. **e)** Correlation plot for consecutive measurement outcomes N(k) and N($k+1$), both for $|+1,\mathrm{D}\rangle$. Dashed lines are the thresholds used to prepare (vertical) and read out (horizontal) the JT and ^{14}N state in panel f. We use $N_{\mathrm{S1}} > 522$ to prepare S1 in $|+1,\mathrm{D}\rangle$, and S2 and S3/S4 in any other state. The condition $N_{\mathrm{notS1}} \leq 477$ prepares a mixture of all other possibilities. A threshold $N_{\mathrm{RO}} = 477$ distinguishes between those two cases in readout. **f)** Conditional probability distributions for both preparations, demonstrating initialisation and single-shot readout of the ^{14}N and JT state of S1. Inset: experimental sequence. Labelled horizontal arrows indicate conditions for passing the initialisation measurement (init).

a typical time trace for continuous measurement, in which groups of K=820 measurements are binned together (see Fig. 4.2b for the sequence). We observe discrete jumps in the signal that indicate individual P1 centers jumping in and out of the $|+1,\mathrm{D}\rangle$ state. The resulting histogram (Fig. 4.2a) reveals multiple discrete peaks that indicate several P1 centers with different coupling strengths to the NV center, as schematically illustrated in Fig. 4.2c. We tentatively assign four P1 centers S1, S2, S3 and S4 to these peaks.

We verify whether these peaks originate from single P1 centers by performing cross-correlation measurements. We first apply a DEER measurement on $|+1,\mathrm{D}\rangle$ followed by a measurement on $|+1,\mathrm{A}\rangle$ (Fig. 4.2d). For a single P1, observing it in $|+1,\mathrm{D}\rangle$ would make it unlikely to subsequently also find it in state $|+1,\mathrm{A}\rangle$. We observe three regions of such anti-correlation (red rectangles in Fig. 4.2d). We define the correlation:

$$C = \frac{\mathrm{P}(N_{\mathrm{A}}^{\mathrm{min}} \leq N_{|+1,\mathrm{A}\rangle} \leq N_{\mathrm{A}}^{\mathrm{max}} \,\big|\, N_{\mathrm{D}}^{\mathrm{min}} \leq N_{|+1,\mathrm{D}\rangle} \leq N_{\mathrm{D}}^{\mathrm{max})}}{\mathrm{P}(N_{\mathrm{A}}^{\mathrm{min}} \leq N_{|+1,\mathrm{A}\rangle} \leq N_{\mathrm{A}}^{\mathrm{max})}}, \tag{4.2}$$

where $N_{\mathrm{A}}^{\mathrm{min}}$, $N_{\mathrm{A}}^{\mathrm{max}}$, $N_{\mathrm{D}}^{\mathrm{min}}$ and $N_{\mathrm{D}}^{\mathrm{max}}$ define the region, and where $\mathrm{P}(X)$ is the probability that X is satisfied. Assuming that the states of different P1 centers are uncorrelated, a value $C < 0.5$ indicates that the signal observed in both the DEER sequences on $|+1,\mathrm{A}\rangle$ and $|+1,\mathrm{D}\rangle$ is associated to a single P1 center, while $C < 2/3$ indicates 1 or 2 centers (Supplementary Note 8[54]).

For the three areas we find $C = 0.40(5)$, $0.22(4)$ and $0.47(5)$ for S1, S2 and S3/S4 respectively. These correlations corroborate the assignments of a single P1 to both S1 and S2 and one or two P1s for S3/S4 (the result is within one standard deviation from 0.5). Additionally, these results reveal which signals for different $|+1,i\rangle$ states belong to which P1 centers. This is non-trivial because the NV-P1 dipolar coupling varies with the JT axis, as exemplified in Fig. 4.2d (see Supplementary Note 3[54] for a theoretical treatment).

Next, we develop single-shot readout and heralded initialisation of the ^{14}N and JT state of individual P1 centers. For this, we represent the time trace data (Fig. 4.2a) as a correlation plot between subsequent measurements k and $k+1$ (Fig. 4.2e)[60–62]. We bin the outcomes using K=820 repetitions, where K is chosen as a trade-off between the ability to distinguish S1 from S2 and the disturbance of the state due to the repeated measurements (1/e value of $\sim 1.5 \times 10^4$ repetitions, see Supplementary Note 6[54]). Separated regions are observed for the different P1 centers. Therefore, by setting threshold conditions, one can use the DEER measurement as a projective measurement to initialize or readout the $|m_I, i\rangle$ state of selected P1 centers, which we illustrate for S1.

First, we set an initialisation condition $\mathrm{N(k)} > N_{\mathrm{S1}}$ (blue dashed line) to herald that S1 is initialized in the $|+1,\mathrm{D}\rangle$ state and that S2, S3/S4 are not in that state. We use $\mathrm{N(k)} \leq N_{\mathrm{notS1}}$ to prepare a mixture of all other other possibilities. The resulting conditional probability distributions of $\mathrm{N(k+1)}$ are shown in Fig. 4.2f. Second, we set a threshold for state readout N_{RO} to distinguish between the two cases. We then optimize N_{S1} for the trade-off between the success rate and signal contrast, and find a combined initialisation and readout fidelity $F = 0.96(1)$ (see Methods). Other states can be prepared and read out by setting different conditions (Supplementary Note 8[54]).

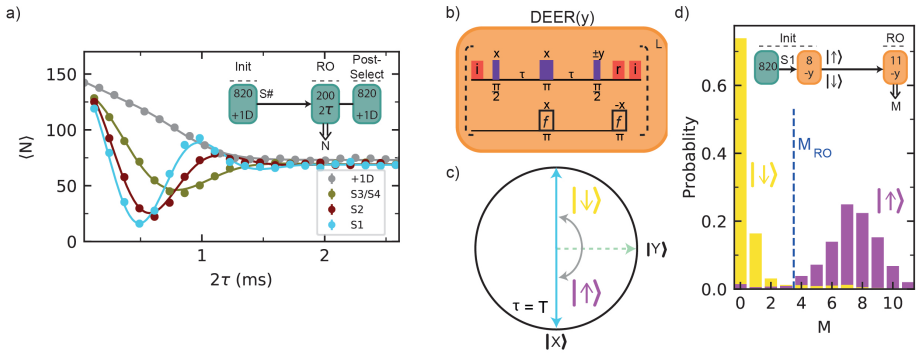

Figure 4.3: **Electron spin initialisation and readout. a)** Measuring the NV-P1 coupling strength. We initialize S1, S2, or S3/S4 in $|+1,\mathrm{D}\rangle$ and vary the interaction time 2τ of a DEER sequence. $\langle N\rangle$ is the mean of the number of NV $m_s = 0$ outcomes for K=200 repetitions. To improve the signal, the results are post-selected on again obtaining $|+1,\mathrm{D}\rangle$. Error bars are one standard deviation (Methods), with a typical value 1, which is smaller than the data points. Grey: without P1 initialisation (data from Fig. 4.1c). **b)** DEER(y) sequence with the readout basis rotated by $\pi/2$ compared to the DEER sequence and $\tau = \pi/2\nu$. An additional π pulse is added to revert the P1 electron spin. Optical initialisation (i) and readout (r) of the NV electron are indicated with red pulses. **c)** XY-plane of the NV Bloch sphere before the second $\pi/2$ pulse, illustrating that the DEER(y) sequence measures the P1 electron spin state (shown for positive NV-P1 coupling). **d)** Single-shot readout of the S1 electron spin. After preparation in $|+1,\mathrm{D}\rangle$, the electron spin is initialized through a DEER(y) measurement (L=8) with thresholds $M_{|\uparrow\rangle}$ (> 6) and $M_{|\downarrow\rangle}$ (≤1). Shown are the conditional probability distributions for a subsequent DEER(y) measurement with L=11 and the readout threshold M_{RO}.

4.4. CONTROL OF THE ELECTRON AND NUCLEAR SPIN

To control the electron spin of individual P1 centers, we first determine the effective dipolar NV-P1 coupling. We prepare, for instance, S1 in $|+1,\mathrm{D}\rangle$ and perform a DEER measurement in which we sweep the interaction time (Fig. 4.3a). By doing so, we selectively couple the NV to S1, while decoupling it from S2 and S3/S4, as well as from all bath spins that are not in $|+1,\mathrm{D}\rangle$. By applying this method we find effective dipolar coupling constants ν of $2\pi\cdot1.910(5)$, $2\pi\cdot1.563(6)$ and $2\pi\cdot1.012(8)$ kHz for S1, S2 and S3/S4 respectively. Note that, if the signal for S3/S4 originates from two P1 centers, the initialisation sequence prepares either S3 or S4 in each repetition of the experiment.

We initialize and measure the electron spin state of the P1 centers through a sequence with a modified readout axis that we label DEER(y) (Fig. 4.3b). Unlike the DEER sequence, this sequence is sensitive to the P1 electron spin state. After initializing the charge, nuclear spin and JT axis, and setting the interaction time $\tau \approx \pi/(2\cdot\nu)$, the DEER(y) sequence projectively measures the spin state of a selected P1 center (Fig. 4.3c). We first characterize the P1 electron spin relaxation under repeated application of the measurement and find a 1/e value of ~250 repetitions (Supplementary Note 4[54]). We then optimize the number of repetitions and the initialisation and readout thresholds to obtain a combined initialisation and single-shot readout fidelity for the S1 electron spin of $F_{|\uparrow\rangle/|\downarrow\rangle}$ = 0.95(1) (Fig. 4.3d).

We now show that we can coherently control the P1 nitrogen nuclear spin (Fig. 4.4a).

To speed up the experiment, we choose a shorter initialisation sequence that prepares either S1 or S2 in the $|+1,\mathrm{D}\rangle$ state (K=420, Methods). We then apply a radio-frequency (RF) pulse that is resonant with the $m_I = +1 \leftrightarrow 0$ transition if the electron spin is in the $|\uparrow\rangle$ state. Varying the RF pulse length reveals a coherent Rabi oscillation. Because the P1 electron spin is not polarized, the RF pulse is on resonance 50% of the time and the amplitude of the Rabi oscillation is half its maximum.

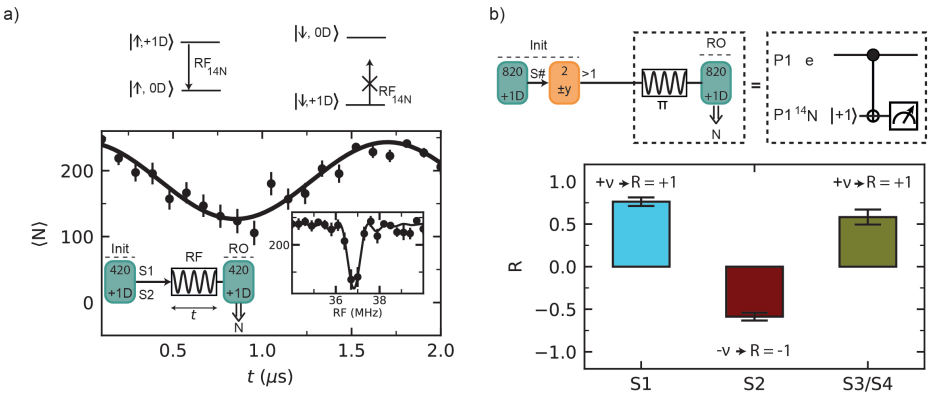

Figure 4.4: **Nitrogen nuclear spin control and NV-P1 coupling sign. a)** ^{14}N Rabi oscillation. Top: energy levels of the P1 electron spin in the {0D, +1D} subspace. Bottom: either S1 or S2 is prepared in $|+1,\mathrm{D}\rangle$ and the length t of a pulse at frequency RF = $\mathrm{RF}_{14\mathrm{N}}$ = 36.8 MHz is varied. The nitrogen nuclear spin is driven conditionally on the electron spin state. Inset: NMR spectrum obtained by varying the frequency RF for a fixed pulse duration t. **b)** We use the ^{14}N spin to determine the sign of the NV-P1 coupling. First, we prepare a selected P1 center (K=820) and initialise its electron spin (L=2). Second, we apply a π pulse at $\mathrm{RF}_{14\mathrm{N}}$, which implements an electron controlled $\mathrm{CNOT}_{\mathrm{e,N}}$ (see level structure in (a)). The coupling sign to the NV determines the P1 electron-spin state, and, in turn, the final ^{14}N state. Finally, we measure the fidelity with the $^{14}\mathrm{N}\,|+1\rangle$ state for two opposite electron spin initialisations (+y and -y final $\pi/2$ pulse of DEER(y)). The normalized difference R of these measurements reveals the sign of the coupling (see Methods). All error bars indicate one statistical standard deviation.

We use the combined control over the electron and nuclear spin to determine the sign of the NV-P1 couplings (Fig. 4.4b). First, we initialize the ^{14}N, JT axis and electron spin state of a P1 center. Because the DEER(y) sequence is sensitive to the sign of the coupling (Fig. 4.3c), the sign affects whether the P1 electron spin is prepared in $|\uparrow\rangle$ or $|\downarrow\rangle$. Second, we measure the P1 electron spin through the ^{14}N nuclear spin. We apply an RF pulse, which implements an electron-controlled CNOT gate on the nuclear spin (see Fig. 4.4a). Subsequently reading out the ^{14}N spin reveals the electron spin state and therefore the sign of the NV-P1 coupling. We plot the normalized difference R (Methods) for two different initialisation sequences that prepare the electron spin in opposite states. The results show that NV-P1 coupling is positive for the cases of S1 and S3/S4, but negative for S2 (Fig. 4.4b). If S3/S4 consists of two P1 centers, then they have the same coupling sign to the NV.

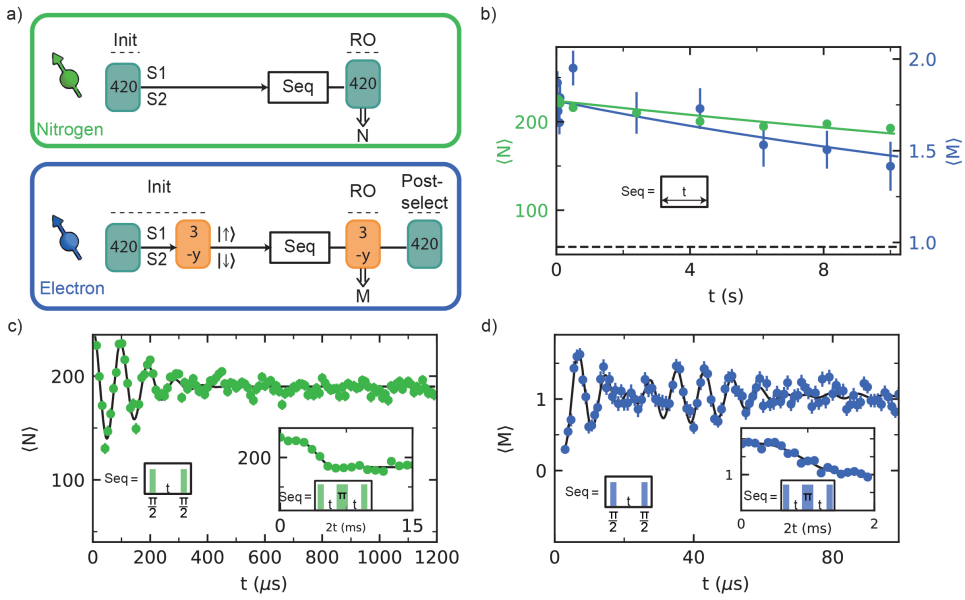

Figure 4.5: **Coherence and timescales. a)** Sequence for initialisation of either S1 or S2 in $|+1,\mathrm{D}\rangle$ (top). Sequence for initializing all degrees of freedom of either S1 or S2, including the electron spin state (bottom). These sequences are used in b, c and d. **b)** Relaxation of a combination of: the nitrogen nuclear spin state, JT axis and charge state (green), and only the electron spin state (blue). We fit (solid lines) both curves to $o + A_0 e^{-t/T}$, where o is fixed to the uninitialized mean value (dashed line) and obtain $T{=}T_{|+1,\mathrm{D}\rangle}$ = 40(4) s and $T{=}T_1$ = 21(7) s. **c)** Ramsey experiment on the nitrogen nuclear spin. We fit the data (solid line) and obtain $T^*_{2\mathrm{N}}$ = 0.201(9) ms. (inset) Nitrogen nuclear spin-echo experiment. From the fit we obtain $T_{2\mathrm{N}}$ = 4.2(2) ms. **d)** Ramsey experiment on the electron spin. A Gaussian decay (T^*_{2e} = 50(3) μs) with a single beating is observed, suggesting a dipolar coupling between S1 and S2. (inset) Electron spin-echo experiment. From the fit we obtain $T_{2\mathrm{e}}$ = 1.00(4) ms. See Methods for complete fit functions and obtained parameters. All error bars indicate one statistical standard deviation.

4.5. SPIN COHERENCE AND RELAXATION

To assess the potential of P1 centers as qubits, we measure their coherence times. First, we investigate the relaxation times. We prepare either S1 or S2 in $|+1,\mathrm{D}\rangle$, the NV electron spin in $m_s = 0$, and vary the waiting time t before reading out the same state (Fig. 4.5a). This sequence measures the relaxation of a combination of the nitrogen nuclear spin state, JT axis and charge state, averaged over S1 and S2. An exponential fit gives a relaxation time of $T_{|+1,\mathrm{D}\rangle} = 40(4)$ s (Fig. 4.5b, green).

We measure the longitudinal relaxation of the electron spin by preparing either $|\uparrow\rangle$ (S1) or $|\downarrow\rangle$ (S2) (Fig. 4.5a). We post-select on the $|+1,\mathrm{D}\rangle$ state at the end of the sequence to exclude effects due to relaxation from $|+1,\mathrm{D}\rangle$, and find $T_{1\mathrm{e}} = 21(7)$ s. The observed electron spin relaxation time is longer than expected from the typical P1-P1 couplings in the bath (order of 1 kHz). A potential explanation is that flip-flops are suppressed due to couplings to neighbouring P1 centers, which our heralding protocol preferentially prepares in other $|m_I, i\rangle$ states. Below, we will show that S1 and S2 have a strong mutual coupling, which could shift them off resonance from the rest of the bath.

Second, we investigate the electron and nitrogen nuclear spin coherence via Ramsey and spin-echo experiments (Figs. 4.5c and d). We find $T^*_{2\mathrm{e}} = 50(3)$ µs and $T_{2\mathrm{e}} = 1.00(4)$ ms for the electron spin, and $T^*_{2\mathrm{N}} = 0.201(9)$ ms and $T_{2\mathrm{N}} = 4.2(2)$ ms for the nitrogen nuclear spin. The ratio of dephasing times for the electron and nitrogen nuclear spins is ~4, while the difference in bare gyromagnetic ratios is a factor ~9000. The difference is partially explained by electron-nuclear spin mixing due to the large value of $A_\perp$, which changes the effective gyromagnetic ratios of the nitrogen nuclear spin and electron spin. Based on this, a ratio of dephasing times of 12.6 is expected (see Supplementary Note 13[54]). The remaining additional decoherence of the nitrogen nuclear spin is currently not understood.

The electron Ramsey experiment shows a beating frequency of 21.5(1) kHz (Fig. 4.5d). As the data is an average over S1 and S2, this suggests an interaction between these two P1 centers. Note that, whilst the signal is expected to contain 11 frequencies due to the different Jahn-Teller and nitrogen nuclear spin state combinations, the observation of a single beating frequency indicates that these are not resolved. Next, we will confirm this hypothesis and use the coupling between S1 and S2 to demonstrate an entangled state of two P1 centers.

4.6. ENTANGLEMENT OF TWO DARK ELECTRON SPINS

Thus far we have shown selective initialisation, control and single-shot readout of individual P1 centers within the bath. We now combine all these results to realize coherent interactions and entanglement between the electron spins of two P1 centers.

We first sequentially initialize both P1 centers (Fig. 4.6a). To overcome the small probability for both P1 centers to be in the desired state, we use fast logic to identify failed attempts in real-time and actively reset the states (Methods). We prepare S1 in the $|+1,\mathrm{D}\rangle$ state and S2 in the $|+1,\mathrm{A}\rangle$ state. By initializing the two P1 centers in these different states, we ensure that the spin transitions are strongly detuned, so that mutual flip-flops are suppressed and the interaction is effectively of the form $S_z S_z$. We then se-

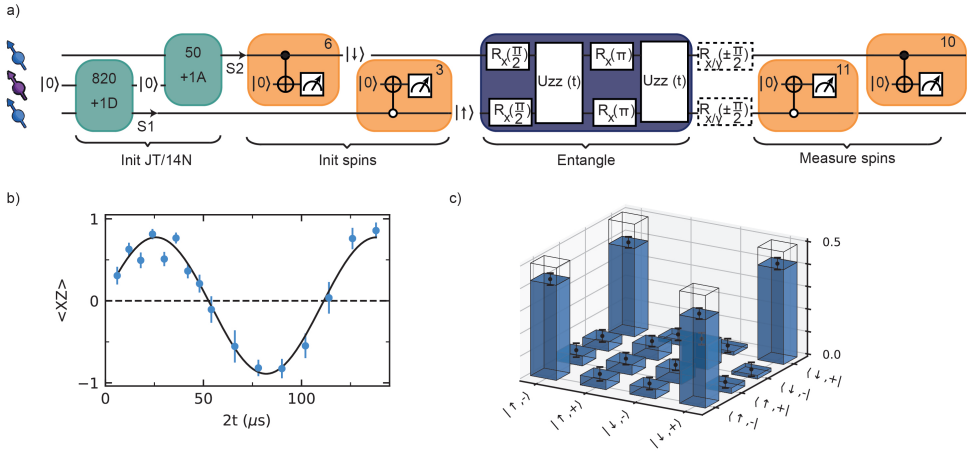

Figure 4.6: **Entanglement between two P1s. a)** Experimental sequence to measure coupling and generate entanglement between S1 and S2. DEER measurements initialize the JT axis and nitrogen state of S1 and S2 (K=820, 50 and $f = f_{+1D}$, f_{+1A}), followed by DEER(y) measurements to initialize their electron spin states (L=6, 3). Two $\pi/2$ pulses and an evolution for time $2t$ under a double echo implements the S_zS_z interaction with both spins in the equatorial plane of the Bloch sphere. This is followed by single qubit gates (dashed boxes) for full 2-qubit state tomography and two final DEER(y) measurements for electron spin readout. We apply an additional initial sequence ($K = 5$, f_{+1A}) to speed up the experiment (not shown in sequence, see Supplementary Note 15[54]). **b)** The coherent oscillation of the $\langle XZ\rangle$ as a function of interaction time $2t$ demonstrates a dipolar coupling J = -2π·17.8(5) kHz between S1 and S2. **c)** Density matrix of the S1 and S2 electron spins after applying the sequence as shown in (a) for $2t = \pi/J$. The fidelity with the target state is $F = 0.81(5)$. Transparent bars indicate the density matrix for the target state $|\Psi\rangle$. All error bars indicate one statistical standard deviation.

quentially initialize both electron spins to obtain the initial state $|\uparrow\rangle_{S1}|\downarrow\rangle_{S2}$. As consecutive measurements can disturb the previously prepared degrees of freedom, the number of repetitions in each step is optimized for high total initialisation fidelity and success rate (Supplementary Note 15C[54]).

Next, we characterize the dipolar coupling J between S1 and S2 (Fig. 4.6b). We apply two $\pi/2$ pulses to prepare both spins in a superposition. We then apply simultaneous echo pulses on each spin. This double echo sequence decouples the spins from all P1s that are not in $|+1,\mathrm{D}\rangle$ or $|+1,\mathrm{A}\rangle$, as well as from the ^{13}C nuclear spin bath and other noise sources. This way, the coherence of both spins is extended from T_2^* to T_2, while their mutual interaction is maintained. We determine the coupling J by letting the spins evolve and measuring $\langle XZ\rangle$ as a function of the interaction time $2t$ through a consecutive measurement of both electron spins (Fig. 4.6b). From this curve we extract a dipolar coupling $J = -2\pi \cdot 17.8(5)$ kHz between S1 in $|+1,\mathrm{D}\rangle$ and S2 in $|+1,\mathrm{A}\rangle$.

Finally, we create an entangled state of S1 and S2 using the sequence in Fig. 4.6a. We set the interaction time $2t = \pi/J$ so that a 2-qubit CPHASE gate is performed. The final state is (see Supplementary Note 14[54]):

$$|\Psi\rangle = \frac{|\uparrow\rangle_{S1}|-\rangle_{S2} + |\downarrow\rangle_{S1}|+\rangle_{S2}}{\sqrt{2}}, \tag{4.3}$$

with $|\pm\rangle = \frac{|\uparrow\rangle \pm |\downarrow\rangle}{\sqrt{2}}$. We then perform full 2-qubit state tomography and reconstruct the density matrix as shown in Fig. 4.6c. The resulting state fidelity with the ideal state is $F = (1 + \langle XZ\rangle - \langle ZX\rangle - \langle YY\rangle)/4 = 0.81(4)$. The fact that $F > 0.5$ is a witness for two-qubit entanglement[63]. The coherence time during the echo sequence (~ 700 μs, see Methods) is long compared to π/J (~ 28 μs), and thus the dephasing during the 2-qubit gate is estimated to be at most 2%. Therefore we expect the main sources of infidelity to be the final sequential single-shot readout of the two electron spin states – no readout correction is made – and the sequential initialisation of the two electron spins (Supplementary Note 15[54]).

4.7. DISCUSSION

In conclusion, we have developed initialisation, control, single-shot readout, and entanglement of multiple individual P1 centers that are part of a bath surrounding an NV center. These results establish the P1 center as a promising qubit platform. Our methods to control individual dark spins can enable enhanced sensing schemes based on entanglement[28,31,32], as well as electron spin chains for quantum computation architectures[33–36]. Larger quantum registers might be formed by using P1 centers to control nearby ^{13}C nuclear spins with recently developed quantum gates[4]. Such nuclear spin qubits are connected to the optically active defect only indirectly through the P1 electron spin, and could provide isolated robust quantum memories for quantum networks[64]. Finally, these results create new opportunities to investigate the physics of decoherence, spin diffusion and Jahn-Teller dynamics[30] in complex spin baths with control over the microscopic single-spin dynamics.

4.8. METHODS

4.8.1. SAMPLE

We use a single nitrogen vacancy (NV) center in a homoepitaxially chemical-vapor-deposition (CVD) grown diamond with a ⟨100⟩ crystal orientation (Element Six). The diamond is isotopically purified to an approximate 0.01% abundance of ^{13}C. The nitrogen concentration is ~75 parts per billion, see Supplementary Note 5 [54]. To enhance the collection efficiency a solid-immersion lens was fabricated on top of the NV center [65,66] and a single-layer aluminum-oxide anti-reflection coating was deposited [67,68].

4.8.2. SETUP

The experiments are performed at 3.3 Kelvin (Montana Cryostation) with the magnetic field **B** applied using three permanent magnets on motorized linear translation stages (UTS100PP) outside of the cryostat housing. We realize a long relaxation time for the NV electron spin ($T_1 > 30$ s) in combination with fast NV spin operations (peak Rabi frequency ~ 26 MHz) and readout/initialisation (~ 40 µs/100 µs), by minimizing noise and background from the microwave and optical controls [13]. Amplifier (AR 20S1G4) noise is suppressed by a fast microwave switch (TriQuint TGS2355-SM). Video leakage noise generated by the switch is filtered with a high pass filter.

4.8.3. ERROR ANALYSIS

The data presented in this work is either a probability derived from the measurements, the mean of a distribution, or a quantity derived from those. For probabilities, a binomial error analysis is used, where p is the probability and $\sigma = \sqrt{p \cdot (1-p)/Q}$, Q being the number of measured binary values. For the mean μ of a distribution, σ_μ is calculated as $\sigma/\sqrt{Q}$, where σ is the square root average of the squared deviations from the mean and Q is the number of measurements. Uncertainties on all quantities derived from a probability or a mean are calculated using error propagation.

4.8.4. NV SPIN CONTROL AND READOUT

We use Hermite pulse envelopes [69,70] to obtain effective microwave pulses without initialisation of the intrinsic ^{14}N nuclear spin of the NV. We initialize and read out the NV electron spin through spin selective resonant excitation ($F = 0.850(5)$) [65]. Laser pulses are generated by acoustic optical modulators (637 nm Toptica DL Pro, for spin pumping and New Focus TLB-6704-P for single-shot spin readout) or by direct current modulation (515 nm laser, Cobolt MLD - for charge state control, and scrambling the P1 center state, see Supplementary Note 7 [54]). We place two modulators in series (Gooch and Housego Fibre Q) for an improved on/off ratio for the 637 nm lasers.

4.8.5. MAGNETIC FIELD STABILIZATION

During several of the experiments we actively stabilize the magnetic field via a feedback loop to one of the translation stages. The feedback signal is obtained from interleaved measurements of the NV $|0\rangle \leftrightarrow |-1\rangle$ transition frequency. We use the P1 bath as a three-

axis magnetometer to verify the stability of the magnetic field during this protocol (see Supplementary Note 11[54]), and find a magnetic field that is stable to <3 mG along **z** and <20 mG along the **x**, **y** directions.

4.8.6. HERALDED INITIALIZATION PROTOCOLS

Initialisation of the P1 ^{14}N spin, JT axis, charge and electron spin states is achieved by heralded preparation. Before starting an experimental sequence, we perform a set of measurements that, given certain outcomes, signals that the system is in the desired state.

A challenge is that the probability for the system to be in a given desired state is low, especially in experiments with multiple P1 centers (e.g. Fig. 4.6). We realize fast initialization by combining the heralded preparation with fast logic (ADwin-Pro II) to identify unsuccessful attempts in real time and then actively reset the system to a random state. This way each step is performed only if all previous steps were successful, and one avoids being trapped in an undesired state.

To reset the P1 centers to a random state, we use photoexcitation[71] of the P1s. We apply a ~5 μs 515 nm laser pulse to scramble the ^{14}N, JT and charge states of P1 centers. See Supplementary Note 7[54] for details and the optimization procedure.

The most time-consuming step is the selective initialization of the Jahn-Teller and ^{14}N spin states, as $K = 820$ repetitions are required to distinguish the signals from the P1 centers (S1, S2 and S3/S4). However, cases for which none of these P1 centers are in the desired state can be identified already after a few repetitions (Supplementary Note 7[54]). So after $K = 5$ repetitions we infer the likelihood for the desired configuration and use fast logic to determine whether to apply a new optical reset pulse or continue with the full sequence ($K = 820$). This procedure significantly speeds up the experiments (Supplementary Note 7[54]). For creating the entangled state (Fig. 4.6) we use a more extensive procedure, which is detailed in Supplementary Note 15C[54].

In the experiments in Figs. 4.4a and 4.5, we take an alternative approach to speed up the experiments by using a shorter initialisation sequence ($K = 420$) that does not distinguish between S1 and S2. Such a sequence prepares either S1 or S2, and the resulting data is an average over the two cases. Note that this method cannot be used in experiments where a selective initialization is required (e.g. Fig. 4.3, Fig. 4.4b, Fig. 4.6).

The optimization of the heralded initialization fidelities are discussed in Supplementary Note 15[54].

4.8.7. INITIALISATION AND SINGLE-SHOT READOUT FIDELITY

We define the combined initialisation and readout fidelity for S1 in $|+1, \mathrm{D}\rangle$ and S2, S3/S4 not in that state as

$$F_{\mathrm{S1}} = \mathrm{P}(\mathrm{N}(k+1) > N_{\mathrm{RO}} | \mathrm{N}(k) > N_{\mathrm{S1}}), \tag{4.4}$$

whereas for a mixture of all other possibilities we define

$$F_{\mathrm{notS1}} = \mathrm{P}(\mathrm{N}(k+1) \leq N_{\mathrm{RO}} | \mathrm{N}(k) \leq N_{\mathrm{notS1}}). \tag{4.5}$$

In both cases $P(X|Y)$ is the probability to obtain X given Y. We then take the average fidelity of these two cases:

$$F = \frac{F_{\mathrm{S1}} + F_{\mathrm{notS1}}}{2}. \tag{4.6}$$

We initialize and measure the electron spin state of P1 centers through a DEER(y) sequence following initialisation of the $|+1,\mathrm{D}\rangle$ state. Similarly, we use the correlation of consecutive measurements $\mathrm{M}(k)$ and $\mathrm{M}(k+1)$ to determine the combined initialisation and readout fidelity $F_{|\uparrow\rangle/|\downarrow\rangle}$. First, we define the fidelity for $|\uparrow\rangle$ as

$$F_{|\uparrow\rangle} = \mathrm{P}(\mathrm{M}(k+1) > M_{\mathrm{RO}} | \mathrm{M}(k) > M_{|\uparrow\rangle}), \tag{4.7}$$

and the fidelity for $|\downarrow\rangle$ as

$$F_{|\downarrow\rangle} = \mathrm{P}(\mathrm{M}(k+1) \leq M_{\mathrm{RO}} | \mathrm{M}(k) \leq M_{|\downarrow\rangle}). \tag{4.8}$$

Finally, the average combined initialisation and readout fidelity is given as

$$F_{|\uparrow\rangle/|\downarrow\rangle} = \frac{F_{|\uparrow\rangle} + F_{|\downarrow\rangle}}{2}. \tag{4.9}$$

For a description of the optimization of the single-shot readout fidelities, we refer to Supplementary Note 15[54].

4.8.8. DATA ANALYSIS

The DEER measurements in Fig. 4.1c are fitted to:

$$a_0 + A_0 \cdot \mathrm{Exp}[-(2\tau/T_{2,\mathrm{DEER}})^2] \cdot (1 + B_0 \cos(\omega \cdot \tau)) \tag{4.10}$$

from which we find $T_{2,\mathrm{DEER}}$ of 0.767(6), 0.756(7), 0.802(6) and 0.803(5) ms for $|+1,\mathrm{A}\rangle$, $|+1,\mathrm{B}\rangle$, $|+1,\mathrm{C}\rangle$ and $|+1,\mathrm{D}\rangle$, respectively. The obtained values for ω are $2\pi\cdot$2.12(5), $2\pi\cdot$2.14(3) and $2\pi\cdot$2.78(6) kHz with corresponding amplitudes B_0 of 0.105(5), 0.218(7), and 0.073(4) for $|+1,\mathrm{A}\rangle$, $|+1,\mathrm{B}\rangle$ and $|+1,\mathrm{C}\rangle$, respectively. For $|+1,\mathrm{D}\rangle$ we fix $B_0 = 0$.

The DEER measurements with P1 initialisation (Fig. 4.3a) and the P1 nitrogen nuclear spin Ramsey (Fig. 4.5c) are fitted to:

$$A_1 \cdot e^{-(t/T)^2}(\cos(\nu \cdot t/2)) + a_1. \tag{4.11}$$

For the dephasing time during the DEER sequence (here $t = 2\tau$) we find T = 0.893(5), 0.763(8) and 0.790(8) ms for S1, S2 and S3/S4 respectively. The obtained respective dipolar coupling constants ν are $2\pi\cdot$1.894(3), $2\pi\cdot$1.572(6) and $2\pi\cdot$1.001(6) kHz. For the P1 nitrogen nuclear spin Ramsey we find a dephasing time of $T = T^*_{2\mathrm{N}}$ = 0.201(9) ms.

Spin-echo experiments (Fig. 4.1c and Fig. 4.5) are fitted to

$$A_2 \cdot e^{-(t/T)^n} + a_2. \tag{4.12}$$

For the NV spin-echo (Fig. 4.1c), $T = T_2$ = 0.992(4) ms with n = 3.91(7). For the P1 nitrogen nuclear spin and electron (insets of Figure 4.5c,d) T is $T_{2\mathrm{N}}$ = 4.2(2) ms or T_{2e} = 1.00(4) ms with the exponents n = 3.9(8) and n = 3.1(5), respectively.

The Ramsey signal for the P1 electron spin in Fig. 4.5d is fitted to a sum of two frequencies with a Gaussian decay according to:

$$a_3 + e^{-(t/T_{2,e}^*)^2} \cdot \sum_{j=1}^{2} (A_j \cos\Big((f_{\text{det}} + (-1)^j f_b/2)\, t\Big) + \phi_j))/2, \tag{4.13}$$

which gives a beating frequency $f_b = 2\pi \cdot 21.5(5)$ kHz.

The value R (Fig. 4.4b) is defined as

$$R = \frac{P_{(+y)} - P_{(-y)}}{P_{(+y)} + P_{(-y)}}, \tag{4.14}$$

where $P_{(+y)}$ ($P_{(-y)}$) is the probability to read out the ^{14}N spin in the $m_I = +1$ state when using a +y (-y) readout basis in the DEER(y) sequence used to initialize the electron spin (Fig. 4.4b, see Supplementary Note 9 [54]).

4.8.9. TWO-QUBIT GATE FIDELITY

We estimate the dephasing during the two-qubit CPHASE gate in Fig. 4.6 by extrapolation of the measured P1 electron $T_{2e} = 1.00(4)$ ms for a single spin-echo pulse (decoupled from all spins except those in $|+1, \text{D}\rangle$). We use the scaling $T_2 \propto 1/\sqrt{\langle n_{\text{spins}} \rangle}$ with $\langle n_{\text{spins}} \rangle$ the average number of spins coupled to during the measurement [53]. The two-qubit gate is implemented by a double echo and the two P1s are thus not decoupled from spins in $|+1, \text{D}\rangle$ and $|+1, \text{A}\rangle$, resulting in $T_2 \sim T_{2e}/\sqrt{2} \approx 700$ µs. Assuming the same decay curve as for T_{2e} ($n = 3.1$) this implies a loss of fidelity due to dephasing of ~0.4%. For a Gaussian decay ($n = 2$) the infidelity would be ~2%.

AUTHOR CONTRIBUTIONS

M.J.D., S.J.H.L., and T.H.T. devised the project and the experiments. C.E.B., M.J.D., S.J.H.L., and H.P.B. constructed the experimental apparatus. M.J.D. and S.J.H.L. performed the experiments. M.J.D., S.J.H.L., H.P.B., and T.H.T. analyzed the data. A.L.M. and M.J.D. performed the preliminary experiments. M.M. and D.J.T. grew the diamond sample. M.J. D., S.J.H.L., and T.H.T. wrote the paper with input from all authors. T.H.T. supervised the project.

REFERENCES

[1] C. L. Degen, F. Reinhard and P. Cappellaro, *Quantum sensing,* Rev. Mod. Phys. **89**, 035002 (2017).

[2] G. Waldherr *et al.*, *Quantum error correction in a solid-state hybrid spin register,* Nature **506**, 204 (2014).

[3] J. Cramer *et al.*, *Repeated quantum error correction on a continuously encoded qubit by real-time feedback,* Nat. Commun. **7**, 1 (2016).

[4] C. Bradley *et al.*, *A ten-qubit solid-state spin register with quantum memory up to one minute,* Phys. Rev. X **9**, 031045 (2019).

[5] J. Cai, A. Retzker, F. Jelezko and M. B. Plenio, *A large-scale quantum simulator on a diamond surface at room temperature,* Nat. Phys. **9**, 168 (2013).

[6] Y. Wang *et al.*, *Quantum Simulation of Helium Hydride Cation in a Solid-State Spin Register,* ACS Nano **9**, 7769 (2015).

[7] H. Bernien *et al.*, *Heralded entanglement between solid-state qubits separated by three metres,* Nature **497**, 86 (2013).

[8] B. Hensen *et al.*, *Loophole-free bell inequality violation using electron spins separated by 1.3 kilometres,* Nature **526**, 682 (2015).

[9] A. Sipahigil *et al.*, *An integrated diamond nanophotonics platform for quantum-optical networks,* Science **354**, 847 (2016).

[10] D. D. Awschalom, R. Hanson, J. Wrachtrup and B. B. Zhou, *Quantum technologies with optically interfaced solid-state spins,* Nat. Photonics **12**, 516 (2018).

[11] M. Atatüre, D. Englund, N. Vamivakas, S.-Y. Lee and J. Wrachtrup, *Material platforms for spin-based photonic quantum technologies,* Nat. Rev. Mater. **3**, 38 (2018).

[12] S. Castelletto and A. Boretti, *Silicon carbide color centers for quantum applications,* J. Phys. Photonics **2**, 022001 (2020).

[13] M. H. Abobeih *et al.*, *One-second coherence for a single electron spin coupled to a multi-qubit nuclear-spin environment,* Nat. Commun. **9**, 1 (2018).

[14] D. D. Sukachev *et al.*, *Silicon-vacancy spin qubit in diamond: a quantum memory exceeding 10 ms with single-shot state readout,* Phys. Rev. Lett. **119**, 223602 (2017).

[15] B. C. Rose *et al.*, *Observation of an environmentally insensitive solid-state spin defect in diamond,* Science **361**, 60 (2018).

[16] R. Nagy *et al.*, *Quantum properties of dichroic silicon vacancies in silicon carbide,* Phys. Rev. Appl. **9**, 034022 (2018).

[17] D. Simin *et al.*, *Locking of electron spin coherence above 20 ms in natural silicon carbide,* Phys. Rev. B **95**, 161201 (2017).

[18] N. Bar-Gill, L. M. Pham, A. Jarmola, D. Budker and R. L. Walsworth, *Solid-state electronic spin coherence time approaching one second,* Nat. Commun. **4**, 1 (2013).

[19] R. Nagy *et al.*, *High-fidelity spin and optical control of single silicon-vacancy centres in silicon carbide,* Nat. Commun. **10**, 1 (2019).

[20] W. F. Koehl, B. B. Buckley, F. J. Heremans, G. Calusine and D. D. Awschalom, *Room temperature coherent control of defect spin qubits in silicon carbide,* Nature **479**, 84 (2011).

[21] S. Maity *et al.*, *Coherent acoustic control of a single silicon vacancy spin in diamond,* Nat. Commun. **11**, 1 (2020).

[22] B. L. Green *et al.*, *Electronic structure of the neutral silicon-vacancy center in diamond,* Phys. Rev. B **99**, 161112 (2019).

[23] F. Dolde *et al.*, *Room-temperature entanglement between single defect spins in diamond,* Nat. Phys. **9**, 139 (2013).

[24] F. Dolde *et al.*, *High-fidelity spin entanglement using optimal control,* Nat. Commun. **5**, 1 (2014).

[25] S. B. Van Dam, J. Cramer, T. H. Taminiau and R. Hanson, *Multipartite Entanglement Generation and Contextuality Tests Using Nondestructive Three-Qubit Parity Measurements,* Phys. Rev. Lett. **123** (2019).

[26] T. K. Unden, D. Louzon, M. Zwolak, W. H. Zurek and F. Jelezko, *Revealing the Emergence of Classicality Using Nitrogen-Vacancy Centers,* Phys. Rev. Lett. **123**, 140402 (2019).

[27] P. Y. Hou *et al.*, *Experimental Hamiltonian Learning of an 11-Qubit Solid-State Quantum Spin Register,* Chin. Phys. Lett. **36** (2019).

[28] V. Vorobyov *et al.*, *Quantum Fourier transform for nanoscale quantum sensing,* npj Quantum Information **7**, 124 (2021).

[29] N. Kalb *et al.*, *Entanglement distillation between solid-state quantum network nodes,* Science **356**, 928 (2017).

[30] X. Xiao and N. Zhao, *Proposal for observing dynamic jahn–teller effect by single solid-state defects,* New J. Phys. **18**, 103022 (2016).

[31] A. Cooper, W. Kyu, C. Sun, J.-C. Jaskula and P. Cappellaro, *Environment-assisted Quantum-enhanced Sensing with Electronic Spins in Diamond,* Phys. Rev. Appl. **10**, 44047 (2019).

[32] G. Goldstein *et al.*, *Environment-assisted precision measurement,* Phys. Rev. Lett. **106**, 140502 (2011).

[33] N. Y. Yao *et al.*, *Scalable architecture for a room temperature solid-state quantum information processor,* Nat. Commun. **3**, 1 (2012).

[34] Y. Ping, B. W. Lovett, S. C. Benjamin and E. M. Gauger, *Practicality of spin chain wiring in diamond quantum technologies,* Phys. Rev. Lett. **110** (2013).

[35] N. Y. Yao *et al.*, *Quantum logic between remote quantum registers,* Phys. Rev. A **87**, 22306 (2013).

[36] L. Schlipf *et al.*, *A molecular quantum spin network controlled by a single qubit,* Science Advances **3**, e1701116 (2017).

[37] T. Gaebel *et al.*, *Room-temperature coherent coupling of single spins in diamond,* Nat. Phys. **2**, 408 (2006).

[38] R. Hanson, F. Mendoza, R. Epstein and D. Awschalom, *Polarization and readout of coupled single spins in diamond,* Phys. Rev. Lett. **97**, 087601 (2006).

[39] R. Hanson and J. Wrachtrup, Private communication.

[40] A. Dréau, J.-R. Maze, M. Lesik, J.-F. Roch and V. Jacques, *High-resolution spectroscopy of single nv defects coupled with nearby 13 c nuclear spins in diamond,* Phys. Rev. B **85**, 134107 (2012).

[41] H. S. Knowles, D. M. Kara and M. Atatüre, *Observing bulk diamond spin coherence in high-purity nanodiamonds,* Nat. Mater. **13**, 21 (2014).

[42] H. S. Knowles, D. M. Kara and M. Atatüre, *Demonstration of a Coherent Electronic Spin Cluster in Diamond,* Phys. Rev. Lett. **117**, 1 (2016).

[43] C. Belthangady *et al.*, *Dressed-state resonant coupling between bright and dark spins in diamond,* Phys. Rev. Lett. **110**, 157601 (2013).

[44] F. Shi *et al.*, *Quantum logic readout and cooling of a single dark electron spin,* Phys. Rev. B **87**, 195414 (2013).

[45] A. Cooper, W. K. C. Sun, J.-C. Jaskula and P. Cappellaro, *Identification and control of electron-nuclear spin defects in diamond,* Phys. Rev. Lett. **124**, 083602 (2020).

[46] T. Yamamoto *et al.*, *Strongly coupled diamond spin qubits by molecular nitrogen implantation,* Phys. Rev. B **88**, 201201 (2013).

[47] E. L. Rosenfeld, L. M. Pham, M. D. Lukin and R. L. Walsworth, *Sensing coherent dynamics of electronic spin clusters in solids,* Phys. Rev. Lett. **120**, 243604 (2018).

[48] M. Grinolds *et al.*, *Subnanometre resolution in three-dimensional magnetic resonance imaging of individual dark spins,* Nat. Nanotechnol. **9**, 279 (2014).

[49] W. K. C. Sun, A. Cooper and P. Cappellaro, *Improved entanglement detection with subspace witnesses,* Phys. Rev. A **101**, 012319 (2020).

[50] W. V. Smith, P. P. Sorokin, I. L. Gelles and G. J. Lasher, *Electron-spin resonance of nitrogen donors in diamond,* Phys. Rev. **115**, 1546 (1959).

[51] R. Ulbricht *et al., Single substitutional nitrogen defects revealed as electron acceptor states in diamond using ultrafast spectroscopy,* Phys. Rev. B **84**, 165202 (2011).

[52] P. Deák, B. Aradi, M. Kaviani, T. Frauenheim and A. Gali, *Formation of nv centers in diamond: A theoretical study based on calculated transitions and migration of nitrogen and vacancy related defects,* Phys. Rev. B **89**, 075203 (2014).

[53] G. De Lange *et al., Controlling the quantum dynamics of a mesoscopic spin bath in diamond,* Sci. Rep **2**, 1 (2012).

[54] *See online available supplementary materials, which are not included in this thesis,* .

[55] J. Loubser and J. van Wyk, *Electron spin resonance in the study of diamond,* Rep. Prog. Phys. **41**, 1201 (1978).

[56] I. M. Zaritskii *et al., Spin-lattice relaxation of a Jahn-Teller nitrogen center in diamond,* Sov. phys., Solid state **18**, 1883 (1976).

[57] L. A. Shul'man, M. I. Zaritskii and G. A. Podzyarei, *Reorientation of the Jahn-Teller distortion in nitrogen impurity centers in diamond,* Sov. phys., Solid State **8**, 1842 (1967).

[58] C. A. Ammerlaan and E. A. Burgemeister, *Reorientation of nitrogen in type-Ib diamond by thermal excitation and tunneling,* Phys. Rev. Lett. **47**, 954 (1981).

[59] R. Cook and D. H. Whiffen, *Electron nuclear double resonance study of a nitrogen centre in diamond,* Proc. Math. Phys. Eng. Sci. **295**, 99 (1966).

[60] A. Dréau, P. Spinicelli, J. Maze, J.-F. Roch and V. Jacques, *Single-shot readout of multiple nuclear spin qubits in diamond under ambient conditions,* Phys. Rev. Lett. **110**, 060502 (2013).

[61] G.-Q. Liu *et al., Single-shot readout of a nuclear spin weakly coupled to a nitrogen-vacancy center at room temperature,* Phys. Rev. Lett. **118**, 150504 (2017).

[62] P. Neumann *et al., Single-shot readout of a single nuclear spin,* Science **329**, 542 (2010).

[63] O. Gühne and G. Tóth, *Entanglement detection,* Phys. Rep. **474**, 1 (2009).

[64] A. Reiserer *et al., Robust quantum-network memory using decoherence-protected subspaces of nuclear spins,* Phys. Rev. X **6**, 021040 (2016).

[65] L. Robledo *et al., High-fidelity projective read-out of a solid-state spin quantum register,* Nature **477**, 574 (2011).

[66] J. Hadden *et al., Strongly enhanced photon collection from diamond defect centers under microfabricated integrated solid immersion lenses,* Appl. Phys. Lett. **97**, 241901 (2010).

[67] W. Pfaff *et al., Unconditional quantum teleportation between distant solid-state quantum bits,* Science **345**, 532 (2014).

[68] T. Yeung, D. Le Sage, L. M. Pham, P. Stanwix and R. L. Walsworth, *Anti-reflection coating for nitrogen-vacancy optical measurements in diamond,* Appl. Phys. Lett. **100**, 251111 (2012).

[69] L. M. Vandersypen and I. L. Chuang, *Nmr techniques for quantum control and computation,* Rev. Mod. Phys. **76**, 1037 (2005).

[70] W. S. Warren, *Effects of arbitrary laser or nmr pulse shapes on population inversion and coherence,* J. Chem. Phys. **81**, 5437 (1984).

[71] F. J. Heremans, G. D. Fuchs, C. F. Wang, R. Hanson and D. D. Awschalom, *Generation and transport of photoexcited electrons in single-crystal diamond,* Applied Physics Letters **94**, 152102 (2009).

5

IMAGING AND CONTROL OF INTERACTING SPIN PAIRS IN AN ELECTRON-SPIN BATH

H.P. Bartling*, N. Demetriou*, N.C.F. Zutt, D. Kwiatkowski, M.J. Degen, S.J.H. Loenen, C.E. Bradley, M. Markham, D. J. Twitchen, T. H. Taminiau

Solid-state spin defects are a promising quantum system. Ensemble experiments have studied spin coherence in electron-spin baths in detail, but in ensembles the underlying quantum dynamics are averaged out. Here, we demonstrate coherent back action of an individual NV center on an electron-spin bath and use it to detect, prepare and control the dynamics of a single pair of electron spins. We image the pair with sub-nanometer resolution and reveal a long dephasing time ($T_2^* = 44(9)$ ms). Our experiment reveals the microscopic quantum dynamics underlying the central spin-qubit decoherence and provides new opportunities for controlling and sensing interacting spin systems.

*Equally contributing authors.

5.1. INTRODUCTION

Solid-state spins provide a versatile platform for quantum science and technology, as well as for studying the fundamentals of spin coherence [1–16]. The canonical case to understand spin coherence is the central spin problem: a single, central spin coupled to a surrounding bath of interacting spins. For a central electron spin in a nuclear-spin bath, the relatively large magnetic moment of the electron spin strongly affects the nuclear-spin bath evolution. This back-action creates rich dynamics under echo sequences on the central spin [1,2,17–19] and has enabled the detection and coherent control of tens of individual nuclear spins [3–5], pairs of coupled nuclear spins [6], and collective excitations [7–9] in the spin bath. These controlled nuclear spins provide qubits with coherence times exceeding minutes and are being explored in a variety of contexts, including quantum networks [10–12], quantum sensing [2,4–6,8,13,19–21], quantum error correction [14,15] and quantum simulations of many body physics [16].

The case of a central electron spin in an electron spin bath is different: the coupling between the bath spins is of similar strength as the coupling to the central spin. The resulting central spin decoherence due to the flip-flop dynamics in the spin bath has been studied in detail for ensembles of electron spins [22–25], for example in the context of quantum sensing [26]. In such ensemble experiments, the underlying microscopic configurations and flip-flop dynamics of the spin bath are averaged out. Single-spin experiments have been performed based on NV centers in diamond [27–31]. However, the signals were time-averaged over the different microscopic configurations of the spin bath, so that the underlying quantum dynamics are obscured. Indeed, the results could be accurately described by an effective magnetic noise field described by an Ornstein-Uhlenbeck process [32,33]. In this classical model of the spin bath, the back-action of the central spin is neglected and the central limit theorem is used to approximate the bath as Gaussian, forgoing the microscopic structure and dynamics.

In this work, we show that the underlying microscopic flip-flop dynamics in an electron-spin bath can be experimentally accessed and controlled. The key difference to previous work is that we observe a single central electron spin, rather than an ensemble average, and use time-resolved correlations to prepare and observe specific configurations of the bath, rather than averaging over all configurations. Additionally, we observe flip-flop dynamics directly as opposed to previous experiments that made use of double-resonance techniques [34–36].

We first demonstrate strong back-action of a central electron spin on the microscopic flip-flop dynamics of a surrounding electron spin bath. Then, we use this coherent interaction to detect, initialize and control an individual electron-spin pair within the bath. We show that such electron-spin pairs form controllable qubits with long coherence times ($T_2^* = 44(9)$ ms), due to a combination of a decoherence-free subspace and a clock transition. Finally, we image the structure and location of the spin pair with sub-nm resolution.

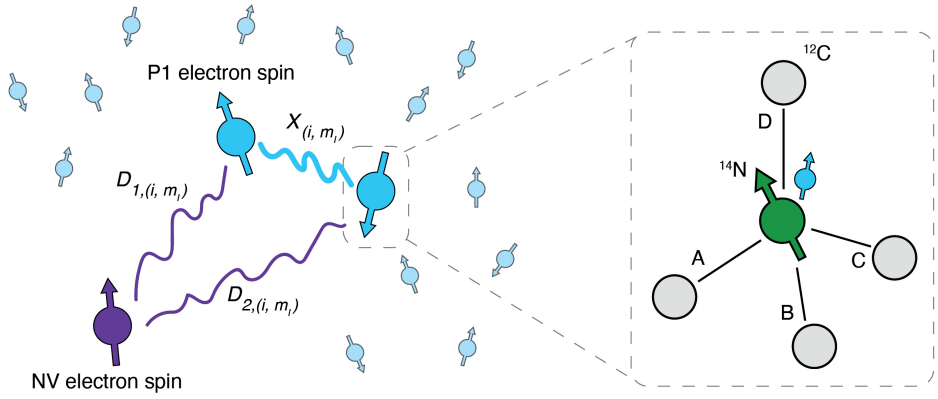

Figure 5.1: **Schematic of the spin system investigated.** We use an NV center to probe the dynamics of a surrounding bath of P1 centers. In particular, we detect and control the dynamics of a single pair of coupled P1 centers. The inset shows the lattice structure of a P1 center in diamond with the ^{14}N nuclear spin (spin states $m_I \in \{-1,0,+1\}$) and four Jahn-Teller axes ($i \in \{A,B,C,D\}$). $X_{(i,m_I)}$ is the effective coupling between the P1 electron spins and $D_{(i,m_I)}$ are the effective couplings with the NV center electron spin.

5

5.2. ELECTRON SPIN PAIRS

We investigate a single nitrogen-vacancy (NV) center in diamond surrounded by a bath of nitrogen defects (P1 centers) at a temperature of 3.3 K (Fig. 5.1). The P1 concentration is ~ 75 ppb, and the estimated ^{13}C concentration is 0.01% [12,36]. The NV electron spin acts as the central spin and is initialized optically and read out in a single shot using spin-selective optical excitation (637 nm) [37].

The P1 centers have multiple internal, dynamic degrees of freedom: the electron spin-1/2, four different Jahn-Teller (JT) axes and a spin-1 ^{14}N nuclear spin (Fig. 5.1). The P1 Hamiltonian for JT axis $i \in \{A,B,C,D\}$ is [38]

$$H_{P1,i} = \gamma_e \mathbf{B}\cdot\mathbf{J} + \gamma_n \mathbf{B}\cdot\mathbf{I} + \mathbf{J}\cdot\mathbf{A}_i\cdot\mathbf{I} + \mathbf{I}\cdot\mathbf{P}_i\cdot\mathbf{I}. \tag{5.1}$$

where $\gamma_e(\gamma_n)$ is the electron (nitrogen) gyromagnetic ratio and $\mathbf{J}$ ($\mathbf{I}$) is the electron spin-1/2 (^{14}N nuclear spin-1) operator vector. $\mathbf{A}_i$ ($\mathbf{P}_i$) is the hyperfine (quadrupole) tensor where the subscript i indicates the Jahn-Teller axis [36,39]. We apply a few-degree misaligned magnetic field with respect to the NV axis $\mathbf{B} = [2.43(2), 1.42(3), 45.552(3)]$ G to lift the degeneracy for the different JT axes of the P1 center.

Under echo sequences that decouple quasi-static noise, the NV center coherence probes the dynamics of the P1 bath [28–31]. The effect of the NV-P1 dipolar coupling can be approximated as pure dephasing of the form $\hat{S}_z\hat{J}_z$ due to the large energy difference caused by the NV zero-field splitting and the large NV and P1 Zeeman energies compared to the NV-P1 coupling. The spin-bath dynamics originate from P1-P1 dipolar couplings that cause energy-conserving flip-flops. Whether flip-flops between two P1 centers are possible depends on their electron and ^{14}N spin states, on their JT axes, and on the local magnetic field due to other nearby P1 and ^{13}C spins. Therefore, the dynamics are generally complex, depend strongly on the specific microscopic configuration, and change

over time.

We probe and prepare specific bath configurations by performing time-resolved experiments through repeated NV measurements. These are made possible by the long lifetime of the P1 JT axis and ^{14}N spin state at cryogenic temperatures[36] and by a low-intensity resonant readout of the NV spin that only weakly perturbs the P1 center[36]. Previous experiments at room temperature with high-power off-resonant lasers rapidly average over all P1 bath configurations[27–29,40–43].

We apply dynamical decoupling sequences consisting of multiple π-pulses with variable spacing 2τ (Fig. 5.2a). Such sequences sense the bath dynamics around a frequency of $1/(4\tau)$. We repeatedly apply the sequence, bin m outcomes together and analyze the signal and correlations over time. Figure 5.2b shows a time trace, revealing discrete jumps in the NV coherence. A longer-time histogram (Fig. 5.2c) reveals that the signal is a rare occurrence, which would be easily lost in the noise in a time-averaged measurement.

We create a map of the bath dynamics by collecting histograms as a function of the interpulse delay τ (Fig. 5.2d). The result shows distinct resonances for various values of τ, which we attribute to a specific pair of two P1 centers in the bath switching to different electron-spin, JT and ^{14}N configurations for which they flip-flop with a characteristic frequency resonant with the sensing sequence for τ.

To analyze the results, we consider a single pair of P1 centers. For simplicity, we first discuss the case of a large magnetic field compared to the hyperfine and quadrupole terms and discuss deviations due to the finite experimental field below. For a large magnetic field, the electron- and nuclear-spin basis states are proper single P1 eigenstates. Energy-conserving electron-spin flip-flops are then allowed when the two P1 centers have identical JT and ^{14}N states. As exploited extensively for nuclear-spin pairs[2,6,19,20], the dynamics can be described by a pseudo-spin in the anti-parallel spin subspace ($|\Uparrow\rangle = |\uparrow\downarrow\rangle$ and $|\Downarrow\rangle = |\downarrow\uparrow\rangle$).

The pseudo-spin Hamiltonian[2,6,19,20] including the effect of the NV center, is:

$$H_{(i,m_I)} = X_{(i,m_I)}\hat{S}_x + m_s Z_{(i,m_I)}\hat{S}_z, \tag{5.2}$$

where $\hat{S}_x, \hat{S}_z$ are spin-1/2 operators, $X_{(i,m_I)}$ is the effective coupling between the two spins forming the spin pair, $Z_{(i,m_I)}$ is a detuning due to the different couplings to the central NV spin, and m_s is the NV spin projection. For large magnetic fields, there are 12 such pseudo-spin Hamiltonians (four JT axes $i = \{A,B,C,D\}$ and three ^{14}N states $m_I = \{-1,0,+1\}$), all with equal values for X and Z (Sec. 5.8.2). For the lower field applied here, the situation is more complex. The field is of the order of the hyperfine interaction so that the electron- and nuclear-spin states mix. Therefore, additional flip-flop interactions involving the nuclear spin are possible, and $X_{(i,m_I)}$ and $Z_{(i,m_I)}$ generally depend on the JT axis and the spin states involved. We keep using the approximate high-field spin labels for simplicity, but take the modified eigenstates and additional flip-flop interactions into account in our analysis.

5.3. CONTROL OF ELECTRON SPIN PAIRS

Next, we demonstrate the initialization, control and measurement of the P1-pair state. From the mathematical equivalence with previous work[1,6], it follows that the Hamil-

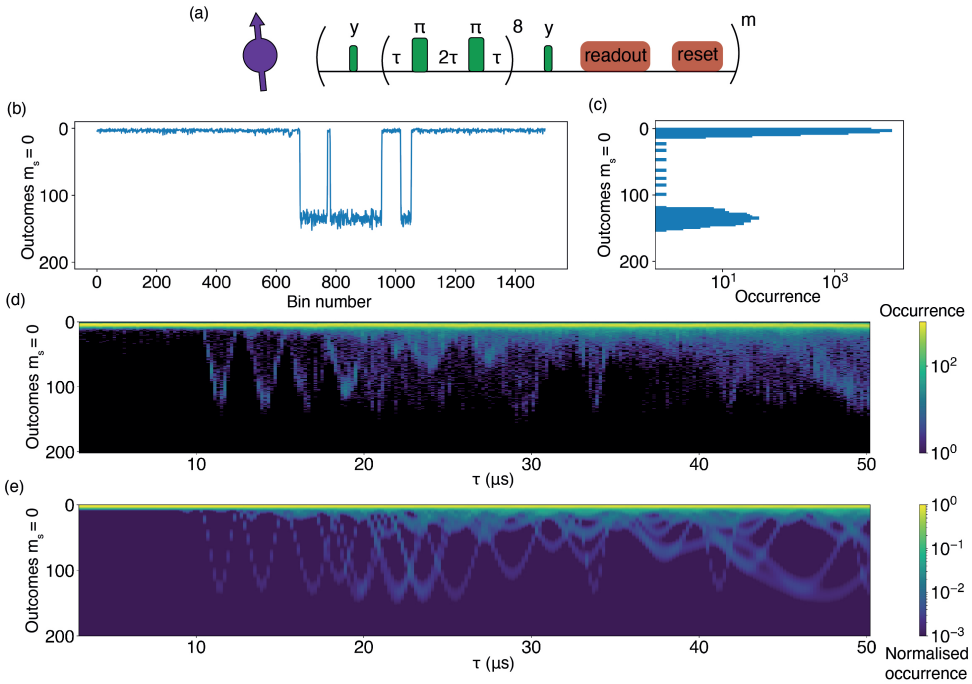

Figure 5.2: **Repetitive dynamical decoupling spectroscopy of a P1 center bath. (a)** Experimental sequence. We apply a dynamical decoupling sequence and repeat it m times. **(b)** Time trace for $\tau = 14.2$ μs and bin-size $m = 200$. A clear jump in signal is observed. **(c)** Histogram of a 3-minute-long time trace for $\tau = 14.2$ μs and $m = 200$. We only rarely observe a high number of $m_s = 0$ occurrences (~ 1.3%). Due to a limited amount of high $m_s = 0$ occurrences, the fraction of ~ 1.3% is likely not representative of the probability of occurrence. **(d)** Repetitive dynamical decoupling spectroscopy of a P1 center bath surrounding an NV center. We apply the sequence shown in (a) for $m = 200$. For each τ we obtain a histogram as in (c), which is plotted as a function of τ. **(e)** Simulation of the repetitive dynamical decoupling spectroscopy in (d) for a system of one NV center and two P1 centers with the positions as obtained later in this work.

tonian in Equation 5.2 yields an effective $\hat{S}_z^{\mathrm{NV}}\hat{S}_z$ interaction under a resonant dynamical decoupling sequence with $2\tau = \pi/\omega_r$ with $\omega_r = \sqrt{X^2 + (Z/2)^2}$. The NV electron spin thus picks up a positive or negative phase depending on the state of the P1-pair pseudo-spin[6]. Note that no phase is picked up when the pair is in the parallel electron-spin subspace ($|\uparrow\uparrow\rangle$, $|\downarrow\downarrow\rangle$), nor for any other combination of JT and ^{14}N states that do not cause flip-flop dynamics at the resonant frequency ω_r.

To initialize the P1 pair in a particular JT and ^{14}N state and in the antiparallel subspace ($|\uparrow\downarrow\rangle$, $|\downarrow\uparrow\rangle$), we apply 50 'parity' readouts (Fig. 5.3a,c). Measuring ≥ 15 counts heralds preparation of the P1 pair in the pseudo-spin subspace. We implement real-time logic to speed up the initialization procedure: during the 50 parity readouts we keep track of the obtained counts and we restart the initialization procedure if heralding successful preparation becomes unlikely (Sec. 5.8.11). This yields a ~ 10x speed-up of the experiments and is essential for enabling the presented measurements.

To initialize the pseudo-spin of the P1 pair, we apply 5 'spin' readouts (Fig. 5.3b,c).

Initialization of the pseudo-spin in $|\uparrow\downarrow\rangle$ ($|\downarrow\uparrow\rangle$) is heralded for ≥ 1 (0) counts. We use 6 spin readouts to measure the pseudo-spin state, where we assign ≥ 2 (≤ 1) counts to $|\uparrow\downarrow\rangle$ ($|\downarrow\uparrow\rangle$). Note that we need to time-match subsequent spin measurements to account for the evolution of the P1 pair pseudo-spin during one spin readout, similar to previous experiments with repeated measurements on precessing nuclear spins[6,13].

By choosing a different interpulse delay τ, we can address different JT and ^{14}N states. We can thus measure the dependence of the electron-electron couplings (X and Z) on the JT and ^{14}N states by performing Ramsey experiments using different values of τ to prepare and measure the P1 pair. In Fig. 5.3c we show this for five values of τ, and we find the effective couplings X between the two P1 centers.

5.4. ELECTRON SPIN PAIR COHERENCE

To investigate the electron spin pair coherence, we measure the decay of the Bloch vector length for $\tau = 14.0$ μs (Fig. 5.3d). We find $T_2^* = 44(9)$ ms, among the longest reported for solid-state electron-spin qubits[44]. Compared to the single P1 center electron spin coherence $T_2^* = 50(3)$ μs[36], this is a three-order-of-magnitude improvement in the same nuclear and electron spin bath.

The electron spin bath is partially common to both P1 centers. Since the two electron spins are in antiparallel spin states, the correlated noise is cancelled out; the two P1 centers form a decoherence-free subspace[6,45,46]. Conversely, the ^{13}C nuclear spin baths are relatively close to the P1 centers. Hence, the noise of this spin bath is less correlated. The effect of the nuclear and remaining electron spin bath noise is reduced due to the P1-P1 coupling. The two antiparallel states form a clock transition, which makes it first-order insensitive to fluctuations of the magnetic field[6]. For more details on the coherence mechanisms, see Section 5.8.10.

5.5. DETERMINING JAHN-TELLER AXIS AND ^{14}N SPIN STATE

Next, we determine what Jahn-Teller axis and ^{14}N spin state are associated with the signals for the different interpulse delays τ. Due to the electron-nuclear hyperfine interaction and misaligned magnetic field, the electron-spin transition frequency is different for each JT and ^{14}N state. Radio-frequency (RF) pulses thus conditionally rotate the electron spin dependent on the specific JT and ^{14}N states. After initializing the electron spin pair in $|\psi\rangle\langle\psi| = \frac{1}{2}|\uparrow\downarrow\rangle\langle\uparrow\downarrow| + \frac{1}{2}|\downarrow\uparrow\rangle\langle\downarrow\uparrow|$ for an unknown JT and ^{14}N state (Fig. 5.4a), we apply an RF pulse that - when resonant - can flip the electron spin pair to the parallel subspace resulting in a change in signal on the NV center (Sec. 5.8.4). The RF frequency at which the electron spin flips occur gives information about the JT and ^{14}N state associated to that particular τ (Sec. 5.8.4).

In Figure 5.4a we show the data for both $\tau = 11.2$ μs and $\tau = 14.0$ μs. In order to map the obtained frequencies to the JT and ^{14}N state, we simulate the application of RF pulses for each JT and ^{14}N configuration (Sec. 5.8.4). From this, we obtain a set of possible Jahn-Teller axis and ^{14}N spin state assignments (Sec. 5.8.4). We perform the same analysis for $\tau = 16.8$ μs, $\tau = 18.6$ μs and $\tau = 29.0$ μs (Sec. 5.8.5).

While the Jahn-Teller axis can be directly assigned, the situation for the ^{14}N spin state

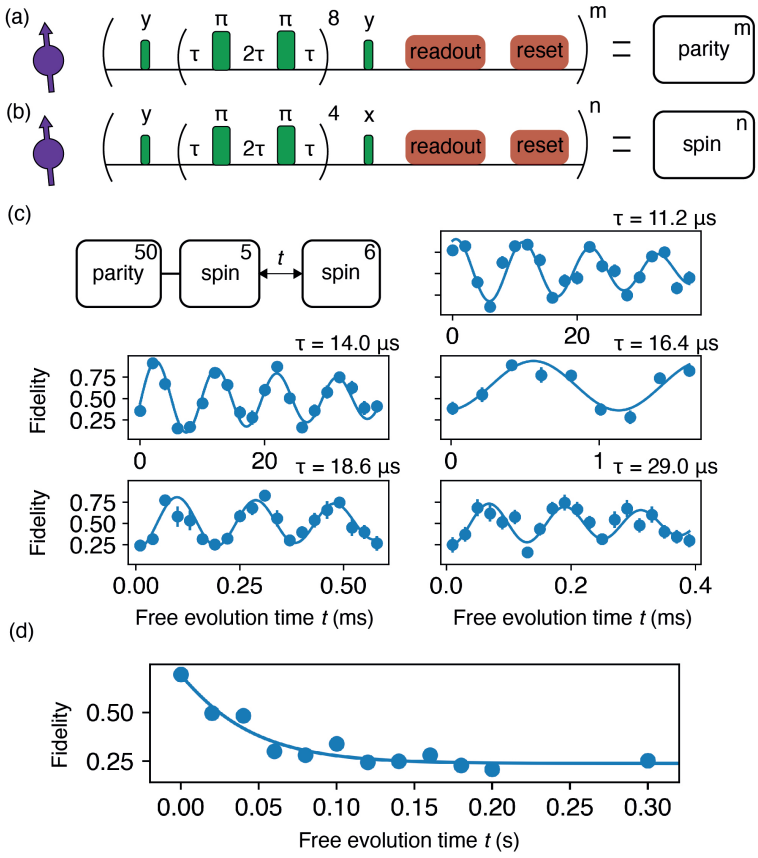

Figure 5.3: **Ramsey measurements and coherence of the P1 electron spin pair. (a,b)** Pulse sequences to measure the parity ($\{|\uparrow\uparrow\rangle, |\downarrow\downarrow\rangle\}$ vs $\{|\uparrow\downarrow\rangle, |\downarrow\uparrow\rangle\}$) and spin ($\{|\uparrow\downarrow\rangle\}$ vs $\{|\downarrow\uparrow\rangle\}$) of the electron spin pair. **(c)** Ramsey measurements for five different interpulse delays τ. We apply 50 parity readouts and herald initialization for ≥ 15 counts in the JT, ^{14}N and antiparallel electron states corresponding to the τ used in the parity sequence. We then apply 5 spin readouts without real-time heralding. Instead, we use both the initialization events in $|\uparrow\downarrow\rangle$ and $|\downarrow\uparrow\rangle$, which we can distinguish based on the obtained counts in these 5 spin readouts. We perform single-shot readout using 6 spin readouts to measure the pseudo-spin state. Each τ corresponds to an identifiable dip in the dynamical decoupling spectrum of Fig. 5.2d. The obtained dipolar coupling X as well as the interpulse delay τ used are indicated. The contrast is limited by the pseudo-spin dephasing during the spin initialization and readout. **(c)** Bloch vector length measurement of the electron spin pair at $\tau = 14.0$ µs. We obtain $T_2^* = 44(9)$ ms. The presented data is not corrected for the readout infidelity.

is more complicated. At our magnetic field, significant electron-nitrogen spin mixing is present ($\gamma_e B \sim A_\parallel, A_\perp$). Due to this spin mixing, flip-flops can occur that involve both the electron and nitrogen spin (Sec. 5.8.2), creating additional possible transitions. We resolve this remaining ambiguity in the assignment by determining for which of the possible state assignments a matching spatial structure of the system can be found.

5.6. IMAGING AN ELECTRON SPIN PAIR

The information about the P1 electron-electron coupling obtained in Fig. 5.3c combined with the information about the associated JT and ^{14}N states allows us to image the P1 electron spin pair. We use a least-squares optimization algorithm to fit five P1-P1 couplings to different spatial configurations of the P1 pair. We benchmark the fitting algorithm on 10 randomly generated P1 pairs (Sec. 5.8.7), after which we apply it to the five measured couplings. The P1-P1 relative position we find is $x = 6.7 \pm 0.21$ nm, $y = -2.5 \pm 0.23$ nm, $z = 7.3 \pm 0.16$ nm (Fig. 5.4b,c).

Due to the electron-nitrogen spin mixing, multiple ^{14}N spin assignments are possible for three out of five measured couplings (Sec. 5.8.2). We resolve this by considering all possible assignments in the fitting algorithm. Then, we select the assignment that minimizes the residual of the measured couplings. We accept this as the final assignment of the JT and ^{14}N configurations of the pair, resolving the discrepancy discussed before. As an alternative approach to using the internal degrees of freedom of the P1 center, one could sweep the external magnetic field angle to image a spin pair[47].

We then find the position of the NV center with respect to the two P1 centers. We use a similar approach and fitting algorithm (Sec. 5.8.7). In Ref.[36] the dipolar couplings between the NV center and each of the two P1 centers were measured. We fix the obtained P1-P1 relative position and minimise the least-squares residual of the NV-P1 couplings. The P1 centers are found at $(x_1, y_1, z_1) = (-13.5(5), -10.2(8), 17.0(3))$ nm and $(x_2, y_2, z_2) = (-20.3(5), -7.7(8), 9.8(2))$ nm with respect to the NV center. Note that the obtained spatial configuration is inversion symmetric, as discussed in more detail in Section 5.8.7.

Finally, we discuss the conditions that enable observing and controlling the flip-flop dynamics of spin pairs in the bath. A selective coherent interaction requires the interaction time (set by $1/Z$) to be small compared to the spin-pair dephasing time (T_2^*) and the central electron spin coherence time under the decoupling sequence (T_2). A key factor in our experiment is that the large number of different internal P1 states facilitate detecting and controlling spin pairs. The energy differences resulting from these internal degrees of freedom slow down the dynamics of the bath spins, so that the central spin coherence is extended. As a result, more internal degrees of freedom imply improved central spin coherence and selective addressing of individual spin pairs, at the cost of a lower success probability for heralding a desired configuration. The full microscopic dynamics involving the P1 bath as well as the ^{13}C nuclear spin bath are complex. Theoretically predicting the distributions for quantities such as the typical number of P1 spin pairs that would be observed for randomly drawn bath instances, will likely require detailed numerical simulation, for example using correlated cluster expansion (CCE), which we do not pursue here.

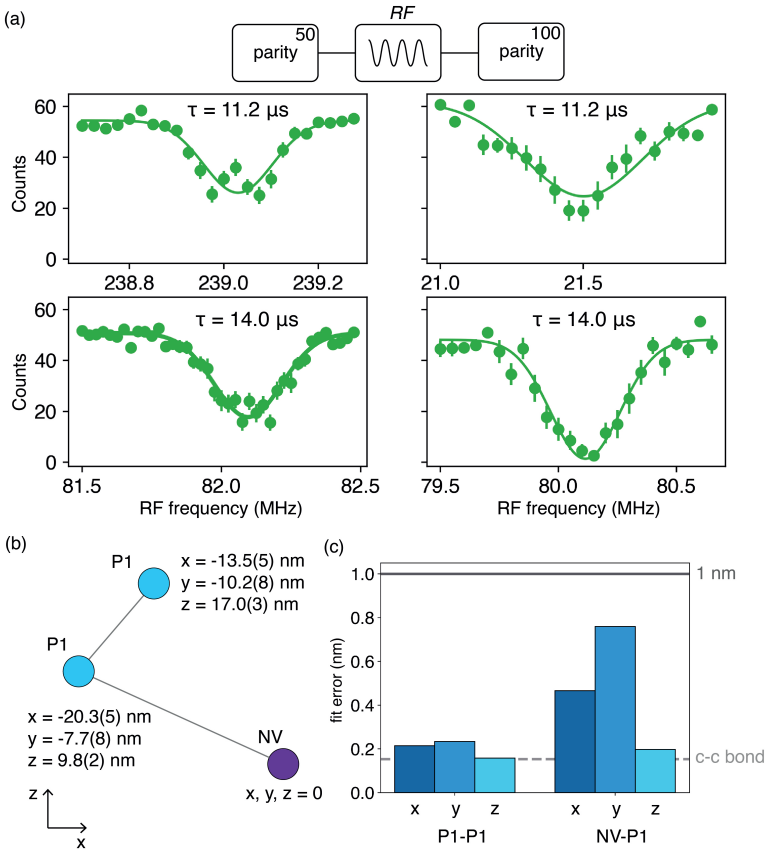

Figure 5.4: **RF driving and imaging of the P1 electron spin pair. (a)** (Top) Pulse sequence for RF driving of the electron spin pair. We initialize the spin pair in $\frac{1}{2}|\uparrow\downarrow\rangle\langle\uparrow\downarrow| + \frac{1}{2}|\downarrow\uparrow\rangle\langle\downarrow\uparrow|$. Afterwards, an RF pulse of varying frequency is applied which can flip the P1 center electron spin (Sec. 5.8.4). Then, we read out whether the electron spin pair is still in its antiparallel subspace. (Bottom) RF frequency sweeps for $\tau = 11.2\,\mu$s (top) and $\tau = 14.0\,\mu$s (bottom). A reduction in the number of counts gives information about the JT and ^{14}N state belonging to that particular τ. **(b)** Fitted positions of the NV center (purple) and two P1 centers (blue). We show one of two possible solutions; the other is the inversion symmetric solution. The positions of the two P1 centers with respect to the NV center are indicated. **(c)** The fit error of the obtained P1-P1 and NV-P1 position in x, y and z. For the P1-P1 position, the error is close to the diamond bond length. The NV-P1 position has an error significantly less than 1 nm.

5.7. DISCUSSION

In conclusion, we experimentally demonstrated the detection and control of the flip-flop dynamics of an electron-spin pair embedded in a spin bath. We have leveraged these methods to initialize the spin pair state and to image the structure of the NV-P1-P1 system. These results directly experimentally access the underlying microscopic quantum dynamics and back-action which are central to various theoretical methods, such as correlated cluster expansion (CCE), that are widely used to understand time- and ensemble-averaged measurements[22,24,48–50]. Additionally, the long dephasing times indicate electron-spin pairs based on P1 centers or other defects[34,35,51–54] might be interesting qubits. While the added complexity from the P1 internal states under a weak misaligned magnetic field is exploited here to isolate, characterize and image the system, the resulting low heralding probability ($\sim 1/288$) limits its use as a qubit. This can be partly overcome by applying a large aligned magnetic field, so that the pseudo-spin parameters (X and Z) are identical for all JT and ^{14}N states and three of the JT states are degenerate, resulting in a higher success probability of $5/48$ (Sec. 5.8.2). Lastly, the presented methods and results could contribute to efforts towards atomic- and nano-scale magnetic resonance imaging of complex spin samples outside of the diamond by directly revealing and isolating spin-pair dynamics[4,55].

5.8. SUPPLEMENTARY MATERIALS

5.8.1. SYSTEM HAMILTONIAN

In this Section, we discuss the Hamiltonian that describes the dynamics of the NV-P1-P1 system. We explain how we calculate the effective coupling between the defects' electron spins. Lastly, we examine the possible orientations of the P1 centers in the diamond lattice.

NV-P1-P1 HAMILTONIAN

The Hamiltonian of the NV-P1-P1 system consists of the individual Hamiltonians of the NV and P1 centers and the Hamiltonians for the dipolar interactions between their respective electron spins[36,38]. Note that we omit the Hamiltonian term that describes the NV nitrogen spin since the zero-field splitting suppresses spin mixing between the NV nitrogen and electron spin and the external magnetic field is aligned along the NV symmetry axis. We also omit any Hamiltonian terms that describe the dipolar coupling between the ^{14}N nuclear spin of one defect and the electron or ^{14}N nuclear spin from other defects. We consider this to be negligible due to the large difference in gyromagnetic ratios ($\gamma_e/\gamma_n \approx 9000$)[36].

$$H = H_{\mathrm{NV}} + \sum_{j=1}^{2} H_{\mathrm{P1,j}} + \sum_{j<k}^{3} H_{D_{jk}} \tag{5.3}$$

where

$$\begin{aligned} H_{\mathrm{NV}} &= \Delta \hat{S}_z^2 + \gamma_e \mathbf{B}\cdot\mathbf{S} \\ H_{\mathrm{P1,j}} &= \gamma_e \mathbf{B}\cdot\mathbf{J}_j + \gamma_n \mathbf{B}\cdot\mathbf{I} + \mathbf{J}_j\cdot\mathbf{A}_i\cdot\mathbf{I} + \mathbf{I}\cdot\mathbf{P}_i\cdot\mathbf{I} \\ H_{D_{\mathrm{P1,j-NV}}} &= D\cdot(3(\mathbf{J}_j\cdot\hat{r})(\mathbf{S}\cdot\hat{r}) - \mathbf{J}_j\cdot\mathbf{S}) \\ H_{D_{\mathrm{P1,j-P1,k}}} &= D\cdot(3(\mathbf{J}_j\cdot\hat{r})(\mathbf{J}_k\cdot\hat{r}) - \mathbf{J}_j\cdot\mathbf{J}_k) \end{aligned} \tag{5.4}$$

$\mathbf{I}$	$= \begin{bmatrix}\hat{I}_x, & \hat{I}_y, & \hat{I}_z\end{bmatrix}$	Spin-1 operators for P1 ^{14}N nuclear spin
$\mathbf{J}_j$	$= \begin{bmatrix}\hat{J}_x, & \hat{J}_y, & \hat{J}_z\end{bmatrix}_j$	Spin-1/2 operators for the jth P1 electron spin
$\mathbf{S}$	$= \begin{bmatrix}\hat{S}_x, & \hat{S}_y, & \hat{S}_z\end{bmatrix}$	Spin-1 operators for the NV electron spin
$\mathbf{B}$	$= \begin{bmatrix}B_x, & B_y, & B_z\end{bmatrix}$	B-field vector
$\mathbf{A}_i$	$= R^T A_{diag} R$	Hyperfine coupling tensor
$\mathbf{P}_i$	$= R^T P_{diag} R$	Quadrupolar coupling tensor

with

$$D = \frac{-\mu_0 \gamma_e^2 \hbar}{4\pi r^3}.$$

μ_0 is the vacuum magnetic permeability, $\gamma_e \approx 2.8024$ MHz/G and $\gamma_n \approx 0.3078$ kHz/G are the gyromagnetic ratios of the electron and ^{14}N spin respectively. r is the physical separation of the electron spins and $\hat{r} = \mathbf{r}/|r|$ the unit vector between them. R are the rotation matrices of the $SO(3)$ group, with Euler angles α, β, γ[36,38]:

$$R(\alpha,\beta,\gamma) = \begin{pmatrix} \cos(\gamma)\cos(\beta)\cos(\alpha) - \sin(\gamma)\sin(\alpha) & \cos(\gamma)\cos(\beta)\sin(\alpha) + \sin(\gamma)\cos(\alpha) & -\cos(\gamma)\sin(\beta) \\ -\sin(\gamma)\cos(\beta)\cos(\alpha) - \cos(\gamma)\sin(\alpha) & -\sin(\gamma)\cos(\beta)\sin(\alpha) + \cos(\gamma)\cos(\alpha) & \sin(\gamma)\sin(\beta) \\ \sin(\beta)\sin(\alpha) & \sin(\beta)\sin(\alpha) & \cos(\beta) \end{pmatrix} \tag{5.5}$$

The rotation matrices R rotate the hyperfine and quadrupolar tensors depending on the Jahn-Teller axis, i.e $\mathbf{A}_i = R(\alpha,\beta)^T A_{diag} R(\alpha,\beta)$. The Euler angles α, β define the Jahn-Teller principal axis (Fig. 5.5). Due to the axial symmetry of the P1 center in its principal axis ($A_x = A_y$ and $P_x = P_y$), we can set $\gamma = 0$ without loss of generality[36]. The rotation matrix R simplifies to

$$R(\alpha,\beta) = \begin{pmatrix} \cos(\beta)\cos(\alpha) & \cos(\beta)\sin(\alpha) & -\sin(\beta) \\ -\sin(\alpha) & \cos(\alpha) & 0 \\ \sin(\beta)\cos(\alpha) & \sin(\beta)\sin(\alpha) & \cos(\beta) \end{pmatrix} \tag{5.6}$$

The hyperfine and quadrupolar tensors are $A_{diag} = \mathrm{diag}[114.03, 81.31, 81.31]$ MHz and $P_{diag} = \mathrm{diag}[2.65, 1.32, 1.32]$ MHz respectively[30].

EFFECTIVE COUPLING

Now, we describe how we calculate the effective couplings between the different defect spins (P1-P1 and NV-P1). These effective couplings provide the parameters $X_{(i,m_I)}$ and $Z_{(i,m_I)}$ of the pseudo-spin Hamiltonian.

We start by constructing the Hamiltonian of the system of interest, i.e $H_{\text{NV-P1}}$ or $H_{\text{P1-P1}}$. To calculate the effective coupling between the electron spins, we consider the energy differences between their eigenstates. For example, for the NV-P1 system, with

the P1 center in a particular Jahn-Teller axis i and its ^{14}N nuclear spin in $|+\rangle$ ($m_I = +1$), the effective coupling between the electron spins is given by[36]

$$D_{+,i} = (\lambda_{|-1,+,\downarrow\rangle,i} - \lambda_{|-1,+,\uparrow\rangle,i}) + (\lambda_{|0,+,\uparrow\rangle,i} - \lambda_{|0,+,\downarrow\rangle,i}), \tag{5.7}$$

where λ are the eigenvalues corresponding to the eigenvectors denoted in their subscripts. The indicated eigenstates correspond to the NV electron spin, the P1 nuclear spin, and the P1 electron spin respectively.

For two P1 centers undergoing flip-flop dynamics, the effective coupling is given by

$$X = \lambda_{\frac{1}{\sqrt{2}}(|+,\downarrow,+,\uparrow\rangle+|+,\uparrow,+,\downarrow\rangle)} - \lambda_{\frac{1}{\sqrt{2}}(|+,\downarrow,+,\uparrow\rangle-|+,\uparrow,+,\downarrow\rangle)}, \tag{5.8}$$

where for this example the nitrogen spin for both P1 centers is in the $|+\rangle$ ($m_I = +1$) state. The indicated eigenstates correspond to the nitrogen and electron spin of the first P1 center respectively, followed by the nitrogen and electron spin of the second P1 center.

P1 CENTER ORIENTATIONS

5

P1 centers appear in the diamond lattice in two different orientations, as depicted in Fig. 5.5. In this Section, we show that these two different orientations do not result in an observable difference in our experiments. The hyperfine and quadrupolar tensors are transformed differently by the two Euler angles α and β depending on the Jahn-Teller axis. In the table in Fig. 5.5, the first (second) set of α, β (α', β') corresponds to the left (right) picture of the P1 center orientations.

We will now show that the transformation of a diagonal matrix $M_i = R^T(\alpha_i,\beta_i)M_iR(\alpha_i,\beta_i)$ is equivalent for both orientations (α_i,β_i) and (α'_i,β'_i). Let $R = R(\alpha,\beta)$ and $R' = R(\alpha',\beta')$. We can then write

$$\begin{aligned} R'M_iR'^T &= R'R^TM_{diag}RR'^T \\ &= M_{diag}R'R^TRR'^T \\ &= M_{diag} \\ \implies M_i &= R'^TM_{diag}R' \end{aligned} \tag{5.9}$$

Here we made use of the fact that $R'R^T = \mathrm{diag}(1,-1,-1)$ is a diagonal matrix for $\alpha' = \alpha+\pi$ and $\beta' = \pi-\beta$. It thus commutes with the diagonal matrix M_{diag}. Since the dipole

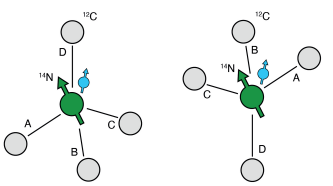

JT	α	β	α'	β'
A	0	109.5	180	70.5
B	120	109.5	300	70.5
C	240	109.5	60	70.5
D	0	0	180	180

Figure 5.5: **Schematic of the two possible orientations of a P1 center with corresponding rotation angles.** On the left, the two possible orientations of a P1 center in the diamond lattice are shown. The Jahn-Teller axes are indicated by A, B, C and D. The Euler angles corresponding to these Jahn-Teller axes are given in degrees on the right, where the left (right) column corresponds to the left (right) orientation.

term in the Hamiltonian is also invariant under the different Jahn-Teller distortions, the couplings describing the dynamics remain unchanged for the two orientations, and we do not expect an observable difference in our measurements.

5.8.2. EFFECTS OF P1 ELECTRON-NITROGEN SPIN MIXING

In the following, we will denote the single P1 eigenbasis as $|-\downarrow\rangle$, $|-\uparrow\rangle$, $|0\downarrow\rangle$, $|0\uparrow\rangle$, $|+\downarrow\rangle$, $|+\uparrow\rangle$, where the first entry refers to the nitrogen spin ($m_I = -1, 0, +1$) and the second entry refers to the electron spin ($\uparrow$ or $\downarrow$). In a simple picture, one would expect to observe flip-flop dynamics of two spins if they are degenerate and have nonzero dipolar coupling. For example, for a pair of P1 centers the states $|-\downarrow-\uparrow\rangle$ and $|-\uparrow-\downarrow\rangle$ are degenerate. The dipolar coupling between the two electron spins can induce flip-flops between them. Then, the eigenstates become $\frac{1}{\sqrt{2}}(|-\downarrow-\uparrow\rangle \pm |-\uparrow-\downarrow\rangle)$. Consider two other states of the pair of P1 centers: $|-\downarrow 0\uparrow\rangle$ and $|0\uparrow-\downarrow\rangle$. These two states are degenerate as well. However, in principle, we do not get any flip-flop dynamics, because the dipolar coupling between the two electron spins cannot induce nitrogen spin flips.

This simple picture holds when the magnetic field is much larger than the hyperfine interaction with the P1 nitrogen spin-1 ($\gamma_e B \gg A_\parallel, A_\perp$). Due to the finite magnetic field we work at ($\gamma_e B \sim A_\parallel, A_\perp$), the single P1 eigenstates are not separable into a nitrogen spin-1 and an electron spin-1/2 part. Instead, the nitrogen and electron spin become mixed. The finite magnetic field mostly leads to mixing of $\{|-\uparrow\rangle, |0\downarrow\rangle\}$ and $\{|0\uparrow\rangle, |+\downarrow\rangle\}$. This implies that the dipolar coupling between the two electron spins can induce flip-flop dynamics between states such as $|0\downarrow-\uparrow\rangle$ and $|-\uparrow 0\downarrow\rangle$.

Therefore, we expect to observe signal on the NV center due to two types of flip-flop states. First, there is the simple case in which the nitrogen spin states are approximately equal and fixed, and the electron spins form superpositions of $|\uparrow\downarrow\rangle$ and $|\downarrow\uparrow\rangle$. Second, the mixing between the nitrogen spin and electron spin of the P1 centers allows for more complicated flip-flop dynamics.

In Fig. 5.6 we show the simulated dynamical decoupling signal on the NV center per Jahn-Teller state for the NV-P1-P1 positions obtained in this work. For each Jahn-Teller state, we calculate the expected NV electron signal per P1-P1 eigenvector. Only eigenvectors generating a significant signal (fidelity loss of > 0.1) are shown. The labels are obtained by calculating the overlap of the P1-P1 eigenvector with the spin basis vectors and indicating the largest overlap.

From Fig. 5.6 it can be seen that most NV electron coherence loss due to P1 electron spin pairs is due to the simple flip-flop states: $|+\uparrow+\downarrow\rangle, |0\uparrow 0\downarrow\rangle, |-\uparrow-\downarrow\rangle$. However, there are more complicated flip-flop states due to the mixing between the nitrogen spin and electron spin of the P1 centers, amongst which are $|0\downarrow-\uparrow\rangle$ and $|+\downarrow 0\uparrow\rangle$.

To further illustrate the origin of the more complicated flip-flop states, we simulate the same system at a high magnetic field ($\mathbf{B} = [1, 1, 100]$ G). It is expected that only the simple flip-flop states remain, because in this regime $\gamma_e B \gg A_\parallel, A_\perp$ resulting in negligible P1 electron-nitrogen spin mixing. The result of the simulation is shown in Fig. 5.7, where we do indeed find that only the simple flip-flop states remain.

At the magnetic field used in the experiments in this paper ($B \sim 45$ G), the P1 electron-nitrogen spin mixing is not negligible. Hence, we have to consider the possibility of measuring dipole-dipole couplings resulting from electron-nitrogen spin mix-

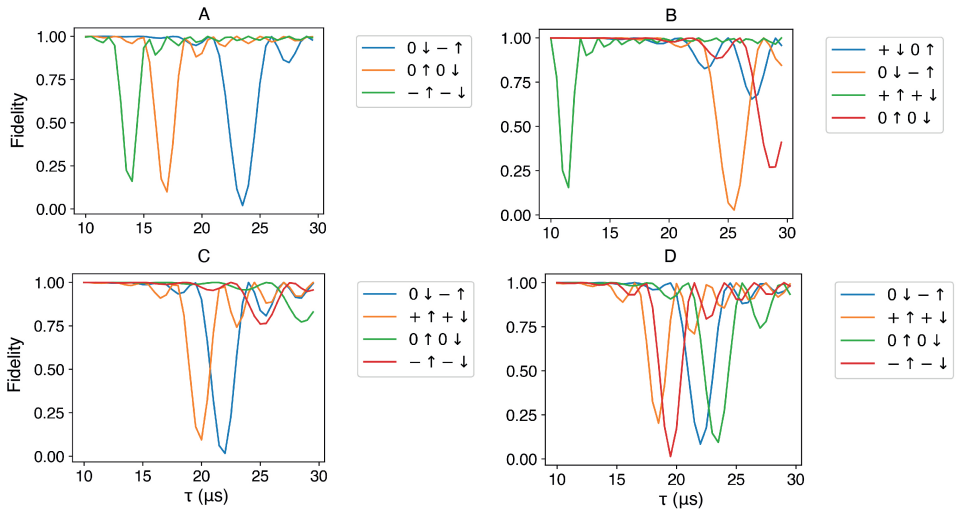

Figure 5.6: **Simulation of the effect of a pair of P1 centers on dynamical decoupling of the NV electron spin grouped per Jahn-Teller state.** We simulate the system discussed in this paper: a single NV center coupled to two P1 centers. We use the same magnetic field as in the experiments: $\mathbf{B} = [2.43, 1.42, 45.552]$ G. The position vectors for the NV center and two P1 centers are the ones extracted in the main text. Then, we consider the two P1 centers to be in the same Jahn-Teller state (A, B, C or D) and calculate the expected signal on the NV center for each P1-P1 eigenvector and for each Jahn-Teller state. Each of the four figures corresponds to a different Jahn-Teller state, indicated by the title. We only show states that lead to a significant coherence loss on the NV electron spin: less than a fidelity of 0.9. The legends on the right of each graph show which P1-P1 states cause the NV electron coherence loss. We observe coherence loss from both types of flip-flop states: when the nitrogen is fixed as well as more complicated flip-flop states that involve nitrogen spin flips. The latter states can give significant signal, comparable to the flip-flop states that do not involve the nitrogen spin.

ing. To address this possibility, we also fit the measurements to these flip-flop states, see Section 5.8.7.

For completeness, we simulate the same system at a very high, but misaligned magnetic field of $\mathbf{B} = [100, 100, 10000]$ G. The result is shown in Fig. 5.8. We observe that all Jahn-Teller axes and nitrogen spin states give approximately the same signal. For these values of the magnetic field, the effect of the electron-nitrogen spin mixing is close to negligible and the P1-P1 electron-electron coupling is therefore almost the same for all configurations.

Importantly, the two P1 centers still need to be in the same Jahn-Teller axis and nitrogen spin state to be degenerate and to flip-flop. However, the amplitude of a dip in the dynamical decoupling signal goes up from 1/288 to 1/24. The ratio of 1/288 comes from 4 Jahn-Teller axes for each P1 center, 3 nitrogen spin states for each P1 center and 2 electron spin states for each P1 center, two of which $(|\uparrow\downarrow\rangle, |\downarrow\uparrow\rangle)$ generate signal. Since all 12 possibilities in Fig. 5.8 give the same signal, the amplitude goes up from 1/288 to 1/24.

When the external magnetic field is very high and aligned, the Jahn-Teller axes A, B and C also become degenerate. This increases the fraction 1/24 further to 5/48, since six additional Jahn-Teller configurations exhibit flip-flop dynamics at the flip-flop rate.

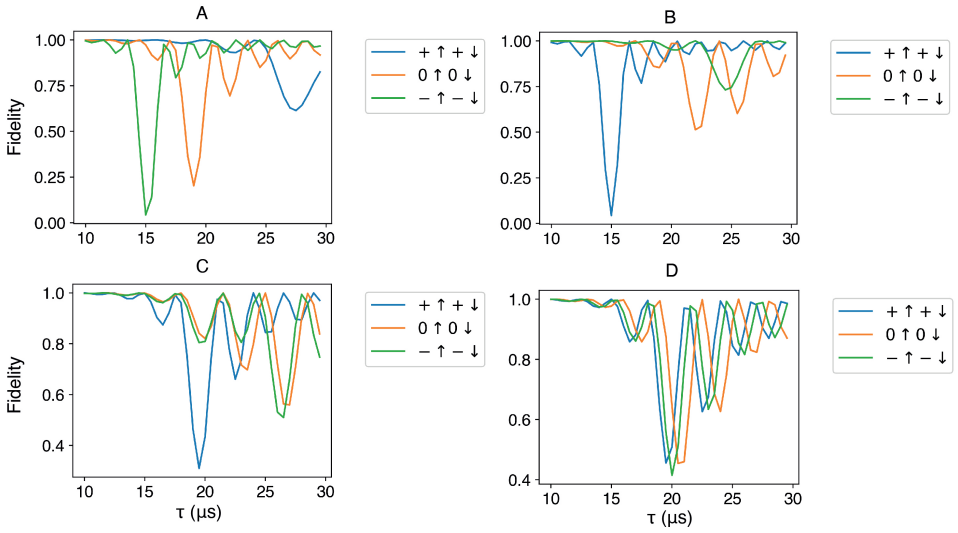

Figure 5.7: **Simulation of the effect of a pair of P1 centers on dynamical decoupling of the NV electron spin grouped per Jahn-Teller state at a high magnetic field.** We simulate the same system as in Fig. 5.6 at a magnetic field of $[B_x, B_y, B_z] = [1, 1, 100]$ G. At magnetic fields significantly greater than the P1 electron-nitrogen hyperfine coupling, only simple flip-flop states generate signal on the NV center.

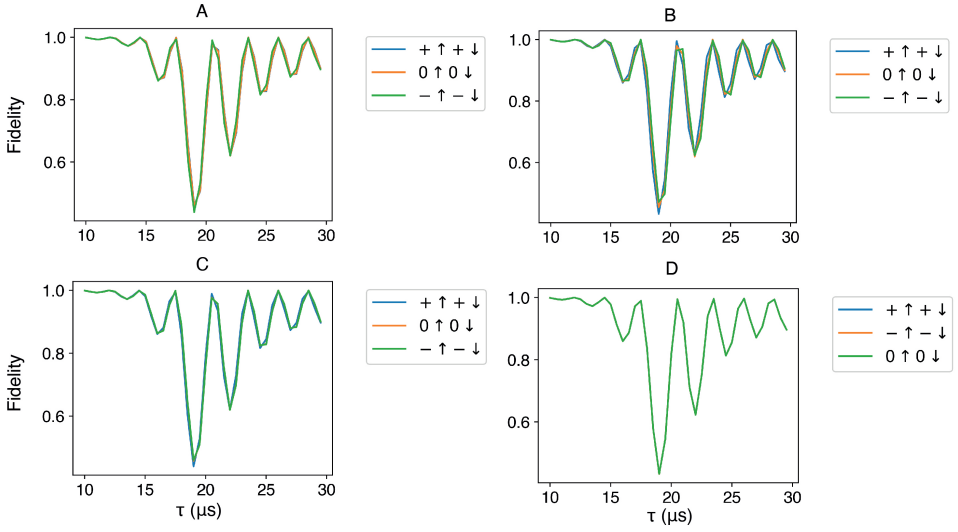

Figure 5.8: **Simulation of the effect of a pair of P1 centers on dynamical decoupling of the NV electron spin grouped per Jahn-Teller state at a very high magnetic field.** We simulate the same system as in Fig. 5.6 at a magnetic field of $[B_x, B_y, B_z] = [100, 100, 10000]$ G. At this magnetic field, the external magnetic field is significantly greater than the electron-nuclear hyperfine interaction and the nuclear quadrupole interaction. Hence, we observe close to the same signal for all Jahn-Teller axes and all nitrogen spin states.

5.8.3. SPIN AND PARITY READOUT

In Fig. 5.9, we show the spin and parity readout together with Bloch spheres indicating the phase picked up by the NV center electron spin. When the P1 electron spin pair is in the parallel state ($\{|\uparrow\uparrow\rangle, |\downarrow\downarrow\rangle\}$), there are no flip-flop dynamics and the NV electron spin does not pick up any phase. However, when the P1 electron spin pair is in the anti-parallel subspace ($\{|\uparrow\downarrow\rangle, |\downarrow\uparrow\rangle\}$), the NV picks up a positive or negative phase depending on the pseudo-spin state. Note that the NV electron spin only picks up phase when the interpulse delay τ is resonant with the P1 pair flip-flop dynamics (and when the P1 pair is thus in that particular JT and ^{14}N configuration).

For the spin readout, we tune the number of dynamical decoupling units such that the NV electron spin picks up a phase of $\pm\pi/2$ for the two anti-parallel spin pair states $|\uparrow\downarrow\rangle$ and $|\downarrow\uparrow\rangle$. If we then read out along the y-axis, we can distinguish between $|\uparrow\downarrow\rangle$ and $|\downarrow\uparrow\rangle$. For the parity readout, we use double the number of dynamical decoupling units such that the NV electron spin picks up a phase of $\pm\pi$. If we read out along the x-axis, we can distinguish between the spin pair being in the parallel and anti-parallel subspace. By combining parity and spin readouts (Fig. 5.3), we can initialize the P1 spin pair in a specific anti-parallel state. In the final readout, we use spin readouts to distinguish between the two anti-parallel states (Fig. 5.3).

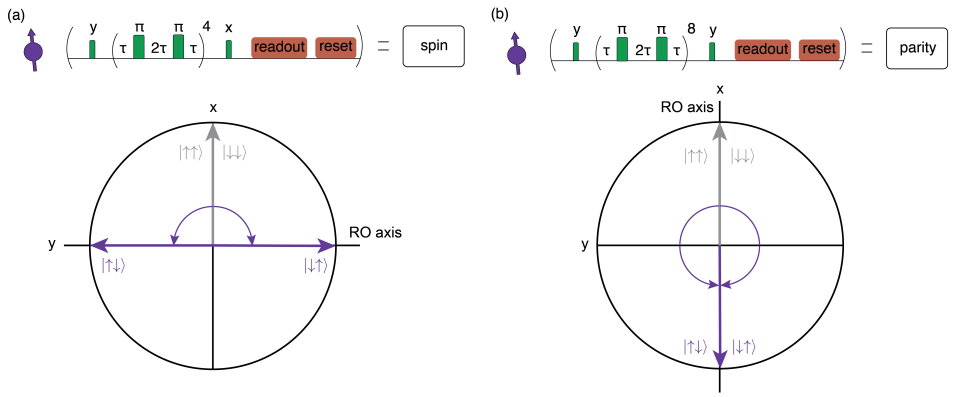

Figure 5.9: **Phase pick-up of the NV center during spin and parity readout. (a)** Spin readout sequence and the corresponding phase pick-up of the NV center for the four different spin-pair states shown on a 2D Bloch sphere. We calibrate the number of dynamical decoupling units such that the NV electron spin picks up a $\pm\pi/2$ phase for $|\uparrow\downarrow\rangle$ and $|\downarrow\uparrow\rangle$. Then, we read out along the y-axis. **(b)** Parity readout sequence and the corresponding phase pick-up of the NV center for the four different spin-pair states shown on a 2D Bloch sphere. We calibrate the number of dynamical decoupling units such that the NV electron spin picks up a $\pm\pi$ phase for $|\uparrow\downarrow\rangle$ and $|\downarrow\uparrow\rangle$. Then, we read out along the x-axis.

5.8.4. RF SIMULATIONS

In this section, we simulate the application of a radio-frequency (RF) pulse on a single P1 center. To take into account the electron-nitrogen interaction in a single P1 center, we simulate the full time-dependent Hamiltonian under application of a single RF pulse by adding the Hamiltonian term

$$H_{\mathrm{RF}} = \Omega \cos\big(2\pi f t + \phi\big)\hat{J}_x + \frac{\gamma_e}{\gamma_n}\Omega \cos\big(2\pi f t + \phi\big)\hat{I}_x \tag{5.10}$$

where γ_e (γ_n) is the electron (nitrogen) spin gyromagnetic ratio. For the simulations, we set Ω = 250 kHz, comparable to the Rabi frequency in the experiment (Sec. 5.8.5). Then, $\Omega \gg X$ which means we can neglect the effect of the P1-P1 dipole-dipole coupling under the application of an RF pulse. Thus, it suffices to simulate the application of an RF pulse on a single P1 center, which makes the simulation of the time-dependent Hamiltonian significantly faster.

In Figs. 5.10, 5.11 the results are shown for each of the four Jahn-Teller axes separately. For each relevant RF frequency, we simulate the evolution of the system for the six different eigenstates the P1 center can be in. For a particular frequency, certain eigenstates will give signal but others do not. Hence, observing a Rabi oscillation gives information about the nitrogen spin state of the P1 center.

Next, we convert Figs. 5.10, 5.11 to truth tables in order to make it straightforward to compare against experiment. If the Rabi oscillation of a particular eigenstate dips below 0.95, we consider that to be an observable signal and indicate it with a "1" in Tables 5.1, 5.2, 5.3, 5.4. If the Rabi oscillation does not dip below 0.95, we do not consider that to be an observable signal and indicate it with a "0" in Tables 5.1, 5.2, 5.3, 5.4. The frequencies between the different tables are different, since each Jahn-Teller axis has different eigenfrequencies due to the misaligned magnetic field. This makes it relatively straightforward to determine the Jahn-Teller axis. To determine the combination of eigenstates that cause flip-flop dynamics, we use a combination of the measurements and the fitting procedure (Sec. 5.8.7).

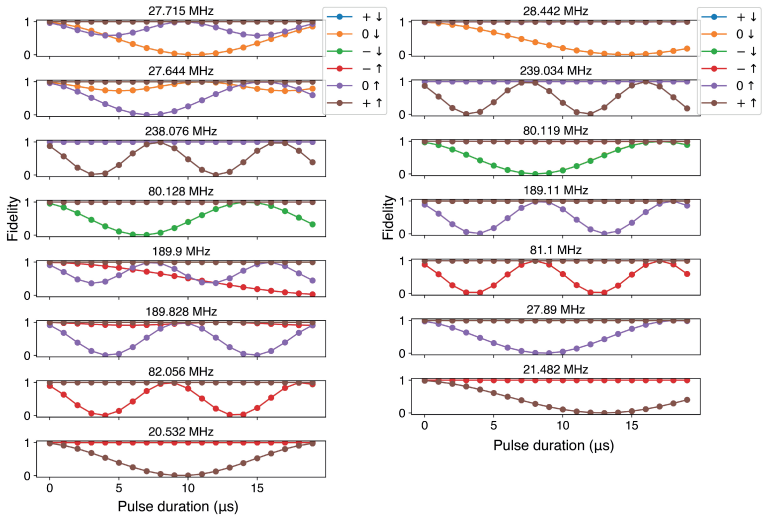

Figure 5.10: **Simulation of Rabi oscillations of a P1 center for various RF frequencies and initial states.** Rabi oscillations are simulated for two different Jahn-Teller axes A (left) and B (right). The frequency at which the RF pulse is applied is indicated on top of each plot. For each plot, we simulate the application of the RF pulse for each eigenstate. We denote the eigenstates with $-/0/+$ indicating the (approximate) nitrogen spin state and $\uparrow / \downarrow$ indicating the (approximate) electron spin state.

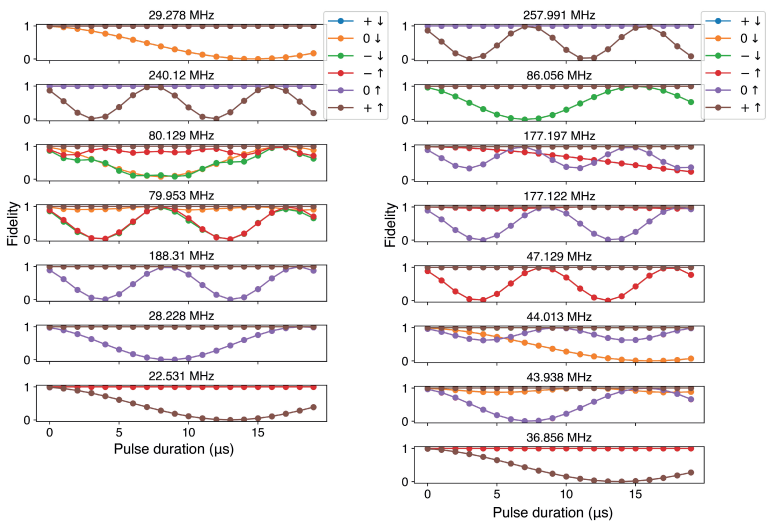

Figure 5.11: **Simulation of Rabi oscillations of a P1 center for various RF frequencies and initial states.** Rabi oscillations are simulated for two different Jahn-Teller axes C (left) and D (right). The frequency at which the RF pulse is applied is indicated on top of each plot. For each plot, we simulate the application of the RF pulse for each eigenstate. We denote the eigenstates with $-/0/+$ indicating the (approximate) nitrogen spin state and $\uparrow / \downarrow$ indicating the (approximate) electron spin state.

f (MHz)	$\|+\downarrow\rangle$	$\|0\downarrow\rangle$	$\|-\downarrow\rangle$	$\|-\uparrow\rangle$	$\|0\uparrow\rangle$	$\|+\uparrow\rangle$
27.645/27.715	1	1	0	1	1	0
238.079	1	0	0	0	0	1
80.127	0	1	1	0	0	0
189.902	1	1	0	1	1	0
189.831	1	1	0	1	1	0
82.06	0	0	1	1	0	0
20.532	0	0	0	0	1	1

Table 5.1: **Truth table for Jahn-Teller state A.** For each frequency, it is indicated per (approximate) P1 eigenstate whether a Rabi oscillation is observed ("1") or not ("0").

f (MHz)	$\|+\downarrow\rangle$	$\|0\downarrow\rangle$	$\|-\downarrow\rangle$	$\|-\uparrow\rangle$	$\|0\uparrow\rangle$	$\|+\uparrow\rangle$
28.441	1	1	0	0	0	0
239.035	1	0	0	0	0	1
80.119	0	1	1	0	0	0
189.114	0	1	0	0	1	0
81.106	0	0	1	1	0	0
27.89	0	0	0	1	1	0
21.48	0	0	0	0	1	1

Table 5.2: **Truth table for Jahn-Teller state B.** For each frequency, it is indicated per (approximate) P1 eigenstate whether a Rabi oscillation is observed ("1") or not ("0").

f (MHz)	$\|+\downarrow\rangle$	$\|0\downarrow\rangle$	$\|-\downarrow\rangle$	$\|-\uparrow\rangle$	$\|0\uparrow\rangle$	$\|+\uparrow\rangle$
29.281	1	1	0	0	0	0
240.127	1	0	0	0	0	1
80.128	0	1	1	1	0	0
79.952	0	1	1	1	0	0
188.31	0	1	0	0	1	0
28.23	0	0	0	1	1	0
22.535	0	0	0	0	1	1

Table 5.3: **Truth table for Jahn-Teller state C.** For each frequency, it is indicated per (approximate) P1 eigenstate whether a Rabi oscillation is observed ("1") or not ("0").

f (MHz)	$\|+\downarrow\rangle$	$\|0\downarrow\rangle$	$\|-\downarrow\rangle$	$\|-\uparrow\rangle$	$\|0\uparrow\rangle$	$\|+\uparrow\rangle$
257.994	1	0	0	0	0	1
86.055	0	1	1	0	0	0
177.2	1	1	0	1	1	0
177.125	0	1	0	0	1	0
47.132	0	0	1	1	0	0
43.938/44.013	1	1	0	1	1	0
36.856	0	0	0	0	1	1

Table 5.4: **Truth table for Jahn-Teller state D.** For each frequency, it is indicated per (approximate) P1 eigenstate whether a Rabi oscillation is observed ("1") or not ("0").

5.8.5. RF RABI OSCILLATIONS

To assign Jahn-Teller axes and nitrogen spin states to signals observed at different values of the interpulse delay τ, we measure Rabi oscillations and compare the frequencies at which signal was observed against Tables 5.1, 5.2, 5.3, 5.4. In Figure 5.12 we show the observed Rabi oscillations for each value of τ. The contrast for $\tau = 18.6$ μs is relatively poor, since there are other resonances close by (Fig. 5.2).

Due to mixing of the electron spin and nitrogen spin (Sec. 5.8.2), the combinations of P1 eigenstates that can generate flip-flop dynamics can also include nitrogen spin flips. In particular, $|0\downarrow\rangle$ and $|-\uparrow\rangle$ as well as $|0\uparrow\rangle$ and $|+\downarrow\rangle$ are mixed at our magnetic field and can therefore exhibit flip-flop dynamics. In Table 5.5 we show the Jahn-Teller axes and potential flip-flop states for each value of τ that we obtain from the combination of the Rabi oscillation experiments in Fig. 5.12 and Tables 5.1, 5.2, 5.3, 5.4. To evaluate which of the potential flip-flop states correspond to our observed dynamics, we enter all this information into the fit (Sec. 5.8.7). Then, we obtain the fitted flip-flop states as shown in Table 5.5.

τ (us)	Jahn-Teller axis	potential flip-flop states	fitted flip-flop states
11.2	B	$\|+\uparrow\rangle, \|+\downarrow\rangle$ or $\|+\downarrow\rangle, \|0\uparrow\rangle$	$\|+\uparrow\rangle, \|+\downarrow\rangle$
14.0	A	$\|0\downarrow\rangle, \|-\uparrow\rangle$ or $\|-\uparrow\rangle, \|-\downarrow\rangle$	$\|-\uparrow\rangle, \|-\downarrow\rangle$
16.4	A	$\|0\uparrow\rangle, \|0\downarrow\rangle$	$\|0\uparrow\rangle, \|0\downarrow\rangle$
18.6	D	$\|0\uparrow\rangle, \|+\downarrow\rangle$ or $\|+\uparrow\rangle, \|+\downarrow\rangle$	$\|+\uparrow\rangle, \|+\downarrow\rangle$
29.0	B	$\|0\uparrow\rangle, \|0\downarrow\rangle$	$\|0\uparrow\rangle, \|0\downarrow\rangle$

Table 5.5: **Potential and fitted flip-flop states for each measured τ.** Each row indicates the Jahn-Teller axis, potential and fitted flip-flop states for the indicated value of τ. The first index of the ket refers to the nitrogen spin, the second to the electron spin. When for example $|+\uparrow\rangle, |+\downarrow\rangle$ are the indicated basis states resulting in flip-flop dynamics, the corresponding P1-P1 eigenstates are $\frac{1}{\sqrt{2}}(|+\uparrow+\downarrow\rangle \pm |+\downarrow+\uparrow\rangle)$.

5.8.6. MAGNETIC FIELD FLUCTUATIONS

The external magnetic field (orientation) can change the P1-P1 electron-electron dipole interaction. The magnetic field fluctuations result from temperature fluctuations of the permanent magnets and from the presence of 6-9 T magnetic field systems in nearby laboratories. The effect of these fluctuations on the measured dipole-dipole interaction (Fig. 5.14) could ultimately limit the accuracy of the fitted P1-P1 position. To that end, we quantify the external magnetic field fluctuations by monitoring four single P1 frequencies using double electron-electron resonance (DEER). See Ref.[36] for more details.

The result is shown in Fig. 5.13. These are all the magnetic field measurements taken during the experimental period in which the Ramsey measurements in Fig. 5.3 were measured. Typical B_x, B_y fluctuations are on the order of 30 mG and the B_z fluctuation is 3 mG. The relative stability of B_z can be explained by the periodic optimisation of the NV electron $m_s = 0$ to $m_s = -1$ frequency. However, during periods of the measurements, larger drifts are observed of about 100 mG peak-to-peak in B_x, B_y and 20 mG in B_z. In both these regimes, we quantify the effect of such fluctuations on the measured dipolar coupling (Fig. 5.14). On average we find fluctuations with a standard deviation of $\sigma \sim 30$

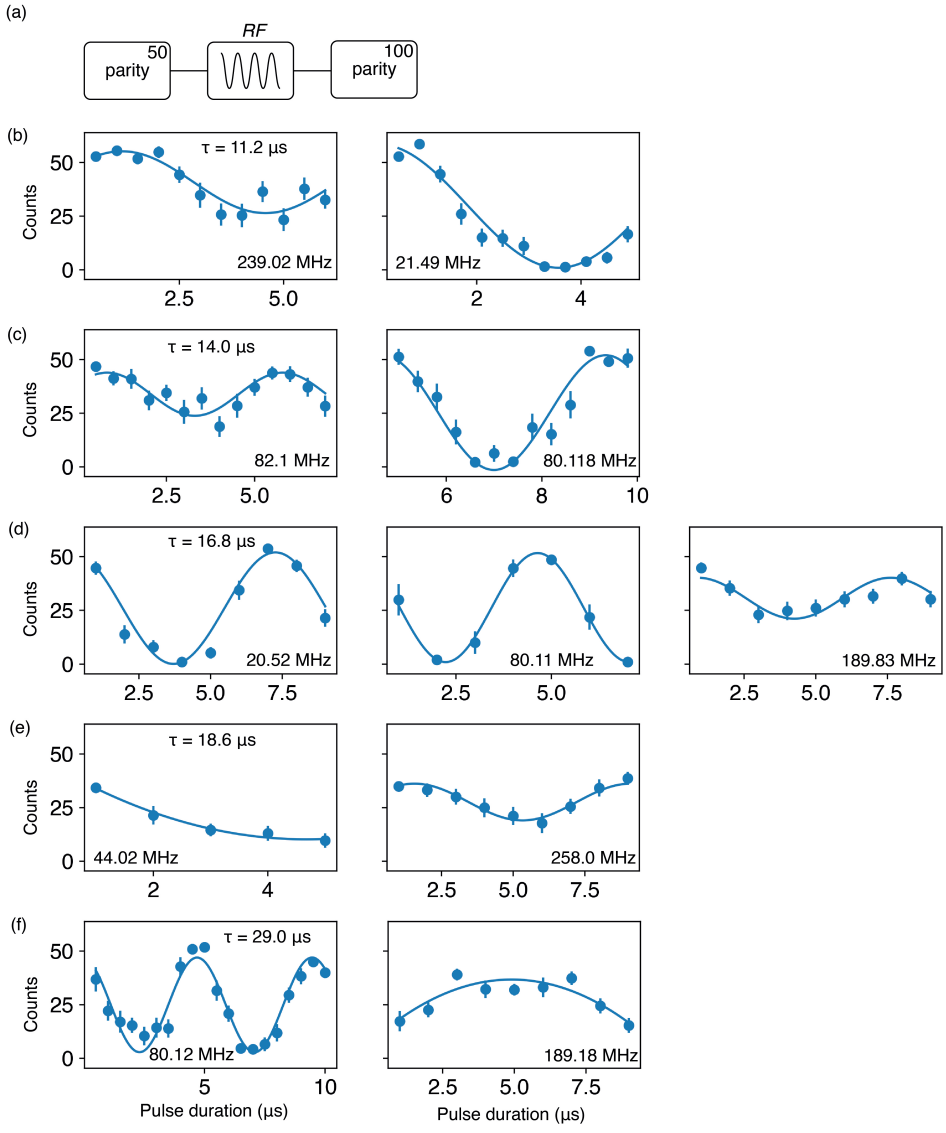

Figure 5.12: **Rabi oscillations for different interpulse delays τ. (a)** Experimental sequence. We use 50 parity readouts to initialize the spin pair in the antiparallel subspace by selecting on $\geq 15/50$ counts. The value of the interpulse delay τ in the parity readout determines which combination of Jahn-Teller and nitrogen spin state we are initializing. Then a radio-frequency (RF) pulse is applied. If resonant, the spin pair can flip to the parallel subspace and a Rabi oscillation is observed. **(b)** Results for $\tau = 11.2$ μs. **(c)** Results for $\tau = 14.0$ μs. **(d)** Results for $\tau = 16.8$ μs. **(e)** Results for $\tau = 18.6$ μs. **(f)** Results for $\tau = 29.0$ μs. **(b-f)** The corresponding RF frequencies are given in the inset of each plot.

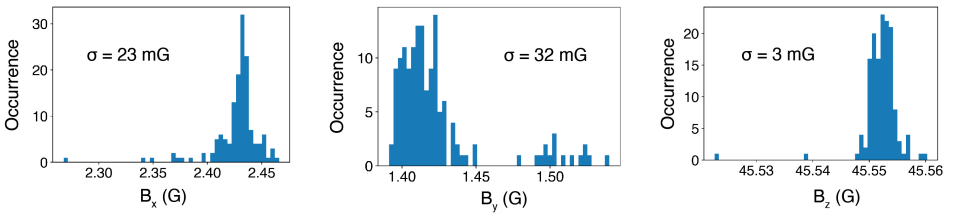

Figure 5.13: **Magnetic field fluctuations during Ramsey experiments.** We plot the magnetic fields in the x, y and z direction during the Ramsey measurements in Fig. 5.3 of the main text. The magnetic fields are B_x = 2.43(2) G, B_y = 1.42(3) G and B_z = 45.552(3) G. The standard deviation of the distribution σ is given in the graphs. The components are obtained by measuring four single P1 frequencies using DEER. See Ref.[36] for more details.

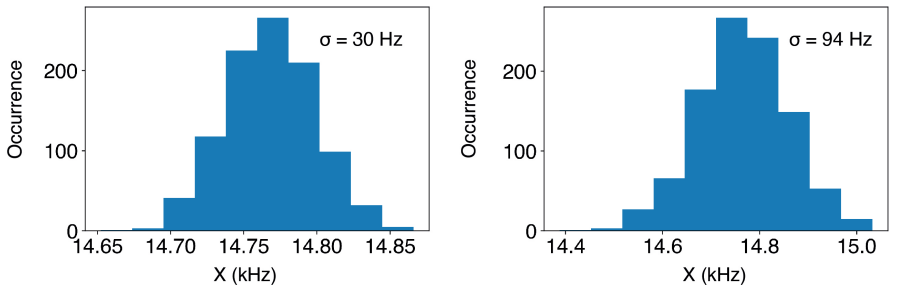

Figure 5.14: **Effect of magnetic field fluctuations on P1-P1 electron-electron coupling.** We calculate the effective P1-P1 electron-electron dipolar coupling with the NV in $m_s = 0$ for various magnetic fields. Specifically, we take the obtained P1-P1 position and monitor the dipolar coupling when both P1 centers are in the Jahn-Teller state A and the nitrogen-spin state $m_I = 0$. The magnetic field is $\mathbf{B} = [2.43(2), 1.42(3), 45.552(3)]$ G. On top of that, we add a random fluctuation on each value drawn from a Gaussian distribution with set standard deviations. (left) The fluctuations on B_x and B_y are 30 mG and the fluctuation on B_z is 3 mG, consistent with σ in Fig. 5.13. (right) The fluctuations on B_x and B_y are 100 mG and the fluctuation on B_z is 20 mG, consistent with the approximate peak-to-peak values in Fig. 5.13. In this worst-case scenario we obtain an error on the dipolar coupling of < 1%.

Hz, which amounts to 0.2% relative to the dipolar coupling.

5.8.7. IMAGING THE SYSTEM

Combining the P1-P1 couplings obtained in this work with the NV-P1 couplings reported in previous work in this sample[36], we aim to resolve the spatial configuration of the NV-P1-P1 system. In our simulations, we construct a function that, given a magnetic field $\mathbf{B}$ and spatial configuration of the P1 centers, returns a set of couplings $\mathbf{C}$:

$$f(\mathbf{B}, \mathbf{r}_{12}, \mathbf{r}_{23}) = \mathbf{C} \tag{5.11}$$

where

$\mathbf{r}_{12} = [r_{12}, \theta_{12}, \phi_{12}]$	vector from the NV center to the first P1 center
$\mathbf{r}_{23} = [r_{23}, \theta_{23}, \phi_{23}]$	vector from the first P1 center to the second P1 center

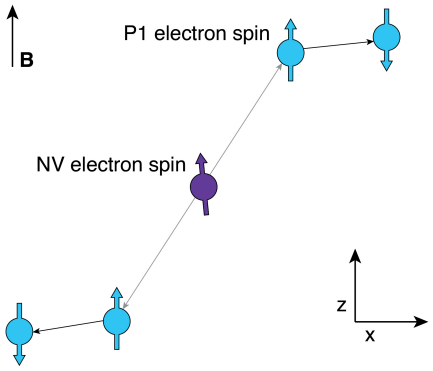

Figure 5.15: **Inversion symmetric solutions of the spatial configuration of the NV-P1-P1 system.** We find the relative position of one P1 center to the other. Due to the system's symmetry there are two possible solutions. For each, there is one unique solution for the relative position of both P1 centers to the NV.

To resolve the physical position of the three defects, we use the least-squares fitting method *scipy.optimize.leastq* which uses the Levenberg-Marquadt algorithm. Using the function in Eq. (5.11), we provide a set of measured couplings $\mathbf{C}'$ and request a position that minimizes the residual sum of squares (RSS) between the calculated and measured couplings sets: $\mathbf{C}'$ and $\mathbf{C}$. The $\mathbf{B}$-field is a known and therefore fixed parameter. Finally, the errors on the obtained variables are the standard deviations. They are calculated from the covariance matrix of the variables returned from the fitting procedure.

We first find the relative position between the two P1 centers, which we label S_1 and S_2. We obtain two possible solutions. These are the two mirrored vectors corresponding to a permutation of the two P1 centers: $S_1 \rightarrow S_2$ or $S_2 \rightarrow S_1$. This symmetry is expected, due to the symmetry of the dipolar coupling. We then lock the P1-P1 position to one of the above vectors and find the position of the NV center with respect to the P1 pair. In total, this allows for two symmetrically inverted solutions. Figure 5.15 shows a simplified schematic of the two possible solutions.

BENCHMARKING

To quantitatively analyse the performance of our imaging algorithm, we benchmark the fitting method in this section, for both the P1-P1 and NV-P1 pair, on numerically generated data for which the ground truth is known. We generate 10 random positions, calculate the exact couplings between the defects and introduce random errors on the couplings that reflects our measurement uncertainties. We sample these coupling errors from a normal distribution with a standard deviation of 0.2%, reflecting the standard deviation of the magnetic field fluctuations during our experiments in Section 5.8.6. We then apply our imaging algorithm and examine its performance by comparing the generated positions with the positions obtained through our fitting method. Due to multiple local minima of the function in Eq. (5.11), the fitting results are sensitive to the initial guess. To tackle this, we fit each case with randomly generated initial guesses; 300 and 400 for the P1-P1 and NV-P1 pair systems respectively. Finally, we accept the outcome

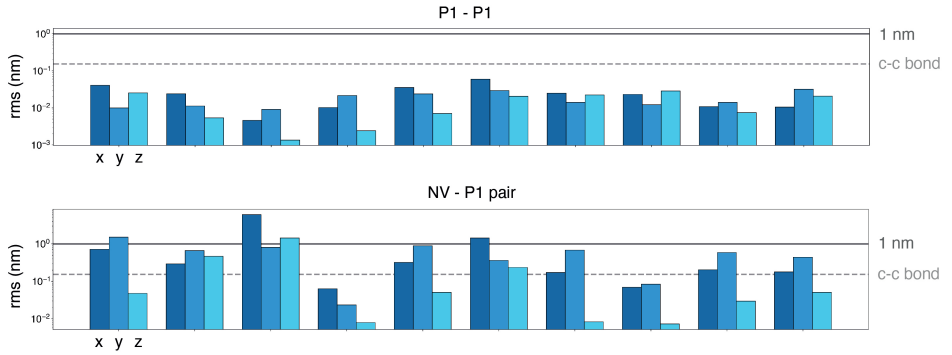

Figure 5.16: **Benchmarking of the fitting algorithm for the P1-P1 position and for the position of the NV center.** For the P1-P1 imaging benchmarking (top) we generate 10 random positions and calculate the exact couplings between them. We then create 200 different erroneous coupling sets and execute our imaging process, with 300 initial guesses for each set. We accept the fit result with the lowest RSS value to the exact couplings and calculate the average deviation from the true position, in Cartesian coordinates. We repeat the same procedure to image the pair with respect to the NV center (bottom), where the P1 centers are explicitly set to their relative position, as obtained from the experimental couplings. We use 400 initial guesses. Note that although for the P1-P1 position, we achieve a resolution better than the diamond bond length, for the NV positions some errors exceed the nanometer mark.

with the lowest RSS as the final position.

PERMUTATIONS

As discussed in Section 5.8.4, the RF measurements provide insight into the Jahn-Teller axis and nitrogen spin state corresponding to a particular interpulse delay τ. However, as discussed in Section 5.8.5, we cannot uniquely identify the Jahn-Teller and nitrogen spin state of the P1 pair directly from those measurements. Using the fitting algorithm described above, we consider all the possible states of the system, as indicated in Table 5.5. Figure 5.17 shows the RSS values of the least square optimization method, for the 8 possible permutations. The assignment with the lowest RSS value corresponds to the states where the nitrogen spin is fixed. For a more detailed discussion on the the effect of electron-nitrogen spin mixing on the observed dynamical decoupling spectrum, see Section 5.8.2.

5.8.8. SIMULATION OF DYNAMICAL DECOUPLING SPECTRUM

The obtained NV-P1-P1 positions allow us to simulate the dynamical decoupling spectrum measured in Fig. 5.2d. The result is shown in Fig. 5.2e. We observe good qualitative agreement between the simulated dynamical decoupling spectrum and the measured spectrum.

To simulate the spectrum, we have to consider all possible Jahn-Teller axes and P1-P1 eigenstates. Therefore, we simulate the dynamical decoupling signal of the NV center electron spin for each Jahn-Teller axis and for each corresponding eigenstate of the P1-P1 Hamiltonian. We then convert the simulated fidelity to an observable number of counts. When the NV center electron spin is in $m_s = 0$, the probability of measuring a photon

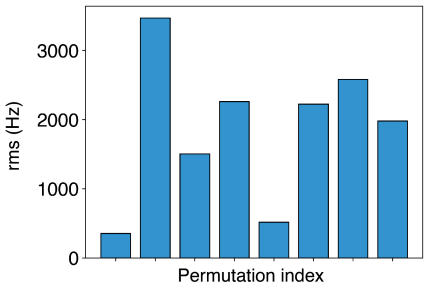

Figure 5.17: **Comparison of the RSS value for all possible nitrogen spin state assignments.** We fit the experimental couplings for all the possible nitrogen spin state combinations allowed by the RF measurements in Section 5.8.5. The permutations are indexed according to Table 5.6. The assignment with the lowest residual is the nitrogen spin state assignment where the nitrogen spin is always the same for both P1 centers.

Perm. Index	$\tau = 11.2\mu$s (B)	$\tau = 14.0\mu$s (A)	$\tau = 16.4\mu$s (A)	$\tau = 18.6\mu$s (D)	$\tau = 29.0\mu$s (B)
1	$\|+\uparrow\rangle, \|+\downarrow\rangle$	$\|-\uparrow\rangle, \|-\downarrow\rangle$	$\|0\uparrow\rangle, \|0\downarrow\rangle$	$\|+\uparrow\rangle, \|+\downarrow\rangle$	$\|0\uparrow\rangle, \|0\downarrow\rangle$
2	$\|+\uparrow\rangle, \|+\downarrow\rangle$	$\|-\uparrow\rangle, \|-\downarrow\rangle$	$\|0\uparrow\rangle, \|0\downarrow\rangle$	$\|0\uparrow\rangle, \|+\downarrow\rangle$	$\|0\uparrow\rangle, \|0\downarrow\rangle$
3	$\|+\uparrow\rangle, \|+\downarrow\rangle$	$\|0\downarrow\rangle, \|-\uparrow\rangle$	$\|0\uparrow\rangle, \|0\downarrow\rangle$	$\|+\uparrow\rangle, \|+\downarrow\rangle$	$\|0\uparrow\rangle, \|0\downarrow\rangle$
4	$\|+\uparrow\rangle, \|+\downarrow\rangle$	$\|0\downarrow\rangle, \|-\uparrow\rangle$	$\|0\uparrow\rangle, \|0\downarrow\rangle$	$\|0\uparrow\rangle, \|+\downarrow\rangle$	$\|0\uparrow\rangle, \|0\downarrow\rangle$
5	$\|+\downarrow\rangle, \|0\uparrow\rangle$	$\|-\uparrow\rangle, \|-\downarrow\rangle$	$\|0\uparrow\rangle, \|0\downarrow\rangle$	$\|+\uparrow\rangle, \|+\downarrow\rangle$	$\|0\uparrow\rangle, \|0\downarrow\rangle$
6	$\|+\downarrow\rangle, \|0\uparrow\rangle$	$\|-\uparrow\rangle, \|-\downarrow\rangle$	$\|0\uparrow\rangle, \|0\downarrow\rangle$	$\|0\uparrow\rangle, \|+\downarrow\rangle$	$\|0\uparrow\rangle, \|0\downarrow\rangle$
7	$\|+\downarrow\rangle, \|0\uparrow\rangle$	$\|0\downarrow\rangle, \|-\uparrow\rangle$	$\|0\uparrow\rangle, \|0\downarrow\rangle$	$\|+\uparrow\rangle, \|+\downarrow\rangle$	$\|0\uparrow\rangle, \|0\downarrow\rangle$
8	$\|+\downarrow\rangle, \|0\uparrow\rangle$	$\|0\downarrow\rangle, \|-\uparrow\rangle$	$\|0\uparrow\rangle, \|0\downarrow\rangle$	$\|0\uparrow\rangle, \|+\downarrow\rangle$	$\|0\uparrow\rangle, \|0\downarrow\rangle$

Table 5.6: **The possible nitrogen spin state assignments for all values of τ.** We fit the measured couplings to all the possible combinations allowed by the Tables 5.1-5.4. The permutation index respects the order of Fig. 5.17. The first entry of the denoted states refers to the nitrogen spin of the P1 center and the second to the electron spin. Each column indicates the possible flip-flop states for that particular interpulse delay τ. The top of each column also indicates the corresponding Jahn-Teller axis in brackets.

count is 70%. And when the electron spin is in $m_s = -1$, the probability of not measuring a photon count is 99%. Given the 200 repetitive dynamical decoupling repetitions, we can thus convert the simulated NV electron spin fidelity to the experimental number of counts. Finally, we add Poissonian noise on the photon counts to simulate shot noise.

Given the expected signal per Jahn-Teller axis and corresponding eigenstate, we now assume each Jahn-Teller axis and eigenstate has equal probability of occurrence. Then, we sum all the individual signals and normalise the result. This procedure results in the simulated dynamical decoupling signal in Fig. 5.2e.

In the simulated spectrum, we observe signal originating from flip-flop states that only involve the electron spin, but we also observe signal from the more complex flip-flop states that involve both the nitrogen and the electron spin. The latter signals mainly occur at $\tau = 20 - 25$ μs (Sec. 5.8.2). In the experimental data (Fig. 5.2d) we also see clear signal at these values of τ, indicating that we observe flip-flop dynamics involving the nitrogen spin in experiment.

5.8.9. RAMSEY DATA WITH THE NV ELECTRON SPIN IN $m_s = -1$

In the main text, we perform Ramsey experiments at five values of the interpulse delay τ (Fig. 5.3). For these measurements, the NV electron spin is in $m_s = 0$ during free evolution. This is done to isolate the P1-P1 dipolar coupling from the NV-P1 dipolar couplings. In that way, we can fit to the P1-P1 position first before bringing in the NV electron spin.

In Fig. 5.18 we show the Ramsey experiments for each of the five values of τ with the NV electron spin in $m_s = -1$. Next to the major contribution of the P1-P1 dipolar coupling, we also get a contribution of the NV-P1 dipolar coupling, which adds a detuning to the P1-P1 coupling and thereby alters the measured flip-flop frequency. In Table 5.7 we compare the measured evolution frequencies of the Ramsey experiment to the expected values from the NV-P1-P1 position found in the main text. Overall we find good agreement, but we do observe deviations of up to a few hundred Hz. In particular, the deviations for $\tau = 16.4$ μs and $\tau = 18.6$ μs with the NV electron spin in $m_s = -1$ are larger than expected. Currently we cannot explain these deviations.

An additional observation from Fig. 5.18 is that the inhomogeneous dephasing times with the NV electron spin in $m_s = -1$ are about an order of magnitude smaller than those with the NV electron spin in $m_s = 0$. This is expected, since the additional presence of the NV electron spin brings the P1 electron spin pair away from the anticrossing making it more susceptible to magnetic field noise.

τ (us)	measured $f_{m_s=-1}$ (kHz)	calculated $f_{m_s=-1}$ (kHz)	measured $f_{m_s=0}$ (kHz)	calculated $f_{m_s=0}$ (kHz)
11.2	22.52(1)	22.378	22.152(2)	22.106
14.0	18.160(7)	18.323	17.943(1)	18.114
16.4	15.55(9)	15.027	14.87(8)	14.837
18.6	13.21(6)	13.856	13.7(1)	13.414
29.0	8.80(4)	8.892	8.2(3)	8.591

Table 5.7: **Measured and calculated frequencies of the P1 electron spin pair.** For each τ, we indicate the measured frequency when the NV electron spin is in $m_s = -1$ as well as the calculated frequency based on the obtained position in the main text. For completeness, we also note the frequencies when the NV electron spin is in $m_s = 0$.

5.8.10. DEPHASING MECHANISMS

In this section we discuss the mechanisms involved in the P1-P1 electron-spin pair T_2^*. The spin pair dephasing originates from magnetic field fluctuations, either from the permanent magnets used to apply our magnetic field or from the local spin baths surrounding the spin pair. The electron spin pairs in our diamond are surrounded by two different spin baths:

- ^{13}C spin bath with a concentration of $\sim 0.01\%$ [12]
- P1 electron spin bath with an estimated concentration of ~ 75 ppb [36]

The combined noise of the external magnetic field and the two local spin baths can have a different effect on the two P1 centers forming the pair, which we will denote as δB_1 and δB_2 respectively. These noise terms affect the evolution frequency of the spin pair, which results in dephasing. To solve this generally, we have to consider the full

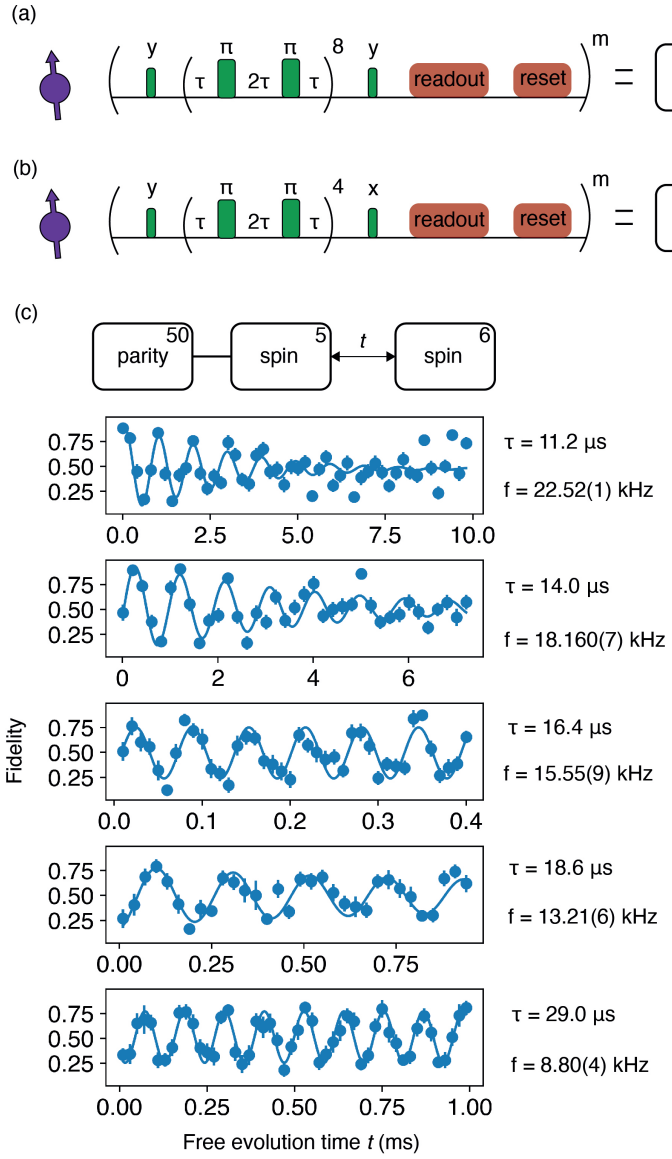

Figure 5.18: **Ramsey measurements of the P1 electron spin pair when the NV electron spin is in $m_s = -1$. (a,b)** Pulse sequences to measure the parity ($\{|\uparrow\uparrow\rangle, |\downarrow\downarrow\rangle\}$ vs $\{|\uparrow\downarrow\rangle, |\downarrow\uparrow\rangle\}$) and spin ($\{|\uparrow\downarrow\rangle\}$ vs $\{|\downarrow\uparrow\rangle\}$) of the electron spin pair. **(c)** Ramsey measurements for five different interpulse delays τ. Each τ corresponds to an identifiable dip in the dynamical decoupling spectrum of Fig. 5.2d. The obtained frequency f as well as the interpulse delay τ used are indicated on the right.

effect of $\delta B_{1,2}$ on the P1-P1 Hamiltonian, including the time dependence of $\delta B_{1,2}$. Here, we will assume that $\delta B_{1,2}$ is quasi-static, which is not necessarily true for the bath of P1 centers. Furthermore, we will consider the effects of global, correlated noise and local, uncorrelated noise separately.

CORRELATED AND UNCORRELATED NOISE

The quantisation axis of the P1 center is generally not along the direction of the external magnetic field due to the strong electron-nuclear hyperfine interaction ($\gamma_e B \sim A_\parallel, A_\perp$). Correlated noise, such as fluctuations of the global magnetic field strength, therefore has a non-negligible effect on the effective coupling X between the two electron spins. In contrast, ^{13}C nuclear spin pairs form a more ideal decoherence-free subspace, since fluctuations of the global magnetic field strength do not influence the nuclear-nuclear effective coupling at all[6]. On the other hand, uncorrelated, local noise from the spin bath affects the detuning of the two P1 center electron spins. In the pseudo-spin picture, we can write this uncorrelated noise ΔZ as[6]:

$$H = X\hat{S}_x + [m_s Z + \Delta Z]\hat{S}_z. \tag{5.12}$$

To examine the difference between the effect of correlated (global) noise and uncorrelated (local) noise on a P1-P1 electron spin pair, we simulate the P1-P1 system obtained in the main text for the resonance at $\tau = 14.0$ μs. We consider correlated noise to be the exact same noise on both P1 centers, also in magnitude, and uncorrelated noise to be completely independent noise on each P1 center. To simulate correlated noise, we vary the z-component of the external magnetic field with a standard deviation of $\sigma = 0.3$ mG, which corresponds to the estimated noise from the nuclear spin bath (Fig. 5.19a). To simulate uncorrelated noise, we vary the z-component of the external magnetic field for only one of the two P1 centers (Fig. 5.19b). From the results in Fig. 5.19, we conclude that the effect on the spin pair frequency of correlated noise is negligible compared to the effect of uncorrelated noise.

Additionally, the two types of noise result in different distributions, which can be understood from the different origins of noise. Correlated noise does not affect the detuning Z between the two spins, but it does affect the coupling X. The noise therefore adds linearly to X, leading to a relatively symmetric distribution. On the other hand, uncorrelated noise adds quadratically to the frequency, as is shown in Equation 5.12. This results in a one-sided distribution, as the effect of negative and positive noise ΔZ is the same. Figure 5.19b also highlights that the spin pair is only second-order sensitive to uncorrelated noise and therefore forms a clock transition.

For similar magnitudes of correlated and uncorrelated noise, the uncorrelated noise dominates in limiting the T_2^* of a spin pair. In other words, it is the difference between δB_1 and δB_2 that determines ΔZ, which is the main contributor to the inhomogeneous dephasing of the spin pair.

NUCLEAR SPIN BATH

To estimate the typical noise strength from both the nuclear spin bath and the electron spin bath, we consider the NV electron spin T_2^*, which is measured to be 94(2) μs[12].

Noise source	Magnitude	Type	Pseudo-spin effect	Expected T_2^*
Nuclear spin bath	0.89(4) kHz	Mostly uncorrelated	X, Z	~ 10 – 40 ms
P1 spin bath	2.22(5) kHz	Uncorrelated & correlated	X, Z	Uncorrelated: ~ 5 ms Correlated: $\gg$ 1 s
External B-field	$[\sigma_x, \sigma_y, \sigma_z]$ = [23, 32, 3] mG $[\sigma_x, \sigma_y, \sigma_z]$ = [3, 3, 3] mG	Correlated	X	~ 7.5 ms ~ 83 ms

Table 5.8: **Summary of noise sources and their effects.** For each noise source, we summarise their magnitude, type (correlated or uncorrelated), expected T_2^* and whether that noise source mainly affects the coupling between the spins X or whether it affects both the coupling X and the detuning between the two spins Z.

Assuming quasi-static, Gaussian noise this gives a standard deviation of the frequency of $\sigma_f = \frac{1}{\sqrt{2}\pi T_2^*} = 2.39(5)$ kHz.

To estimate what part of this noise is typically due to the ^{13}C bath, we follow Ref. [12] where the T_2^* of a ^{13}C spin due to the ^{13}C bath in the same device was measured to be 0.66(3) s. This gives $\sigma_f = 0.34(2)$ Hz. To convert this to the noise on the electron spin, we multiply by $\frac{\gamma_e}{\gamma_c}$ where γ_e (γ_c) is the electron (^{13}C) gyromagnetic ratio. We obtain $\sigma_f = 0.89(4)$ kHz. As an alternative approach, we simulate 10^4 configurations of ^{13}C spins surrounding an electron spin with a concentration of 0.01%. The result is shown in Fig. 5.20. The average noise an electron spin experiences due to a ^{13}C bath is 1.2 kHz, similar to the value of 0.89(4) kHz obtained from the measurement in Ref. [12]. Note that the exact values for each spin depend strongly on the local environment, and therefore these numbers should only be interpreted as estimates for typical values of the standard deviation of the noise and its distribution.

Importantly, the ^{13}C spins are relatively close to the P1 centers. Therefore, the noise due to the ^{13}C spins on both P1 centers of the pair is likely uncorrelated (local), although we cannot quantify how uncorrelated it is exactly. Since the effect of uncorrelated noise relative to correlated noise is large, we can follow the analyses of Dobrovitski et al. [56] and Bartling et al. [6] to analyse Equation 5.12. We plot the analytical solution in Fig. 5.22a for a quasi-static bath with a noise magnitude of 0.3 mG and a coupling $X = 18.114$ kHz. We roughly reproduce the timescales of the observed decay, suggesting that the uncorrelated noise from the ^{13}C spin bath plays an important role in limiting the P1 pair inhomogeneous dephasing time. Note that we have assumed that all estimated ^{13}C bath noise is uncorrelated, while it is conceivable it is partially correlated. That would increase the inhomogeneous dephasing time in Fig. 5.22a.

ELECTRON SPIN BATH

We estimate the noise from the electron spin bath on a single electron spin considering the noise on the NV center (2.39(5) kHz) and the nuclear spin bath noise (0.89(4) kHz): $b_{\text{electron}} = \sqrt{b_{\text{total}}^2 - b_{\text{nuclear}}^2} = 2.22(5)$ kHz. This noise figure consists of a correlated and an uncorrelated part on the pair of P1 centers. We do not know exactly what part of the 2.22(5) kHz noise is correlated and what part is uncorrelated. In Fig. 5.21 we show the effect of the P1 bath noise either being fully correlated or fully uncorrelated. When we assume the noise to be fully correlated, we obtain a modulation of the coupling X with a standard deviation of 6 mHz, resulting in T_2^* values exceeding a second.

When the noise is uncorrelated, we can perform the same analysis as for the nuclear

spins. We follow the analyses of Dobrovitski et al.[56] and Bartling et al.[6] to analyse Equation 5.12. This results in the dephasing as shown in Fig. 5.22b. We observe a decay time of a few milliseconds. Note that in this analysis we assume that the P1 bath is quasi-static, which is likely not a valid assumption for longer times.

EXTERNAL MAGNETIC FIELD

The long-term magnetic field fluctuations are $\sigma_x = 23$ mG, $\sigma_y = 32$ mG and $\sigma_z = 3$ mG. In Figure 5.14 we simulate the effect of external magnetic field fluctuations on the electron-electron coupling. Due to the relative magnitude of the σ_x and σ_y fluctuations, a significant standard deviation of $\sigma = 30$ Hz on the electron-electron coupling is obtained. This translates to $T_2^* \approx 7.5$ ms, smaller than the observed value of $T_2^* = 44(9)$ ms.

For the Bloch vector measurements in Fig. 5.2d, we measure $\langle Y \rangle$ and $\langle Z \rangle$ for each point after which we obtain the Bloch vector length as $\sqrt{\langle Y \rangle^2 + \langle Z \rangle^2}$. Slow magnetic field fluctuations over the course of the measurement do not affect the Bloch vector measurement as much as a Ramsey measurement. Only the relative phase between $\langle Y \rangle$ and $\langle Z \rangle$ within a single data point is prone to fluctuations, but the Bloch vector measurement is not sensitive to different external magnetic fields between data points, contrary to a Ramsey measurement.

In our experiment, the external magnetic field fluctuations are typically much slower than the duration of a single measurement point. If we then assume more conservative fluctuations during the Bloch vector measurement of $\sigma_x = \sigma_y = \sigma_z = 3$ mG, we observe an effect on the coupling X as shown in Fig. 5.23. The standard deviation on the coupling X is 2.7 Hz, which translates to $T_2^* = 83$ ms.

We conclude that all three noise sources can have a significant effect on the observed inhomogeneous dephasing time of $T_2^* = 44(9)$ ms. In Table 5.8 we summarise the effects of the three noise sources.

For the nuclear and electron spin baths, the correlated noise is negligible compared to the uncorrelated noise. The nuclear spin bath noise is likely more uncorrelated due to their closeness to the P1 centers. However, it is unclear exactly what part of the noise is correlated and what part is uncorrelated. To obtain a more thorough description of the spin bath noise, the complex dynamics of the P1 bath would have to be taken into account using for example correlated cluster expansion (CCE).

The magnetic field fluctuations are larger in magnitude, but only introduce correlated noise. The Bloch vector length measurement is crucial to mitigate the longer-time fluctuations of the external magnetic field.

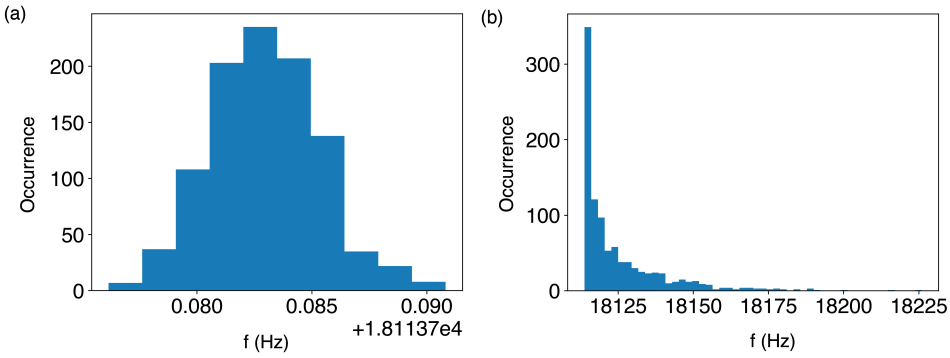

Figure 5.19: **Simulation of the effect of correlated and uncorrelated noise of the nuclear spin bath on the two P1 centers at τ = 14.0 µs.** We simulate the P1-P1 system discussed in this paper for Jahn-Teller axis A and nitrogen spin state $m_I = -1$, which corresponds to the resonance at τ = 14.0 µs. Then, we calculate the effective electron-electron coupling for two different situations. **(a)** We add noise with a standard deviation of $\sigma = 0.3$ mG to the z-direction of the external magnetic field. The value of 0.3 mG corresponds to the estimated noise due to the ^{13}C bath. In this simulation, we assume the noise is common to both P1 centers and therefore correlated. Therefore, its main effect is to modulate the effective electron-electron coupling. **(b)** We vary the magnetic field in the z-direction of only one of the P1 centers. The standard deviation is also $\sigma = 0.3$ mG. This simulation emulates the noise from nearby nuclear spins that have a different effect on each of the P1 centers forming the pair. The noise is therefore uncorrelated.

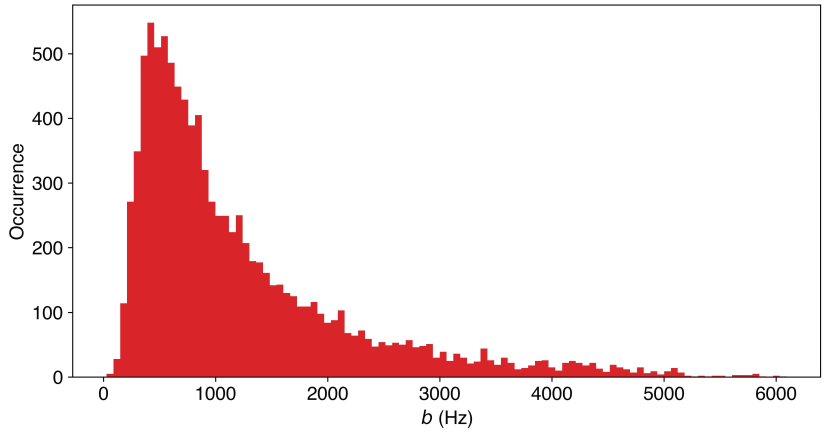

Figure 5.20: **Simulated electron spin noise for varying ^{13}C spin configurations.** We simulate 10^4 configurations of ^{13}C spins surrounding an electron spin in a diamond lattice for a concentration of 0.01 %. The standard deviation of the noise generated by one such ^{13}C spin bath is b. The average of the distribution is 1.2 kHz. The right tail is due to more strongly coupled spins (we excluded spins with a coupling larger than 10 kHz).

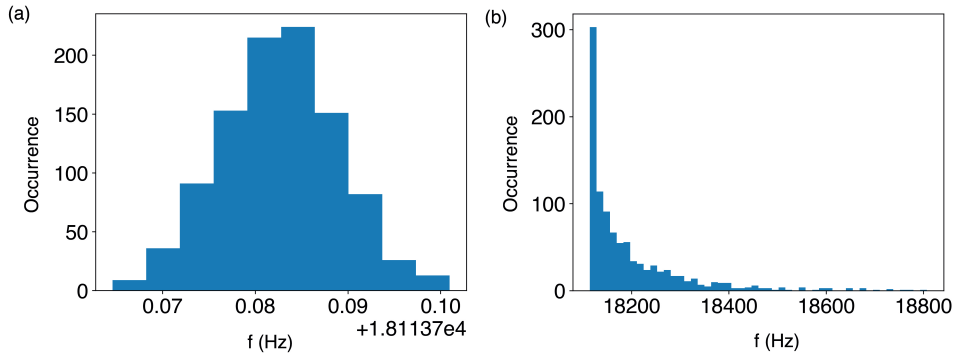

Figure 5.21: **Simulation of the effect of correlated and uncorrelated noise of the P1 bath on the two P1 centers at $\tau = 14.0$ µs.** We simulate the P1-P1 system discussed in this paper for Jahn-Teller axis A and nitrogen spin state $m_I = -1$, which corresponds to the resonance at $\tau = 14.0$ µs. Then, we calculate the effective electron-electron coupling for two different situations. **(a)** We add noise with a standard deviation of $\sigma = 0.8$ mG to the z-direction of the external magnetic field. The value of 0.8 mG corresponds to the estimated noise due to the P1 bath. This noise is common to both P1 centers and therefore correlated. Therefore, its main effect is to modulate the effective electron-electron coupling. **(b)** We vary the magnetic field in the z-direction of only one of the P1 centers. The standard deviation is also $\sigma = 0.8$ mG. This simulation emulates the noise from nearby electron spins that have a different effect on each of the P1 centers forming the pair. The noise is therefore uncorrelated.

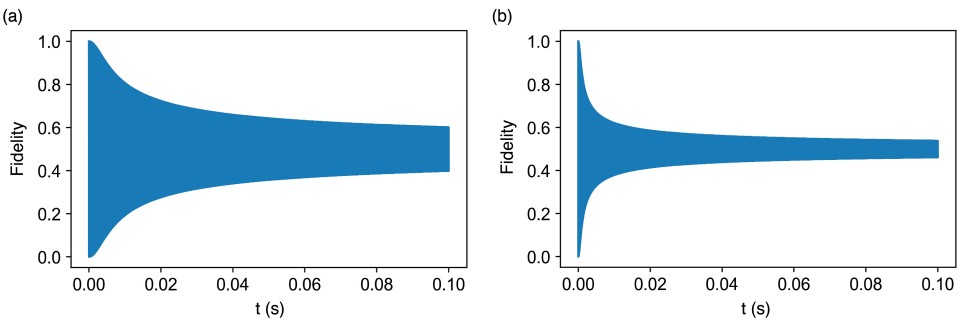

Figure 5.22: **The expected P1 pair inhomogeneous dephasing under the assumption of uncorrelated noise.** We plot the analytical solutions to Equation 5.12 obtained from Refs.[6,56]. **(a)** The spin pair coupling is $X = 18.114$ kHz and the standard deviation of the noise is 0.3 mG, consistent with the expected noise from the nuclear spin bath. We find a timescale comparable to the experimentally observed $T_2^* = 44(9)$ ms. **(b)** With a noise of 0.8 mG, consistent with the noise from the electron spin bath under the assumption that all P1 bath noise is uncorrelated and quasi-static.

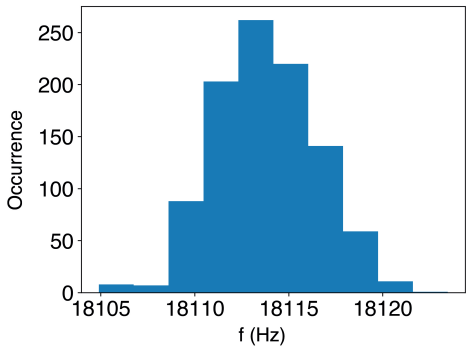

Figure 5.23: **Simulation of the effect of correlated and uncorrelated noise of the external magnetic field on the two P1 centers at $\tau = 14.0$ µs.** We simulate the P1-P1 system discussed in this paper for Jahn-Teller axis A and nitrogen spin state $m_I = -1$, which corresponds to the resonance at $\tau = 14.0$ µs. Then, we calculate the effective electron-electron coupling for a standard deviation of $\sigma = 3.0$ mG on the x-, y- and z-direction of the external magnetic field. This noise is common to both P1 centers and therefore correlated. Therefore, its main effect is to modulate the effective electron-electron coupling.

5.8.11. OPTIMIZATION OF PARITY INITIALIZATION

We perform initialization through measurement: measurements are performed to confirm that the system is currently in the desired state (JT, ^{14}N spin and spin state for both P1 centers). Due to the many possible states the P1 pair can take, the probability to start in the subspace is approximately 1/288, making initialization time consuming. In this Section, we describe how we optimize the initialization procedure for speed and fidelity, by using repeated measurements and intermediate dynamic decision making combined with the capability to scramble the states. The factor ~ 10x speed-up realized is essential for enabling the experiments.

To initialize the P1 electron spin pair, we execute m parity measurements, followed by n spin measurements. The parity measurement initializes the two electron spins of the P1 centers into the antiparallel subspace and the desired ^{14}N and JT configuration. The spin measurement initializes in one of the two antiparallel spin states. If the P1 centers are in a particular configuration, such that their coupling is resonant with the dynamical decoupling interpulse delay, the NV electron is projected into the bright state and we detect photons (Fig. 5.2). To find a robust initalization scheme, we implement repetitive parity measurements, at some specific interpulse delay τ, and obtain a time-trace for the pair, as shown in Fig. 5.2b. By collapsing the time-trace in bins of 200 parity measurements we make two observations (Fig. 5.2c). We note a well-separated peak between 120 and 150 counts. This allows us to introduce a threshold check for initialization, which we implement with 50 parity measurements. If we observe more than 15 photons in 50 parity measurements, the pair is initialized in the Jahn-Teller and nitrogen spin configuration resonant to the used interpulse delay τ, and in the anti-parallel electron spin state.

To speed up the initialization time, we introduce intermediate photon count thresholds. We check after a number of parity measurements whether we already have observed photon counts, and decide whether we want to abort and restart the initialization. For example, consider a total of 50 parity measurements with a threshold of 15 photon counts. If we perform an intermediate check at the 30th iteration and we have not detected any photons, it is highly unlikely to detect 15 photons at the 50th parity measurement. In this scenario, we abort the sequence early. We randomize the Jahn-Teller axes, and nitrogen spin states of the P1 centers by applying a green laser pulse and restart the initialization procedure[36].

We optimize for minimum initialization time by analyzing data sets such as in Fig. 5.2b with a Monte Carlo sampling method. By starting at a random point along the time trace, we emulate parity measurements of P1 pairs that are in a random Jahn-Teller and nitrogen configuration. To emulate restarting the initialization procedure, we jump to another random point along the trace, simulating the scrambling of the P1 pair Jahn-Teller axis and nitrogen spin state with the green laser.

We examine an initialization scheme with a single intermediate threshold check by sampling the data set for varying bin sizes $\Theta = 3,5,7,9$ and thresholds $\Lambda = [0,9]$. We find the minimum initialization time by sweeping over the possible thresholds Λ for each size Θ. As a figure of merit, we calculate the total time needed to achieve 5,000 successful P1 pair initializations. This is defined as both the intermediate and final check of 50 parity outcomes surpassing their respective thresholds. The results are plotted in Fig. 5.24. We

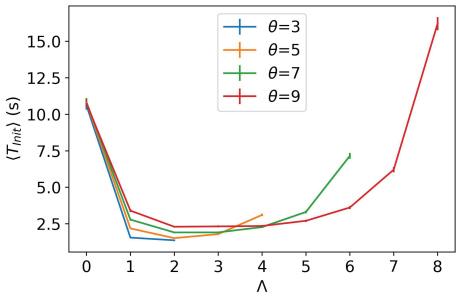

Figure 5.24: **Optimization of the initialization with a single threshold check.** We optimize the initialization time by sampling at different bin sizes θ and sweep the allowed thresholds Λ. We find that the optimal combination is $\theta = 3$ and $\Lambda = 2$, where the average initialization time is 1.38(4)s.

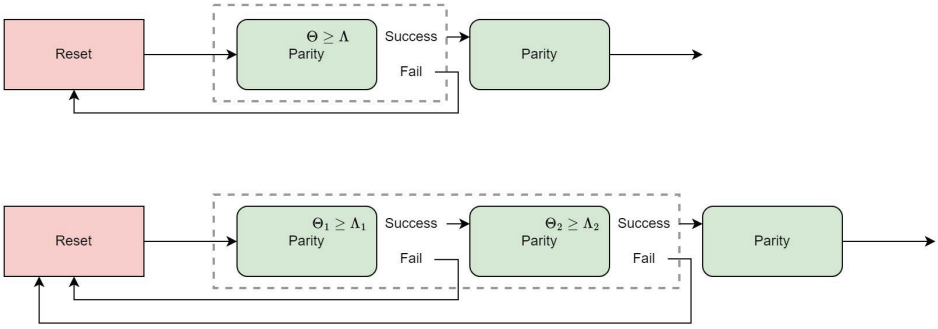

Figure 5.25: **Initialization schemes with single and double intermediate threshold checks.** For a successful initialization we check for 15 observed photons out of a total of 50 parity measurements. However, we abort the procedure at one (top) or two (bottom) intermediate stages, depending on the photon counts thus far. With intermediate checks at 2 out of 3 photons, followed by 3 out of 10, we achieve an average initialization time of 1.37(4) s.

find an optimum set of parameters for a single check of $\Theta = 3$ and $\Lambda = 2$. In this setting, the average time for each successful P1 pair initialization is 1.38(4) s. By introducing another intermediate check with bin size $\Theta = 10$ and threshold $\Lambda = 3$ the initialization time slightly improves to 1.37(4) s.

The final result provides a factor 10 improvement over the basic initialization without intermediate thresholds, essential to make the experiments feasible. We note that this is a crude coarse-grained optimisation and that more advanced methods like Bayesian inference or techniques based on machine learning are likely to provide additional speed ups.

5.8.12. SPIN READOUT CALIBRATION

In this section, we describe the optimization of the spin readout. In particular, we show results for $\tau = 11.2\,\mu$s, but note that the procedure and results are similar for other values

of τ. The experiments typically consist of a two-step initialization process, containing first parity readouts and then spin readouts, and a one-step readout process, containing only spin readouts (Fig. 5.3). The optimization of the parity initialization has been described in detail in Section 5.8.11. In the following, we will therefore assume that we aim to distinguish between the two anti-parallel states $|\uparrow\downarrow\rangle$ and $|\downarrow\uparrow\rangle$.

For spin initialization, we do not perform any real-time thresholding. Passing the parity readout is a rare event (Sec. 5.8.11) and it is therefore beneficial to collect all data. In the analysis, we then distinguish between the two pseudo-spin states by thresholding on the number of counts obtained in the spin readouts ($> 0/5$ or $< 1/5$).

During a spin readout, the electron spin-pair evolves with frequency X, the dipolar coupling between the two spins of the spin pair. To make sure that each spin readout repetition measures along the same basis, we calibrate the time between subsequent spin readouts (Fig. 5.26a). If the timing is correct, $|\uparrow\downarrow\rangle$ and $|\downarrow\uparrow\rangle$ will show a difference in obtained counts during the spin readout. The optimal timing is found around 48.5 μs. Note that the spin readout wait time has to be calibrated for each τ separately since the frequency X is different for each τ.

We perform the readout optimisation as described in the supplementary material of Ref.[6]. We also discuss the process here for completeness. The two states that we want to optimally distinguish are $|\uparrow\downarrow\rangle$ and $|\downarrow\uparrow\rangle$, which we will write as $|a\rangle$ and $|b\rangle$ for simplicity. In the initialization step, we use k repetitions and record $N(k)$ counts. We set strict thresholds to make the initialization as good as possible: $N(k) > N_a$ and $N(k) < N_b$ where N_a (N_b) is the threshold to initialize in $|a\rangle$ ($|b\rangle$). In the readout step, we use n repetitions and obtain $N(n)$ counts. To optimally distinguish states $|a\rangle$ and $|b\rangle$, we sweep a threshold T and obtain the combined initialization and readout fidelity as:

$$F = \frac{F_{|a\rangle} + F_{|b\rangle}}{2} = \frac{1}{2}P(N(n) \geq T | N(k) > N_a) + \frac{1}{2}P(N(n) < T | N(k) < N_b). \tag{5.13}$$

We then optimize F for the number of readouts n and the threshold T. In Fig. 5.26b, we show a histogram of the obtained counts for the two different spin states $|\uparrow\downarrow\rangle$ and $|\downarrow\uparrow\rangle$ for $n = 6$ spin readouts, obtained using strict initialization thresholds of $> 8/10$ and $< 1/10$. In Fig. 5.26c, we sweep the number of spin readouts n as well as the threshold T. We find an optimal number of readouts $n = 6$ with a threshold $T = 2$ obtaining a combined initialization and readout fidelity of $F = 94.8(6)\%$. In Fig. 5.26d, we show a sweep of the threshold T for $n = 6$ spin readouts, giving the optimal threshold of 2.

For each value of τ, we performed this characterization separately. However, the optimal parameters are very similar for other values of τ. Hence, the number of spin readouts $n = 6$ and threshold $T = 2$ was used for all measured values of τ.

AUTHOR CONTRIBUTIONS

H.P.B. played a leading role in all the aspects of the work, together with N.D., with support from all authors.

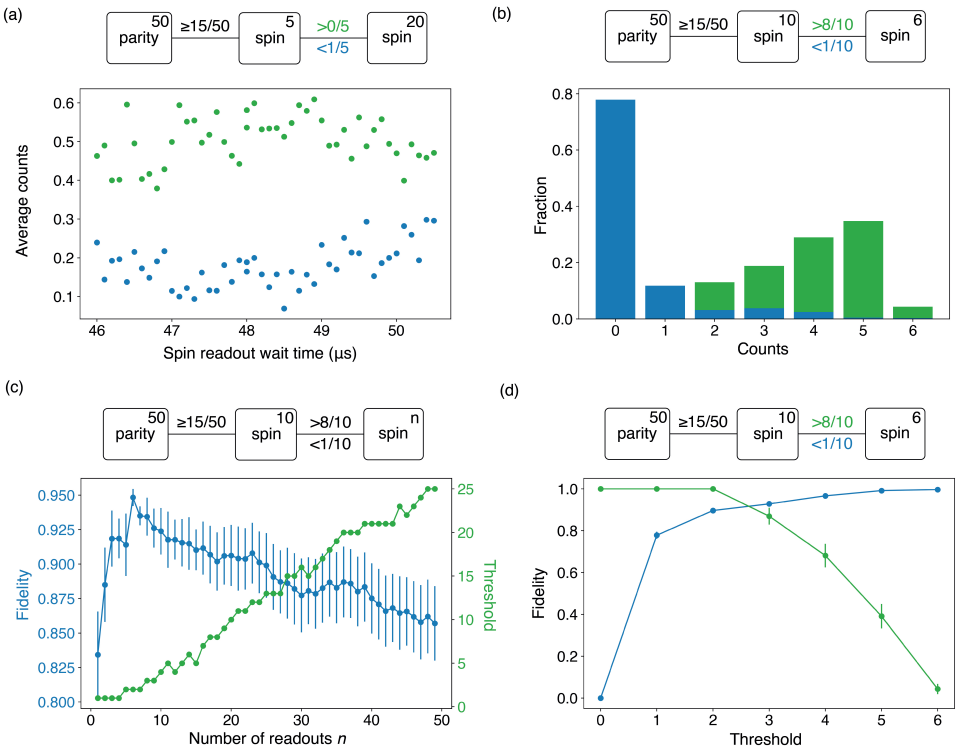

Figure 5.26: **Optimization of spin readout for $\tau = 11.2$ μs.** **(a)** Sweep of the wait time between subsequent spin readouts. We find a maximum contrast between the two spin states around 48.5 μs. **(b)** Histogram for the two different spin states $|\uparrow\downarrow\rangle$ and $|\downarrow\uparrow\rangle$ for $n = 6$ spin readouts. **(c)** Sweep of the number of readouts n, showing the optimal fidelity F and optimal threshold T for each number of readouts. **(d)** Sweep of the threshold T for $n = 6$ spin readouts. The optimal spin readout parameters are $n = 6$ readouts with a threshold of $T = 2$, giving a combined initialization and readout fidelity of $F = 94.8(6)\%$.

REFERENCES

[1] T. Taminiau *et al.*, *Detection and control of individual nuclear spins using a weakly coupled electron spin,* Phys. Rev. Lett. **109**, 137602 (2012).

[2] M. H. Abobeih *et al.*, *One-second coherence for a single electron spin coupled to a multi-qubit nuclear-spin environment,* Nat. Commun. **9**, 1 (2018).

[3] C. E. Bradley *et al.*, *A ten-qubit solid-state spin register with quantum memory up to one minute,* Phys. Rev. X **9**, 031045 (2019).

[4] M. H. Abobeih *et al.*, *Atomic-scale imaging of a 27-nuclear-spin cluster using a quantum sensor,* Nature **576**, 411 (2019).

[5] G. L. van de Stolpe *et al.*, *Mapping a 50-spin-qubit network through correlated sensing,* (2023), arXiv:2307.06939 [quant-ph] .

[6] H. P. Bartling *et al.*, *Entanglement of Spin-Pair Qubits with Intrinsic Dephasing Times Exceeding a Minute,* Physical Review X **12**, 11048 (2022).

[7] E. V. Denning, D. A. Gangloff, M. Atatüre, J. Mørk and C. Le Gall, *Collective quantum memory activated by a driven central spin,* Phys. Rev. Lett. **123**, 140502 (2019).

[8] D. M. Jackson *et al.*, *Quantum sensing of a coherent single spin excitation in a nuclear ensemble,* Nature Physics **17**, 585 (2021).

[9] A. Ruskuc, C.-J. Wu, J. Rochman, J. Choi and A. Faraon, *Nuclear spin-wave quantum register for a solid-state qubit,* Nature **602**, 408 (2022).

[10] M. Pompili *et al.*, *Realization of a multinode quantum network of remote solid-state qubits,* Science **372**, 259 (2021).

[11] S. L. N. Hermans *et al.*, *Qubit teleportation between non-neighbouring nodes in a quantum network,* Nature **605**, 663 (2022).

[12] C. E. Bradley *et al.*, *Robust quantum-network memory based on spin qubits in isotopically engineered diamond,* npj Quantum Information **8**, 122 (2022).

[13] K. S. Cujia, J. M. Boss, K. Herb, J. Zopes and C. L. Degen, *Tracking the precession of single nuclear spins by weak measurements,* Nature **571**, 230 (2019).

[14] G. Waldherr *et al.*, *Quantum error correction in a solid-state hybrid spin register,* Nature **506**, 204 (2014).

[15] M. H. Abobeih *et al.*, *Fault-tolerant operation of a logical qubit in a diamond quantum processor,* Nature **606**, 884 (2022).

[16] C. E. Bradley *et al.*, *Robust quantum-network memory based on spin qubits in isotopically engineered diamond,* npj Quantum Information **8**, 122 (2022).

[17] N. Zhao *et al.*, *Sensing single remote nuclear spins,* Nature Nanotechnology **7**, 657 (2012).

[18] S. Kolkowitz, Q. P. Unterreithmeier, S. D. Bennett and M. D. Lukin, *Sensing distant nuclear spins with a single electron spin,* Phys. Rev. Lett. **109**, 137601 (2012).

[19] F. Shi *et al., Sensing and atomic-scale structure analysis of single nuclear-spin clusters in diamond,* Nat. Phys. **10**, 21 (2013).

[20] N. Zhao, J. L. Hu, S. W. Ho, J. T. Wan and R. B. Liu, *Atomic-scale magnetometry of distant nuclear spin clusters via nitrogen-vacancy spin in diamond,* Nat. Nanotechnol. **6**, 242 (2011).

[21] A. Ajoy, U. Bissbort, M. D. Lukin, R. L. Walsworth and P. Cappellaro, *Atomic-scale nuclear spin imaging using quantum-assisted sensors in diamond,* Phys. Rev. X **5**, 011001 (2015).

[22] W. M. Witzel, M. S. Carroll, A. Morello, L. Cywiński and S. Das Sarma, *Electron spin decoherence in isotope-enriched silicon,* Phys. Rev. Lett. **105**, 187602 (2010).

[23] A. M. Tyryshkin *et al., Electron spin coherence exceeding seconds in high-purity silicon,* Nature Materials **11**, 143 (2012).

[24] W. M. Witzel, M. S. Carroll, L. Cywiński and S. Das Sarma, *Quantum decoherence of the central spin in a sparse system of dipolar coupled spins,* Phys. Rev. B **86**, 035452 (2012).

[25] H. Park, J. Lee, S. Han, S. Oh and H. Seo, *Decoherence of nitrogen-vacancy spin ensembles in a nitrogen electron-nuclear spin bath in diamond,* npj Quantum Information **8**, 95 (2022).

[26] E. Bauch *et al., Decoherence of ensembles of nitrogen-vacancy centers in diamond,* Phys. Rev. B **102**, 134210 (2020).

[27] R. Hanson, V. V. Dobrovitski, A. E. Feiguin, O. Gywat and D. D. Awschalom, *Coherent Dynamics of a Single Spin Interacting with an Adjustable Spin Bath,* Science **320**, 352 (2008).

[28] G. de Lange, Z. H. Wang, D. Ristè, V. V. Dobrovitski and R. Hanson, *Universal Dynamical Decoupling of a Single Solid-State Spin from a Spin Bath,* Science **330**, 60 (2010).

[29] G. De Lange *et al., Controlling the quantum dynamics of a mesoscopic spin bath in diamond,* Sci. Rep **2**, 1 (2012).

[30] H. S. Knowles, D. M. Kara and M. Atatüre, *Observing bulk diamond spin coherence in high-purity nanodiamonds,* Nat. Mater. **13**, 21 (2014).

[31] H. S. Knowles, D. M. Kara and M. Atatüre, *Demonstration of a coherent electronic spin cluster in diamond,* Phys. Rev. Lett. **117**, 100802 (2016).

[32] J. R. Klauder and P. W. Anderson, *Spectral diffusion decay in spin resonance experiments,* Phys. Rev. **125**, 912 (1962).

[33] W. M. Witzel, K. Young and S. Das Sarma, *Converting a real quantum spin bath to an effective classical noise acting on a central spin,* Phys. Rev. B **90**, 115431 (2014).

[34] E. L. Rosenfeld, L. M. Pham, M. D. Lukin and R. L. Walsworth, *Sensing coherent dynamics of electronic spin clusters in solids,* Phys. Rev. Lett. **120**, 243604 (2018).

[35] A. Cooper, W. K. C. Sun, J.-C. Jaskula and P. Cappellaro, *Identification and control of electron-nuclear spin defects in diamond,* Phys. Rev. Lett. **124**, 083602 (2020).

[36] M. J. Degen *et al.*, *Entanglement of dark electron-nuclear spin defects in diamond,* Nature Communications **12**, 3470 (2021).

[37] L. Robledo *et al.*, *High-fidelity projective read-out of a solid-state spin quantum register,* Nature **477**, 574 (2011).

[38] W. V. Smith, P. P. Sorokin, I. L. Gelles and G. J. Lasher, *Electron-spin resonance of nitrogen donors in diamond,* Phys. Rev. **115**, 1546 (1959).

[39] R. J. Cook and D. H. Whiffen, *Electron nuclear double resonance study of a nitrogen centre in diamond,* Proceedings of the Royal Society of London. Series A. Mathematical and Physical Sciences **295**, 99 (1966).

[40] I. M. Zaritskii, V. Bratus, V. S. Vikhnin and A. A. Konchits, *Spin-lattice relaxation of the Jahn-Teller nitrogen center in diamond,* Sov. Phys. Solid State **18**, 1883 (1976).

[41] L. Shulman, M. Zaritskii and G. Podzyarei, *Reorientation of the jahn-teller distortion in nitrogen impurity centers in diamond,* Sov. Phys. Solid State **8**, 1842 (1967).

[42] C. A. Ammerlaan and E. A. Burgemeister, *Reorientation of nitrogen in type-Ib diamond by thermal excitation and tunneling,* Phys. Rev. Lett. **47**, 954 (1981).

[43] F. J. Heremans, G. D. Fuchs, C. F. Wang, R. Hanson and D. D. Awschalom, *Generation and transport of photoexcited electrons in single-crystal diamond,* Applied Physics Letters **94**, 152102 (2009).

[44] K. C. Miao *et al.*, *Universal coherence protection in a solid-state spin qubit,* Science **369**, 1493 (2020).

[45] C. Langer *et al.*, *Long-lived qubit memory using atomic ions,* Physical Review Letters **95**, 060502 (2005).

[46] D. A. Lidar, I. L. Chuang and K. B. Whaley, *Decoherence-free subspaces for quantum computation,* Physical Review Letters **81**, 2594 (1998).

[47] D. Yudilevich, R. Stöhr, A. Denisenko and A. Finkler, *Mapping single electron spins with magnetic tomography,* Phys. Rev. Appl. **18**, 054016 (2022).

[48] N. Zhao, S. W. Ho and R. B. Liu, *Decoherence and dynamical decoupling control of nitrogen vacancy center electron spins in nuclear spin baths,* Phys. Rev. B **85**, 115303 (2012).

[49] M. Ye, H. Seo and G. Galli, *Spin coherence in two-dimensional materials,* npj Comput. Mater **5**, 44 (2019).

[50] H. Seo *et al., Quantum decoherence dynamics of divacancy spins in silicon carbide,* Nat. Commun. **7**, 1 (2016).

[51] F. Shi *et al., Quantum logic readout and cooling of a single dark electron spin,* Physical Review B - Condensed Matter and Materials Physics **87**, 1 (2013).

[52] T. Yamamoto *et al., Strongly coupled diamond spin qubits by molecular nitrogen implantation,* Phys. Rev. B **88**, 201201 (2013).

[53] M. S. Grinolds *et al., Subnanometre resolution in three-dimensional magnetic resonance imaging of individual dark spins,* Nature Nanotechnology **9**, 279 (2014).

[54] W. K. C. Sun, A. Cooper and P. Cappellaro, *Improved entanglement detection with subspace witnesses,* Phys. Rev. A **101**, 012319 (2020).

[55] E. Janitz *et al., Diamond surface engineering for molecular sensing with nitrogen—vacancy centers,* J. Mater. Chem. C **10**, 13533 (2022).

[56] V. V. Dobrovitski, A. E. Feiguin, R. Hanson and D. D. Awschalom, *Decay of Rabi oscillations by dipolar-coupled dynamical spin environments,* Phys. Rev. Lett. **102**, 237601 (2009).

6

HIGH-FIDELITY QUANTUM CONTROL OF AN ELECTRON-NUCLEAR SPIN REGISTER IN DIAMOND

H.P. Bartling*, J. Yun*, K.N. Schymik, M. van Riggelen, L.E. Enthoven, H.B. van Ommen, M. Babaie, F. Sebastiano, T. H. Taminiau

Spins associated to solid-state colour centers are a promising platform for quantum computation and networks. In recent years, gate fidelities exceeding 99% *have been demonstrated. However, to reach the high gate fidelities required for large-scale quantum information processing, careful characterisation and optimisation of individual gates will be required. In this work, we use gate set tomography (GST) to characterise and optimise the single- and two-qubit gates on the electron-nitrogen spin system of the nitrogen-vacancy center in diamond. We design gates for different operational regimes and optimise the gate parameters using our knowledge of the electron-nitrogen Hamiltonian. We demonstrate single-qubit gate fidelities of* 99.999(1)% *and two-qubit gate fidelities exceeding* 99.9%. *Finally, we use the characterised gate set to implement a SWAP circuit, an important building-block in quantum network applications. This work shows promise for high-fidelity gates in solid-state colour centers and can be extended to other electron-nuclear spin systems.*

*Equally contributing authors.

6.1. INTRODUCTION

Solid-state colour centers are promising qubit systems for quantum computation and networks[1]. Recent experiments include the demonstration of a rudimentary quantum network[2,3], control of multi-qubit systems[4–6] and the implementation of quantum algorithms[7–9] and simulations[10,11]. To carry out quantum algorithms of increasing complexity, the implementation of quantum error correction will be necessary to overcome inherent control imperfections[12–14]. However, the single- and two-qubit gates need be of sufficient quality to reach error-correcting thresholds, below which error rates decrease for increasing numbers of physical qubits per logical qubit[12–14]. It is therefore essential to improve the single- and two-qubit gate fidelities in solid-state colour centers.

In recent years, fidelities exceeding 99% have been demonstrated for NV centers[15–17], as well as for other quantum platforms[18–31]. However, detailed characterisation of quantum gates is still an outstanding challenge for NV centers and other colour centers in diamond and other materials. In particular, randomized benchmarking methods only produce a single fidelity metric, which gives limited information about the error sources of a gate.

Here, we optimise and characterise the quantum gates on the electron spin and nitrogen spin of the NV center in diamond. We use gate set tomography (GST) to obtain the full process matrix of both single- and two-qubit gates in different, realistic operational regimes. Using this detailed characterisation, we identify undesired interactions between the two qubits that we mitigate with our gate designs. We demonstrate single-qubit gates with fidelities exceeding 99.9% for the electron spin and fidelities of 99.999(1)% for the nitrogen spin. Additionally, we show an electron-nitrogen two-qubit gate fidelity exceeding 99.9%. Finally, we compile an electron-nitrogen SWAP circuit from our characterised gates to store information on the nitrogen quantum memory, a necessary building block of network operation.

6.2. ELECTRON AND NITROGEN SPIN

In this work, we consider a single NV center in a type-IIa isotopically purified diamond (targeted ^{13}C concentration of 0.01%) at 4 K. Since the spin environment is sparse, we can consider the device as a well-isolated two-spin system, consisting of the NV electron spin and the nitrogen (^{14}N) nuclear spin (Fig. 6.1a). The Hamiltonian of this system is[34]:

$$\begin{aligned} H = {} & DS_z^2 + \gamma_e B_z S_z + QI_z^2 + \gamma_n B_z I_z \\ & + A_{xx} S_x I_x + A_{yy} S_y I_y + A_{zz} S_z I_z, \end{aligned} \tag{6.1}$$

where $D \approx 2.876$ GHz is the zero-field splitting of the electron spin, $\gamma_e = 2.8024$ MHz/G ($\gamma_n = -307.7$ Hz/G) is the gyromagnetic ratio of the electron (nitrogen) spin, $Q \approx -4.949$ MHz is the quadrupole splitting of the nitrogen spin, $[A_{xx}, A_{yy}, A_{zz}] \approx [2.68, 2.68, 2.188]$ MHz are the diagonal hyperfine components of the spin-spin interaction between the electron spin and the nitrogen spin. $[S_x, S_y, S_z]$ ($[I_x, I_y, I_z]$) are the spin-1 operators for the electron (nitrogen) spin (Sec. 6.9.3). We work at an aligned, external magnetic field of $B_z \approx 62.29$ G. We choose two levels of each qutrit to encode a qubit: $m_s = \{0, -1\}$ and $m_I = \{0, -1\}$ for the electron and nitrogen spin respectively (Fig. 6.1b).

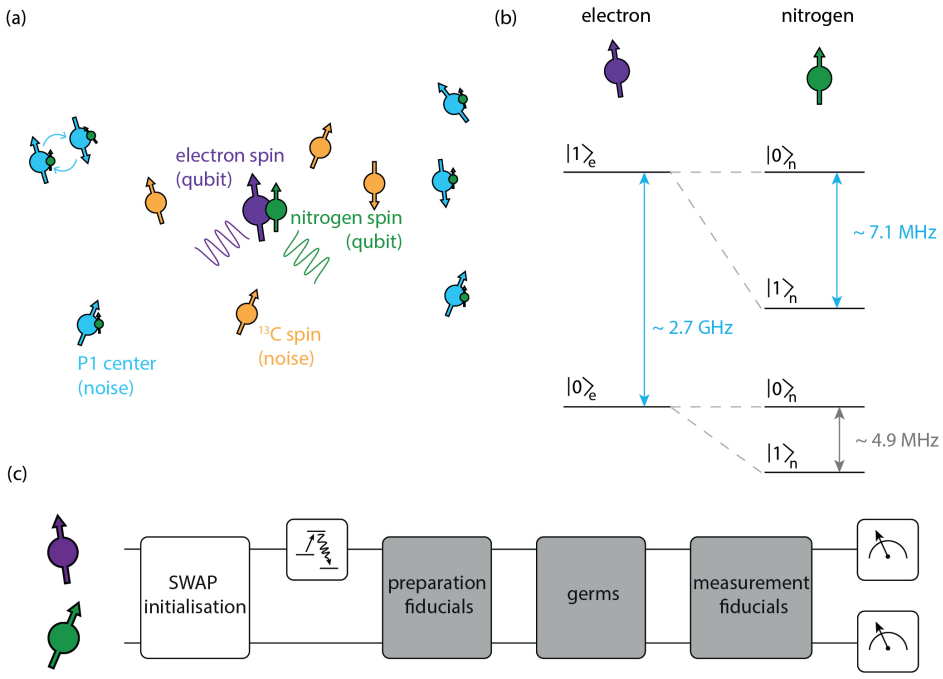

Figure 6.1: **System and experiment overview. a.** The system under consideration is the NV center in diamond. The electron spin-1 (purple) and ^{14}N spin-1 (green) are surrounded by two spin baths that generate noise: nuclear ^{13}C spins and P1 centers. **b.** Schematic level diagram of the electron and nitrogen spin. The transitions indicated in blue are used for the electron and nitrogen gates. **c.** Experimental implementation of gate set tomography. We initialise the electron spin optically and the nitrogen spin via SWAP initialisation (Sec. 6.9.9). Then, we run a set of preparation circuits, germs and measurement circuits, after which the electron and nitrogen spin are read out. The germs are longer sequences of gates meant to amplify specific types of errors [32,33].

We characterize a complete set of gates on the electron-nitrogen two-qubit system. Many methods exist to benchmark small quantum processors, such as randomized benchmarking [35–40], interleaved randomized benchmarking [37,41,42] and cross-entropy benchmarking [43,44]. While benchmarking methods are useful to extract global properties of a quantum processor, such as average gate fidelity, they do not provide information about specific gate errors. To that end, process tomography can be used to obtain more detailed insight into particular quantum circuits, at the cost of increased sensitivity to state preparation and measurement errors [36].

In this work, we use gate set tomography (GST). GST is a calibration-free tomography method to characterize an informationally complete set of quantum gates [32,33]. As opposed to process tomography, it does not need separate characterization of state preparation and measurement. It requires the execution of a set of quantum circuits, consisting of preparation and measurement circuits (or fiducials) and germs that are used to amplify specific types of gate errors (Fig. 6.1c), all consisting out of the same set of quantum gates. In previous work, it has been applied on a variety of systems such as

ion traps[45,46], quantum dots[21], silicon donors[22,47] and others[48].

We initialise and read out the NV center electron spin through resonant, optical excitation[49]. Additionally, we perform a check before the start of each experiment to verify that the NV center is in the negative charge state and that the lasers are resonant with the NV transitions[2,3]. To initialise the nitrogen spin, we swap the electron $m_s = 0$ state to the nitrogen in a two-step SWAP initialisation process (Sec. 6.9.9). To read out the nitrogen spin, we map its spin state on the electron spin, which is then read out optically (Sec. 6.9.10).

The NV center electron and nitrogen spin have an always-on hyperfine interaction (Eqn. 6.1). Therefore, the action of a gate on one spin generally depends on the state of the other spin. The most truthful characterisation of this two-qubit system is thus the full two-qubit process matrix of both single- and two-qubit gates (Fig. 6.4). However, the most optimal single-qubit gate design can depend on the state of the idling qubit. Therefore, we discern different regimes for which we design and implement different gate sets.

During electron operation, the nitrogen spin may be in a mixed state. An example is remote entanglement generation between the electron spins of two NV centers[2,3]. However, the nitrogen spin may be initialised in $m_I = 0$, for example for its use as an ancilla qubit in error correction protocols[50]. In Fig. 6.2 we characterise two different gate sets for each of these situations. Similarly, we consider two situations for operation of the nitrogen spin: with the electron spin in an eigenstate and in an unknown state (Fig. 6.3). Note that if, for example, a remote entangled state is present on the electron spin, the effect of the nitrogen single-qubit gate on the electron spin is essential, and we need the full two-qubit process matrix to capture this (Fig. 6.4).

6.3. ELECTRON-SPIN GATES

The basic operations on the electron spin are π and $\pi/2$ pulses, out of which we build composite $\pi/2$ and identity gates. We implement these by applying Hermite pulse shapes modulated by the electron spin frequency ($\sim$ 2.7 GHz). A Hermite pulse shape is chosen to minimize detuning effects introduced by the different nitrogen spin states (Sec. 6.9.7). We design different composite $\pi/2$ gates for different operational regimes (Fig. 6.2b). When the nitrogen spin is mixed, dynamical decoupling of the electron spin is needed to avoid nitrogen-induced dephasing due to the electron-nuclear interaction. However, when the nitrogen spin is in $m_I = 0$, the need for decoupling subsides and a simple $\pi/2$ Hermite pulse can be used. To optimize the electron gates, we calibrate the amplitude of the electron π and $\pi/2$ pulses for each phase individually, as well as the interpulse delay τ (Sections 6.9.6, 6.9.13).

The results for electron operation in these two regimes are shown in Fig. 6.2b. In both regimes, we achieve high-fidelity single-qubit gates, exceeding 99.9% for most gates. However, the electron gates are significantly better when the nitrogen spin resides in $m_I = 0$. The explanation for this lies firstly in the hyperfine interaction between the electron and nitrogen spin ($A_{zz} \approx 2.188$ MHz, maximum Rabi frequency $\Omega \sim 27$ MHz), which induces a different electron spin rotation for different nitrogen states, resulting in a lower average gate fidelity. Secondly, electron decoherence occurs during XY8 decou-

Figure 6.2: **Single-qubit GST on the electron spin. a.** Pulse sequences for the electron gates. The basic pulse is a Hermite-shaped microwave drive, indicated by X/Y for a π-pulse and x/y for a $\pi/2$-pulse. Depending on the regime, we either apply single $\pi/2$ pulses or $\pi/2$ pulses combined with XY8 decoupling. Unless indicated otherwise $\tau = 7.304$ μs. **b.** Average gate fidelities for electron operation in the two different operation regimes.

pling, which we will discuss later.

6.4. NITROGEN-SPIN GATES

The basic operation on the nitrogen spin is a radio-frequency (RF) drive at the nitrogen spin frequency (~ 7.1 MHz). We introduce a risetime of 1 μs and additionally we match the pulse length (~ 100 μs) to be a multiple of the nitrogen spin precession frequency to avoid any effective z rotation during the gate. During operation of the nitrogen spin with the electron in $m_s = -1$, such an RF drive suffices (Fig. 6.3). The nitrogen identity gate consists of an electron decoupling sequence, with an interpulse delay $\tau = 7.304$ μs, tuned such that the nitrogen spin picks up an effective 2π phase during XY8 decoupling. For the nitrogen spin $\pi/2$ gates in this regime, we observe fidelities of 99.999(1)% (Fig. 6.3b), limited by the measurement accuracy. These are among the highest single-qubit gate fidelities reported in any platform [15,20,21,30,51–55].

Next to nitrogen operation in a specific electron state, nitrogen single-qubit opera-

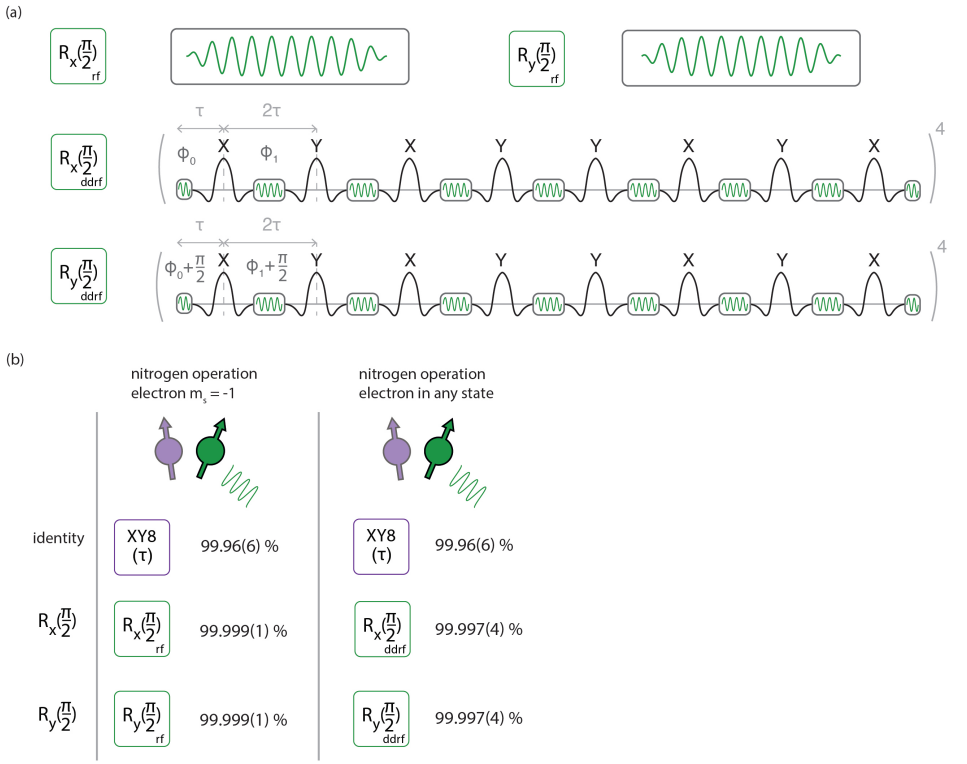

Figure 6.3: **Single-qubit GST on the nitrogen spin. a.** Pulse sequences for the nitrogen gates. Radio-frequency driving (~ 7.1 MHz, risetime 1 μs) of the nitrogen spin is indicated by green waves. Depending on the nitrogen operation regime, we either apply RF pulses (top) or DDRF pulses (bottom). In both cases, we change the RF phase to do x and y gates. **b.** Average gate fidelities for nitrogen operation in the two different regimes.

tions for a random electron state are required. To this end, we use a dynamical decoupling radio-frequency (DDRF) gate on the nitrogen spin[4,9]. The DDRF gate consists of dynamical decoupling (DD) on the electron spin interspersed with RF pulses (~ 7.1 MHz) on the nitrogen spin (Fig. 6.3a). This decouples the electron spin from the environment while simultaneously driving the nitrogen spin. By updating the phases between consequent RF pulses to account for the nitrogen spin precession, an effective rotation builds up[4]. In this manner, we drive the nitrogen spin regardless of the electron spin state. Additionally, by introducing an overall phase shift of the RF pulses, we can apply $\pi/2$ gates around both x and y. For the DDRF gate, we obtain fidelities for x and y of 99.997(4)% (Fig. 6.3b). These fidelities are measured with the electron spin in $m_s = 0$, but we obtain similar fidelities with the electron in $m_s = -1$ (Sec. 6.9.19). To optimize the DDRF gate fidelity, we carefully calibrate the amplitude of the electron pulses and nitrogen RF pulses, as well as the interpulse delay τ (Sections 6.9.6, 6.9.13).

6.5. TWO-QUBIT GATES

Now, we discuss operation of the full two-qubit system. Therefore, we characterise the two-qubit process matrices of both single- and two-qubit gates using two-qubit GST. In this regime, we need to apply single-qubit gates on the electron spin with XY8 decoupling (Fig. 6.2b) and with DDRF on the nitrogen spin (Fig. 6.3b). Additionally, the DDRF gate can be straightforwardly adapted to an electron-nitrogen two-qubit gate (Fig. 6.4a). By adding a π phase shift to all odd RF pulses, the nitrogen spin will rotate along an axis shifted by a π phase if the initial electron state is flipped, thus creating a two-qubit interaction[4]. This two-qubit interaction is a controlled $\pm\pi/2$ gate around x. Due to the similarity of the two-qubit gate to the nitrogen single-qubit gate, we do not have to do any additional calibrations.

For full two-qubit operation, we achieve single- and two-qubit gate fidelities exceeding 99.9% for all gates (Fig. 6.4b), amongst the best fidelities achieved in any system[20,21,24,25,28,30,31]. Compared to a previous characterisation of the NV center gates using subspace randomized benchmarking[16], the fidelities we obtain are best-estimates rather than upper limits, and we implement a complete gate set including the nitrogen-spin single-qubit gates.

An important gate optimisation step is to make sure that the nitrogen spin does not undergo any unwanted rotation during all electron, nitrogen and two-qubit gates. To that end, we impose that $1/\tau$ is a multiple of the average precession frequency of the nitrogen spin in the two electron states ($\tau = 4\pi n/(\omega_0 + \omega_{-1})$) as well as a multiple of the effective electron-nitrogen interaction ($\tau = 2\pi m/(\omega_0 - \omega_{-1})$).

We impose the first condition to make sure the nitrogen spin does not pick up any effective phase during a gate. However, a coherent rotation on the nitrogen spin builds up when applying XY8 decoupling on the electron spin at a value of τ that satisfies this condition (Fig. 6.5). The coherent rotation of the nitrogen spin likely originates from a previously unidentified effective $S_z I_x$ interaction between the electron and nitrogen spin (Sec. 6.9.6).

The second condition on τ ensures that the nitrogen spin undergoes a multiple of a 2π rotation during 2τ evolution within a decoupling sequence, regardless of the electron-spin state. This way, no effective nitrogen rotation can build up during the dynamical decoupling sequence (Fig. 6.5, Sec. 6.9.6).

6.6. GATE LIMITATIONS

Using GST, we retrieve completely-positive trace-preserving process matrices for the gate set[32,33]. Since the process matrix offers a complete description of the two-qubit evolution under the action of a specific gate, we gain knowledge about the origin and magnitude of infidelities in our system. Error generators used within the GST framework dissect the process matrices in distinct error sources with simple physical interpretations[33].

In particular, the coherent Hamiltonian and the incoherent stochastic error generators provide insight into the gate limitations, as they distinguish between unitary error processes, such as over- and under-rotations, and stochastic errors, such as qubit de-

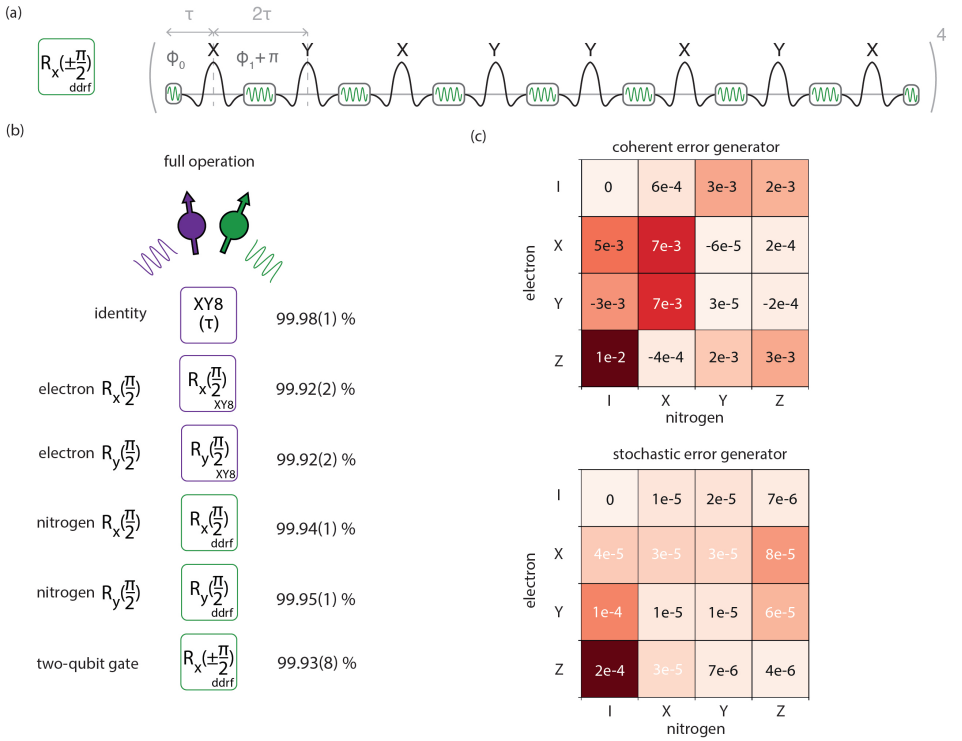

Figure 6.4: **Two-qubit GST on the electron-nitrogen system. a.** The two-qubit gate implemented using DDRF. All odd RF pulses get an additional π phase shift, which makes the nitrogen rotation conditional on the electron spin. **b.** Average gate fidelities for full operation of the electron-nitrogen system. The single-qubit gate fidelities now also take into account the effect on the other qubit. **c.** Coherent and stochastic error generator for the two-qubit gate. We find that dephasing of the electron spin is the main contribution to the average gate infidelity.

phasing. For our two-qubit gate, the biggest error source is the electron single-qubit coherent error around z (Fig. 6.4c). However, coherent errors only contribute quadratically to the average gate fidelity[45,56,57]. Therefore, we conclude that the average gate fidelity of the gates in this work are mainly limited by single-qubit dephasing ($Z_e I_n$) and single-qubit bit flips ($Y_e I_n$) of the electron-spin qubit.

Electron-spin dephasing and bit flips likely originate from magnetic field noise. The main sources are the fluctuating external magnetic field and the spin environment of the NV center (Fig. 6.1a). Quasi-static noise, which fluctuates slowly and can be considered as constant within a single gate, has no significant effect on the gate fidelity due to the incorporation of XY8 decoupling (Sections 6.9.7, 6.9.8). However, dynamic noise, which fluctuates within a single gate, may explain the observed electron-spin dephasing and bit flips. A likely source are the spin-bath dynamics, in particular flip-flops of interacting P1 centers (~ 75 ppb).

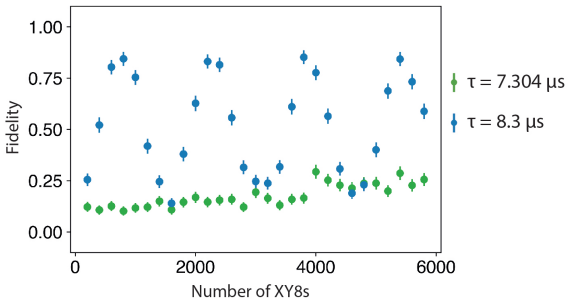

Figure 6.5: **Effect of electron dynamical decoupling on the nitrogen spin.** We initialise the nitrogen spin in $m_I = 0$ and apply XY8 decoupling at $\tau = 7.304$ μs (green) or $\tau = 8.3$ μs (blue). We find a coherent rotation of the nitrogen spin at $\tau = 8.3$ μs whereas this is absent for $\tau = 7.304$ μs.

6.7. IMPLEMENTATION OF SWAP GATE

An important building block for quantum technologies based on colour centers is a SWAP operation. Concretely, an entangled state is swapped from the optically active electron spin to a nuclear memory qubit (see e.g.[2]). While the memory qubit stores the entanglement, the electron spin is free to run further network operations. At a later stage, the quantum memory can be read out, at which moment the nuclear spin state is swapped back to the electron spin.

Here, we implement an electron-nitrogen SWAP gate using the 5 gates we characterized using two-qubit GST. We require a total of 17 gates for a single SWAP gate (Fig. 6.6a). While in practice a SWAP operation can be compiled with less elementary gates, this choice allows us to validate the predictive power of the obtained GST process matrices.

First, we investigate how often we can perform a SWAP gate until the final electron state is fully mixed (Fig. 6.6b). We apply the SWAP sequence an even number of times with the electron initialised in each of its cardinal axes. After about 20 SWAP gates, the resulting average fidelity of the six cardinal electron states reaches 0.5. Predictions of these extended circuit outcomes using the process matrices obtained with GST are in good agreement with the experimental results, even beyond 800 elementary gates (Sec. 6.9.16).

Next, we analyse the limitations of the SWAP gate using the error generators of the two-qubit process matrices (Fig. 6.4c). We conclude that the main source for the observed decay of the average fidelity of the six cardinal states originates from coherent errors. Upon removing the coherent errors from the process matrices, GST predicts that we could increase the number of SWAP gates well beyond 150 (Fig. 6.6b). Removing all coherent errors is not easily achieved experimentally, as it would require further improvement in calibration of the gates. However, based on the explicit knowledge of our coherent error processes, tailored sequences can be designed to cancel their effect. A simple example is to add two extra electron $\frac{\pi}{2}$ gates between every SWAP gate, which increases the expected average gate fidelity significantly (Fig. 6.6b). Alternatively, error

mitigation techniques such as Pauli twirling can be used to prevent coherent errors from adding up (Sec. 6.9.17).

The example in Fig. 6.6b also underlines the limitation of using a single number as a metric of the quality of a gate. By using the average gate fidelity, we capture the effect of decoherence during the gates properly. However, when there is a significant amount of unintended unitary error in the gates, it becomes difficult to predict the error rate from the average gate fidelity alone[57]. Namely, unitary errors contribute quadratically to the average gate fidelity, whereas decoherence contributes linearly[45,56,57].

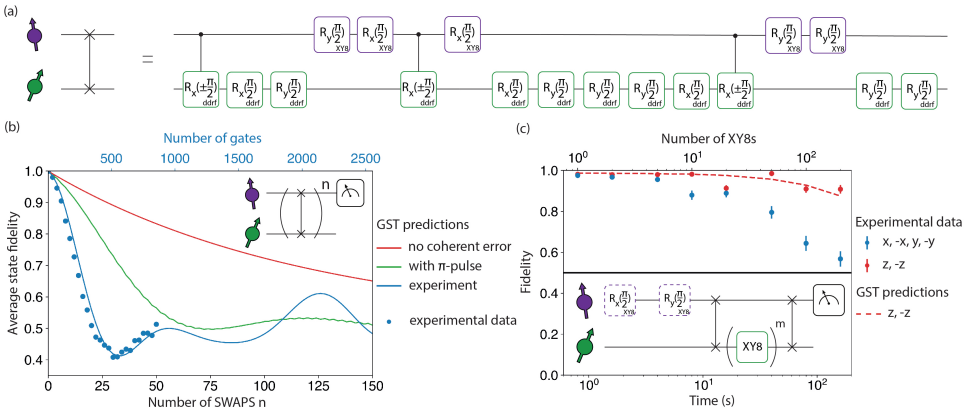

Figure 6.6: **Implementation of an electron-nitrogen SWAP gate. a.** Sequence to perform an electron-nitrogen SWAP gate composed of the gates characterised by two-qubit GST (Fig. 6.4). The compiled sequence is not optimal, but demonstrates the utility of GST in predicting the action of extended circuits. **b.** Application of n sequential SWAP gates. The experimental data (blue points) are predicted well by GST (blue line). The GST predictions without any coherent error (red) and with an additional π-pulse between sequential SWAP gates (green) are also shown. **c.** Storage of all six electron cardinal states ($\pm x, \pm y, \pm z$) on the nitrogen spin with the SWAP gate. We can store a quantum state on the nitrogen spin for over 100 s. We compare the experimental data for $\pm z$ to a GST prediction that does not include any free evolution. We find that the $\pm z$ decay is well explained by the obtained process matrix and thus caused by gate imperfections. The nitrogen XY8 decoupling is implemented with the DDRF $\pi/2$ gates around x and y characterised by two-qubit GST.

Finally, we demonstrate the use of the nitrogen-spin qubit as a quantum memory. First, we use the SWAP gate to prepare the nitrogen spin in one of six cardinal states. Then, we apply XY8 dynamical decoupling on the nitrogen using the GST-characterised DDRF $\pi/2$ gates. We measure the average state fidelity of the nitrogen spin as a function of the number of XY8 decoupling sequences (Fig. 6.6c). We find that the information on the nitrogen spin can be maintained for over 100 s.

We compare the experimental data with a simulation based on the obtained two-qubit GST process matrices without the inclusion of a free evolution time. From this simulation, we find that the errors in the nitrogen $\pi/2$ gates can explain the decay of the nitrogen $\pm z$ eigenstates (Fig. 6.6c). Additionally, we find that the electron spin population decays at a timescale similar to the nitrogen $\pm x$ and $\pm y$ states (Sec. 6.9.18). This suggests that the nitrogen coherence is limited by the nitrogen $\pi/2$ gate imperfections. Therefore, the storage time can be prolonged by designing tailored gates that can cancel out the introduced unitary errors.

6.8. DISCUSSION

In conclusion, we have optimized and characterized the single- and two-qubit gates on the electron-nitrogen spin system of the NV center using gate set tomography. The nature of the always-on electron-nitrogen hyperfine interaction, allows us to discern different operation regimes in which different gates are optimal. We have demonstrated single-qubit gate fidelities of 99.999% and two-qubit gate fidelities exceeding 99.9%. These are among the best quantum gates achieved on any platform [15,16,20,21,24,25,28,30,31,51–55]. The gates can be further improved by combatting coherent errors as present in our compiled SWAP gate and by optimizing the dynamical decoupling sequence to reduce the effect of the spin-bath noise.

As a next step, the methods presented in this chapter can be applied to other nuclear spins such as ^{13}C spins surrounding the NV center [4,50]. The addition of nuclear spins generates more quasi-static noise, but our gate designs are relatively insensitive to this type of noise due to the incorporation of decoupling pulses (Sections 6.9.7, 6.9.8). An additional complication of ^{13}C spin gate characterization is crosstalk between different nuclear spins, which can be addressed by GST directly or characterized separately. Lastly, our methods and gate designs are transferable to other colour centers in diamond and other materials [58–60].

6.9. SUPPEMENTARY MATERIALS

6.9.1. GENERAL INFORMATION ABOUT EXPERIMENTAL SETUP

The experiments are performed on a type-IIa isotopically purified (targeted 0.01% ^{13}C) ⟨100⟩ diamond substrate (Element Six). We use a home-built confocal microscope to address a single NV center at 4 K. A solid immersion lens and anti-reflection coating are fabricated around the NV center to increase the collection efficiency [49]. We use three orthogonal permanent neodymium magnets mounted on linear actuators (Newport UTS100PP) to apply an external magnetic field aligned along the NV symmetry axis. To initialise and read out the NV electron spin state, we use resonant optical excitation (Toptica DLPro and New Focus TLB-6704-P). We measure typical readout fidelities of 83.3(4)% for the $m_s = 0$ spin state and 98.9(1)% for the $m_s = -1$ spin state, obtaining an average readout fidelity of 91.1(2)%. We use 515 nm (green, Cobolt MLB) excitation to prepare the NV in its NV$^-$ charge state and on resonance with the 637 nm lasers. Through direct current modulation or cascaded acousto-optical modulators, we achieve on/off ratios exceeding 100 dB for all lasers.

6.9.2. EXPERIMENTAL SETUP (MICROWAVE, RADIO-FREQUENCY)

In this section, we discuss the experimental setup to drive electron microwave pulses and nitrogen radio-frequency pulses. In Fig. 6.7 we show a schematic containing all relevant components. To drive the electron spin at ~ 2.7 GHz, we use single-sideband modulation at 250 MHz, which allows us to filter out low-frequency noise originating from the AWG. We calibrate the I & Q channel offsets with an external signal analyzer. The signal is then passed through an amplifier (25 W), followed by a microwave switch,

which is shut when microwaves are not applied. The ~ 7.1 MHz frequency to drive the nitrogen spin is synthesized directly from the AWG. We add a ferrite coil to remove high-frequency electronic noise. The MHz nitrogen frequency and GHz electron frequency are combined on a home-built diplexer, after which it passes through a DC block and goes to the sample which is located in a Montana Cryostation S50. To get the microwave and radio-frequency signals close to the NV center, we pattern a gold stripline on the diamond surface.

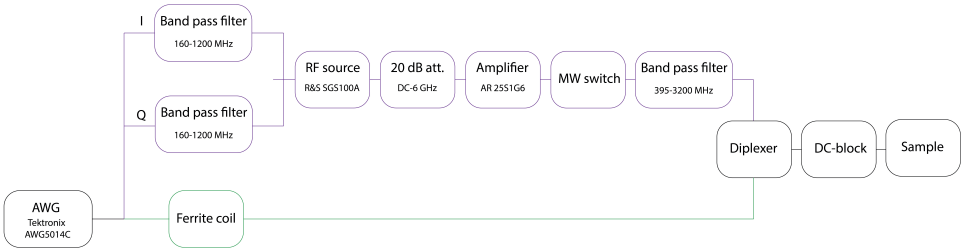

Figure 6.7: **Diagram of the microwave and radio-frequency delivery system.** For the electron spin (purple), we generate single-sideband modulated pulses at 250 MHz, which are fed into the RF source. We attenuate by 20 dB to protect the amplifier. The MW switch aims to reduce noise when no pulses are applied. Band pass filters are added to filter low-frequency noise originating from the AWG or MW switch. For the nitrogen spin (green), we synthesize the pulses directly from the AWG. A ferrite coil is used to suppress high-frequency electronic noise. The electron and nitrogen drives are combined on a diplexer, fed through a DC block and then to the sample.

6.9.3. HAMILTONIAN OF THE SYSTEM

In this work, we look at an NV center in an isotopically purified diamond (targeted 0.01% ^{13}C). The Hamiltonian of this system can be well approximated by an isolated two-spin system[34]:

$$H = DS_z^2 + \gamma_e B S_z + QI_z^2 + \gamma_n B I_z + A_{xx} S_x I_x + A_{yy} S_y I_y + A_{zz} S_z I_z \tag{6.2}$$

where $D \approx 2.876$ GHz is the zero-field splitting of the electron spin, γ_e (γ_n) is the electron (nitrogen) gyromagnetic ratio, Q is the quadrupole splitting of the nitrogen spin, and $[A_{xx}, A_{yy}, A_{zz}]$ are the diagonal hyperfine components of the spin-spin interaction between the electron spin and the nitrogen spin. Interactions with other spins in the environment can be considered as a second order effect due to their relatively small interaction strength (~ kHz). In this work, we approximately align the external magnetic field to the NV axis, so we only consider the z-axis of the Zeeman term. In Figure 6.8, we show a level diagram of the electron and nitrogen spin-system.

To obtain the coefficients for the Hamiltonian of our system, we measure 6 resonance frequencies of the system: the nitrogen $m_I = 0$ to $m_I = \pm 1$ transition for the two different electron states $m_s = 0$ and $m_s = -1$ and the two electron $m_s = 0$ to $m_s = -1$ transitions for the two different nitrogen states $m_I = 0$ and $m_I = -1$. These values correspond to the eigenenergy differences between the corresponding energy levels. The eigenenergies can be calculated by diagonalizing the Hamiltonian of the system. Since

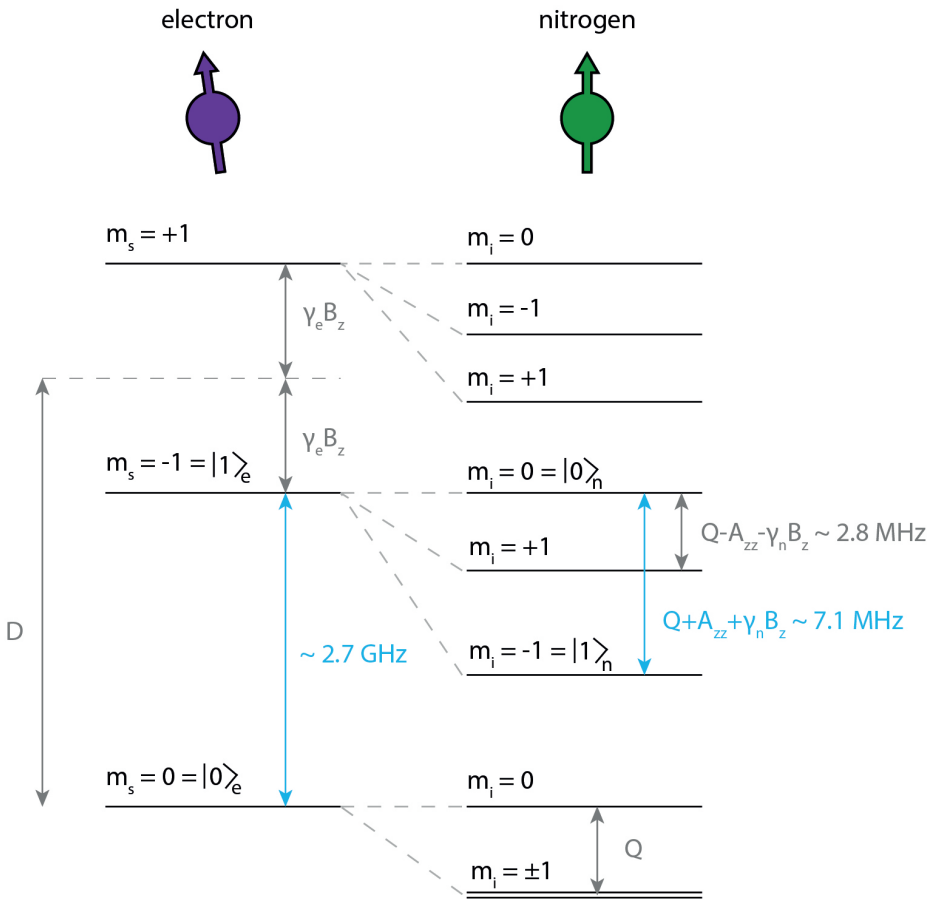

Figure 6.8: **Level diagram of the electron-nitrogen spin-system.** m_s (m_I) is the electron (nitrogen) spin, γ_e (γ_n) is the electron (nitrogen) gyromagnetic ratio, $D \approx 2.876$ GHz is the electron zero-field splitting, $Q \approx -4.949$ MHz is the nitrogen quadrupole splitting, and A_{zz} is the zz-component of the electron-nitrogen hyperfine interaction. The qubit levels used in this work are indicated by $|0\rangle_{e/n}$ and $|1\rangle_{e/n}$. The transitions used for driving are indicated in blue, and the ~ 2.8 MHz nitrogen transition is used for SWAP initialisation (Sec. 6.9.9).

the off-diagonal components are smaller than the difference between the diagonal components, we can approximate the diagonalized Hamiltonian with only first-order effects of the hyperfine coupling between the electron and nitrogen spin. In this framework, we obtain six equations:

$$\omega(m_I : 0 \leftrightarrow -1 | m_s = -1) = Q - \gamma_n B_z - A_{zz} - A_\perp^2 / D \tag{6.3}$$

$$\omega(m_I : 0 \leftrightarrow +1 | m_s = -1) = Q + \gamma_n B_z + A_{zz} \tag{6.4}$$

$$\omega(m_I : 0 \leftrightarrow +1 | m_s = 0) = -Q - \gamma_n B_z - A_\perp^2 / D \tag{6.5}$$

$$\omega(m_I : 0 \leftrightarrow -1 | m_s = 0) = -Q + \gamma_n B_z - A_\perp^2 / D \tag{6.6}$$

$$\omega(m_s : 0 \leftrightarrow -1 | m_I = -1) = D - \gamma_e B_z - A_{zz} + A_\perp^2 / D \tag{6.7}$$

$$\omega(m_s : 0 \leftrightarrow -1 | m_I = 0) = D - \gamma_e B_z + 3A_\perp^2 / D \tag{6.8}$$

where $A_\perp = A_{xx} = A_{yy}$. These four frequencies can be obtained by measuring the resonance lines from optically detected magnetic resonance (ODMR) measurements. Using the measured values $\omega(m_I : 0 \leftrightarrow -1 | m_s = -1) = -7.120706(1)$ MHz, $\omega(m_I : 0 \leftrightarrow +1 | m_s = -1) = -2.780105(6)$ MHz, $\omega(m_I : 0 \leftrightarrow +1 | m_s = 0) = 4.965825(3)$ MHz, $\omega(m_I : 0 \leftrightarrow -1 | m_s = 0) = 4.927491(1)$ MHz, $\omega(m_s : 0 \leftrightarrow -1 | m_I = 0) = 2.701294(1)$ GHz and $\omega(m_s : 0 \leftrightarrow -1 | m_I = -1) = 2.699101(1)$ GHz, the coefficients of the Hamiltonian are $D \approx 2.876$ GHz, $B_z \approx 62.29$ G, $Q \approx -4.949$ MHz, $A_{zz} \approx 2.188$ MHz, and $A_\perp \approx 2.68$ MHz. Note that these values are approximated up to first order in $A_\perp / D$, assume that the external magnetic field is aligned with the NV axis and that the gyromagnetic ratio of the electron spin is $\gamma_e = 2.8024$ MHz/G and of the nitrogen spin is $\gamma_n = -307.7$ Hz/G. For the simulations throughout this work, we use these values to represent our system.

When a microwave drive is applied to this system, we introduce an additional time-dependent Hamiltonian:

$$H_{int} = \Omega_e S_x \cos\big(\omega t + \phi_e\big) + \Omega_n I_x \cos\big(\omega t + \phi_n\big). \tag{6.9}$$

where Ω_e (Ω_n) is the electron (nitrogen) Rabi frequency, ϕ_e (ϕ_n) is the phase of the microwave for the electron (nitrogen) spin, ω is the frequency of the microwave drive and the x axis is defined to be along the microwave driving axis.

6.9.4. SIMULATION DETAILS

In this work, we developed a simulation tool based on QuTiP[61,62] to simulate the electron-nitrogen spin system. The simulation assumes that there are no other spins. For the ideal two-spin system, we use the Hamiltonian described in equation 6.2. The simulation of the unitary operation of the gates was done using the propagator function in QuTiP. To also consider non-rotating frame effects, we solve the master equation with the full time-dependent Hamiltonian to obtain the unitary representation of our gates.

6.9.5. DATA ANALYSIS

In this section, we discuss the interpretation of the error bars on the parameters obtained from our fits. In general, the objective of a least-squares fit is to minimize the goodness-of-fit parameter χ^2 [63]:

$$\chi^2 = \sum_i \left[\frac{y_i - y(x_i)}{\sigma_i} \right]^2, \tag{6.10}$$

where the sum is over the experimental data points, y_i is the experimental data, σ_i the experimental error bar, and $y(x_i)$ the prediction of the fit for x_i. Ideally, the error bars describe the deviation of the data from the fit accurately. That would result in $\chi^2 = N - M$ where N is the number of data points and M the number of fit parameters. Alternatively, we can define the reduced goodness-of-fit parameter as [63]

$$\chi^2_r = \chi^2/\text{DOF}, \tag{6.11}$$

where DOF $= N - M$ is the number of degrees of freedom of the fit.

Obtaining $\chi^2_r = 1$ implies that the deviation of the data from the fit is well explained by the error bars σ. However, if $\chi^2_r \gg 1$ ($\chi^2_r \ll 1$), this implies that the error bars significantly underestimate (overestimate) the actual, underlying experimental error. Other explanations, such as the fit model being incorrect, can also be the cause of a deviation from $\chi^2_r = 1$.

One common approach is to rescale the covariance matrix by χ^2_r [63]. This is the default method in Python packages such as `lmfit` and `scipy`, and we also follow this approach. Alternatively, the covariance matrix is not rescaled and this results in different (larger or smaller, depending on χ^2_r) error bars on the fit parameters.

Throughout this work, we report χ^2_r for each fit as a metric of the goodness of that fit.

6.9.6. XY8 SEQUENCE: DECOUPLING THE ELECTRON-NUCLEAR INTERACTION

In this work, two important conditions for the interpulse delay τ in dynamical decoupling have to be satisfied. First, τ has to be a multiple of the average precession frequency of the nitrogen spin in $m_s = 0$ and $m_s = -1$. Second, τ has to be a multiple of the effective electron-nitrogen interaction. In other words, if ω_0 (ω_{-1}) is the precession frequency of the nitrogen spin when the electron spin is in $m_s = 0$ ($m_s = -1$), we require that $\tau = 4\pi n/(\omega_0 + \omega_{-1})$ where n is an integer and that $\tau = 2\pi m/(\omega_0 - \omega_{-1})$ where m is an integer.

The first condition ensures that the nitrogen spin undergoes a multiple of a 2π rotation around z for each gate. This is essential to reduce the control errors around z. Due to a hardware constraint τ is limited to multiples of 4 ns, which is relatively easy to satisfy when the average precession frequency is already a multiple of 2 ns. Therefore, we require that the average precession frequency of the nitrogen spin is a multiple of 2 ns.

The first magnetic field adjustment is done with the two electron spin resonance frequencies: the transitions from $m_s = 0$ to $m_s = \pm 1$. This is an efficient way to approximately align the magnetic field by minimizing the sum of the $m_s = 0$ to $m_s = \pm 1$ transitions [64]. Additionally, we move to a magnetic field magnitude that satisfies the first

condition described above: we set the magnetic field such that the period of the average nitrogen precession frequency is 166 ns.

After satisfying the first condition, we observe a coherent rotation of the nitrogen spin under dynamical decoupling of the electron spin (Fig. 6.9). The second condition is important to minimise this nitrogen rotation induced by the first condition. Namely, the first condition is analogous to the condition for an unconditional rotation of a ^{13}C spin during dynamical decoupling[65]. The presence of a previously unidentified effective $S_z I_x$ term for the nitrogen spin could also induce such rotations for the nitrogen spin (Fig. 6.10). To ensure that no unconditional rotation of the nitrogen spin occurs, even when the first condition is satisfied, we require that τ is also a multiple of the effective electron-nitrogen interaction.

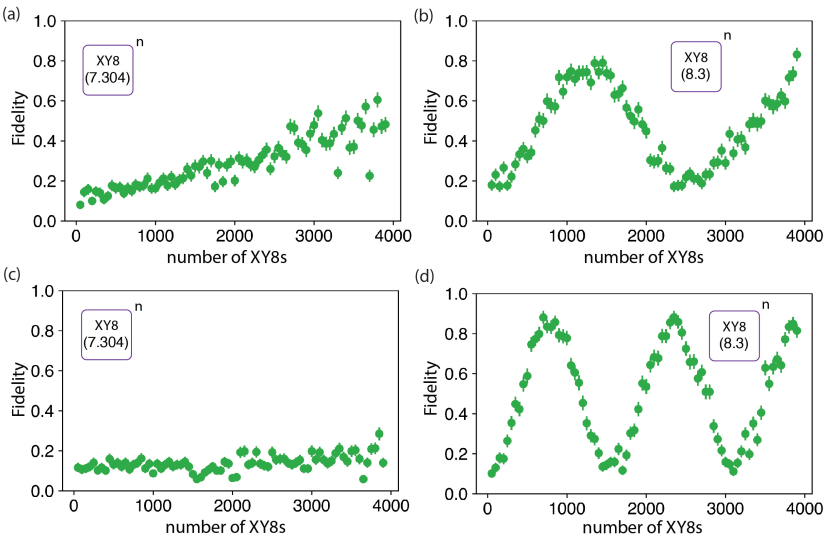

Figure 6.9: **Nitrogen rotation under electron XY8 decoupling under two different magnetic fields. a.** The nitrogen spin is initialised in $m_I = 0$ and under electron XY8 decoupling at $\tau = 7.304$ µs, we observe a slow rotation of the nitrogen spin. This indicates that the condition $\tau = 2\pi m/(\omega_0 - \omega_{-1})$ is not exactly matched for $\tau = 7.304$ µs. **b.** Nitrogen rotation under electron XY8 decoupling at $\tau = 8.3$ µs. The absence of a full-contrast oscillation indicates that the condition $\tau = 4\pi n/(\omega_0 + \omega_{-1})$ is not exactly matched for $\tau = 8.3$ µs and thus for $\tau = 7.304$ µs. **c.** Nitrogen rotation under electron XY8 decoupling at $\tau = 7.304$ µs for an optimal external magnetic field. No rotation of the nitrogen spin under XY8 decoupling is observed, since $\tau = 7.304$ µs satisfies both conditions at this magnetic field: $\tau = 4\pi n/(\omega_0 + \omega_{-1})$ and $\tau = 2\pi m/(\omega_0 - \omega_{-1})$. **d.** For the optimal magnetic field setting, we observe a full-contrast rotation under decoupling at $\tau = 8.3$ µs. This happens because $\tau = 8.3$ µs is not a multiple of the effective electron-nitrogen interaction ($\tau \neq 2\pi m/(\omega_0 - \omega_{-1})$), while it is a multiple of the average nitrogen-spin precession frequency ($\tau = 4\pi n/(\omega_0 + \omega_{-1})$).

When we require both $\tau = 4\pi n/(\omega_0 + \omega_{-1})$ and $\tau = 2\pi m/(\omega_0 - \omega_{-1})$, we can show that the nitrogen spin undergoes an effective 2π evolution during 2τ regardless of the electron spin state. In other words, we can show explicitly that

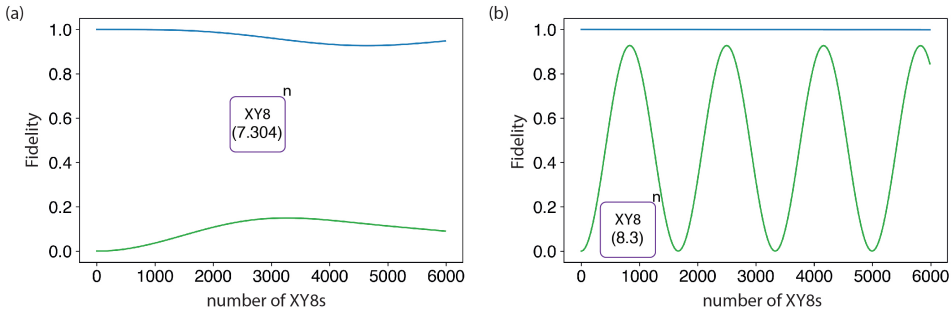

Figure 6.10: **Simulation of electron-nitrogen evolution under electron XY8 decoupling. a.** Decoupling at $\tau = 7.304$ µs reveals dynamics that weakly affect the electron and nitrogen spin for high numbers of XY8s. The blue (green) curve indicates the electron (nitrogen) spin. **b.** Decoupling at $\tau = 8.3$ µs shows coherent driving of the nitrogen spin, since τ is not a multiple of the effective electron-nitrogen interaction. The blue (green) curve indicates the electron (nitrogen) spin. Note that for both simulations the actual τ-values used ($\tau = 7.3038$ µs, $\tau = 8.2998$ µs) differ slightly from the experimental ones, because there is a finite precision on the Hamiltonian parameters.

$$2\tau = \frac{2\pi(2n+m)}{\omega_0}, \tag{6.12}$$

$$2\tau = \frac{2\pi(2n-m)}{\omega_{-1}}. \tag{6.13}$$

By requiring that the nitrogen spin always undergoes a full 2π evolution during 2τ, no effective rotation can build up.

At the magnetic field obtained in the first step, $\tau = 7.304$ µs is already a close multiple of the effective electron-nitrogen interaction, while $\tau = 8.3$ µs is not. To measure the leftover rotation of the nitrogen spin at these values of τ, we apply many XY8 dynamical decoupling sequences with the nitrogen starting in $m_I = 0$ (Fig. 6.9). For a suboptimal external magnetic field, we find that the nitrogen spin is rotated from $m_I = 0$ to $m_I = -1$ by XY8 decoupling sequence at $\tau = 7.304$ µs (Fig. 6.9a). Additionally, the nitrogen rotation present at $\tau = 8.3$ µs does not show full contrast (Fig. 6.9b). We optimize the magnetic field such that no nitrogen rotation is visible when decoupling at $\tau = 7.304$ µs (Fig. 6.9c) and a full-contrast nitrogen rotation is visible when decoupling at $\tau = 8.3$ µs. This is equivalent to optimizing the magnetic field such that $\tau = 7.304$ µs satisfies both conditions: $\tau = 4\pi n/(\omega_0 + \omega_{-1})$ and $\tau = 2\pi m/(\omega_0 - \omega_{-1})$. This magnetic field makes sure that no spurious nitrogen rotations are introduced at $\tau = 7.304$ µs by the XY8 decoupling. In Fig. 6.9c we verify that for our magnetic field we see no visible rotation of the nitrogen spin up to 4000 XY8 sequences on the electron spin.

To investigate the origin of this effect, we simulate the action of XY8 decoupling sequences on the electron-nitrogen spin system. We take the Hamiltonian in equation 6.2 and add an additional term: $A_{zx} S_z I_x$. While the origin of this term is currently not understood, we empirically observe that the addition of this term can reproduce our experimental results. In Figure 6.10, we show the simulation result for the electron (blue)

and nitrogen (green) spin for $A_{zx} = 4$ kHz for different values of τ. The electron and nitrogen spin start in $m_s = 0$ and $m_I = 0$ respectively. For $\tau = 7.304$ μs, we observe a small oscillation on both the electron spin and the nitrogen spin (Fig. 6.6.10a). This is in line with the experimental results (Fig. 6.5). For $\tau = 8.3$ μs, we observe coherent driving of the nitrogen spin due to the A_{zx} electron-nitrogen interaction. The value $A_{zx} = 4$ kHz is in line with the experimentally observed oscillation frequency (Fig. 6.5).

The simulations in Figure 6.10 together with the data presented in Figure 6.5 and Figure 6.9 show that the conditions outlined above are important to avoid any coherent rotation of the nitrogen spin. In future experiments, the necessity of the first condition ($\tau = 4\pi n/(\omega_0 + \omega_{-1})$) can be avoided through the use of more advanced phase-tracking methods.

6.9.7. GATE DESIGNS

In this section, we discuss some details of the electron and nitrogen pulses. For the electron gates, we use a Hermite envelope microwave pulse of 144 ns. We use a microwave frequency resonant with the $m_s = 0$ to $m_s = -1$ transition when $m_I = 0$. The main issue for the electron single-qubit gate is the relatively large interaction strength between the electron and nitrogen nuclear spin. Since the detuning induced by the coupling of the nitrogen spin (~ 2 MHz) is comparable to our peak Rabi frequency (~ 27 MHz), we use a Hermite envelope[66,67]. This makes it possible to rotate the electron spin as similarly as possible regardless of the nitrogen spin state. We can write the Hamiltonian of the NV electron spin for a given nitrogen eigenstate m_I as

$$H_e = DS_z^2 + \gamma_e B S_z + m_I A_{zz} S_z, \tag{6.14}$$

where $A_{zz} \approx 2.188$ MHz is the electron-nitrogen hyperfine interaction. If we now add a time-dependent Hamiltonian rotating at $D + \gamma_e B$ and move into the rotating wave frame of this frequency, the Hamiltonian after applying rotating wave approximation is:

$$H_e = m_I A_{zz} S_z + \Omega_e(\cos(\phi) S_x + \sin(\phi) S_y). \tag{6.15}$$

Thus the electron has a different detuning depending on the nitrogen spin state. Therefore, when applying the same microwave pulse, the effective rotation is along a different rotation axis and has a different angle for different m_I. The fact that the qubit gains different phase during the microwave application is especially problematic since it makes it difficult to cancel this phase effect using XY8 decoupling. To avoid this problem, we use the Hermite envelope for the microwave pulse which helps the phase accumulation during the microwave pulse to be more robust to detuning[66,67]. Figure 6.11 shows a simulation of the fidelity of a Hermite $\pi/2$ pulse sandwiched between XY8 decoupling sequences as a function of the microwave frequency detuning, as well as that of a square $\pi/2$ pulse. For both $\pi/2$ pulses, we use the same maximum Rabi frequency of ~ 13 MHz and for the π pulses in the XY8 sequence, we use the same maximum Rabi frequency of ~ 27 MHz. For the Hermite pulse envelope, a gate with fidelity over 99.9% over a range of ±2 MHz of detuning is possible, whereas for a square envelope the fidelity drops and fluctuates rapidly as a function of detuning outside the ±1 MHz range.

Nitrogen gates consist of electron gates as described above combined with radio-frequency pulses. Alternatively, we apply only radio-frequency pulses of ~ 100 μs in

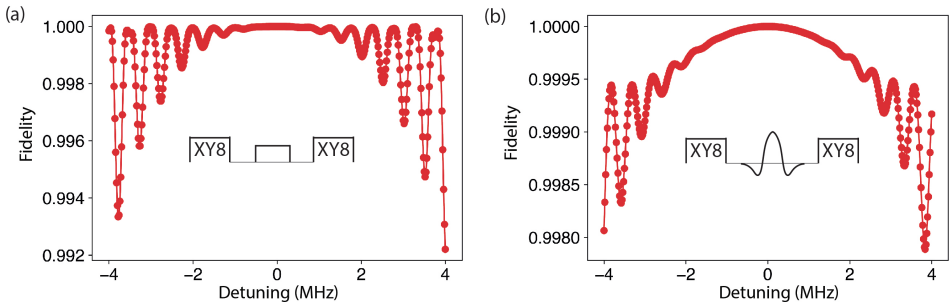

Figure 6.11: **Pulse fidelity of a square and Hermite $\pi/2$ pulse as a function of detuning. a.** Square $\pi/2$ pulse fidelity as a function of microwave frequency detuning. We find a rapid deterioration of pulse fidelity in the presence of detuning. We sandwich the square $\pi/2$ pulse in between XY8 decoupling sequences made of square π pulses. **b.** Hermite $\pi/2$ pulse fidelity as a function of microwave frequency detuning. We obtain high pulse fidelities for a much larger range of detunings compared to the square pulse. For both the square pulse and Hermite pulse, we use a maximum Rabi frequency of ~ 13 MHz for the $\pi/2$ pulse. We sandwich the Hermite $\pi/2$ pulse in between XY8 decoupling sequences made of Hermite π pulses with a maximum Rabi frequency of ~ 27 MHz.

duration with the electron in $m_s = -1$ (Fig. 6.3). We apply the radio-frequency pulses resonant with the $m_I = 0, -1$ transition for $m_s = -1$ at a frequency of 7.120706 MHz. We add an error function envelope to each RF pulse with a risetime of 1 μs.

6.9.8. EFFECT OF QUASI-STATIC NOISE ON XY8 DECOUPLING

In this section, we discuss the effect of quasi-static magnetic noise on the electron XY8 decoupling sequence. Such noise can originate from magnetic field fluctuations, either from the externally applied magnetic field or from the spin bath (^{13}C nuclear spins and P1 center electron spins). For quasi-static noise, we take the magnetic field as constant for the duration of a gate. For almost all gates that we discuss, we use a decoupling sequence on the electron spin. This makes sure that any phase picked up by the electron spin due to the quasi-static bath is cancelled out. Figure 6.12 shows a simulation of how an XY8 sequence (identity gate) responds to a constant magnetic field detuning. From this result, we see that for a quasi-static environment, this gate should ideally not show any additional infidelity.

6.9.9. NITROGEN SPIN INITIALISATION

In this section, we discuss the initialisation of the nitrogen spin to its $m_I = 0$ state. In the gate set tomography results presented in the main text, we use SWAP-type initialisation of the nitrogen spin. In Fig. 6.13 we show the corresponding sequence. Since the nitrogen spin is a spin-1 system, we need a two-step SWAP process. First, we perform a swap on the $m_I = \{0, -1\}$ subspace of the nitrogen spin. Then we reinitialise the electron spin after which we perform a swap on the $m_I = \{0, +1\}$ subspace. Note that we use a reduced type of SWAP gate: as the electron spin is set to an eigenstate, one two-qubit gate can be omitted compared to the full SWAP gate of Fig. 6.6.

An alternative to SWAP is to use measurement-based initialisation (MBI). The se-

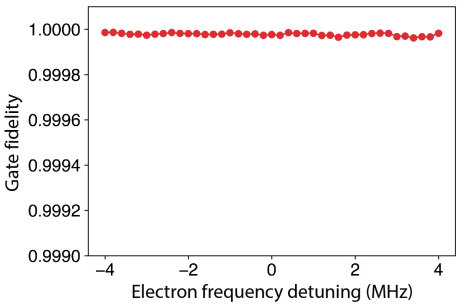

Figure 6.12: **Simulation of the effect of electron frequency detuning on the average gate fidelity of XY8 decoupling.** We simulate the application of a single XY8 decoupling block as a function of the electron frequency detuning. We find that the effect of detuning is negligible.

quence is given in the inset of Fig. 6.14a,b. First, we initialise the electron spin in $m_s = -1$, after which we apply a weak microwave pulse. This microwave flips the electron spin back to $m_s = 0$ only when the nitrogen spin is in $m_I = 0$. Finding the electron spin in $m_s = 0$ upon reading out, initializes the nitrogen spin in $m_I = 0$.

To compare the different initialisation methods, we measure an electron spin resonance (ESR) spectrum after initialisation of the nitrogen spin. In Fig. 6.14a, we perform a single round of MBI initialisation. In Fig. 6.14b, we perform two rounds of MBI intialisation. At the cost of a slower experimental rate, we find a significantly improved initialisation fidelity. In Fig. 6.14c, we show the ESR spectrum after SWAP initialisation as in Fig. 6.13. We find a marginally improved fidelity compared to double MBI initialisation.

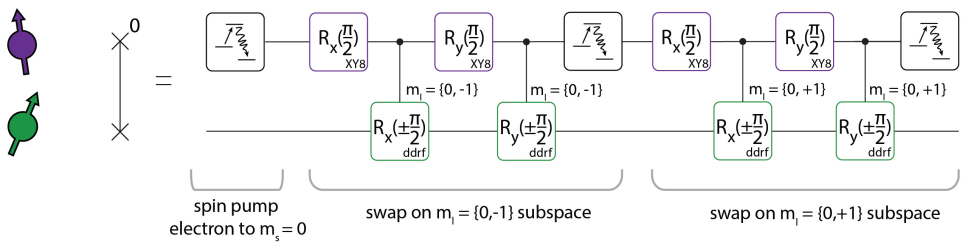

Figure 6.13: **Experimental sequence for SWAP initialisation of the nitrogen spin.** We perform a two-step SWAP process due to the spin-1 nature of the nitrogen spin. First, we perform a swap on the $m_I = \{0,-1\}$ subspace, after which we perform a swap on the $m_I = \{0,+1\}$ subspace. The gates are as defined in the main text. However, the gates on the subspace $m_I = \{0,+1\}$ of the nitrogen spin utilise a different RF frequency (Sec. 6.9.19).

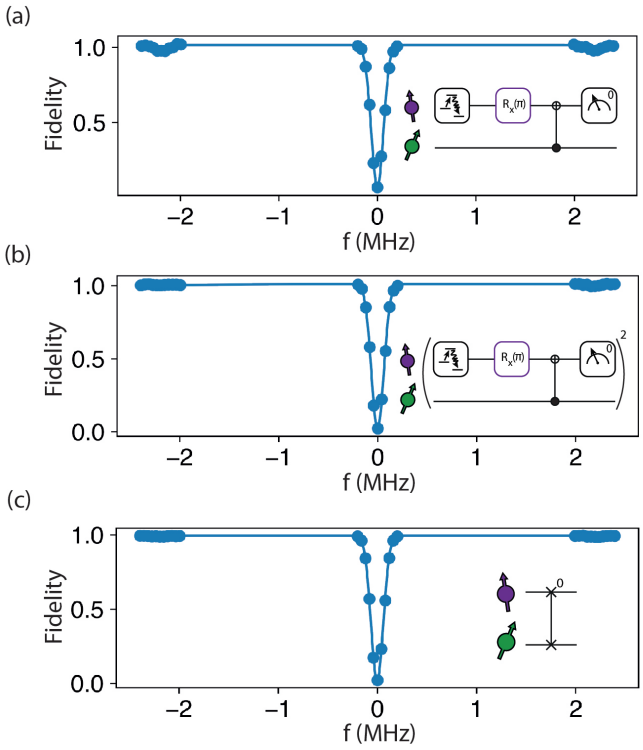

Figure 6.14: **ESR spectra for different initialisation methods. a.** We use a single round of measurement based initialisation (MBI) to initialise the nitrogen spin. The data is fitted to the sum of three Gaussians: $a - A_1 \exp\left(-(x-x_1)^2/(2\sigma_1^2)\right) - A_2 \exp\left(-(x-x_2)^2/(2\sigma_2^2)\right) - A_3 \exp\left(-(x-x_3)^2/(2\sigma_3^2)\right)$. We fit to Gaussian functions, because we used a Gaussian pulse shape to measure the ESR spectrum. We find the contrast as $A_2/(A_1+A_2+A_3)$ where A_2 is the amplitude of the middle dip. We find a value of 0.924(8) with $\chi_r^2 = 1.9$. **b.** We use two rounds of MBI to initialise the nitrogen spin. We find a contrast of 0.979(6) with $\chi_r^2 = 3.7$. **c.** We used SWAP initialisation (Fig. 6.13) to initialise the nitrogen spin. We find an initialisation fidelity of 0.985(7) with $\chi_r^2 = 21.6$.

6.9.10. NITROGEN READOUT

After each gate set tomography experiment performed in this work, we measure both the electron spin and the nitrogen spin. The full sequence to do so is given in Fig. 6.15. We read out the electron spin optically in a single shot[49]. Afterwards, we reinitialise the NV electron spin in $m_s = 0$ and read out the nitrogen spin. Since we principally work in the subspace $m_I = \{0, -1\}$ of the nitrogen spin, we compile our readout out of gates characterised by GST. The applied sequence of gates maps the nitrogen z-projection to the electron spin z-projection, after which we read out the electron spin optically.

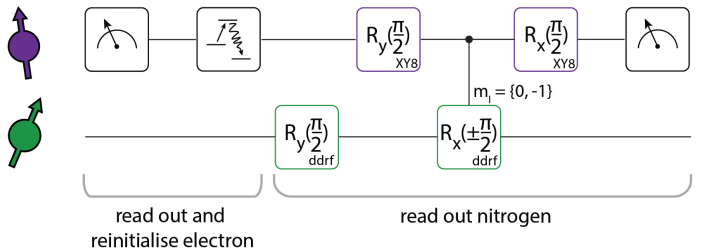

Figure 6.15: **Sequence to read out the electron and nitrogen spin sequentially.** The electron spin is read out and initialised optically. The nitrogen spin is then mapped to the electron spin using only gates characterised with gate set tomography. Finally, we read out the electron spin.

6

6.9.11. NITROGEN COHERENCE

In this section, we discuss coherence measurements of the nitrogen spin independent of those presented in the main text. To bring the nitrogen spin in a superposition and to apply echo pulses, we use the DDRF gates (Fig. 6.16). First, we measure the inhomogeneous dephasing time of the nitrogen spin for the electron spin in $m_s = 0$ (Fig. 6.16a) and $m_s = -1$ (Fig. 6.16b). We find that T_2^* is dependent on the electron spin state, obtaining a factor ~ 3 larger T_2^* in $m_s = 0$ compared to $m_s = -1$. We do not currently have a good explanation for this observed difference.

In Fig. 6.16c we show a nitrogen spin echo measurement with the electron spin in $m_s = 0$. In Fig. 6.16d we show the same measurement with the electron spin in $m_s = -1$. Here, we find that the coherence time in $m_s = -1$ is longer than in $m_s = 0$, which is the opposite finding from the T_2^* measurement presented above. The observed increase in T_2 time for $m_s = -1$ may have to do with the presence of a frozen core around the NV center, which implies that more quasi-static noise can be echoed out.

In Fig. 6.16e, we show the nitrogen coherence for different numbers of echo pulses. We find an increase of coherence with increasing number of pulses, as expected. For $N = 64$, we find a coherence time of $T_2 = 73(9)$ s.

6.9.12. ELECTRON COHERENCE

In this section, we discuss the electron coherence under dynamical decoupling. In Fig. 6.17a, we show the electron coherence as a function of the number of π-pulses applied to the electron spin. We make sure that the interpulse delay τ is a multiple of the ^{13}C

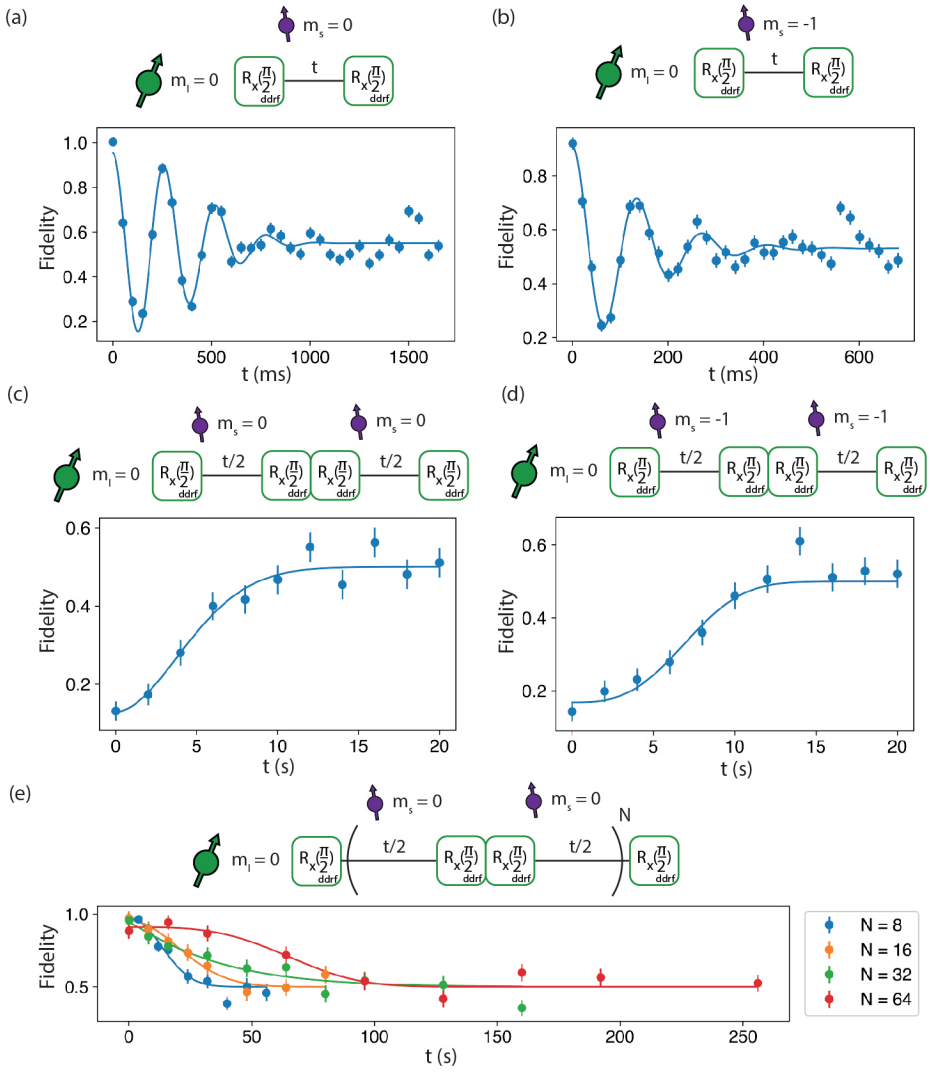

Figure 6.16: **Nitrogen coherence.a.** Ramsey experiment with the electron in $m_s = 0$. We find $T_2^* = 553(46)$ ms ($\chi_r^2 = 4.1$). **b.** Ramsey experiment with the electron in $m_s = -1$. We find $T_2^* = 172(24)$ ms ($\chi_r^2 = 3.2$). **c.** Spin echo measurement with the electron in $m_s = 0$. We find $T_2 = 5.7(5)$ s ($\chi_r^2 = 0.97$). **d.** Spin echo measurement with the electron in $m_s = -1$. We find $T_2 = 8.0(7)$ s ($\chi_r^2 = 1.5$). **e.** Nitrogen coherence for different numbers of echo pulses N. For N = 8, we find $T_2 = 18(2)$ s ($\chi_r^2 = 1.2$). For N = 16, we find $T_2 = 28(3)$ s ($\chi_r^2 = 0.7$). For N = 32, we find $T_2 = 37(10)$ s ($\chi_r^2 = 1.6$). For N = 64, we find $T_2 = 73(9)$ s ($\chi_r^2 = 1.2$).

Larmor frequency to mitigate resonances from electron-nuclear interaction. While we see a steady increase in coherence time for increasing number of pulses (Fig. 6.17b), significant outliers in the data are also visible. We attribute these to the presence of 50 Hz noise. While detrimental at large values of τ, at $\tau = 7.304$ μs we are not significantly affected by this.

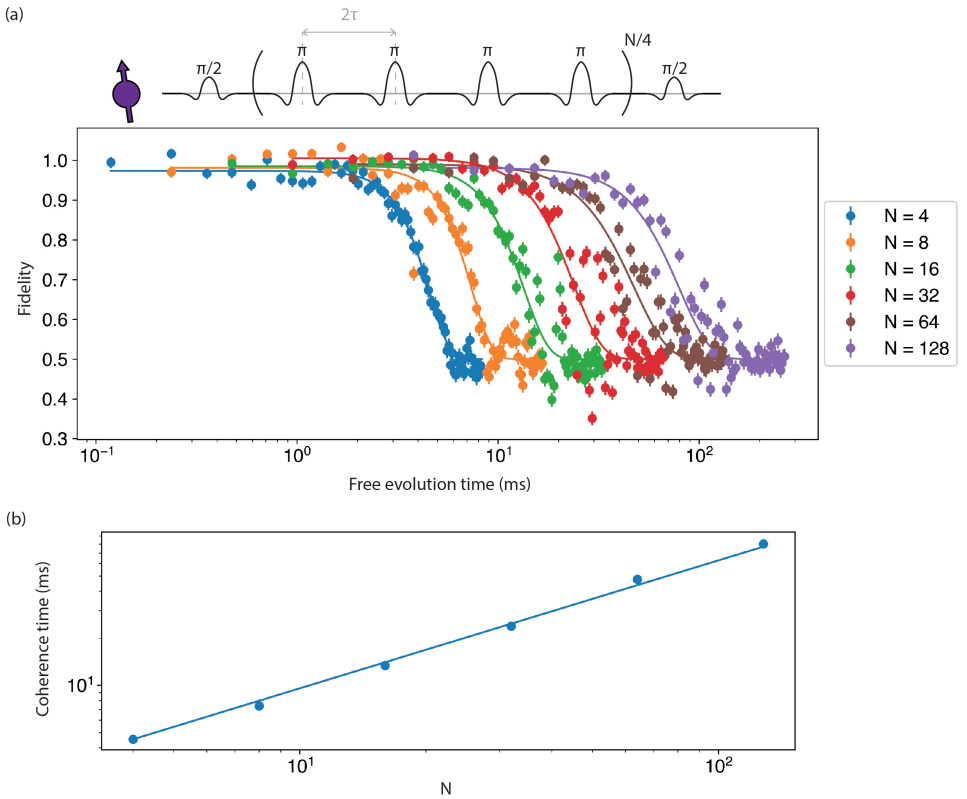

Figure 6.17: **Electron coherence. a.** (Top) Sequence to measure the electron coherence. We prepare the electron in a superposition and apply a number of π-pulses N. (Bottom) Experimental result. From $N = 4$ to $N = 128$ we find respectively $T_2 = 4.53(4)$ ms ($\chi_r^2 = 1.9$), $T_2 = 7.4(2)$ ms ($\chi_r^2 = 7.5$), $T_2 = 13.4(4)$ ms ($\chi_r^2 = 9.5$), $T_2 = 23.9(9)$ ms ($\chi_r^2 = 17.7$), $T_2 = 48(2)$ ms ($\chi_r^2 = 9.3$), $T_2 = 80(3)$ ms ($\chi_r^2 = 7.7$). **b.** Scaling of the coherence time with the number of pulses N. We fit to $T_{N=4}(N/4)^\eta$ where $T_{N=4}$ is the coherence time for $N = 4$. We find $\eta = 0.82(2)$ ($\chi_r^2 = 27.3$).

6.9.13. GATE PARAMETER CALIBRATIONS

In this section, we discuss the calibrations performed for each gate. Next to magnetic field adjustment (Sec. 6.9.6) and balancing of the I & Q channels of the IQ modulator, we perform amplitude calibration of each single-qubit gate. The amplitude of the two-qubit gate requires no separate amplitude calibration, as it is based on the DDRF single-qubit gates. The only difference constitutes a π-phase shift of half of the RF pulses (Fig. 6.4).

In Fig. 6.18, we show two examples of amplitude calibration. In Fig. 6.18a we apply 82 electron $\pi/2$ pulses and read out the electron spin while the nitrogen spin is in $m_I = 0$. We vary the amplitude of the $\pi/2$ pulse in the gate. The minimum is found by fitting a parabola to obtain the optimal amplitude. The π pulses that make up the XY8 sequence are calibrated similarly. In Fig. 6.18b we apply 98 nitrogen $\pi/2$ pulses with DDRF and read out the nitrogen spin. We vary the amplitude of the RF driving of the nitrogen spin. The maximum value of the fit gives the optimal amplitude for the RF driving.

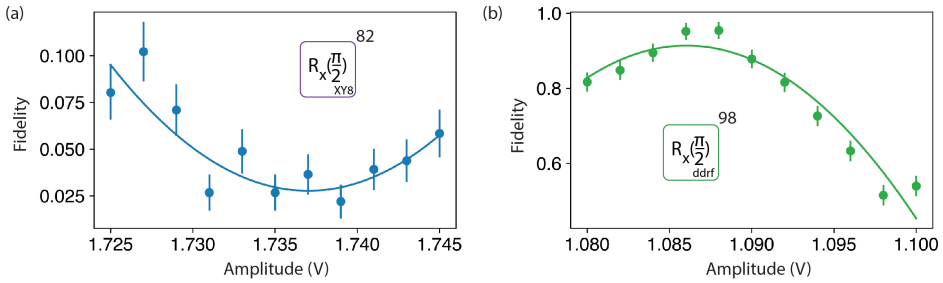

Figure 6.18: **Amplitude calibration of electron and nitrogen gates. a.** We apply 82 electron $\pi/2$ gates while sweeping the amplitude of the $\pi/2$ pulse. By fitting to $A + a(x - x_0)^2$, we obtain the optimal amplitude of 1.7370(9) V ($\chi^2_r = 1.4$). **b.** We apply 98 nitrogen $\pi/2$ gates while sweeping the RF amplitude in the DDRF gate. We find the optimal amplitude at 1.0860(9) V ($\chi^2_r = 3.6$).

6.9.14. SINGLE-SHOT READOUT CORRECTION

For the results shown in Figures 6.5 and 6.6 as well as in many other figures (Figs. 6.9, 6.14, 6.16, 6.17, 6.18, 6.19, 6.20, 6.21, 6.22, 6.23, 6.24), we correct the electron measurement results for known readout errors. We do this by using single-shot readout (SSRO) correction following Pompili et al.[2]. Before and during our measurements, we run SSRO calibrations to find $F_0 = P(\text{measure } m_s = 0 | \text{state is } m_s = 0)$ and similarly F_1. Now the measurement of the electron spin can be described by

$$\mathbf{m} = \begin{pmatrix} F_0 & 1-F_1 \\ 1-F_0 & F_1 \end{pmatrix} \mathbf{p} \tag{6.16}$$

Here, $\mathbf{m} = \begin{pmatrix} m_0 & m_1 \end{pmatrix}^{\mathrm{T}}$ is a vector with measured populations and $\mathbf{p} = \begin{pmatrix} p_0 & p_1 \end{pmatrix}^{\mathrm{T}}$ is a vector with the true populations we expect based on the measurement fidelities. Measuring m_0, m_1, F_0 and F_1, we obtain p_0 and p_1 by matrix inversion. For example, for 500 repetitions of preparing the electron spin in $m_s = 0$ and reading it out, one could measure 406 occurrences of $m_s = 0$. This gives $m_0 = 406/500$ and $m_1 = 94/500$. Using typical values of $F_0 = 82\%$ and $F_1 = 99\%$ this gives $p_0 = 0.99$ and $p_1 = 1 - p_0 = 0.01$. Note that this method can return non-physical central values due to noise (e.g. a population number exceeding one). An alternative method to do SSRO correction is Iterative Bayesian Unfolding[68].

For readout of the nitrogen spin, its state is mapped to the electron spin and subsequently measured as an electron spin state. Therefore we also use the correction described in this section for measurements of the nitrogen spin state. Note that we do not

correct for the infidelity of the readout circuit of the nitrogen spin, which explains why the fidelities are typically not perfect (see e.g. Fig. 6.16).

The error bars on the data in the relevant figures (Figs. 6.5, 6.6, 6.9, 6.14, 6.16, 6.17, 6.18, 6.19, 6.20, 6.21, 6.22, 6.23, 6.24) represent one standard deviation and are calculated using the measured populations m_0, m_1. The error on m_0, m_1 is binomial:

$$\sigma_{m_0} = \sigma_{m_1} = \sqrt{\frac{m_0(1-m_0)}{N}}, \tag{6.17}$$

where N is the number of experimental repetitions. We can invert equation 6.16 to obtain the error on the expected populations[2]:

$$\sigma_{p_0} = \sigma_{p_1} = \frac{\sigma_{m_0}}{F_0 + F_1 - 1}. \tag{6.18}$$

6.9.15. RANDOMIZED BENCHMARKING

A common method to characterize quantum gates is randomized benchmarking (RB)[35–40]. Randomized benchmarking gives a metric for how well a quantum state 'survives' sequences of random quantum gates. In contrast to the GST that we use in the main text, randomized benchmarking does not provide the full process matrix. Here, we perform (single-qubit) Clifford RB and compare against the results obtained with single-qubit gate set tomography (GST). The protocol is as follows:

1. Random sequences of Clifford gates of different depths (lengths) are generated.
2. An inversion gate is calculated and appended to the random sequence, such that the total sequence is ideally identity.
3. The Clifford gates are compiled out of native gates (Identity, $X(\pi/2)$, $Y(\pi/2)$). The native gates were chosen to be the same as the gates characterized with GST. The average number of native gates per Clifford gate is $N = 3.125$.
4. The compiled sequences are run on either the electron spin (500 repetitions) or the nuclear spin (1000 repetitions). The obtained counts are corrected for electron readout fidelity (Sec. 6.9.14).
5. We plot the survival probability P of the quantum state as a function of native gate sequence depth m. We fit $P = A + Bp^m$ to the average survival probabilities per depth and extract the depolarizing parameter p. Here, A and B are values that capture the state preparation and measurement (SPAM) errors. A is fixed to 0.5.
6. The average gate infidelity r is calculated using $r = \frac{(2^n-1)(1-p)}{2^n}$ where n is the number of qubits. The average gate fidelity is $F_{ave} = 1 - r$.

To be able to compare the results from RB and GST, we use a simulation to generate RB data based on the process matrices of the native gates, that were obtained using GST[45]. The simulated RB data is analysed in a similar fashion as the experimental RB data. Then, the average gate fidelities of both methods can be compared. GST gives gate

fidelities for the native gates separately. As a sanity check, we took the average of these gate fidelities, weighted by their occurrence in the RB sequences used for both experiment and simulation. In all three cases described below, this weighted average was - within error - the same as the result of the RB simulation. This indicates that one can directly compare the weighted average gate fidelity of the GST report to an average gate fidelity found with RB.

RB ON THE ELECTRON SPIN

We generate 30 random sequences of Clifford gates for each depth $m_C = \{5, 10, 20, 50, 100, 200, 500, 750\}$ Clifford gates. The inversion gate (also a Clifford gate) theoretically returns the quantum state to the measurement basis, which we alternate between the electron state $m_s = 0$ and $m_s = -1$.

Figure 6.19a shows the survival probability for each sequence. For this experiment, the nitrogen spin was initialised in $m_I = 0$. The identity gate consists of an XY8 decoupling sequence (Fig. 6.2a). The $\pi/2$ gates around x and y are Hermite pulses without XY8 decoupling sequences around them (Fig. 6.2a). We find a depolarizing parameter $p = 0.99991(1)$ ($\chi^2_r = 40.7$). The average gate fidelity of a native gate is $F_{ave} = 0.999956(6)$.

With GST, we also investigated this experimental regime with the nitrogen initialized in $m_I = 0$ and no decoupling sequences around the $\pi/2$ gates. The results are shown on the right hand side of Fig. 6.2b. With the process matrices obtained from this GST characterization, we simulate RB data (with a binomial spread) using the pygsti package[69]. For this, the same random sequences are used as for the actual RB experiment. The results are shown in Fig. 6.19b. We found a depolarizing parameter $p = 0.999717(4)$ ($\chi^2_r = 1.30$), resulting in an average gate fidelity of $F_{ave} = 0.999859(2)$. This is in correspondence with the weighted (for their occurrence in the RB sequences) average of the gate fidelities from GST, which is 0.99985(3).

Interestingly, the average gate fidelity found with experimental RB ($F_{ave} = 0.999956(6)$) is significantly higher than the average gate fidelity reported by the experimental GST ($F = 0.99985(3)$). This can be an indication of non-Markovianity in our system, for example in the form of slow fluctuations of the magnetic field. This type of error manifests as a coherent error that is the same within one measurement repetition, but differs from repetition to repetition. Since GST amplifies coherent errors, it is relatively sensitive to such low-frequency noise, whereas the random nature of RB sequences makes it relatively insensitive[45]. The large spread in survival probabilities for the actual RB experiment (especially for long sequences) may also be related to the non-Markovianity in our system. The large χ^2_r can also be an indication of the noise being non-Markovian[37,70].

The results in Fig. 6.20 are from a similar experiment. Except here, there are XY8 sequences around the $\pi/2$ pulses around x and y (Fig. 6.2a). The nitrogen was initialised in $m_I = 0$. For the fit, we obtain a depolarizing parameter $p = 0.99941(2)$ ($\chi^2_r = 11.6$). The average gate fidelity of a native gate is $F_{ave} = 0.99970(1)$. Figure 6.20b shows simulated data based on the process matrices of the gates, that were obtained by the GST experiment reported in Fig. 6.25b, second column. We find a depolarizing parameter $p = 0.999578(8)$ ($\chi^2_r = 2.42$). The average gate fidelity of a native gate is $F_{ave} = 0.999789(4)$. This value is the same as the weighted average of the gate fidelities of the GST report, which is 0.99979(5).

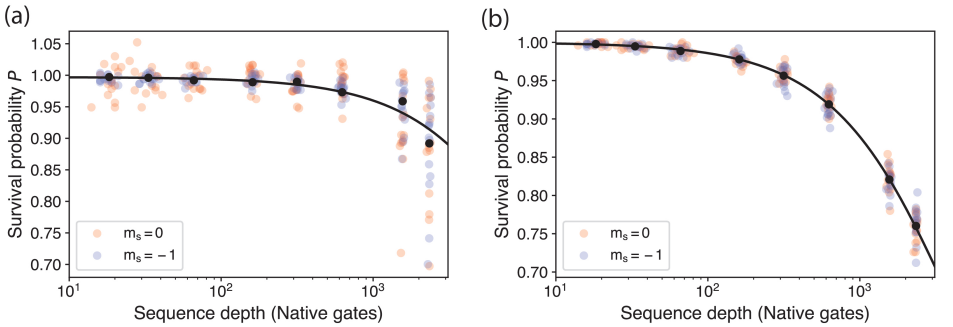

Figure 6.19: **Electron RB results.** The nitrogen spin is initialized in $m_I = 0$ and no decoupling sequences are used around the $\pi/2$ gates. Red (blue) dots are values resulting from a sequence ending with an inversion gate bringing the spin to $m_s = 0$ ($m_s = -1$). Black dots are the average of all survival probabilities belonging to one Clifford depth $m_C = \{5, 10, 20, 50, 100, 200, 500, 750\}$. The black line is a fit to the black dots. Errorbars on the black dots are binomial errors and smaller than the datapoints. **a.** Experimental result. The depolarizing parameter is $p = 0.99991(1)$ ($\chi^2_r = 40.7$), resulting in an average gate fidelity of $F_{ave} = 0.999956(6)$. **b.** Simulation of the RB experiment based on the process matrices obtained with GST. The depolarizing parameter $p = 0.999717(4)$ ($\chi^2_r = 1.30$) results in an average gate fidelity of $F_{ave} = 0.999859(2)$.

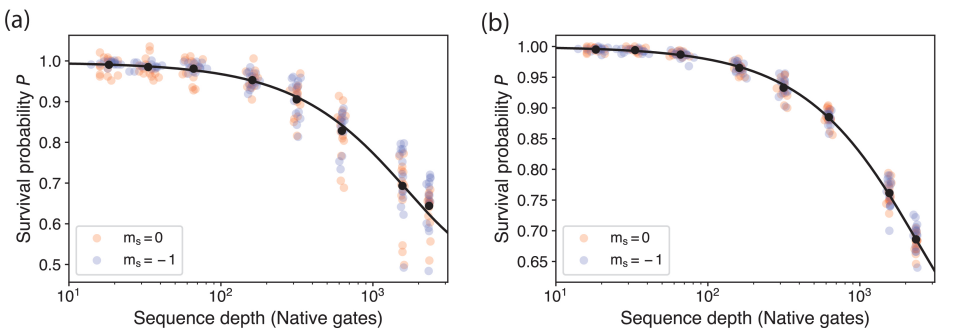

Figure 6.20: **Electron RB results.** The nitrogen spin is initialized in $m_I = 0$ and there are XY8 decoupling sequences around the $\pi/2$ gates. Red (blue) dots are values resulting from a sequence ending with an inversion gate bringing the spin to $m_s = 0$ ($m_s = -1$). Black dots are the average of all survival probabilities belonging to one Clifford depth $m_C = \{5, 10, 20, 50, 100, 200, 500, 750\}$. Black line is a fit to the black dots. Errorbars on the black dots are binomial errors and smaller than the datapoints. **a.** Experimental results. The depolarizing parameter is $p = 0.99941(2)$ ($\chi^2_r = 11.6$), resulting in an average gate fidelity of $F_{ave} = 0.99970(1)$. **b.** Simulation of RB experiment based on the process matrices obtained with GST. The depolarizing parameter $p = 0.999578(8)$ ($\chi^2_r = 2.42$) results in an average gate fidelity of $F_{ave} = 0.999789(4)$.

Again, there is a discrepancy between the average gate fidelity found with RB and the average gate fidelity found with GST. However, it is significantly smaller, possibly because the XY8 decoupling sequences around the Hermite pulses reduce the non-Markovianity in our system.

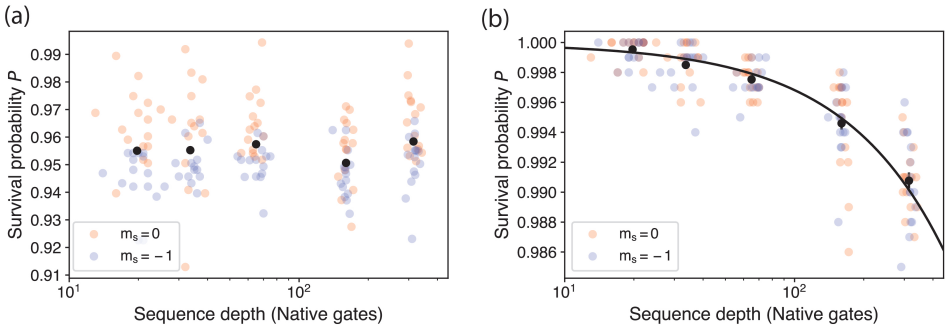

Figure 6.21: **Nitrogen RB results.** The electron was initialized in $m_s = 0$ and DDRF gates were used (Fig. 6.3a). Red (blue) dots are values resulting from a sequence ending with an inversion gate bringing the nitrogen spin to the state that is mapped to $m_s = 0$ ($m_s = -1$) during readout. Black dots are the average of all survival probabilities belonging to one Clifford depth $m_C = \{5, 10, 20, 50, 100\}$. **a.** Experimental result. There is no visible decay. The RB experiment took ~ 3 hours compared to ~ 1.5 hours for the GST results in Fig. 6.3b. **b.** Simulation of RB experiment based on the process matrices obtained with GST. Black line is a fit to the black dots, yielding a depolarizing parameter of $p = 0.999537(6)$ ($\chi^2_r = 3.12$). This gives an average gate fidelity of $F_{ave} = 0.999968(3)$.

RB ON THE NITROGEN SPIN

The results for RB on the nitrogen spin are shown in Fig. 6.21a. Here, the electron is in an eigenstate ($m_s = 0$) and we use DDRF gates (Fig. 6.3a). As expected, there is no visible decay for these depths. This data should be compared to the GST results shown on the right hand side of Fig. 6.3b. Using the process matrices obtained with that GST experiment, we simulate the RB experiment in Fig. 6.21b. We find $p = 0.999937(6)$ ($\chi^2_r = 3.12$). The average gate fidelity of a native gate is $F_{ave} = 0.999968(3)$. The weighted average of the gate fidelities from the GST report is 0.99996(3).

6.9.16. SWAP: COMPARISON TO THE GST PREDICTION

In Figure 6.6a, we apply the compiled SWAP gate n times. After an even number of SWAPs, we then measure the average state fidelity of the six cardinal states:

$$F_{\text{avg}} = \frac{1}{6}\sum_{i=1}^{6} \langle\psi|_i \, \rho \, |\psi\rangle_i \,, \tag{6.19}$$

with $|\psi\rangle_i \in \{|Z\rangle, |-Z\rangle, |X\rangle, |-X\rangle, |Y\rangle, |-Y\rangle\}$.

For this purpose, the electron is initialized to each of the cardinal axes and the nitrogen is initialised in $m_I = 0$. At the end of an even number of SWAP gates, we measure the projections of the electron spin onto all cardinal axes, and the nitrogen spin along z.

In addition to the average state fidelity after n SWAP gates, the action of the extended gate sequence on the individual spin components of both electron and nitrogen spin are well reproduced by the process matrices obtained with two-qubit GST. This is illustrated in Figure 6.22 which shows an example of state preparation and measurement in different bases and its comparison to the GST prediction. The results corroborate the accuracy of the process matrices obtained from GST.

Even though the average state fidelity after $n = 20$ SWAP operations reaches 0.5, the individual electron spin components clearly show coherent rotations well beyond that, which are expected to come from coherent errors. Together with the predictive power of GST, this can be used to design tailored error mitigation to cancel the effect of accumulated coherent errors in specific extended gate sequences (Sec. 6.9.17).

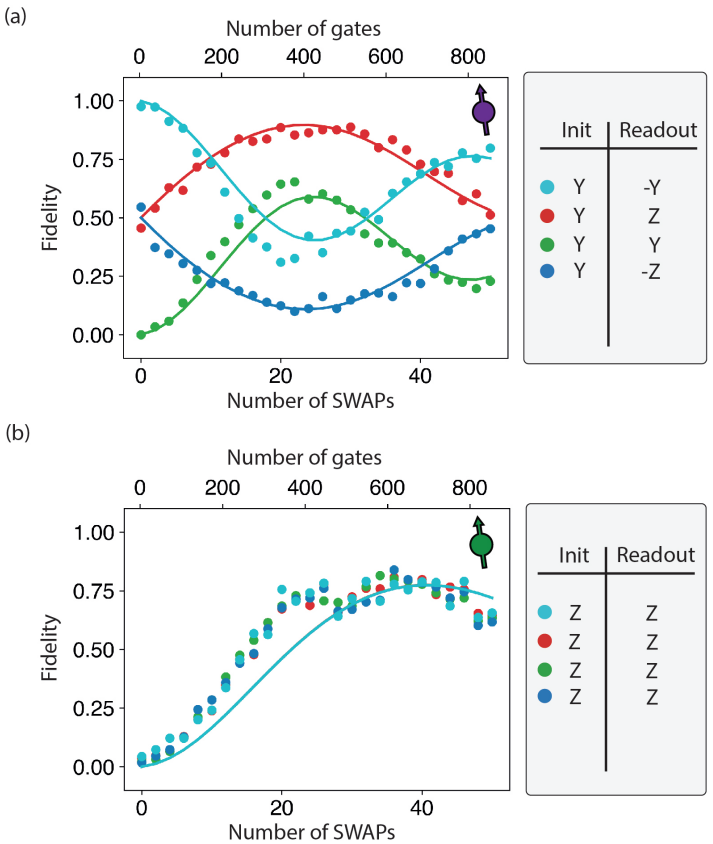

Figure 6.22: **Comparison of GST-based prediction to experiment for different spin components. a.** Electron spin population measured along different cardinal axes (points) and corresponding GST predictions (lines). **b.** Nitrogen spin population measured along z (points) and corresponding GST predictions (lines).

6.9.17. SWAP: ERROR MITIGATION TECHNIQUES

As illustrated in Figure 6.6b, the average fidelity of the six cardinal electron states after an even number of SWAPs is mainly limited by a build-up of coherent errors. The particular sequence is close to a worst-case scenario, as the same gate is repeated n times, allowing coherent errors to add up with circuit depth. However, circuits of practical interest are in general not random, so the effect of coherent errors on the results will likely be significant. The direct solution is to improve the precision of the calibration of the basic gate parameters in order to further reduce the coherent errors. However, this can be challenging at the high-fidelity levels achieved here.

We highlight two different solutions to this issue using GST process matrix simulations, the results of which are illustrated in Figure 6.23. First, using GST, we can determine the accumulated coherent error of a particular larger circuit block. In principle, this could allow one to tailor a specific gate sequence that cancels the effect of the coherent error completely. In the particular sequence at hand, a significant portion of the coherent error is due to a $Z_e I_n$ error during the controlled two-qubit gate. Therefore, echo-pulses on the electron after each swap (compiled as two electron $X_{\pi/2}$ gates), can significantly decrease the accumulated coherent error (Fig. 6.23).

Second, we can use error mitigation techniques such as Pauli-twirling which was recently also used in the context of error extrapolation [71–74]. Due to the twirling, the coherent errors cannot add up. In our case, we can build a Pauli-twirling set from our characterized gates as $\{I, X_{\pi/2} * X_{\pi/2}, Y_{\pi/2} * Y_{\pi/2}, X_{\pi/2} * Y_{\pi/2} * X_{\pi/2} * Y_{\pi/2}\}$. The twirling operations are compiled as illustrated in Figure 6.23. For the simulation, we average over ten different realisations, picking a Pauli P_1 and P_2 randomly from the twirling set for each SWAP in the sequence. As we can see in the figure, the Pauli-twirling does not allow for a coherent build-up of errors, resulting in an exponential decay of the average fidelity of the six cardinal states. Comparing to ideal Pauli gates, we note that the effectiveness of this error mitigation technique relies on high-fidelity single qubit gates. These theoretical simulations for the example case (repeated SWAPs) illustrate that the GST characterisation can be used to determine tailored error mitigation methods to improve the fidelity of circuit blocks.

6.9.18. QUANTUM MEMORY: ELECTRON-SPIN DEPOLARISATION DURING NITROGEN-SPIN DECOUPLING

In this section, we discuss additional data accompanying Fig. 6.6c. In Figure 6.6c, we read out the electron spin, which gives information about the state stored on the nitrogen spin. In Figure 6.24, we read out the nitrogen spin, which gives information about what happens to the electron spin during the decoupling sequence on the nitrogen spin. We find that the electron spin population decays during XY8 decoupling of the nitrogen spin. A similar decay is predicted from the two-qubit GST process matrices, even though this prediction does not include electron-spin dephasing during the free evolution time. The electron spin depolarisation occurs at the same timescale as the nitrogen spin decoherence in Fig. 6.6c, which suggests that electron-spin control errors in the DDRF gate are the underlying cause of the observed nitrogen spin decay, instead of direct decoherence of the nitrogen spin due to the surrounding spin bath.

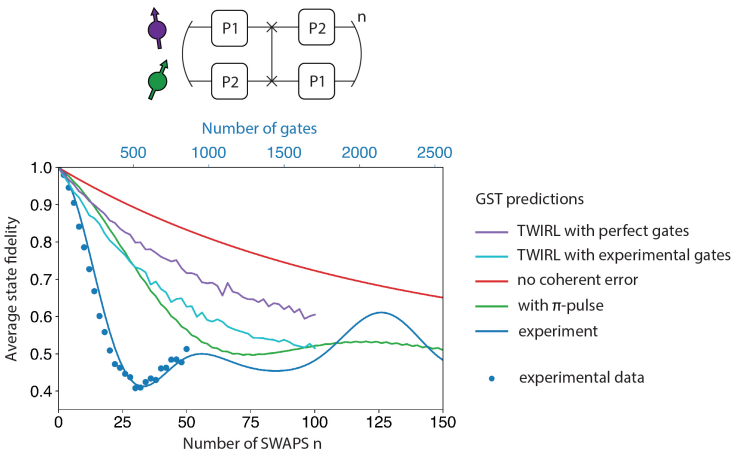

Figure 6.23: **The effect of error mitigation techniques on the electron-nitrogen SWAP gate sequence.** Similar to Figure 6.6b, with the addition of Pauli twirling to mitigate the build-up of coherent errors. Top: Pauli Twirling compilation for the SWAP gate. For each realisation and each SWAP we choose P_1 and P_2 at random. For perfect Pauli operations, this block is identical to a simple SWAP. Bottom: Comparison of different mitigation techniques for the n sequential SWAP gate sequence. Both electron π-pulse echo (green) and Pauli twirling with experimental gates (light blue) or perfect gates (purple) are simulated to improve the average state fidelity.

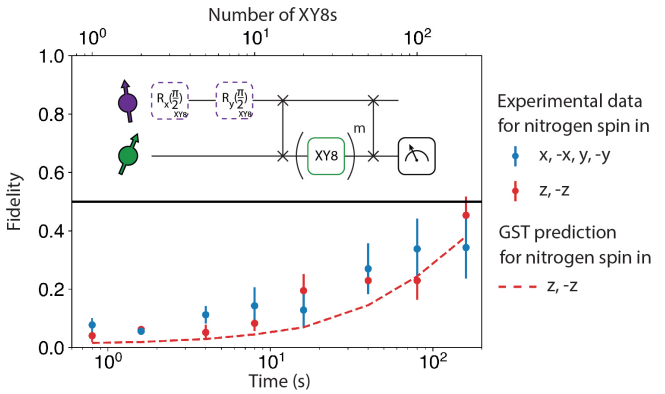

Figure 6.24: **Electron spin population during nitrogen decoupling.** After storing a quantum state ($\pm x$, $\pm y$ or $\pm z$) on the nitrogen spin and swapping it to the electron spin, we measure the nitrogen spin to determine what happened to the electron spin during nitrogen decoupling. The electron spin population decays for increasing numbers of XY8s. The timescale is similar to the decay of the nitrogen spin in Fig. 6.6c, suggesting that control errors in the DDRF $\pi/2$ gates that make up the nitrogen spin XY8 decoupling sequence lead to the observed decay.

6.9.19. ADDITIONAL GST RESULTS

In this section, we show a range of additional gate set tomography results that complement those in the main text. In the electron-nitrogen system of the NV center, there are many possible modes of operation depending on how each qubit is used at a particular point in an algorithm (e.g. nitrogen spin initialised or mixed) , which can correspond to different implementations (e.g. including or excluding XY8 decoupling sequences). Therefore there are a wide variety of situations that are useful to characterize.

SINGLE-QUBIT GST ON THE ELECTRON SPIN

In Fig. 6.25, we show six additional GST results for the electron spin. While we only show and discuss the obtained average gate fidelities, we obtained a full process matrix of each gate. These are provided separately, together with the data.

For completeness, we calibrate and characterize another important ingredient of a universal gate set: the T-gate or $\pi/4$ gate. The implemented T-gate is based on the $\pi/2$ gate, but has approximately half the amplitude. In Fig. 6.25a, we show how each electron gate is compiled out of electron pulses. In Fig. 6.25b, we show the electron GST results, with the T-gate in the left column. We find that we can implement the $\pi/4$ gate in similar fashion with comparable (and even slightly better) fidelities to the electron $\pi/2$ gate.

Then, we turn to the situation discussed in Fig. 6.2 of the main text, where we operate the electron with electron pulses sandwiched between XY8 sequences for when the nitrogen spin is mixed. In the second column in Fig. 6.25b, we show the same results with the nitrogen initialised in $m_I = 0$. We find that the fidelity is significantly improved for both $\pi/2$ gates, suggesting that the mixed nitrogen state reduces the average gate fidelity of electron gates. For this operation regime we also did a randomized benchmarking experiment, as shown in Fig. 6.20.

While we typically decouple at $\tau = 7.304$ μs to avoid nitrogen phase pick-up and driving (Sec. 6.9.6), we can decouple at another value of τ when just controlling the electron spin. In the third column of Fig. 6.25b, we show this situation for $\tau = 2.0$ μs. We find comparable fidelities to $\tau = 7.304$ μs (second column), suggesting that decoupling at a different τ has no significant influence on the fidelity of the electron gates.

In the fourth column in Fig. 6.25b, we perform the same experiment as in the second column, but without fiducial pair reduction and without characterising the identity gate. Fiducial pair reduction is a method to reduce the number of quantum circuits that have to been run, making a gate set tomography experiment significantly more efficient[32,75]. Unless mentioned, all experiments in this work are performed with fiducial pair reduction. To verify that this simplification does not introduce deviations, we also report an experiment without reduction here. We find similar results, regardless of whether we use fiducial pair reduction or not (column 4 vs. column 2). Note that running GST without fiducial pair reduction is only realistic for single-qubit GST, not for two-qubit GST.

Next, we consider what happens when we operate the electron with single $\pi/2$ pulses instead of the composite $\pi/2$ gate with XY8s when the nitrogen is mixed (Fig. 6.25b, column 5). Compared to Fig. 6.2 of the main text, right-hand side, we find a significantly reduced fidelity for the $\pi/2$ pulse when the nitrogen is mixed compared to when it is initialised in $m_I = 0$. Compared to Fig. 6.2 of the main text, left-hand side, we see that applying XY8s around a $\pi/2$ pulse helps to improve the average gate fidelity.

The effect of the mixed nitrogen spin is that the electron spin picks up a different phase depending on the nitrogen spin state. To counteract this effect, we can either apply XY8s or we can make sure the time between two consequent $\pi/2$ pulses is a multiple of the electron-nitrogen interaction strength. This case is shown in the final column of Fig. 6.25b. We find no significant improvement compared to the results in column 5. One explanation could be that the native time between consequent $\pi/2$ pulses in column 5 is 1344 ns, which is already a close multiple of the electron-nitrogen interaction strength.

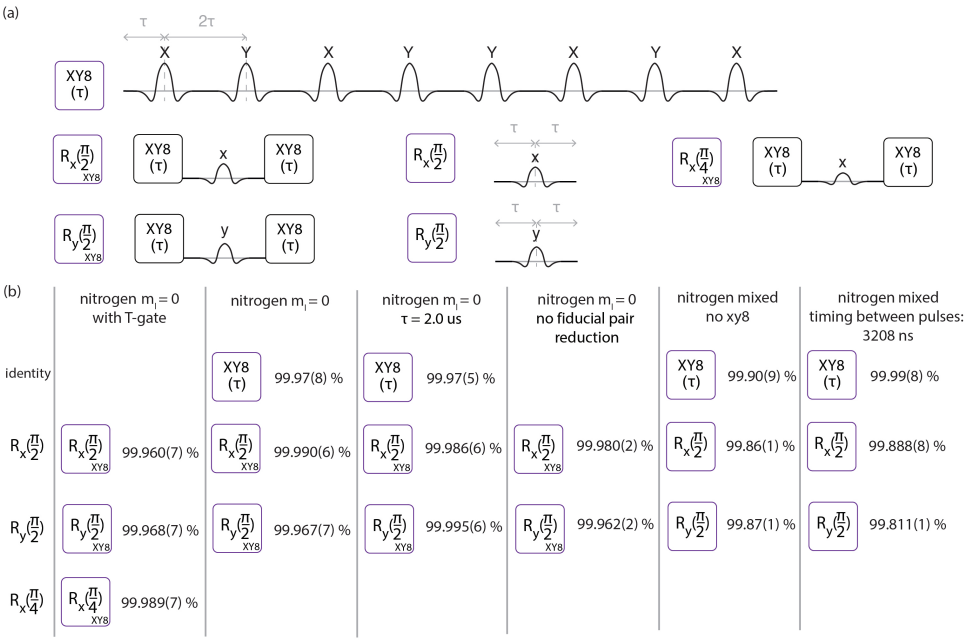

Figure 6.25: **Additional electron single-qubit GST results. a.** The collection of electron gates applied in the various GST experiments. The XY8 sequence consists of multiple Hermite π pulses with an interpulse delay of $\tau = 7.304$ μs unless indicated otherwise. Next to the gates in the main text, we also calibrate an electron $\pi/4$ gate around x. **b.** Average gate fidelities for the additional electron single-qubit GST results. (column 1) GST on the electron gates with an additional T-gate or $\pi/4$ gate. (column 2) Electron gates with XY8 with the nitrogen spin in $m_I = 0$. (column 3) Electron gates with XY8 for an interpulse delay of $\tau = 2.0$ μs instead of $\tau = 7.304$ μs. (column 4) Electron gates with XY8 without fiducial pair reduction. (column 5) Electron gates without XY8 with the nitrogen spin in a mixed state. The time delay between two $\pi/2$ pulses is 1344 ns. (column 6) Electron gates without XY8 with the nitrogen in a mixed state. We apply a specific timing (3208 ns) between two consequent $\pi/2$ pulses, which is a multiple of the electron-nitrogen interaction strength.

SINGLE-QUBIT GST ON THE NITROGEN SPIN

Similarly to the electron spin, we implement a T-gate or $\pi/4$ gate on the nitrogen spin using the DDRF gate. We do not do any separate calibrations, but simply half the number of DDRF units for the $\pi/4$ gate compared to the $\pi/2$ gate (Fig. 6.26a). We find a comparable but somewhat worse fidelity for the $\pi/4$ gate, which could be due to the lack of separate amplitude calibration for that gate.

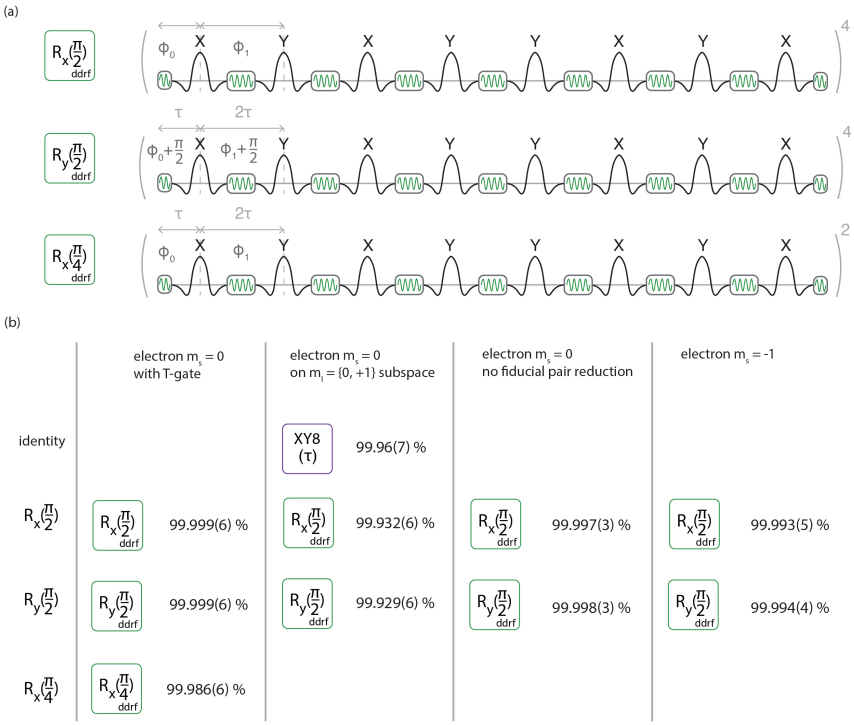

Figure 6.26: **Additional nitrogen single-qubit GST results. a.** The collection of nitrogen gates applied in the various GST experiments. Next to the DDRF $\pi/2$ gates already discussed in the main text, we implement a T-gate or $\pi/4$ gate by halving the number of DDRF units and without doing any further amplitude calibration. **b.** Average gate fidelities for the additional nitrogen single-qubit GST results. (column 1) Next to the previously characterised $\pi/2$ gates (Fig. 6.3), we characterise a DDRF $\pi/4$ gate. (column 2) Nitrogen gates on the $m_I = \{0,+1\}$ subspace, important for the nitrogen SWAP initialisation (Sec. 6.9.9). (column 3) Nitrogen gates without fiducial pair reduction. (column 4) Nitrogen gates with the electron in $m_s = -1$ instead of $m_s = 0$.

Next, we characterise the single-qubit gates on the $m_I = \{0, +1\}$ subspace of the nitrogen spin as opposed to the $m_I = \{0, -1\}$ subspace that we mostly discuss. The importance of the $m_I = \{0, +1\}$ gates lies in the SWAP initialisation of the nitrogen spin where such sequences are used (Sec. 6.9.9). Instead of RF driving at the $m_I = 0, -1$ transition with the electron in $m_s = -1$, we now drive at the $m_I = 0, +1$ transition with the electron in $m_s = -1$, at a frequency of 2.780105 MHz. We find fidelities exceeding 99.9% for the nitrogen $\pi/2$ gates in the $m_I = \{0, +1\}$ subspace. Compared to the gates on the $m_I = \{0, -1\}$ subspace, these fidelities are significantly worse. The origin of this is in the value of $\tau = 7.304$ µs, which has been optimised for the $m_I = \{0, -1\}$ subspace to avoid any unwanted rotations on the nitrogen spin during the application of an XY8 sequence on the electron spin (Sec. 6.9.6). For the gates on the $m_I = \{0, +1\}$ subspace, we also use $\tau = 7.304$ µs, thereby introducing unwanted rotations on the nitrogen spin during the DDRF gate. We partly counteract this by calibrating the amplitudes for the x and y gates separately, but this results in a worse fidelity than the gates on the $m_I = \{0, -1\}$ subspace. Further optimisation of the gates on the $m_I = \{0, +1\}$ subspace is therefore possible, for example by adjusting τ to a more suitable value. But, this is not pursued here.

Next, we characterise the single-qubit gates on the nitrogen spin without fiducial pair reduction (Fig. 6.26b, final column). We find comparable fidelities to the results obtained without fiducial pair reduction (Fig. 6.3). Finally, we consider the nitrogen DDRF gate with the electron in $m_s = -1$ instead of $m_s = 0$ (see also Fig. 6.3). We find no discernible difference, suggesting that the nitrogen DDRF gate is a suitable gate for the regime where the electron spin is in an unknown or mixed state.

6.9.20. GST SETTINGS AND MODEL VIOLATION

In this section, we show the settings for all experimental results with gate set tomograhpy presented in this work (Table 6.1). We group the results per figure and indicate the corresponding name in that figure. First, we show the maximum circuit depth L used for that experiment. When we indicate $L = 128$, that implies that germs of depth $1, 2, 4, 8, 16, 32, 64$ and 128 were run[32]. Then, we indicate the experimental repetitions used for each circuit. The estimation error of gates in GST is typically of the order $O(1/L\sqrt{N})$ where N is the number of repetitions[32]. Lastly, we report the N_σ metric for $L = 128$, which quantifies the model violation[32]. Another important element of the GST experiments is the preparation fiducials, germs and measurement fiducials used. We provide these separately, together with the data.

AUTHOR CONTRIBUTIONS

H.P.B. played a leading role in all the aspects of the work, together with J.Y., with support from all authors.

Fig. 6.2			
name	L	repetitions	N_σ
electron operation nitrogen mixed	128	1000	15.4
electron operation nitrogen $m_I = 0$	128	1000	8.71
Fig. 6.3			
nitrogen operation electron $m_s = -1$	512	1000	2.76
nitrogen operation electron in any state	128	2000	1.3
Fig. 6.4			
full operation	128	2000	15.3
Fig. 6.25			
name	L	repetitions	N_σ
nitrogen $m_I = 0$ with T-gate	128	1000	38.3
nitrogen $m_I = 0$	128	1000	-0.75
nitrogen $m_I = 0$ $\tau = 2.0\,\mu$s	128	1000	2.81
nitrogen $m_I = 0$ no fiducial pair reduction	128	1000	19
nitrogen mixed no xy8	128	1000	49.8
nitrogen mixed timing between pulses: 3208 ns	128	1000	28.2
Fig. 6.26			
name	L	repetitions	N_σ
electron $m_s = 0$ with T-gate	128	1000	4.9
electron $m_s = 0$ on $m_I = \{0, +1\}$ subspace	128	1000	1.79
electron $m_s = 0$ no fiducial pair reduction	128	1000	-0.02
electron $m_s = -1$	128	1000	0.72

Table 6.1: **Settings and model violation for all GST experiments.** Grouped per figure, we show the settings and model violation for every GST experiment in this work. L is the maximum circuit depth, repetitions is the number of experimental repetitions per circuit and N_σ quantifies the model violation[32].

REFERENCES

[1] D. D. Awschalom, R. Hanson, J. Wrachtrup and B. B. Zhou, *Quantum technologies with optically interfaced solid-state spins,* Nature Photonics **12**, 516 (2018).

[2] M. Pompili *et al.*, *Realization of a multinode quantum network of remote solid-state qubits,* Science **372**, 259 (2021).

[3] S. L. N. Hermans *et al.*, *Qubit teleportation between non-neighbouring nodes in a quantum network,* Nature **605**, 663 (2022).

[4] C. E. Bradley *et al.*, *A ten-qubit solid-state spin register with quantum memory up to one minute,* Phys. Rev. X **9**, 031045 (2019).

[5] C. T. Nguyen *et al.*, *Quantum network nodes based on diamond qubits with an efficient nanophotonic interface,* Phys. Rev. Lett. **123**, 183602 (2019).

[6] A. Bourassa *et al.*, *Entanglement and control of single nuclear spins in isotopically engineered silicon carbide,* Nature Materials **19**, 1319 (2020).

[7] V. Vorobyov *et al.*, *Quantum Fourier transform for nanoscale quantum sensing,* npj Quantum Information **7**, 124 (2021).

[8] S. B. van Dam, J. Cramer, T. H. Taminiau and R. Hanson, *Multipartite entanglement generation and contextuality tests using nondestructive three-qubit parity measurements,* Phys. Rev. Lett. **123**, 050401 (2019).

[9] T. van der Sar *et al.*, *Decoherence-protected quantum gates for a hybrid solid-state spin register,* Nature **484**, 82 (2012).

[10] J. Randall *et al.*, *Many-body-localized discrete time crystal with a programmable spin-based quantum simulator,* Science **374**, 1474 (2021).

[11] E. J. Davis *et al.*, *Probing many-body dynamics in a two-dimensional dipolar spin ensemble,* Nature Physics **19**, 836 (2023).

[12] E. Knill, *Quantum computing with realistically noisy devices,* Nature **434**, 39 (2005).

[13] P. Aliferis, D. Gottesman and J. Preskill, *Quantum accuracy threshold for concatenated distance-3 codes,* Quantum Info. Comput. **6**, 97–165 (2006).

[14] B. M. Terhal, *Quantum error correction for quantum memories,* Rev. Mod. Phys. **87**, 307 (2015).

[15] X. Rong *et al.*, *Experimental fault-tolerant universal quantum gates with solid-state spins under ambient conditions,* Nature Communications **6**, 8748 (2015).

[16] T. Xie *et al.*, *99.92%-fidelity cnot gates in solids by noise filtering,* Phys. Rev. Lett. **130**, 030601 (2023).

[17] H. H. Vallabhapurapu *et al., High-fidelity control of a nitrogen-vacancy-center spin qubit at room temperature using the sinusoidally modulated, always rotating, and tailored protocol,* Phys. Rev. A **108**, 022606 (2023).

[18] W. Huang *et al., Fidelity benchmarks for two-qubit gates in silicon,* Nature **569**, 532 (2019).

[19] A. R. Mills *et al., Two-qubit silicon quantum processor with operation fidelity exceeding 99%,* Science Advances **8**, eabn5130 (2022).

[20] A. Noiri *et al., Fast universal quantum gate above the fault-tolerance threshold in silicon,* Nature **601**, 338 (2022).

[21] X. Xue *et al., Quantum logic with spin qubits crossing the surface code threshold,* Nature **601**, 343 (2022).

[22] M. T. Mądzik *et al., Precision tomography of a three-qubit donor quantum processor in silicon,* Nature **601**, 348 (2022).

[23] I. N. Moskalenko *et al., High fidelity two-qubit gates on fluxoniums using a tunable coupler,* npj Quantum Information **8**, 130 (2022).

[24] A. Kandala *et al., Demonstration of a high-fidelity cnot gate for fixed-frequency transmons with engineered zz suppression,* Phys. Rev. Lett. **127**, 130501 (2021).

[25] Y. Sung *et al., Realization of high-fidelity cz and zz-free iswap gates with a tunable coupler,* Phys. Rev. X **11**, 021058 (2021).

[26] I. S. Madjarov *et al., High-fidelity entanglement and detection of alkaline-earth Rydberg atoms,* Nature Physics **16**, 857 (2020).

[27] S. J. Evered *et al., High-fidelity parallel entangling gates on a neutral atom quantum computer,* (2023), arXiv:2304.05420 [quant-ph] .

[28] P. Scholl *et al., Erasure conversion in a high-fidelity rydberg quantum simulator,* (2023), arXiv:2305.03406 [quant-ph] .

[29] Y. Wang *et al., High-fidelity two-qubit gates using a microelectromechanical-system-based beam steering system for individual qubit addressing,* Phys. Rev. Lett. **125**, 150505 (2020).

[30] C. J. Ballance, T. P. Harty, N. M. Linke, M. A. Sepiol and D. M. Lucas, *High-fidelity quantum logic gates using trapped-ion hyperfine qubits,* Phys. Rev. Lett. **117**, 060504 (2016).

[31] C. R. Clark *et al., High-fidelity bell-state preparation with* $^{40}\mathrm{ca}^{+}$ *optical qubits,* Phys. Rev. Lett. **127**, 130505 (2021).

[32] E. Nielsen *et al., Gate Set Tomography,* Quantum **5**, 557 (2021).

[33] R. Blume-Kohout *et al.*, *A taxonomy of small markovian errors,* PRX Quantum **3** (2022).

[34] M. W. Doherty *et al.*, *Theory of the ground-state spin of the nv^- center in diamond,* Phys. Rev. B **85**, 205203 (2012).

[35] J. Emerson, R. Alicki and K. Życzkowski, *Scalable noise estimation with random unitary operators,* Journal of Optics B: Quantum and Semiclassical Optics **7**, S347 (2005).

[36] E. Magesan, R. Blume-Kohout and J. Emerson, *Gate fidelity fluctuations and quantum process invariants,* Phys. Rev. A **84**, 012309 (2011).

[37] J. Helsen, I. Roth, E. Onorati, A. Werner and J. Eisert, *General framework for randomized benchmarking,* PRX Quantum **3**, 020357 (2022).

[38] J. J. Wallman and S. T. Flammia, *Randomized benchmarking with confidence,* New Journal of Physics **16**, 103032 (2014).

[39] T. Proctor, K. Rudinger, K. Young, M. Sarovar and R. Blume-Kohout, *What randomized benchmarking actually measures,* Phys. Rev. Lett. **119**, 130502 (2017).

[40] J. M. Epstein, A. W. Cross, E. Magesan and J. M. Gambetta, *Investigating the limits of randomized benchmarking protocols,* Phys. Rev. A **89**, 062321 (2014).

[41] E. Magesan *et al.*, *Efficient measurement of quantum gate error by interleaved randomized benchmarking,* Phys. Rev. Lett. **109**, 080505 (2012).

[42] S. Sheldon *et al.*, *Characterizing errors on qubit operations via iterative randomized benchmarking,* Phys. Rev. A **93**, 012301 (2016).

[43] S. Boixo *et al.*, *Characterizing quantum supremacy in near-term devices,* Nature Physics **14**, 595 (2018).

[44] F. Arute *et al.*, *Quantum supremacy using a programmable superconducting processor,* Nature **574**, 505 (2019).

[45] R. Blume-Kohout *et al.*, *Demonstration of qubit operations below a rigorous fault tolerance threshold with gate set tomography,* Nature Communications **8**, 14485 (2017).

[46] T. Proctor *et al.*, *Detecting and tracking drift in quantum information processors,* Nature Communications **11**, 5396 (2020).

[47] J. P. Dehollain *et al.*, *Optimization of a solid-state electron spin qubit using gate set tomography,* New Journal of Physics **18**, 103018 (2016).

[48] G. White, C. Hill and L. Hollenberg, *Performance optimization for drift-robust fidelity improvement of two-qubit gates,* Phys. Rev. Appl. **15**, 014023 (2021).

[49] L. Robledo *et al.*, *High-fidelity projective read-out of a solid-state spin quantum register,* Nature **477**, 574 (2011).

[50] M. H. Abobeih *et al.*, *Fault-tolerant operation of a logical qubit in a diamond quantum processor,* Nature **606**, 884 (2022).

[51] T. P. Harty *et al.*, *High-fidelity preparation, gates, memory, and readout of a trapped-ion quantum bit,* Phys. Rev. Lett. **113**, 220501 (2014).

[52] A. D. Leu *et al.*, *Fast, high-fidelity addressed single-qubit gates using efficient composite pulse sequences,* (2023), arXiv:2305.06725 [quant-ph] .

[53] R. Barends *et al.*, *Superconducting quantum circuits at the surface code threshold for fault tolerance,* Nature **508**, 500 (2014).

[54] C. H. Yang *et al.*, *Silicon qubit fidelities approaching incoherent noise limits via pulse engineering,* Nature Electronics **2**, 151 (2019).

[55] J. Yoneda *et al.*, *A quantum-dot spin qubit with coherence limited by charge noise and fidelity higher than 99.9%,* Nature Nanotechnology **13**, 102 (2018).

[56] M. A. Nielsen, *A simple formula for the average gate fidelity of a quantum dynamical operation,* Physics Letters A **303**, 249 (2002).

[57] Y. R. Sanders, J. J. Wallman and B. C. Sanders, *Bounding quantum gate error rate based on reported average fidelity,* New Journal of Physics **18**, 012002 (2015).

[58] R. Nagy *et al.*, *High-fidelity spin and optical control of single silicon-vacancy centres in silicon carbide,* Nature Communications **10**, 1954 (2019).

[59] B. Pingault *et al.*, *Coherent control of the silicon-vacancy spin in diamond,* Nature Communications **8**, 15579 (2017).

[60] E. I. Rosenthal *et al.*, *Microwave spin control of a tin-vacancy qubit in diamond,* Phys. Rev. X **13**, 031022 (2023).

[61] J. R. Johansson, P. D. Nation and F. Nori, *QuTiP: An open-source Python framework for the dynamics of open quantum systems,* Computer Physics Communications **183**, 1760 (2012).

[62] J. R. Johansson, P. D. Nation and F. Nori, *QuTiP 2: A Python framework for the dynamics of open quantum systems,* Computer Physics Communications **184**, 1234 (2013).

[63] P. R. Bevington and D. K. Robinson, *Data reduction and error analysis for the physical sciences, 3rd ed.* (McGraw-Hill, New York, NY, 2003).

[64] G. Balasubramanian *et al.*, *Nanoscale imaging magnetometry with diamond spins under ambient conditions,* Nature **455**, 648 (2008).

[65] T. Taminiau *et al.*, *Detection and control of individual nuclear spins using a weakly coupled electron spin,* Phys. Rev. Lett. **109**, 137602 (2012).

[66] W. S. Warren, *Effects of arbitrary laser or nmr pulse shapes on population inversion and coherence,* J. Chem. Phys. **81**, 5437 (1984).

[67] L. M. Vandersypen and I. L. Chuang, *Nmr techniques for quantum control and computation,* Rev. Mod. Phys. **76**, 1037 (2005).

[68] B. Nachman, M. Urbanek, W. A. de Jong and C. W. Bauer, *Unfolding quantum computer readout noise,* npj Quantum Information **6**, 84 (2020).

[69] *Pygsti, http://www.pygsti.info/, doi: 10.5281/zenodo.1209246,* .

[70] J. J. Wallman, *Randomized benchmarking with gate-dependent noise,* Quantum **2**, 47 (2018).

[71] Y. Li and S. C. Benjamin, *Efficient variational quantum simulator incorporating active error minimization,* Physical Review X **7** (2017).

[72] K. Temme, S. Bravyi and J. M. Gambetta, *Error mitigation for short-depth quantum circuits,* Physical Review Letters **119** (2017).

[73] S. Endo, S. C. Benjamin and Y. Li, *Practical quantum error mitigation for near-future applications,* Physical Review X **8** (2018).

[74] Y. Kim *et al.*, *Evidence for the utility of quantum computing before fault tolerance,* Nature **618**, 500 (2023).

[75] K. M. Rudinger *et al.*, *Two-qubit gate set tomography with fewer circuits,* (2023), arXiv:2307.15767 [quant-ph] .

7

CONCLUSIONS AND OUTLOOK

In this chapter, I will first summarise the key findings of this thesis. Looking ahead, I will then outline interesting avenues for future research, as well as discuss the long-term prospects for quantum information processing with defect centers in diamond and other materials.

7.1. SUMMARY

In this thesis, we have demonstrated new & optimised control methods for nuclear and electron spins surrounding a central NV center electron spin. Here, we will summarise the findings per chapter:

- In **Chapter 3**, we demonstrated control of ^{13}C spin pairs surrounding the NV center. We utilised dynamical decoupling sequences resonant with the spin-pair flip-flop dynamics to initialise, read out and control a qubit encoded in the anti-parallel subspace of the spin pair with high fidelity. Then, we measured the coherence time of this ^{13}C spin pair: $T_2^* = 1.9(6)$ min. This could be explained by a combination of three effects: a decoherence-free subspace, a clock transition and motional narrowing. The presence of two spin pairs allowed us to create an entangled state between them through projective parity measurements. The inherent coherence protection makes spin pairs promising systems for a variety of applications, such as robust memories for optically connected quantum networks and memory-enhanced sensing.

- In **Chapter 4**, we demonstrated initialisation, control and readout of individual P1 centers surrounding the NV center. We implemented projective measurements to prepare the multiple degrees of freedom of the P1 center and subsequently demonstrated control and single-shot readout of both its nuclear and electron spin. Finally, we used the developed control to demonstrate an entangled state of two P1 centers. The presented methods to control individual P1 centers can enable enhanced sensing schemes based on entanglement, as well as electron spin chains for quantum computation architectures.

- In **Chapter 5**, we realised initialisation, control and readout of a pair of P1 centers. We used dynamical decoupling sequences to directly observe the back-action of the NV center electron spin on the flip-flop dynamics of P1 centers in the bath. Using heralded initialisation to prepare two P1 centers in specific Jahn-Teller axes and nitrogen spin states, we measured the dependence of the flip-flop dynamics on these degrees of freedom. This allowed us to image a pair of P1 centers with sub-nm resolution. The presented methods and results could contribute to efforts towards atomic- and nano-scale magnetic resonance imaging of complex spin samples outside of the diamond by directly revealing and isolating spin-pair dynamics. Additionally, the long dephasing times indicate electron-spin pairs based on P1 centers or other defects might be interesting qubits.

- In **Chapter 6**, we used gate set tomography (GST) to characterise and optimise the single- and two-qubit gates of the electron-nitrogen spin system native to the NV center. We discerned different operation regimes in which different gates are optimal, and implemented tailored control sequences to mitigate small, unwanted rotations. Finally, we demonstrated single-qubit gate fidelities as high as 99.999(1)% and two-qubit fidelities exceeding 99.9%. The presented results show promise for high-fidelity gates in hybrid electron-nuclear systems of the NV center and other

colour centers. Additionally, the methods presented in this paper can be applied to other nuclear spins such as ^{13}C spins surrounding a central electron spin.

7.2. NEAR-TERM PROSPECTS

In this section, we discuss the prospects for near-term advances following from the work presented in this thesis.

7.2.1. SPIN-PAIR QUANTUM MEMORY

In this thesis, we have demonstrated high-fidelity initialisation, control and readout of spin-pair qubits surrounding an NV center. Due to their exceptional coherence properties, they are an interesting candidate for a quantum memory. In particular, single ^{13}C spins suffer from dephasing during remote entanglement generation due to the stochastic reinitialisation of the NV electron spin[1–4]. However, the frequency shift of a ^{13}C pair is only on the order of a few Hz (Ch. 3), making it potentially extremely robust against dephasing due to stochastic reinitialisation as well as ionisation of the NV.

While ^{13}C pairs are promising quantum memories, there are several challenges. First, the control involves dynamical decoupling around $\tau \approx 120$ μs, where significant decoherence on the electron spin is present. Since initialisation and readout can be done repetitively (Ch. 3), this is not a fundamental limitiation for initialisation and readout fidelities. However, the two-qubit gate between the electron spin and ^{13}C pair is intrinsically limited by electron decoherence. This can potentially be mitigated by polarisation of the nuclear-spin bath[5,6].

Second, the presence of multiple ^{13}C pairs with relatively strong coupling to the NV complicates their use as a quantum memory. NV centers can be selected on the presence of a single dominant ^{13}C pair, for which the probability is relatively high at about 35% (Ch. 3). Alternatively, new control methods could make use of the different absolute hyperfine couplings of the ^{13}C spins making up the spin pair.

Next to ^{13}C pairs, isotopic purification can reduce the NV-^{13}C couplings to make single ^{13}C spins suitable as quantum memories[3]. An interesting question arises here about the presence of ^{13}C pairs in isotopically purified samples. For natural abundance ^{13}C (1.1%), the diamond lattice limits the observable couplings to a discrete set of values (Ch. 3). However, for lower ^{13}C abundance, this spectrum becomes close to continuous, potentially allowing ^{13}C pairs to be better distinguishable.

7.2.2. COUPLED DEFECTS

In this thesis, we have developed control over both single P1 centers and a pair of P1 centers surrounding an NV center. These results provide interesting prospects, with respect to both quantum sensing and quantum memories. Regarding the former, the methods demonstrated to image a pair of P1 centers might be useful for imaging electron spins in individual molecules outside the diamond[7–9]. Even in the absence of the internal degrees of freedom of the P1 center, a rotating magnetic field can be used to the same effect[10]. An interesting possibility here is to develop an algorithm that uses the full dynamical decoupling data, as opposed to fitting to separately measured couplings.

As discussed previously, nuclear spin memories typically suffer from dephasing during remote entanglement generation [1–4]. To combat this, the diamond can be isotopically purified to lower the ^{13}C abundance or ^{13}C spin pairs can be further developed as quantum memories. An interesting alternative is to use nuclear spins coupled to another defect, such as a P1 center, as quantum memories. The electron spin of the P1 center then serves as a 'bus' between the nuclear spin quantum memory and the NV center. It may be possible to use the nitrogen spin of the P1 center as a quantum memory. To that end, the strong electron-nitrogen spin mixing present in this thesis has to be avoided by using a large external magnetic field. It is still an outstanding challenge to demonstrate control over nuclear spins close to a P1 center. The large number of degrees of freedom of the P1 center makes this a challenging endeavour. Other defect electron spins coupled to the NV center may offer an alternative [11–16].

7.2.3. HIGH-FIDELITY CONTROL OF NUCLEAR SPIN REGISTERS

In this thesis, we have demonstrated high-fidelity control of the two-qubit electron-nitrogen spin system of the NV center with two-qubit fidelities exceeding 99.9%. However, the results obtained through gate set tomography (GST) clearly point to remaining noise sources, chief among which are coherent gate errors and electron spin dephasing. The origin of the coherent errors is likely a combination of suboptimal calibration routines and electronics imperfections. Through improvements in these areas, the coherent errors can be improved. On the other hand, electron spin dephasing is likely due to the nuclear- and electron-spin bath surrounding the NV center. To combat this, we can either look at improving the gate design or at new samples with lower abundance of ^{13}C spins and P1 centers.

A natural next step is to apply the same techniques to the control of ^{13}C nuclear spins. Compared to the control of the electron-nitrogen system, there are a number of differences and associated challenges. First, gates on ^{13}C spins can be applied with dynamical decoupling (DD) or dynamical decoupling with RF (DDRF) (Ch. 2). While the results in Chapter 6 suggest the presence of a weak electron-nitrogen $S_z I_x$ interaction, the number of required decoupling pulses is prohibitive for the use of DD gates on the nitrogen spin. In this sense, the nitrogen spin can be viewed as a ^{13}C spin at high magnetic field ($\sim$ kG).

Second, there is a bath of ^{13}C spins instead of just a single ^{14}N spin. Quantum gates on one ^{13}C spin are therefore likely to exhibit crosstalk. Since two-qubit GST is particular to the electron spin and a specific ^{13}C spin, a first challenge here is to characterise crosstalk efficiently. Namely, full three-qubit GST is practically extremely time-consuming. To avoid crosstalk, a balance between Rabi frequency of the ^{13}C spin and gate time needs to be found. Higher Rabi frequency leads to faster gates and therefore less decoherence, but reduces the selectivity and thus increases the risk of crosstalk. In the long term, optimal control methods may offer potential to improve control over a large register of ^{13}C nuclear spins [17–21].

Third, ^{13}C spins are spin-1/2. At low magnetic fields ($\sim$ 100 G), the energy level splitting is therefore relatively small ($\sim$ 100 kHz). Low-frequency noise of electronic equipment can then hinder control fidelities [22]. This can be circumvented by utilising higher magnetic fields ($\sim$ 2 kG) allowing better filtering of low-frequency noise. An additional

benefit for DDRF gates is that the effect of the perpendicular hyperfine component $A_\perp$ is diminished at higher magnetic fields[22].

7.2.4. OPERATION OF THE NV CENTER AT INTERMEDIATE TEMPERATURES

Recent work on the temperature dependence of the photophysics of the NV center[23–25], has shown promise for operating the NV center at intermediate temperatures. In particular, at around 100 K the contrast of the optically detected magnetic resonance (ODMR) revives[23]. The advantage of operation at intermediate temperatures compared to room temperature is the relatively long T_1 of the NV electron spin[26–28]. A short T_1 limits the fidelity of quantum gates as well as the number of nuclear spins that can be accessed. However, such intermediate temperatures do not possess the resonant readout mechanisms available at $\lesssim 20$ K. To make use of the toolbox of electron-nuclear quantum gates developed at low temperature, several challenges need to be addressed.

First, off-resonant readout of the NV center has fidelities close to 50% at room temperature[29–31]. At intermediate temperatures between around 300 and 100 K, the photophysics of the NV is similar[23,25], requiring other methods to improve the single-shot readout fidelity of the NV center. One way forward is to use spin-to-charge conversion. This involves spin-selective ionisation of NV^- to NV^0, after which the charge state of the NV center can be read out[29,32,33]. An alternative is nuclear-assisted readout, which has demonstrated readout fidelities exceeding 90%[34–36]. An important requirement for nuclear-assisted readout is high magnetic field (~ 5 kG), which aligns with the requirements outlined in the previous section.

A second challenge is to control the charge state of the NV center. Off-resonant excitation leaves the NV in its correct NV^- charge state only about 70% of the time[37]. At low temperature we perform a charge resonance (CR) check to make sure the NV center is in the NV^- charge state and the lasers are resonant with the optical transitions of the NV center (Ch. 2). At intermediate temperatures, resonant transitions are not available to validate the NV charge state. Therefore, an alternative solution is required. One alternative is to use a probe pulse and check if the collected photon counts exceed a certain threshold. It has been shown at room temperature that charge state initialisation fidelities exceeding 97% can be achieved in this manner[32,33].

Finally, scaling up an NV-based qubit register at intermediate temperatures is not straightforward. Architectures relying on the generation of remote entanglement are not feasible, since the emitted NV photons do not have a well-defined frequency due to its broad optical lines. The requirements on spectral diffusion of the emitter are therefore relaxed, and implantation of NV centers to create electron spin arrays becomes a real possibility. In this architecture, dipolar coupling between neighbouring NV centers (or other defects) enables controlled gates as has been demonstrated for NV-NV[34,38,39] and NV-P1 systems[40]. One can imagine creating larger chains of like and non-like coupled electron spins for quantum simulation or computation[41–44] as well as enhanced sensing with entangled electron spins[45,46].

7.3. DEFECT-BASED DISTRIBUTED QUANTUM COMPUTING

Scaling up a quantum processor to thousands or potentially millions of qubits is a daunting task. An increasing number of qubits on a single chip typically induces additional crosstalk and control complexity. Therefore, a promising approach is to build a modular quantum processor, where subsystems with a limited number of qubits are connected with links between them[47,48]. Important requirements for such a distributed architecture are a local register of data & memory qubits that are used to run error correction and store quantum information when remote entanglement is being generated. Additionally, a high-quality interface between the remote nodes with flying qubits in the form of photons or phonons is essential.

Defects in solid-state materials are promising candidates for a distributed architecture due to their combination of a nuclear spin register and an optical interface. Theoretical proposals have been put forth on how to run fault-tolerant computations in such an architecture[49–52] and early demonstrations have shown remote entanglement generation[1,2,53–55] as well as control over a register of nuclear spin qubits[22,56,57]. In other systems, such as trapped ions[58] and quantum dots[59], remote entanglement generation has also been demonstrated successfully, as well as control over a long-lived memory qubit[60].

To improve the network performance, it is vital to improve the quantum link efficiency $\eta = r_{\text{ent}}/r_{\text{dec}}$ where r_{ent} is the rate at which entanglement is generated and r_{dec} is the rate at which memory qubits decohere during entanglement generation. In other words, entanglement needs to be generated faster than it is lost. There are two ways to go about it. First, the coherence of the memory qubit under entanglement generation can be improved. In this chapter, we have highlighted some solutions in this direction, for example isotopic purification[3]. Second, the entanglement generation process can be improved.

A long-term disadvantage of the NV center is the relatively low emission in the zero-phonon line (ZPL) at $\sim 3\%$[61–63]. One solution is to embed the NV center in an optical cavity, which can help boost the ZPL emission as well as improve the collection efficiency[64]. However, the NV center is relatively sensitive to electric fields, making it challenging to embed it in cavities where it is close to the surface[64]. While difficult, a recent demonstration has shown some promise in this direction[65].

The difficulty of embedding the NV center in nanophotonic structures has motivated the search for other defects that are less sensitive to surface charges. In particular, group-IV colour centers in diamond such as the silicon-vacancy[66,67] and tin-vacancy[68–71] are first-order insensitive to electric fields due to inversion symmetry[72–76]. Recent demonstrations include memory-enhanced quantum communication[66] as well as integrated error detection[67]. For its good optical properties, ground-state spin control of group-IV colour centers can be challenging due to its large spin-orbit coupling, requiring the presence of strain to induce spin-orbit mixing[70]. Future improvements in spin control as well as optical stability make group-IV colour centers in diamond an exciting candidate for distributed quantum computation.

To scale defect-based distributed architectures to thousands of qubits, integration with on-chip photonics will likely be essential[64,77]. Defects in materials used for inte-

grated photonics such as silicon[78], silicon carbide[79] and lithium niobate[80] may therefore prove to have a decisive advantage. Recent results on defects in silicon carbide[81–83] and silicon[84–86] show promise. Alternatively, heterogeneous integration of material platforms may combine the strenghts of different platforms[77,87].

Regardless of the material platform and defect of choice, the methods for controlling the nuclear- and electron-spin environment presented in this thesis can be utilised. Extensions to spin-1/2 and spin->1 systems for spin-pair control (Ch. 3,5), double resonance experiments (Ch. 4) as well as DDRF (Ch. 6) are interesting possibilities. While such details need to be worked out still, I certainly hope that the work in this thesis finds its use in years to come.

REFERENCES

[1] M. Pompili *et al.*, *Realization of a multinode quantum network of remote solid-state qubits,* Science **372**, 259 (2021).

[2] S. L. N. Hermans *et al.*, *Qubit teleportation between non-neighbouring nodes in a quantum network,* Nature **605**, 663 (2022).

[3] C. E. Bradley *et al.*, *Robust quantum-network memory based on spin qubits in isotopically engineered diamond,* npj Quantum Information **8**, 122 (2022).

[4] N. Kalb, P. C. Humphreys, J. Slim and R. Hanson, *Dephasing mechanisms of diamond-based nuclear-spin memories for quantum networks,* Phys. Rev. A **97**, 062330 (2018).

[5] I. Schwartz *et al.*, *Robust optical polarization of nuclear spin baths using hamiltonian engineering of nitrogen-vacancy center quantum dynamics,* Sci. Adv. **4**, eaat8978 (2018).

[6] J. Randall *et al.*, *Many-body-localized discrete time crystal with a programmable spin-based quantum simulator,* Science **374**, 1474 (2021).

[7] R. Schirhagl, K. Chang, M. Loretz and C. L. Degen, *Nitrogen-vacancy centers in diamond: nanoscale sensors for physics and biology,* Annu. Rev. Phys. Chem. **65**, 83 (2014).

[8] C. L. Degen, F. Reinhard and P. Cappellaro, *Quantum sensing,* Rev. Mod. Phys. **89**, 035002 (2017).

[9] E. Janitz *et al.*, *Diamond surface engineering for molecular sensing with nitrogen—vacancy centers,* J. Mater. Chem. C **10**, 13533 (2022).

[10] D. Yudilevich, R. Stöhr, A. Denisenko and A. Finkler, *Mapping single electron spins with magnetic tomography,* Phys. Rev. Appl. **18**, 054016 (2022).

[11] F. Shi *et al.*, *Quantum logic readout and cooling of a single dark electron spin,* Physical Review B - Condensed Matter and Materials Physics **87**, 1 (2013).

[12] A. Cooper, W. K. C. Sun, J.-C. Jaskula and P. Cappellaro, *Identification and control of electron-nuclear spin defects in diamond,* Phys. Rev. Lett. **124**, 083602 (2020).

[13] T. Yamamoto *et al.*, *Strongly coupled diamond spin qubits by molecular nitrogen implantation,* Phys. Rev. B **88**, 201201 (2013).

[14] E. L. Rosenfeld, L. M. Pham, M. D. Lukin and R. L. Walsworth, *Sensing coherent dynamics of electronic spin clusters in solids,* Phys. Rev. Lett. **120**, 243604 (2018).

[15] M. S. Grinolds *et al.*, *Subnanometre resolution in three-dimensional magnetic resonance imaging of individual dark spins,* Nature Nanotechnology **9**, 279 (2014).

[16] W. K. C. Sun, A. Cooper and P. Cappellaro, *Improved entanglement detection with subspace witnesses,* Phys. Rev. A **101**, 012319 (2020).

[17] N. Khaneja, T. Reiss, C. Kehlet, T. Schulte-Herbrüggen and S. J. Glaser, *Optimal control of coupled spin dynamics: design of NMR pulse sequences by gradient ascent algorithms,* Journal of Magnetic Resonance **172**, 296 (2005).

[18] S. Machnes *et al., Comparing, optimizing, and benchmarking quantum-control algorithms in a unifying programming framework,* Phys. Rev. A **84**, 022305 (2011).

[19] P. Doria, T. Calarco and S. Montangero, *Optimal control technique for many-body quantum dynamics,* Phys. Rev. Lett. **106**, 190501 (2011).

[20] T. Caneva, T. Calarco and S. Montangero, *Chopped random-basis quantum optimization,* Phys. Rev. A **84**, 022326 (2011).

[21] N. Rach, M. M. Müller, T. Calarco and S. Montangero, *Dressing the chopped-random-basis optimization: A bandwidth-limited access to the trap-free landscape,* Phys. Rev. A **92**, 062343 (2015).

[22] C. E. Bradley *et al., A ten-qubit solid-state spin register with quantum memory up to one minute,* Phys. Rev. X **9**, 031045 (2019).

[23] S. Ernst, P. J. Scheidegger, S. Diesch, L. Lorenzelli and C. L. Degen, *Temperature dependence of photoluminescence intensity and spin contrast in nitrogen-vacancy centers,* Phys. Rev. Lett. **131**, 086903 (2023).

[24] S. Ernst, P. J. Scheidegger, S. Diesch and C. L. Degen, *Modeling temperature-dependent population dynamics in the excited state of the nitrogen-vacancy center in diamond,* Phys. Rev. B **108**, 085203 (2023).

[25] J. Happacher *et al., Temperature-dependent photophysics of single nv centers in diamond,* Phys. Rev. Lett. **131**, 086904 (2023).

[26] A. Jarmola, V. Acosta, K. Jensen, S. Chemerisov and D. Budker, *Temperature-and magnetic-field-dependent longitudinal spin relaxation in nitrogen-vacancy ensembles in diamond,* Phys. Rev. Lett. **108**, 197601 (2012).

[27] N. Bar-Gill, L. M. Pham, A. Jarmola, D. Budker and R. L. Walsworth, *Solid-state electronic spin coherence time approaching one second,* Nat. Commun. **4**, 1 (2013).

[28] S. Takahashi, R. Hanson, J. van Tol, M. S. Sherwin and D. D. Awschalom, *Quenching spin decoherence in diamond through spin bath polarization,* Phys. Rev. Lett. **101**, 047601 (2008).

[29] D. A. Hopper, H. J. Shulevitz and L. C. Bassett, *Spin readout techniques of the nitrogen-vacancy center in diamond,* Micromachines **9**, 437 (2018).

[30] M. Steiner, P. Neumann, J. Beck, F. Jelezko and J. Wrachtrup, *Universal enhancement of the optical readout fidelity of single electron spins at nitrogen-vacancy centers in diamond,* Phys. Rev. B **81**, 035205 (2010).

[31] A. Gupta, L. Hacquebard and L. Childress, *Efficient signal processing for time-resolved fluorescence detection of nitrogen-vacancy spins in diamond,* J. Opt. Soc. Am. B **33**, B28 (2016).

[32] D. A. Hopper, J. D. Lauigan, T.-Y. Huang and L. C. Bassett, *Real-time charge initialization of diamond nitrogen-vacancy centers for enhanced spin readout,* Phys. Rev. Appl. **13**, 024016 (2020).

[33] B. J. Shields, Q. P. Unterreithmeier, N. P. de Leon, H. Park and M. D. Lukin, *Efficient readout of a single spin state in diamond via spin-to-charge conversion,* Phys. Rev. Lett. **114**, 136402 (2015).

[34] P. Neumann *et al.*, *Single-shot readout of a single nuclear spin,* Science **329**, 542 (2010).

[35] A. Dréau, P. Spinicelli, J. Maze, J.-F. Roch and V. Jacques, *Single-shot readout of multiple nuclear spin qubits in diamond under ambient conditions,* Phys. Rev. Lett. **110**, 060502 (2013).

[36] G.-Q. Liu *et al.*, *Single-shot readout of a nuclear spin weakly coupled to a nitrogen-vacancy center at room temperature,* Phys. Rev. Lett. **118**, 150504 (2017).

[37] G. Waldherr *et al.*, *Dark states of single nitrogen-vacancy centers in diamond unraveled by single shot nmr,* Phys. Rev. Lett. **106**, 157601 (2011).

[38] F. Dolde *et al.*, *Room-temperature entanglement between single defect spins in diamond,* Nat. Phys. **9**, 139 (2013).

[39] F. Dolde *et al.*, *High-fidelity spin entanglement using optimal control,* Nat. Commun. **5**, 3371 (2014).

[40] M. Degen *et al.*, *Entanglement of dark electron-nuclear spin defects in diamond,* Nat. Commun. **12**, 1 (2021).

[41] N. Y. Yao *et al.*, *Scalable architecture for a room temperature solid-state quantum information processor,* Nature Communications **3**, 800 (2012).

[42] N. Y. Yao *et al.*, *Quantum logic between remote quantum registers,* Phys. Rev. A **87**, 022306 (2013).

[43] Y. Ping, B. W. Lovett, S. C. Benjamin and E. M. Gauger, *Practicality of spin chain wiring in diamond quantum technologies,* Phys. Rev. Lett. **110**, 100503 (2013).

[44] L. Schlipf *et al.*, *A molecular quantum spin network controlled by a single qubit,* Science Advances **3**, 3 (2017).

[45] A. Cooper, W. K. C. Sun, J.-C. Jaskula and P. Cappellaro, *Environment-assisted quantum-enhanced sensing with electronic spins in diamond,* Phys. Rev. Appl. **12**, 044047 (2019).

[46] G. Goldstein *et al.*, *Environment-assisted precision measurement,* Phys. Rev. Lett. **106**, 140502 (2011).

[47] L. Jiang, J. M. Taylor, A. S. Sørensen and M. D. Lukin, *Distributed quantum computation based on small quantum registers,* Phys. Rev. A **76**, 062323 (2007).

[48] J. I. Cirac, A. K. Ekert, S. F. Huelga and C. Macchiavello, *Distributed quantum computation over noisy channels,* Phys. Rev. A **59**, 4249 (1999).

[49] S. Wehner, D. Elkouss and R. Hanson, *Quantum internet: A vision for the road ahead,* Science **362** (2018).

[50] N. H. Nickerson, Y. Li and S. C. Benjamin, *Topological quantum computing with a very noisy network and local error rates approaching one percent,* Nat. Commun. **4**, 1756 (2013).

[51] N. H. Nickerson, J. F. Fitzsimons and S. C. Benjamin, *Freely scalable quantum technologies using cells of 5-to-50 qubits with very lossy and noisy photonic links,* Phys. Rev. X **4**, 041041 (2014).

[52] S. de Bone, R. Ouyang, K. Goodenough and D. Elkouss, *Protocols for creating and distilling multipartite ghz states with bell pairs,* IEEE Trans. Quantum Eng. **1**, 1 (2020).

[53] H. Bernien *et al.*, *Heralded entanglement between solid-state qubits separated by three metres,* Nature **497**, 86 (2013).

[54] B. Hensen *et al.*, *Loophole-free bell inequality violation using electron spins separated by 1.3 kilometres,* Nature **526**, 682 (2015).

[55] P. C. Humphreys *et al.*, *Deterministic delivery of remote entanglement on a quantum network,* Nature **558**, 268 (2018).

[56] M. Abobeih *et al.*, *Atomic-scale imaging of a 27-nuclear-spin cluster using a quantum sensor,* Nature **576**, 411 (2019).

[57] M. H. Abobeih *et al.*, *Fault-tolerant operation of a logical qubit in a diamond quantum processor,* Nature **606**, 884 (2022).

[58] L. Stephenson *et al.*, *High-rate, high-fidelity entanglement of qubits across an elementary quantum network,* Phys. Rev. Lett. **124**, 110501 (2020).

[59] R. Stockill *et al.*, *Phase-tuned entangled state generation between distant spin qubits,* Phys. Rev. Lett. **119**, 010503 (2017).

[60] P. Drmota *et al.*, *Robust quantum memory in a trapped-ion quantum network node,* Phys. Rev. Lett. **130**, 090803 (2023).

[61] G. Davies, *Vibronic spectra in diamond,* Journal of Physics C: Solid state physics **7**, 3797 (1974).

[62] A. Faraon, P. E. Barclay, C. Santori, K.-M. C. Fu and R. G. Beausoleil, *Resonant enhancement of the zero-phonon emission from a colour centre in a diamond cavity,* Nat. Photonics **5**, 301 (2011).

[63] D. Riedel *et al.*, *Deterministic enhancement of coherent photon generation from a nitrogen-vacancy center in ultrapure diamond,* Phys. Rev. X **7**, 031040 (2017).

[64] M. Ruf, N. H. Wan, H. Choi, D. Englund and R. Hanson, *Quantum networks based on color centers in diamond,* Journal of Applied Physics **130**, 70901 (2021).

[65] L. Orphal-Kobin *et al.*, *Optically coherent nitrogen-vacancy defect centers in diamond nanostructures,* Phys. Rev. X **13**, 011042 (2023).

[66] M. K. Bhaskar *et al.*, *Experimental demonstration of memory-enhanced quantum communication,* Nature **580**, 60 (2020).

[67] P.-J. Stas *et al.*, *Robust multi-qubit quantum network node with integrated error detection,* Science **378**, 557 (2022).

[68] A. E. Rugar *et al.*, *Quantum photonic interface for tin-vacancy centers in diamond,* Phys. Rev. X **11**, 031021 (2021).

[69] J. Arjona Martínez *et al.*, *Photonic indistinguishability of the tin-vacancy center in nanostructured diamond,* Phys. Rev. Lett. **129**, 173603 (2022).

[70] E. I. Rosenthal *et al.*, *Microwave spin control of a tin-vacancy qubit in diamond,* Phys. Rev. X **13**, 031022 (2023).

[71] R. A. Parker *et al.*, *A diamond nanophotonic interface with an optically accessible deterministic electronuclear spin register,* (2023), arXiv:2305.18923 [quant-ph] .

[72] T. Iwasaki *et al.*, *Germanium-vacancy single color centers in diamond,* Sci. Rep. **5**, 12882 (2015).

[73] R. E. Evans, A. Sipahigil, D. D. Sukachev, A. S. Zibrov and M. D. Lukin, *Narrow-linewidth homogeneous optical emitters in diamond nanostructures via silicon ion implantation,* Phys. Rev. Appl. **5**, 044010 (2016).

[74] G. Thiering and A. Gali, *Ab initio magneto-optical spectrum of group-iv vacancy color centers in diamond,* Phys. Rev. X **8**, 021063 (2018).

[75] M. E. Trusheim *et al.*, *Lead-related quantum emitters in diamond,* Phys. Rev. B **99**, 075430 (2019).

[76] M. E. Trusheim *et al.*, *Transform-limited photons from a coherent tin-vacancy spin in diamond,* Phys. Rev. Lett **124**, 023602 (2020).

[77] N. H. Wan *et al.*, *Large-scale integration of artificial atoms in hybrid photonic circuits,* Nature **583**, 226 (2020).

[78] B. Jalali and S. Fathpour, *Silicon photonics,* Journal of Lightwave Technology **24**, 4600 (2006).

[79] D. M. Lukin *et al., 4H-silicon-carbide-on-insulator for integrated quantum and nonlinear photonics,* Nature Photonics **14**, 330 (2020).

[80] D. Zhu *et al., Integrated photonics on thin-film lithium niobate,* Adv. Opt. Photon. **13**, 242 (2021).

[81] R. Nagy *et al., High-fidelity spin and optical control of single silicon-vacancy centres in silicon carbide,* Nat. Commun. **10**, 1 (2019).

[82] D. M. Lukin, M. A. Guidry and J. Vučković, *Integrated quantum photonics with silicon carbide: challenges and prospects,* PRX Quantum **1**, 020102 (2020).

[83] A. Bourassa *et al., Entanglement and control of single nuclear spins in isotopically engineered silicon carbide,* Nat. Mater. **19**, 1319 (2020).

[84] W. Redjem *et al., Single artificial atoms in silicon emitting at telecom wavelengths,* Nature Electronics **3**, 738 (2020).

[85] D. B. Higginbottom *et al., Optical observation of single spins in silicon,* Nature **607**, 266 (2022).

[86] A. Gritsch, L. Weiss, J. Früh, S. Rinner and A. Reiserer, *Narrow optical transitions in erbium-implanted silicon waveguides,* Phys. Rev. X **12**, 041009 (2022).

[87] D. Riedel *et al., Efficient photonic integration of diamond color centers and thin-film lithium niobate,* (2023), arXiv:2306.15207 [physics.optics] .

ACKNOWLEDGEMENTS

This thesis may have my name on its cover, but I am indebted to many people I have been fortunate enough to work with over these past years.

First off, **Tim**, thank you for giving me the opportunity to do my Ph.D. in your group. It started off with a M.Sc. project back in 2017/2018, after which I was convinced I wanted to continue for a Ph.D. The amazing group of people you have managed to bring together speaks volumes about your qualities as a group leader. I have thoroughly enjoyed our many discussions about spin pairs, spin physics, gate characterisation and the many other topics that came up. And if there ever was a time when I was not as excited about my results, your enthusiasm would get me right back on track! **Ronald**, thank you for being my promotor and all the discussions & advice along the way. As the Founding Father of Team Diamond, you have built a very positive & encouraging scientific environment here in Delft. It has been inspiring to be a part of that.

Sander Otte, my first research project during my M.Sc. was in your group. Thank you for teaching me how experimental physics research is done - I learned a lot from my time in your group! **Patrice Bertet, Floris Zwanenburg, Leo DiCarlo, Barbara Terhal**, thank you all for taking the time to participate in my Ph.D. committee. I admire all the work you do. **Christian Degen, Kristan** and others at the Degen group, thank you for hosting me for almost three months back in my M.Sc. The valuable experience I gained in your group has made me a better researcher.

Slava, thank you for the many discussions, be it scientific or about the first word in the English dictionary (it is not aardvark). I hope you keep visiting the 'nanotennis'-office! **Fabio, Masoud**, thank you for the collaborations over the past two years, it's been exciting to see our 'worlds' come together in a single experiment!

Team Diamond has been an amazing, inspiring environment to work in. There are many people that preceded me and many more that will come after. I would like to thank everyone in Team Diamond for making the past years so wonderful.

Mohamed, thank you for teaching me the ropes. My M.Sc. project with you was my entryway into my Ph.D. and I learned a lot from you about physics, how to perform experiments and what *should* be considered a proper lunch. I hope you are well. **Conor**, my many questions and your many answers have made me a better researcher, so thank you for that. It's been exciting to see the new results from Chicago and I wish you all the best there! **Joe**, you and Conor laid the 'DDRF'-foundation that we're all very much building on today. Thank you for the good times. **Maarten**, I really enjoyed working together on 'Gretel' back when I started my Ph.D. I learned a lot from you about the experimental setup and the piezo experience we built up in those days is still proving useful!

Nicolas, we have learned a lot together these past years: P1 centers are complicated, especially if they come in pairs! I have really enjoyed working with you - you're always

enthusiastic and eager to understand. I'm really fascinated by the current experiments you're doing and I'm excited to see where it goes! Thank you for these past years.

Jiwon, we have worked together closely for about a year and a half now. I have really enjoyed staring at error generators, understanding puzzling nitrogen rotations and pushing gate fidelities, as well as playing table tennis. Together with Kai and Margriet, we make a great team, which is what allowed us to finish the 'HFSQG' project in such a short amount of time!

Margriet, we started the new endeavour of 100 K experiments during your M.Sc. I'm really happy you decided to stay for a Ph.D. and it's been a lot of fun working together on high-fidelity gates and the 100 K project. I'm excited to see these projects come together in the future! **Kai**, it basically feels like we shared an office due to your frequent presence on the couch in F027. Next to the many discussions about GST, it was great to be able to discuss cycling in detail - in particular the Tour de France. And to play some office-sports. I hope one of the future samples will set a new benchmark for high-fidelity gates! **Benjamin (van Ommen)**, I really enjoyed our physics discussions, and you certainly helped a lot in providing new (and clarifying old) insights into the DDRF gate. I'm looking forward to see where we can push ^{13}C control! Still, the most important open question remains unanswered: nanotennis backhand or forehand smash, which is more powerful?

Nico, you jumped into spin-pair control for your M.Sc. project and we're still building on your work. Your uncurbed enthusiasm is missed here, but I'm sure you're doing an awesome job in Waterloo! **Sjoerd**, we have overlapped for a long while now. I've always appreciated your critical & positive attitude, even when strange AWG issues keep popping up. I enjoyed our extended P1 center discussions. You're next in line, now! **Guido**, your drive to understand difficult topics by coming up with an intuitive interpretation is astounding. It's been fun discussing all sorts of topics, be it spin physics or economics & investment plans back in Barcelona. **Damian**, you provided valuable theoretical insights in the experiments we were doing. Your sense of humour certainly made us all happier. I hope the clogs walk okay and all is well in Poland! **Benjamin (Pingault)**, the work on ^{13}C pairs we did together finally resolved the mystery of the minute-long coherence times! It was great having you in Delft for a longer period after that. All the best in Chicago!

Laurens, it's been great sharing an office with you! It's admirable how you - together with Sjoerd, Guido, Gerben and Tijmen - built up the SiC wing of our group. It's exciting to see the first results coming in. Your outreach activities and in particular the nanoart project are wonderful! I hope to still play you in table tennis one of these days. **Christina**, inheriting a 50-spin cluster has its pros and cons. The determination with which you've been able to sift through the code is admirable, and I'm curious what interesting physics you can uncover in the future! **Gerben**, your cleanroom magic amazes me every time you show new pictures, both the nanoart images and the actual devices! Good luck for the years to come. **Anta**, dankjewel for all the advice on thesis-related topics. En heel veel succes in Barcelona!

Bachelor and master students make up an integral part of any research group, so **Thomas, Beer, Tijmen, Dani, Asier, Remon, Floris, Peter**, thank you all for your lasting contributions and good luck with your next steps!

Luc, we have worked together for quite a while now. It's been enlightening - to say

the least - to discuss electronics-related topics with you. You helped start the 'HFSQG' project which later turned into the 'HFTQG' project. It's been a lot of fun working together and I'm excited for future experiments. **Niels**, it's been valuable to learn from you about microwave driving, and it's great to see things come together now. **Takashi**, your diamond magic will have a long-lasting impact in the years to come.

Julia, I'm really happy you ended up joining Team Diamond! I'm thankful for all the dinners we shared with Bart & Dawn, and I'm sure we'll both be much better swimmers in twenty weeks from now! **Alejandro**, thank you for all the laughs! I wish we could've played more table tennis with volleys still; good luck with everything in London! **Hans**, I will certainly miss the 'Hee Hans', 'Hee Hans' exchanges. Your enthusiasm for physics (and generalised code) are contagious and I've really enjoyed our discussions. I'm looking forward to you & Chris unleashing the power of GST.

Arian, **Kian**, it's been a privilege to see all the hard work you put in come to fruition over these past years. Good luck with the final steps of your Ph.D.s! **Tim**, you've become my office-neighbour only recently, but it's been great to watch your progress in making paper figures. Good luck these next few years!

Yanik, the trip after the March Meeting in Las Vegas certainly stands out, and in particular your fondness for driving. Now we know what to expect from Utah winters. **Julius**, your performance at the Diamond Cup was something special - you excelled in every sport. Fortunately there was still a ball throwing competition. I wish you and Yanik all the best with the next-generation cavity experiments!

Matteo (Pasini), thank you for your initiative to host TPKV, and for encouraging everyone to join. Good luck with the final steps of your Ph.D.! **Christopher**, your experiments are looking promising, good luck! **Mariagrazia**, I'm excited to see what the new round of network experiments will produce! Thank you and Chris for organising a wonderful Uitje last year.

Christian, I hope the piezos will be kind! I'm sure you'll do wonderful work during your Ph.D. **Nina**, thank you for the hallway talks, it's always exciting to see what cleanroom magic you manage to pull off! **Lorenzo**, good luck with your next step!

Max (Ruf), I still remember my meeting with you for a potential M.Sc. project. I hope to run into you in Delft again before long. **Sophie**, I have now inherited your desk. The experiments you, **Matteo (Pompili)**, **Simon** and Hans performed will remain defining ones. Matteo, your technical proficiency has helped streamline all our experiments. Simon, I'm excited to see where your future research takes you. **Matthew**, all the best at QphoX, and **Marie-Christine**, good luck back in Austria! **Peter, Norbert, Suzanne**, we only briefly overlapped, but thank you for making Team Diamond such a special place! I would also like to pay tribute to all the M.Sc. students of the Hanson lab: **Zarije, Elvis, Colin, Caroline, Sezer, Sarel, Otmar, Lisa, Annick, Kamiel, Stein, Thomas, Marianne, Guus, Santiago, Romy, Mark, Airat**. Thank you for all your contributions!

Johannes, our discussions about gate set tomography certainly helped us move forward. **Max (Russ)**, thank you for your insights into GST and good luck starting your own group here in Delft. **Jelmer** and **Chien-An**, we briefly shared an office, thank you for the good times!

QuTech is a complicated organism and it would not function properly - or even at all - without its amazing support staff. **Sara, Esther, Marja, Chantal**, thank you for all your

help. And to the technical support staff, **Raymond, Raymond, Remco, Jelle, Roy, Vinod, Mark, Siebe, Jason, Olaf, Nico, Mariya, Régis, Pieter, Henry, Ravi**, you have made all our experiments possible. **Leonie, Grazia, Aldo, Erik**, thank you for all your efforts to bring 'quantum' to a wider audience.

Naturally, I won't be able to mention everybody that I've interacted with over the years at QuTech. So, I would like to acknowledge and thank everyone that made my time here memorable. I'm sure all of you will do great things.

To **Anthony, Arjan, Bas, Chris, Hidde, Luuk, Mark, Martijn, Milan, Mitchel**, thank you for all the laughs, distraction and encouragement. Not only over these last few years, but ever since we've met.

To **Dawn, Bart** and Julia, thank you for all the 'eetclub' nights, Brouwhuis experiences and places we've been to. I'm very thankful all of you decided to come to Delft and are still here. And I'm sure one of these days we'll commercialise 'BELP'. **Victoria**, thank you for all your help, my thesis would not have looked remotely as nice without it.

To my family, I want to thank each and everyone of you for your continuing interest & support. **Toos & Wenno**, many of my favourite childhood memories involve you, whether it is a holiday in Sweden or simply table tennis under the carport. **Sjoerd**, from trading Pokémon cards when we were younger to playing chess today, you've been there for everything. **Dick & Marijke**, our family dinners are without question one of my favourite moments of the year. I'm already looking forward to the next one.

Papa & mama, thank you for your love & support, in good and bad times. I hope you're proud. And you know as well as I do that these acknowledgements wouldn't be complete without mentioning our cat **Gerrit**.

Hans Bartling
Delft, August 2023

List of Publications

6. *High-fidelity quantum control of an electron-nuclear spin register in diamond.*
H.P. Bartling*, J. Yun*, K.N. Schymik, M. van Riggelen, L.E. Enthoven, H.B. van Ommen, M. Babaie, F. Sebastiano, & T.H. Taminiau,
in preparation.

5. *Imaging and control of interacting spin pairs in an electron-spin bath.*
H.P. Bartling*, N. Demetriou*, N.C.F. Zutt, D. Kwiatkowski, M.J. Degen, S.J.H. Loenen, C.E. Bradley, M. Markham, D.J. Twitchen, & T.H. Taminiau,
in preparation.

4. *Robust quantum-network memory based on spin qubits in isotopically engineered diamond.*
C. E. Bradley, S. W. de Bone, P. F. W. Möller, S. Baier, M. J. Degen, S. J. H. Loenen, **H. P. Bartling**, M. Markham, D. J. Twitchen, R. Hanson, D. Elkouss & T. H. Taminiau,
npj Quantum Information **8**, 122 (2022).

3. *Entanglement of spin-pair qubits with intrinsic dephasing times exceeding a minute.*
H. P. Bartling, M. H. Abobeih, B. Pingault, M. J. Degen, S. J. H. Loenen, C. E. Bradley, J. Randall, M. Markham, D. J. Twitchen, & T. H. Taminiau,
Physical Review X **12** (1), 011048 (2022).

2. *Entanglement of dark electron-nuclear spin defects in diamond.*
M. J. Degen*, S. J. H. Loenen*, **H. P. Bartling**, C. E. Bradley, A. L. Meinsma, M. Markham, D. J. Twitchen, & T. H. Taminiau,
Nat. Commun. **12**, 3470 (2021).

1. *Atomic-scale imaging of a 27-nuclear-spin cluster using a quantum sensor.*
M. H. Abobeih, J. Randall, C. E. Bradley, **H. P. Bartling**, M. A. Bakker, M. J. Degen, M. Markham, D. J. Twitchen, & T. H. Taminiau,
Nature **576**, 411 (2019).

*Equally contributing authors

CURRICULUM VITÆ

Hans Peter Bartling

2019 - 2023	Ph.D. in Physics, *Delft University of Technology* Thesis: Quantum Control of Interacting Nuclear and Electron Spins in Diamond Group: Taminiau Lab, QuTech Promotors: Dr. ir. T.H. Taminiau & Prof. dr. ir. R. Hanson Delft, the Netherlands
2016 - 2018	M.Sc. in Physics, *Delft University of Technology* Thesis: Controlling Nuclear Spin Clusters in Diamond: a Novel Qubit Advisor: Dr. ir. T.H. Taminiau Delft, the Netherlands
2015 - 2016	Imperial College International Diploma in Physics London, UK
2013 - 2016	B.Sc. in Technology and Liberal Arts & Sciences, *University of Twente* Thesis at Imperial College London: Centrality on Directed Acyclic Graphs: A Comparison of Various Centrality Indices Advisor: Dr. Timothy Evans Enschede, the Netherlands
2007 - 2013	Secondary School, *Christelijk Lyceum Apeldoorn* Apeldoorn, the Netherlands
13/10/1994	Born in Apeldoorn, the Netherlands